

Sol-Gel derived Ferroelectric Thin Films for Voltage Tunable Applications

by

Arne Lüker

Supervisor: Dr. Paul B. Kirby
Co-Supervisor: Dr. Qi Zhang

A thesis which is presented to the

University of Cranfield
School of Applied Sciences,
Department of Materials,
Microsystems and Nanotechnology Centre,

in partial fulfillment of the requirement for the degree of

Ph.D

in

Material Science/Nanotechnology

Cranfield, England, and Holsen, Germany, 2009

© Arne Lüker, 2009

J or psi
(a physicist's four footed sonnet)

*Where is the thing beneath the thing?
When can we say we have found it all?
Is there an end or just a string
That dangles down like an endless fall?*

*Molecules, yes, and atoms too,
Electrons we know, and nuclei;
Neutrons, protons, the particle zoo,
And enter now the J or psi.*

*Can we not try to knot the string,
To start from the bottom and see what grows?
Plant us a seed and see what we get
When unity doubles and does its thing
And triples, quadruples, quintuples. Who knows
What patterns will show? What world is there yet?*

Roger E. Clapp

Abstract

Ferroelectric perovskite thin films for voltage tunable applications, namely (Ba,Sr)TiO₃ (Barium Strontium Titanate or BST) and (Pb,Sr)TiO₃ (Lead Strontium Titanate or PST), are synthesized via the so-called sol-gel route. While BST shows the tendency to severe film cracking, PST can be grown crack free onto platinised Si standard substrates and even directly onto SiO₂, SiN_x or bare Si.

The growth kinetics of PST on platinised SiO₂/Si and directly on SiO₂/Si are studied in detail using X-ray diffractometry (XRD), scanning electron and atomic force microscopy, SEM and AFM respectively. It is shown that PST begins to crystallise at 500°C on Ti/Pt and 550°C directly on SiO₂. After a thermal treatment of 650°C for 15 min both films are fully crystallised with random (100) and (110) orientation and a smooth surface.

The dielectric properties, e.g. dielectric constant, loss and tunability, of PST 50/50 are measured using a standard Ti/Pt bottom electrode with Cr/Au top electrodes and a TiW/Cu bottom electrode on which the PST thin film was bonded with TiW/Cu top electrodes. The Cu/PST/Cu system shows an enhanced performance in terms of loss resulting in a larger device quality factor and a figure of merit (FOM) of 18.25 compared to 16.6 for the configuration using a Pt bottom electrode. The maximum tunability is 73% with an applied voltage of 35V and the dielectric constant at zero bias is ~ 420 with a loss < 4 %.

(Pb_{0.4}Sr_{0.6})(Mn_xTi_{1-x})O₃ (Mn doped PST 40/60) thin films with x = 0, 0.01, 0.03, and 0.05 are grown on Ti/Pt coated SiO₂/Si substrates. The surface morphologies, dielectric and tunable properties of these films are investigated as a function of Mn content (x). It is found that the grain size/roughness, dielectric constant, loss, tunability and figure of merit are affected by the Mn doping level. Further on it is found that the ferroelectricity and the transition temperature between the cubic paraelectric and tetragonal ferroelectric state increase with Mn content. The dielectric constant at zero bias reaches a maximum of 1100 and the maximum FOM is 23.96 with 3 mol% Mn; whereas the maximum value of the tunability is 76.72% at 10 V with 1 mol% Mn.

A detailed understanding of the effect of Mn doping is developed and presented. It is found and explained that a doping level of 2 mol% Mn results in optimal properties in terms of tunability and loss.

Auger spectroscopy is used to study the compositional change in the interfacial region between PST and PZT thin films and SiO₂/Si substrates to understand the growth kinetics of PST directly onto SiO₂ in more detail. The thin films from both materials are annealed under the same conditions (temperature and time). It is found that strontium stops the lead diffusion into SiO₂ by forming SrSiO₃/Sr₂SiO₄ and/or SrO, maintaining a well defined SiO₂ region, while PbSiO₃ is formed in the PZT/SiO₂ system. It is shown that SrO covalently saturates all Si dangling bonds by forming SrSiO₃ and/or Sr₂SiO₄. This provides the necessary ionic template towards the perovskite SrO-terminated SrTiO₃, on which PST can grow further on.

A single layer of PST is finally used as a buffer layer for the growth of piezoelectric PZT directly onto SiO₂ to replace the common Ti/Pt bottom electrode. The initial characterisation of PZT device structures shows that PZT films with PST as a diffusion buffer had fully crystallized in the perovskite phase exhibiting good dielectric and ferroelectric behaviour. Although the piezoelectric coefficients of the PZT films were not measured directly in this study, it is envisaged from the experimental data of the dielectric constant and hysteresis loop that the PZT/PST composite has the potential to provide good and comparable piezoelectric performances as typically observed in PZT device structures grown on commonly used Ti/Pt.

Acknowledgements

I want to take this opportunity to thank all the people who have helped me and who continue to inspire me.

My supervisor, Paul B. Kirby, is the most influential person in my academic life so far. I learned him to know not only as a kind supervisor, who showed a real interest in my work, gave me free space to work in my own way (always late mornings and sometimes early evenings) and pushed me when it was really necessary, but also as a great friend, who helped me personally, whenever the time was hard. I am really grateful that his door was always open for me whenever I needed guidance and an ear to listen to my problems, whether they were of academic nature or personal.

As a student who had only a basic background of chemistry, I am really happy that my co-supervisor, Qi Zhang, never lost patience to answer my silly questions. He always pointed me in the right direction and is, without doubt, a great teacher and the driving force throughout my studies of sol-gel chemistry, publications and this thesis.

Without the help from Margaret Norwich, Lynne Badr, Teresa Townsend and Dawn Packham the latter never would have been written. I do not want to go into details, but without them I would have surely given up my studies at Cranfield. I will be deeply thankful forever for all the power, understanding, help and friendly words they gave me, whenever I really needed them.

A true inspiration and friend for many years now is Karl Dieter Möller. Until now I do not know what he wrote in my recommendation to get accepted as a PhD student at Cranfield, but I believe it gave the kick. Without him I would not have started it in my age. And Paris was just fantastic!

Joachim Schulz, Herbert Hein and Rainer Fettig were leading me into the field of serious science before I went to Cranfield and I am grateful that I can still call them friends. I would like to thank especially Rainer Fettig and his family, who gave me a friendly home whenever I visited Karlsruhe and who helped me preparing this thesis.

It is long ago, but I have to thank Jürgen Chlebek, my first Professor of Microtechnology. His course in Steinfurt/Münster was the foundation stone for my academic career up to now and sometimes I still consult the script of it, thank you.

To all my friends in Cranfield (in no particular order and sorry if I forgot one or two): Robert Wright, Carlos Fragkiadakis, Petros Gkotsis, Hannah Gardner, David Darbyshire, Glen Leighton, Silvana Corkovic, Diego Gallardo, Debu Bhattacharyya, Emma Worthington, Paul Jones and Ghazal Hakemi, thank you! It was a pleasure to know you, and I wish you all the best for your future, wherever it will lead you. Hopefully we see us again sometimes - somewhere.

Special thanks go to Andrew Stallard and Matthew Taunt for their never ending effort to keep our labs running. You are doing a marvelous job, guys! And thank you for your jump lead, Andy!

I want to thank also the panel of my first and second year review: Dr. Robert Dorey and Dr. Robert Allwood as well as my internal examiner Dr. Zhaorong Huang and external examiner Prof. Dr. Bernd Ploss. They treated me critical but fair and always nice. I appreciated that. And sorry for the delay of these reviews.

And I have to thank Peng Bao for his help with the measurements at high frequencies in Birmingham and fruitful discussions, and Andreas Fritz for printing and binding several copies of this thesis.

But the biggest thank you goes to my parents, Inge and Rolf Lüker! I started school at seven and I am now 34. That means 27 years of hope and suffering, pride and worries, joy and tears and money spending. Who else would have endured all this for so long, except you? I love you and can not thank you sufficiently enough. This thesis is dedicated to you!

I thank you all!

Arne Lüker, Holsen, 29th of November 2009

Table of Content

Introduction and Motivation	7
Historical Remarks.....	12
1.1 A Short History of Ferroelectricity.....	12
1.2 A Short History of Sol-Gel	20
1.3 Materials for Tunable Applications – State of the Art.....	23
1.4 References.....	27
Theoretical Considerations and Literature Review.....	32
2.1 Theory of the Dielectric Response of Tunable Materials	32
2.1.1 Dielectric Permittivity.....	32
2.1.2 Tunability.....	34
2.1.3 Figure of Merit	36
2.2 Dielectric Loss in Ferroelectrics	37
2.2.1 Intrinsic Losses	37
2.2.2 Extrinsic Losses	40
2.4 Crystallography of Perovskites	43
2.4.1 The crystal structure of perovskite.....	43
2.4.2 Electronic and Magnetic Properties of Perovskites	48
2.5 Sol-Gel Chemistry	54
2.5.1 Solution Preparation.....	54
2.5.2 Film Deposition	59
2.5.3 Gel to Ceramic Conversion.....	63
2.6 References.....	64
Characterisation of Ferroelectric Thin Films.....	70
3.1 Sputter deposition and Thermal Evaporation	71
3.1.1 Sputter Deposition	71
3.1.2 Thermal evaporation.....	72
3.2 Analysis.....	73
3.2.1 X-ray Diffraction Analysis (XRD)	73
3.2.2 Scanning Electron Microscopy (SEM).....	74
3.2.3 Polarisation Hysteresis Measurement.....	75
3.2.4 Atomic Force Microscopy (AFM).....	76
3.2.5 Curie Temperature Measurement	76
3.2.6 Auger Emission Spectroscopy (AES).....	77
3.3 References.....	79
Barium Strontium Titanate (BST)	81
4.1 A Short Review of BST Deposition.....	82
4.2 Synthesis and Characterisation of BST.....	85
4.3 Discussion	89
4.4 References.....	92
Lead Strontium Titanate (PST).....	95
5.1 Synthesis and Crystallisation of PST.....	96
5.2 Dielectric Properties of PST 50/50	100
5.3 PST 50/50 Varactors with Copper Electrodes	102
5.4 References.....	107

B Site Doping of PST 40/60	110
6.1 Synthesis and Characterisation of $(\text{Pb}_{0.4}, \text{Sr}_{0.6})(\text{Ti}_{1-x}, \text{Mn}_x)\text{O}_3$	110
6.2 Enhanced Tunability and Ferroelectricity in Mn doped PST	118
6.3 References.....	123
PST directly on SiO_2	127
7.1 The growth of PST on SiO_2	128
7.1.1 The interface between SrTiO_3 and Si.....	132
7.2 Auger Analysis of PST on SiO_2	134
7.3 References.....	139
PST as a buffer layer for PZT on SiO_2	142
8.1 XRD-Studies	144
8.2 Microstructure Evaluation	148
8.3 Electrical Characterisation of PZT with a PST buffer layer	151
8.4 References.....	153
Final Discussions, Conclusions and Future Work	156
9.1 References.....	160
Appendix A: PZT actuated Diamond Cantilever Technology.....	162
A.1 Introduction.....	162
A.2 Design	163
A.2.1 Modes of operation	163
A.2.2 Resonance Behaviour.....	164
A.2.3 Cantilever deflection.....	166
A.3 Technology	168
A.4 Results.....	169
A.5 Conclusions.....	170
A.6 References.....	171
Appendix B: Curriculum Vitae.....	172

Introduction and Motivation

Ferroelectricity was discovered in the beginning of the last century by J. Valasek in Rochelle salt (potassium sodium tartrate) which was originally produced in France in 1665 by an apothecary Elie Seignette. Rochelle salt was originally used in medicine as a mild purgative. Crystals of Rochelle salt were easily grown and were subsequently used in piezoelectric devices such as crystal microphones and phonograph pickup cartridges. Historically, ferroelectricity was discovered after piezoelectricity and pyroelectricity. The ceramic BaTiO₃ (Barium Titanate), was found by B. Wul and I. M. Goldman. This discovery triggered considerable efforts in search of additional ferroelectrics having the same perovskite structure. A significant progress in applications was made possible after the discovery of Lead Zirconate Titanate - Pb(Zr,Ti)O₃ or PZT – which has a very strong piezoelectric response, and a large remnant ferroelectric polarization. Lead-based materials have since become the dominant compounds in this field.

Later on it was discovered that one could decrease the Curie temperature (ferroelectric-paraelectric transition temperature) T_C of pure BaTiO₃ ($T_C \sim 120$ °C) down to room temperature by adding Strontium (Sr). From there on Ba_{1-x}Sr_xTiO₃ (BST) began to rock the world. The initial interest in BST thin films was due to its high dielectric constant, low dielectric loss, high dielectric breakdown and composition dependent Curie temperature enabling it to be in the paraelectric state as well as in the ferroelectric state, all of which makes it a candidate for replacing SiO₂ as charge storage dielectric for DRAMs (dynamic random access memories), MEMS-switches and varactors in phase shifters.

It is worthwhile to define some basic physical characteristics within ferroelectrics:

1. Pyroelectricity

Pyroelectricity was probably first observed in tourmaline by ancient Greeks, but quantitatively investigated only in the eighteenth century, during the early studies of electrostatics. Sir David Brewster, a Scottish scientist, was the first to use the term pyro-(fire)-electricity in 1824 when describing this phenomena in one of his numerous and famous contributions to the Encyclopaedia Britannica. Pyroelectric

materials have a spontaneous polarization whose amplitude changes under the influence of temperature gradients. The discovery of PZT triggered many applications based on this phenomenon, such as infrared detection, thermal imaging (absorption of energy resulting in polarisation changes) and dielectric bolometers.

2. **Piezoelectricity**

Piezoelectricity was discovered later, around 1880, by Pierre and Jacques Curie who were the first to demonstrate the generation of electricity (surface charges) on well prepared crystals of quartz as a result of mechanical pressure. Inversely, when a voltage is applied across a piezoelectric material, it can undergo a mechanical distortion in response. The beginning of the twentieth century gave birth to most of the classic applications of piezoelectrics, such as quartz resonators, accelerometers and those already mentioned above. After World War II and following the discovery of PZT, the advances made in material science allowed the development of numerous applications based on tailored piezoelectric properties.

3. **Ferroelectricity**

All ferroelectrics are piezoelectric and pyroelectric, but they additionally possess a reversible, non-volatile macroscopic spontaneous electric dipole moment in the absence of an external electric field. In simple words, ferroelectric crystals can be seen as an assembly of batteries with a particular orientation, which remains stable unless an external electric field is applied to change its direction. Their polar state is a consequence of the structural transition from a high-temperature, high-symmetry paraelectric phase to a low-temperature, low-symmetry ferroelectric phase. These materials also behave as high dielectric-constant insulators useful in the development of capacitors and energy storage materials.

Ferroelectrics, especially perovskites, are truly multifunctional materials widely used in electronic, optical, acoustic and magnetic components. The first attempts of microwave

applications date back to early 1950s. In the past most of the developed microwave devices have been based on bulk ceramics such as $BaTiO_3$, $SrTiO_3$ and their solid solutions - $Ba_xSr_{1-x}TiO_3$. However, the high microwave losses associated with the poor quality of the used ceramics limited their applications in practical microwave devices. With the advances in modern technology the quality of the epitaxial thin film ferroelectrics has been substantially improved making them qualified for industrial applications. Although there are many other perovskite systems with promising microwave performances $Ba_xSr_{1-x}TiO_3$ still remains the workhorse for the agile microwave applications since it is more studied both in terms of electrical performance, manufacturability and reliability. Thin film varactors and bulk acoustic resonators are the basic components that are used in modern microwave circuits and systems. Ferroelectric varactors have superior performances, in comparison with the competing semiconductor analogues, both in terms of the Q-factor and tunability; especially at frequencies above 10-20 GHz. Apart from the high tuning speed they have extremely low leakage currents offering design flexibilities and low control power consumption. Today there are several small, and well established companies marketing microwave components based on ferroelectrics. Nevertheless the full potential, especially their multifunctionality, of these materials is not yet employed.

This thesis focuses on the synthesis and characterisation of ferroelectric thin films, namely Barium Strontium Titanate, $(Ba,Sr)TiO_3$ or BST, and Lead Strontium Titanate, $(Pb,Sr)TiO_3$ or PST, for voltage tunable devices. Ferroelectrics show the highest tunability in the paraelectric phase close to the Curie temperature. Therefore the discussion of these materials will be mostly focused on the paraelectric state. The films were developed via the so-called sol-gel method. Compared to Pulsed Laser Deposition (PLD), a method which produces ferroelectric films with superior properties, this method is comparable cheap and allows the deposition onto large substrates. Initially this work was part of a joined project between the University of Birmingham, the Heriot Watts University Edinburgh and Cranfield University. Birmingham provided BST films made via PLD for devices designed at Heriot Watts. Cranfields (and my) task was to produce BST films made by sol-gel with comparable properties for larger scale production (Birmingham is restricted to sample sizes $5 \times 5 \text{ mm}^2$). Therefore this thesis starts with sol-

gel synthesis and characterization of BST. Reasons for a reorientation towards (Pb,Sr)TiO₃, which is a relative new material for tunable applications and to a lesser extent characterized, are given and explained. PST offers a higher tunability and a lower loss than BST and has some remarkable properties, which are unique, therefore the main focus in this thesis will be on PST.

This thesis is presented in nine chapters. Chapter 1 deals with the history of ferroelectrics and sol-gel techniques and reviews the state-of-the-art of materials for tunable applications with the main focus on varactors. The purpose of this chapter is to give an easy to read introduction in these fields of science. The subject of chapter 2 are physical and chemical issues which did not fit in chapter 1 e.g. the theory of the dielectric response according to the Landau-Theory, a theoretical treatment of losses in ferroelectric crystals, the crystallography of perovskite materials and the theory of sol-gel synthesis. Chapter 3, entitled *Characterisation of Ferroelectric Thin Films*, describes the experimental details within this work.

$Ba_xSr_{1-x}TiO_3$ is the subject of chapter 4. Because this material is of scientific interest for decades now an individual literature review of sol-gel prepared BST films and applications is given here. Despite numerous attempts this material could not be deposited successfully. Serious crack formation were a major obstacle and led at the end to a reorientation towards (Pb,Sr)TiO₃, the subject of chapter 5. Apart from the crystallisation pathway and dielectric properties of PST 50/50 thin films a simple application is described in this chapter: a varactor using copper electrodes to boost the overall quality factor. Chapter 6 deals with the effect of B site doping of PST 40/60. Three different theories from the literature are presented, one was adopted to explain the properties of Mn doped PST.

The growth of PST directly on SiO₂ is the subject of chapter 7. Actually the ability of PST to grow crack free on SiO₂ was discovered by accident while working with a patterned Pt bottom electrode. BST and PZT crack and blister directly on SiO₂ and the question “Why does PST grow without an additional interlayer like Pt?” led to an in-depth analysis of the interfacial regions between PST/SiO₂ and PZT/SiO₂ by Auger Emission Spectroscopy.

The multifunctionality of PST is the topic of chapter 8, where PST serves as a buffer layer for piezoelectrical PZT. PST has a similar perovskite-type structure and a lattice mismatch of only ~3% to PZT. The specialty of PST to grow crack free on SiO₂ would help to incorporate PZT with patterned bottom electrodes, a matter which is still fairly complex and difficult.

The thesis ends with a conclusion chapter that also looks towards the future and assesses the ramifications of this research.

Historical Remarks

1.1 A Short History of Ferroelectricity

It all began with a salt in La Rochelle, a small but important city at the south-west coast of France. Jehan Seignette, born in 1592, a militant protestant, succeeded to run a pharmacy in spite of serious obstacles opposed to him by the clerics. One of his sons, Pierre, born in 1623, became a medical doctor at the University of Montpellier and his younger brother Elie, born in 1632, took over his father's business. In these years pharmacy consisted mainly in extracting plants and distilling essences. Apparently purgatives such as "folia sennae" introduced to Europe by Arab medical men in the early middle age, played an important role. Because of unpleasant side effects patients were very reluctant to take them. This was the reason Dr. Seignette suggested to his brother to look for some mineral drugs or to make some. Although "mineralia" were in use for curing various diseases in eastern countries already 2000 years B.C., Pierres idea was decisive. As the result of hard work Elie came out with a salt in approximately 1665, which he called "sel polychreste" derived from the greek *πολυχρηστος*, which means a salt of various utilities. It was a real creation and the way he produced the salt was kept secret for ever it seems [1].



Fig. 1.1: David Brewster

Only 65 years later the French pharmacist and chemist Simon Boulduc in Paris found out by analysis that sel polychreste must be "some soda" [2]. It is likely that Elie Seignette started from crème of tartrate (potassium hydrogen tartrate) he obtained from wines – so famous and abound in the Bordeaux region – and soda which makes the tartrate soluble in water. The "sel polychreste" – or Rochelle salt as we know it today - conquered the market in France, especially in Paris and it was in widespread use for more than two centuries as a mild drug.

In the nineteenth century – nearly 200 years after its discovery - the physical properties of Rochelle salt began to excite interest. In 1824 David Brewster had observed the phenomenon of pyroelectricity in various crystals, among which was Rochelle Salt [3] but perhaps the first systematic studies were those of

the brothers Pierre and Paul-Jacques Curie in 1880 [4]. This classic work established unequivocally the existence of the piezoelectric effect and correctly identified Rochelle Salt and a number of other crystals as being piezoelectric. They also noticed that Rochelle salt was by far more active than quartz for instance and all the rest of the crystals they investigated. But the fascinating dielectric features of Rochelle salt escaped them.

Thomas Alva Edison was maybe the first who used its piezoelectrical effect in a commercial application in 1899 –



Fig.1.3: Thomas Alva Edison with his phonograph, 1899

the phonograph. However, his invention was just a curiosity and far too expensive. At this time Rochelle salt was of pure academic significance.

During World War I, however, physicists and electrical engineers showed an increasing interest in its physical properties mainly because of its unusually high piezoelectric moduli. At the beginning of the war 1914-18 A.M. Nicholson in the USA [5] and Paul Langevin in France [6], a former student of Pierre Curie and a lover of Marie Curie after Pierres death, began to perfect independently an ultrasonic submarine detector. Their transducers were very similar: a mosaic of thin quartz crystals glued between two steel plates (the composite having a resonant frequency of about 50 KHz), mounted in a housing suitable for submersion. Working on past the end of the war, they did achieve their goal of emitting a high frequency "chirp" underwater and measuring depth by timing the return echo. The strategic importance of their achievement was not



Fig. 1.2: Jacques and Pierre Curie with parents



Fig. 1.4 Paul Langevin



Fig.1.5: Peter Debye

overlooked by any industrial nation, however, and since that time the development of sonar transducers, circuits, systems, and materials has never ceased.

Petrus Josephus Wilhelmus Debye, or Peter Debye as we know him today, professor of theoretical Physics at the University of Zürich had carefully observed the work on piezoelectricity and in 1912 he came up with an idea. To explain the results he knew he brought forth the hypothesis that certain classes of molecules carry a *permanent electric dipole moment* in analogy to the magnetic moment of the atoms of paramagnetic substances. Following Langevin's theory of paramagnetism Debye gave the equation $(\epsilon - 1)/(\epsilon + 2) = a + b/T$, where a is proportional to the density of the substance and b to the square of the electric dipole moment [7]. This relation was perfectly confirmed later in many cases.

Debye came to a further conclusion. According to his relation for a critical temperature $T_K = b/(1-a)$ the dielectric constant reaches infinity. Therefore, he proposed T_K to be the analogue to the Curie temperature of a ferromagnet. For temperatures lower than T_K a *permanent dielectric* polarisation ought to be expected even in the absence of an electric field. To his knowledge, he said, no such a phenomenon had been observed so far. The

basic feature of *ferroelectricity* was anticipated, however!



Fig. 1.6: Erwin Schrödinger 1933

Erwin Schrödinger in his "Habilitationsschrift" submitted at the University of Vienna late in 1912, the year Debye published his „Vorläufige Mitteilung“, went a step further. He elaborated on Debye's simple model and tried to extend it to solids. If this could be done successfully, Schrödinger speculated, then all solids should become "ferroelektrisch" at a sufficiently low temperature [8]. So, in fact, the term ferroelectric or ferroelectricity was coined by Schrödinger as early as 1912!

Another major contributor to the early Rochelle Salt period was Joseph Valasek. Born on April 27, 1897 in Cleveland,

Ohio, he got his bachelor's degree in physics at Case Institute of Technology where Prof. D. C. Miller started him on a career in physics. His first employment was at the National Bureau of Standards in Washington D.C., where he got familiar with various methods of pyrometry applied in steel industry. In this connection he learned about the phenomenon of ferromagnetism both theoretically and experimentally. In 1919 he came to the University of Minnesota in Minneapolis as a graduate teaching assistant.

Under the supervision of Prof. W. F. G. Swann, a physicist known by his theoretical work in cosmic rays physics but also known to have a wide overview in many other directions, Valasek began a systematic study of the analogy between the magnetic properties of ferromagnetics and the dielectric properties of Rochelle Salt. Joseph

Valasek presented his first paper on "Piezoelectric and allied Phenomena in Rochelle salt" at the meeting of the American Physical Society in Washington in April 1920. He stated: "... the dielectric displacement D , electric intensity E , and polarisation P ... are analogous to B , H and I in case of magnetism." The data ... "is due to a hysteresis in P analogous to magnetic hysteresis. This would suggest a parallelism between the behavior of Rochelle salt as a dielectric and steel, for example, as a ferromagnetic substance.

Bearing out this idea, typical hysteresis curves were obtained for Rochelle salt, analogous to the B , H curves of magnetism." The full version of his presentation was submitted to Physical Review in December 1920 [9]. It marks two milestones. Here Valasek stated for the first time that "permanent polarisation is the natural state" of Rochelle salt and published the first hysteresis curve of a ferroelectric material (Fig. 1.8). In the same year he became Master of Arts.



Fig. 1.7: Joseph Valasek 1922

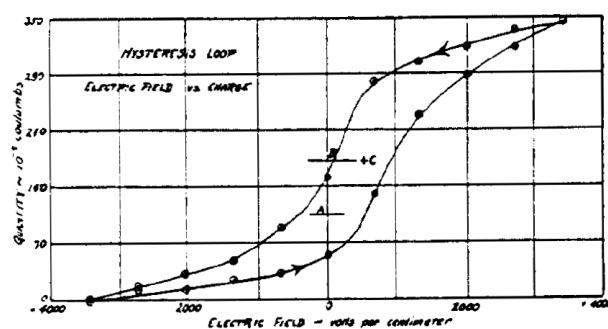


Fig. 1.8: The first published hysteresis curve [9]

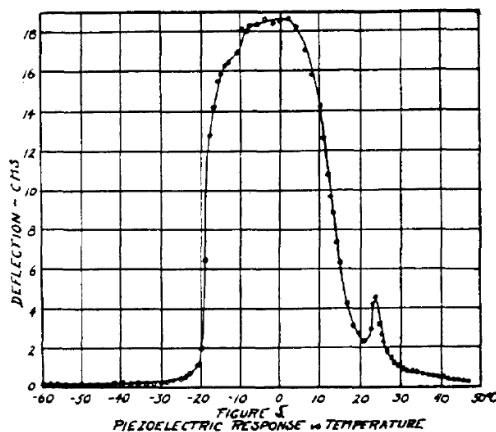


Fig. 1.9: Piezoelectric activity of Rochelle salt vs. temperature indicates the existence of two phase transitions [10]

Valaseks Ph.D Thesis “Piezo-electric activity of Rochelle salt under various conditions” is dated 1922 [10]. Perhaps the most history-making graph is that of the temperature dependence of piezoelectric response, indicating the existence of a relatively narrow temperature range of high piezoelectric activity, in fact indicating the existence of two phase transitions (Fig. 1.9). Indeed Valasek speaks here for the first time about the existence of two Curie points in Rochelle salt.

Valaseks studies were to lead later to the firm establishment of the term *ferroelectricity* to describe this set of phenomena. Yet it is interesting to observe that he never used the word ferroelectricity. Maybe he never heard about Erwin Schrödingers proposal. Who knows?

Until now Rochelle salt was the only known material with ferroelectric characteristics and scientist all over the world began to ask, if there are more. Among them Paul Scherrer, who is well known in the material science community for his formula to calculate the grain size from the rocking curve of X-ray diffraction measurements (XRD). Together with Peter Debye he worked at the “Physikalisches Institut” at the “Eidgenössische Technische Hochschule” (ETH) in Zürich on dielectrics. Scherrer



Fig. 1.10: Paul Scherrer

believed in the molecules of water of crystallisation to be essential for a material to be ferroelectric. Together with his student Georg Busch he searched the literature which was still scarce and came across a paper by Gert Steulmann at the “Institut für allgemeine Elektrotechnik” of the “Technische Hochschule” in Dresden [11]. The average dielectric constants of various potassium salts had been measured by an immersion method, amongst others K_3PO_4 , K_2HPO_4 and KH_2PO_4 ! Quite normal values of 7.75 and 9.05 respectively for the first two salts were observed, but for KH_2PO_4 a value higher than 30 was found. In view of the orthorhombic symmetry of potassium-dihydrogen phosphate this was surprising and it supported Busch’s vague idea, that mobile hydrogen atoms might be responsible for

ferroelectricity, rather than the water molecules – the hypothesis of his supervisor. That indeed O-H-O bonds do exist in KH_2PO_4 was shown by J. West at Bragg's laboratory in Manchester by a quantitative X-ray analysis of its structure [12]. It was Steulmann also who speculated about the existence of some sort of dipoles in these crystals without elaborating further on his conjecture, however. These ideas proved to be true and early in March 1935 KH_2PO_4 was found to be ferroelectric with a critical temperature of about 123 K by Busch and Scherrer [13].

This discovery was a breakthrough in the field of ferroelectricity and KH_2PO_4 has become a model substance up to the present. Furthermore in his thesis, which appeared in 1938 [14], Busch suggested the *hydrogen bonds* between adjacent oxygen atoms to be responsible for ferroelectricity. The same idea was applied by Slater [15] in 1941, who gave the first significant molecular theory of ferroelectricity based on the model of hydrogen bonds.

After having finished his thesis Busch suggested to investigate $\text{NH}_4\text{H}_3\text{IO}_6$, a material in which hydrogen bonds were known to exist also. It was shown much later that ammonium iodate is antiferroelectric. Today many substances exhibiting hydrogen-bond-ferroelectricity are known and ferroelectricity is no longer a singularity of Rochelle salt.

September 1st 1939: Germany invaded Poland, the beginning of the Second World War. This triggered the interest in ferroelectrics, mainly for sonar systems to detect submarines and other military applications. Barium Titanate, BaTiO_3 , the first man-made perovskite ferroelectric was discovered in 1942 and 1944 in the United States, Russia and Japan. At least in the USA the research was accelerated because of the war. At that time, mica was used in most capacitors, but U-boats threatened the supplies of mica to the USA from South America. The initial reports were based on doping studies of TiO_2 with BaO , which produced ceramic materials with enhanced dielectric permittivities. The mixed oxides were made by Thurnmaurer and Deaderick at the American Lava Corporation as early as 1941, the filing date of U.S. Patent No. 2,429,588 [16]. The high permittivities were found by measurements made at the Erie Resistor Company, with dielectric constants exceeding 1000, ten times greater than any other ceramic known at that time, such as TiO_2 ($\epsilon_r=110$).

The race to understand the nature of the dielectric anomaly in BaO-TiO₂ ceramics continued, and in 1945 and 1946, von Hippel (USA), and Wul and Goldman (Russia) demonstrated ferroelectric switching in these ceramics [17, 18]. The discovery of ferroelectricity in BaO-TiO₂ ceramics was extremely important, as it demonstrated for the first time that ferroelectricity could exist in simple oxide materials, and it was not always associated with hydrogen bonding. BaTiO₃ is a member of the perovskite family named

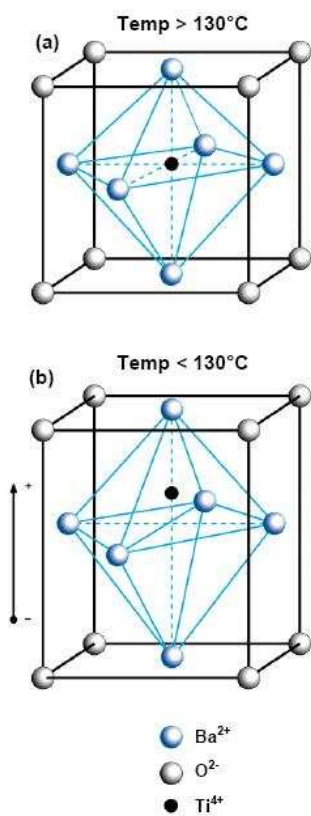


Fig. 1.11: The BaTiO₃ crystal structure above (a) and below (b) the phase transition between cubic and tetragonal

after the naturally occurring mineral perovskite CaTiO₃. The simplicity of the structure of BaTiO₃ (Fig. 1.11) seduced several investigations to undertake X-ray diffraction studies of the structural changes occurring at the phase transitions [19] and it enabled the investigation of the most important theoretical backgrounds of these materials. A.F. Devonshire developed his phenomenological model of ferroelectrics on the basis of the electromechanical, structural and thermal properties of BaTiO₃ in 1951 [20]. This approach built upon the earlier ideas of Landau and Ginzberg and invoked the point group symmetry and nonlinear elasto-dielectric coupled interactions with electrostriction and piezoelectric coefficients. The resulting Landau-Devonshire-Ginzberg Theory (LDGT) of ferroelectrics is still the most powerful tool for the understanding of ferroelectrics.

At the end of the war, public disclosure led to intense interest not only in academic circles, but in practical markets, in particular high capacitance, small volume capacitors in early television and radio circuits, as well as active elements for phonograph pick-ups, accelerometers, and ultrasonic generators. The British Navy, for instance, used some underwater sonar devices based on the

piezoelectric response of BaTiO₃ ceramics until the end of the last century. Lately, the BaTiO₃ piezoelectric properties have been revisited in the form of single crystals and textured ceramics because of environmental concerns with the lead-based perovskites based on the perovskite PbZrO₃-PbTiO₃ system (PZT).

The next significant perovskite with ferroelectric properties was Barium-Strontium Titanate, $(\text{Ba,Sr})\text{TiO}_3$ or BST. In this system the A site of BaTiO_3 is doped with Sr. This alters the Curie temperature of BaTiO_3 (Fig. 1.12). Below the Curie temperature a ferroelectric material behaves like a “normal” ferroelectric; e.g. it has a hysteresis like Valasek observed in Rochelle Salt. But above the Curie temperature the material becomes *paraelectric*, the hysteresis can not be observed anymore. In terms of tunability (the change of the permittivity with an applied voltage) the paraelectric state offers the opportunity for varactors (variable capacitors) and phase shifters with a linear change of the permittivity in a certain voltage region.

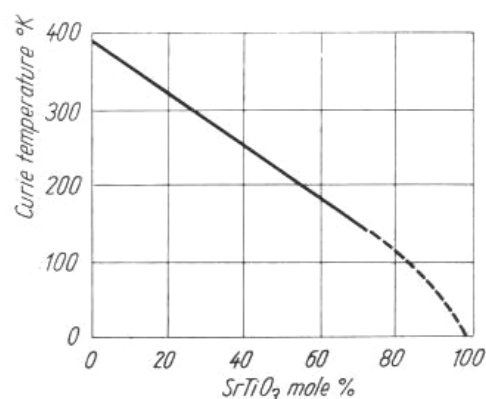


Fig. 1.12: Temperature of phase transition in solid solution of $(\text{Ba,Sr})\text{TiO}_3$ vs. composition (Rushman and Strivens, 1946)

Despite the fact that BST was (and still is) a matter of investigation for over 60 years now, there are problems with this material. First of all the leaked current is high increasing the loss ($\tan\delta$) of the film. Second, it is difficult to realise a crack free thin film via the sol-gel method (Chapter 4).

In recent years a new perovskite material, namely Lead Strontium Titanate, $(\text{Pb,Sr})\text{TiO}_3$ or PST, has attracted the interest of researchers. Although there are health and environmental concerns with lead-based materials, this material has remarkable advantages compared to BST. It is easy to deposit crack-free via the sol-gel route, has relatively low loss and a high tunability ($\sim 80\%$), and can even be deposited on SiO_2 or SiN_x . Therefore $(\text{Pb,Sr})\text{TiO}_3$ in its paraelectric state is the main subject of this thesis.

Coming back to Seignette Salt and the term *ferroelectric*, Helen D. Megaw from the United Kingdom said in 1957: “... perhaps the real reason for its [i.e. of the name Seignette-electricity] rejection ... is its failure to fit comfortably into the English language. As an adjective, *ferroelectric* is euphonious, while *Seignette-electric* grates on the ear” [21].

1.2 A Short History of Sol-Gel

Sol-gel materials encompass a wide range of inorganic and organic/inorganic composite materials which share a common preparation strategy. They are prepared via sol-gel processing involving the generation of colloidal suspensions (“sols”) which are subsequently converted to viscous gels and thence to solid materials [22].

Surprisingly this method is very old. To have a feeling how old, this section gives an



Fig. 1.13: Cave paintings in Lascaux

overview about the development of the sol-gel technique. The preparation of perovskite materials is covered in a later chapter.

The earliest use of colloids to prepare functional materials is seen in the cave painting at Lascaux in France, dating back 17,000 years. The pigments used were based on iron oxide, carbon and clays, ground into fine powders, graded by sedimentation and dispersed in water using

natural oils as surface active stabilisers.

Some 8000 years ago firing methods were developed to alter the chemistry of the mineral precursors so as to produce plasters and bricks. At Yiftah El in Israel, for example, we can still see a 180 m² polished floor, which needed over 2 tons of lime and over 10 tons of wood to fire the kiln [23, 24]. In this example we see the beginnings of the sol-gel ideas, in that fine powdered or colloidal material in suspension was moulded and then dried and densified by chemical action or by firing at high temperatures.

Glazing methods were developed next and became quite sophisticated in Mesopotamia by the second century. A very fine haematite-rich illitic clay fraction made by sedimentation was painted onto vessels and fired in a reducing atmosphere to reduce the iron to black magnetite. After sintering of the glaze, the atmosphere was made oxidising by admission of air, thus oxidising the iron in the nonglazed areas to a red colour and producing a shiny black glazed decorative pattern on a matt red base.

Even earlier (4000BC) in Egypt an aqueous paste of crushed sand and a sodium salt flux and binder was moulded and fired to produce *faience* by binding the silica particles

together with the molten flux. Addition of copper salts to the paste led to migration of these mobile salts to the surface during firing, with formation of a translucent blue glaze.

The idea of using chemically-linked particles as a matrix for a composite of other particulate material led to the development of concrete in about 700BC. For example in the 260 m aqueduct bridge at Jerwan in Iraq. Stones of graded sizes mixed with sand and a binding paste of quicklime (CaO) and water formed the first concrete, but required an asphalt lining as the lime cement tended to crumble in water. The Romans developed concrete between 200BC and 400AD and discovered that addition of the volcanic ash from Pozzuoli near Mount Vesuvius led to a much stronger concrete that would even set under water. In fact the ash contained oxides of aluminum, silicon and iron and the product, similar to modern Portland cement, proved more durable in underwater conditions than recently-laid modern concrete in the same location. Much the same material was rediscovered by the British engineer John Smeaton in his search for a reliable hydraulic cement for the third Eddystone lighthouse [25] in the English Channel in 1756-9. He found that the best hydraulic cement was produced by burning limestone with some clay content. His lighthouse can still be seen on the british pre-decimal One Penny Coin.

Strangely, many of these early technologies became lost in the Dark Ages after the decline of the Roman Empire, and probably the next significant development was the discovery of “water glass” by von Helmont in 1644 [26]. He dissolved silicate material (stones, sand, flint etc.) in alkali and found that on acidification a precipitate of silica equal in weight to the original silicate material was obtained. In 1779 Bergman [27] reported that if the correct amount of diluted acid was used the mixture gelled on acidification. This preparation of a silica gel led to a series of applications remarkably similar to those of today’s sol-gel chemistry.

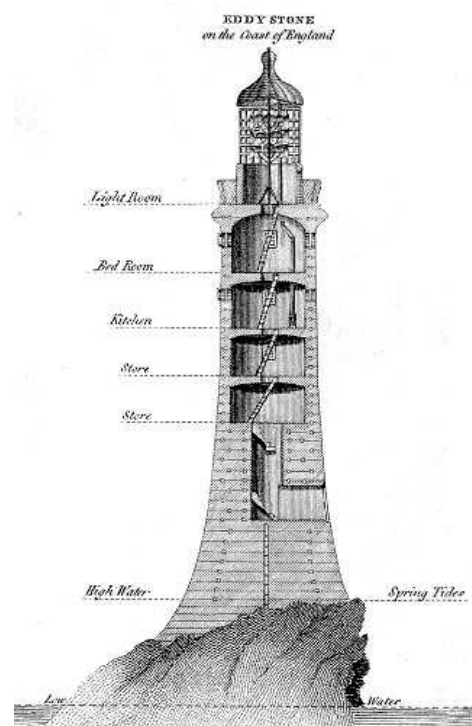


Fig. 1.14: Smeaton's Eddystone Lighthouse

In the 19th century two major developments occurred which were to prove foundation stones for sol-gel processing: the physical properties of colloids came under intensive

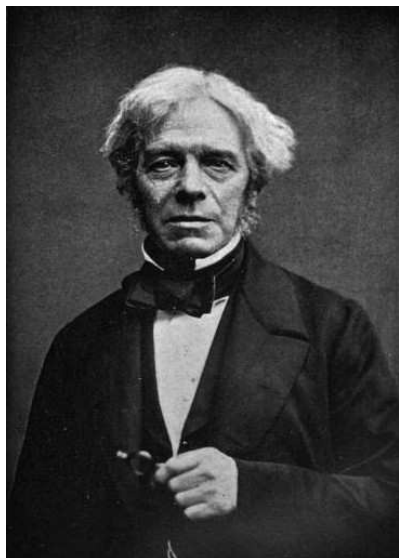


Fig. 1.15: Michael Faraday

study by such giants as Becquerel and Faraday (his gold sols were so stable that they are still in existence at the Royal Institution in London); and the chemistry became very sophisticated. In 1846 Ebelmen [28] prepared the first silicon alkoxides by the reaction between silicon tetrachloride and alcohol, observing that the product gelled on prolonged exposure to atmosphere with normal humidity. In 1876 Troost and Hautefeuille [29] made hydrolysed derivatives of silicon alkoxides. In 1884 Grimaux [30] hydrolysed tetramethoxysilane to prepare silicic acid sols, and made colloidal iron oxides from iron alkoxide. However, for the next 50 years these developments had little scientific impact for the

development of the sol-gel materials field.

The one notable exception in this period was the work of W.A. Patrick, who pioneered the field of silica gel desiccants, catalysts and absorbent materials, starting with the drying and firing of a homogeneous silica gel at up to 700°C to produce a very porous form of silica [31]. In 1923 he went on to show that impregnation of the partially dried materials with metal salts led to the formation of supporting catalysts [32], and by 1930 he had filed many patents for supporting catalysts, including the use of sol-gel methods [33].

This signaled the beginning of an intensive period of technological development using sol-gel methods, which produced a very large number of patents, many useful materials, and a large body of data and experience. Only later, with the advent of modern characterisation methods, could a set of firmly-based theoretical principles begin to be established to interpret all these data. Indeed it could be said that despite the new methods now available, the subject is still strongly influenced by this empirical approach. It is therefore important that the large amount of early work in the field is not overlooked, only to be re-discovered as the topics attract interest for a new reason, just as was the case with the Roman cement.

1.3 Materials for Tunable Applications – State of the Art

The appropriate level of tunability for tunable applications ($n \geq 1.5$ or $n(\%) \geq 0.3$, see Section 2.1.2) is practically achievable in materials with a relatively high dielectric permittivity at the frequencies of choice. For non-composite bulk materials, a value of the dielectric constant exceeding some 1000 is required whereas in thin films (where the application of higher fields is possible) the dielectric constant should be larger than some 300. This limitation together with the requirement of relatively low values of the loss (below a few percent) narrows the scope of the materials of interest to the displacive type ferroelectrics (incipient or regular in the paraelectric phase). Up to now, many materials have been addressed as possible candidates for tunable applications, the most attention has been paid to SrTiO_3 and its solid solution with BaTiO_3 : $(\text{Ba,Sr})\text{TiO}_3$. In the present section the state of the art of this scientific field is reviewed

Motivated by increasing speed and bandwidth requirements, the III-V semiconductor industry has recently made considerable progress in developing transistors with transit time and maximum oscillation frequencies well above 100 GHz. The traditional digital silicon industry also, driven by increasing market demands and cost constraints, has put substantial effort in developing analog microwave circuits. Silicon based bipolar and CMOS transistors with transit times and maximum oscillation frequencies above 100 GHz are now available, making it possible to develop monolithic microwave ICs (MMICs) for frequencies up to 50 GHz. Along with the transistors, varactors are the other widely used components used in microwave technology for analog (nondigital) tuning purposes. In spite of the progress achieved in the transistor technology, no semiconductor varactors with high enough Q factor and tunability are available for frequencies above 10–20 GHz. Typically, the Q factors of semiconductor varactors decrease with the increased frequency as $Q \sim f^{-1}$, and at 50 GHz it is of the order 10 or less. There is a lack of varactors with adequate (compatible with the transistors) performance in this frequency range.

The current progress indicates that, to a certain degree, the “varactor gap” may be filled in by ferroelectric varactors. After several decades of research considerable progress has

been achieved in tunable permittivity ferroelectrics, making it possible to develop ferroelectric varactors with performances better than semiconductor analogs in the frequency range above 10–20 GHz [34, 35]. Thin film ferroelectric varactors have a substantially higher Q factor at microwave and millimeter wave frequencies, higher tuning speed, and lower drive power consumption. Ferroelectric varactors, and tunable devices based on them, have the potential for easy integration with standard Si and GaAs processes. Additionally, due to the high dielectric permittivity, the sizes of tunable components based on ferroelectrics may be smaller in comparison with other technologies. Extra flexibility in terms of tuning, enhanced functionalities, and performances of tunable devices may be achieved by combination of ferroelectrics with ferrites [36, 37], ferroelectrics with semiconductors [38], or ferrites with semiconductors [39]. Devices based on such multifunctional materials offer dual, i.e., electric, magnetic tuning possibility, and extra flexibility in designing and shaping the device performances. For example, in delay lines it is possible to tune the delay time while maintaining the input/output impedances at a desired level.

Both ferroelectric (polar) and paraelectric phases may be useful in tunable microwave devices [40]. However, the paraelectric phase is often preferred since it has no hysteresis associated with the domain walls. In this respect the quantum paraelectrics - SrTiO₃, KTaO₃, and CaTiO₃ [41, 42] - have been given priority for some time, although they need to be cooled down to cryogenic temperatures in order to get reasonable tunabilities. On the other hand in thin film devices based on these materials, and especially in the solid solutions of BST, high electric fields and reasonable tunability may be achieved at room temperature at relatively low dc voltages. For applications in industrial devices BST seems to be the material of choice at the moment. It is the most studied material at microwave frequencies, which allows microwave engineers to use the available data without getting too much involved in a materials study. In addition, it allows control of the Curie temperature by simply changing the Ba content.

The performance of ferroelectric devices depends not only on the composition of the film but also on the strain, defects, electrode/ferroelectric interface chemistry, fabrication method, design, etc. Ferroelectric varactors, and devices based on them, may have

parallel-plate or coplanar-plate designs. The former offers smaller tuning voltages, while the latter offers the possibility of trading tunability for lower losses.

Typical frequency dependencies of the capacitance and Q factor of a parallel-plate ferroelectric varactor are shown in Fig. 1.16.

In this case the varactor is fabricated on a high resistivity ($5 \text{ k}\Omega \text{ cm}$) silicon substrate with adhesive TiO_2 (15 nm) and Pt (100 nm) layers. The $\text{Ba}_{0.25}\text{Sr}_{0.75}\text{TiO}_3$ film is 300 nm thick. The bottom and top electrodes are made of a $0.5 \mu\text{m}$ thick Au film and 50 nm Pt layer. The diameter of the top plate is $10 \mu\text{m}$. For comparison, in Fig. 1.16(b), the performance of varactor based on Pt(200 nm)/ TiO_2 /SiO₂/Si structure (i.e., thinner bottom electrode) is also shown. The use of thicker Au bottom electrode substantially increases the Q factor of the varactor. The capacitance and the tunability are fairly frequency independent. The tunability of a BST varactor at 25 V, is more than 40% in the frequency range of 1 MHz–45 GHz. In the frequency range of 5–40 GHz the Q factor of BST varactors fabricated on thick bottom Au/Pt electrode is more than 40, which is competitive with the best semiconductor

analogs, Fig. 1.16(b) [35]. Additionally, ferroelectric varactors have symmetric C - V characteristics, as do heterojunction barrier varactors (HBVs) [43]

The frequency independent tunability (up to 50% or more), high tuning speed ($< 1.0 \text{ ns}$), extremely small leakage currents and dc control power, high breakdown field, and radiation hardness are the main advantages of ferroelectric varactors. Recently substantial progress has been achieved in commercialization of tunable microwave components

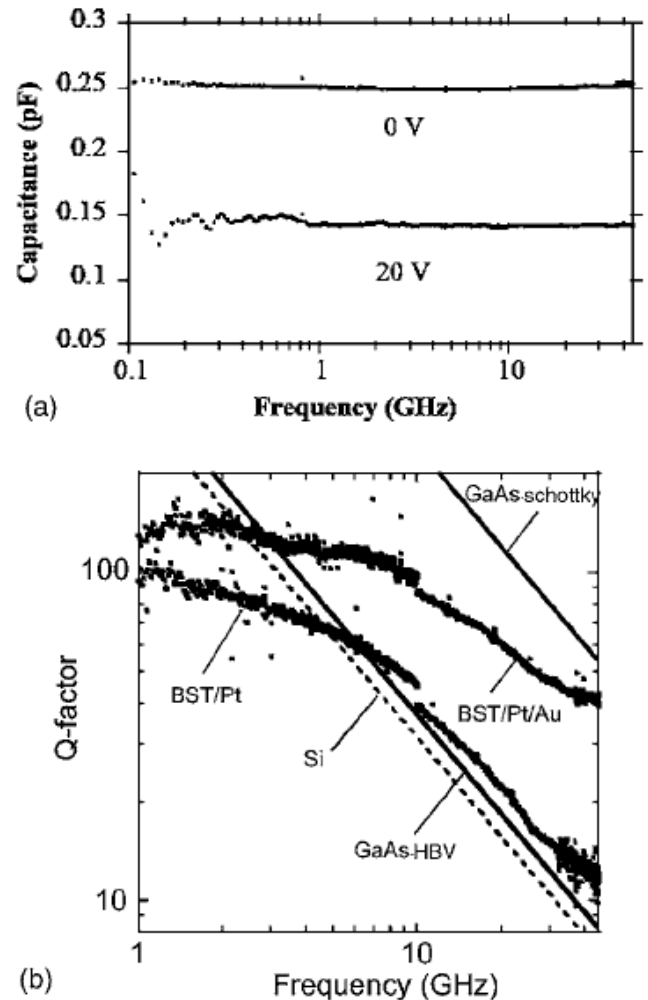


Fig. 1.16: Capacitance (a) and Q factor (b) of varactors vs frequency [35].

based on ferroelectrics [44, 45]. In fact, ferroelectrics are gaining ground for tunable microwave applications, including lumped element (device sizes much smaller than the microwave wavelength) and distributed element devices, such as varactors, phase shifters, delay lines, tunable filters, antennas, etc... Nevertheless, problems such as hysteresis, temperature dependence of parameters (such as permittivity of the ferroelectric material), etc., still need adequate treatment. One of the fundamental problems concerning the practical use of tunable ferroelectric devices has to do with the

strong temperature dependence of the parameters of tunable ferroelectric devices associated with the inherent temperature dependence of the ferroelectric's permittivity.

Recently the group around Stammer *et al.* introduced a new non-ferroelectric material: bismuth zinc niobate (BZN), which has a cubic pyrochlore structure [46]. To understand the origin of the tunability of BZN, which would aid in the discovery of new tunable materials, models were developed that describe the temperature dependence of the tunability of non-ferroelectrics. BZN films thus have a practical advantage over tunable ferroelectric materials, as they would allow temperature-stable tunable devices. It was also shown that, in a first approximation, at temperatures above the dielectric relaxation, the temperature dependence of the BZN film tunability can be described by a simple model of hopping dipoles under the influence of random fields.

This is consistent with the chemical and displacive randomness of the BZN structure that controls the dielectric behavior [47, 48]. However, the origin of the large electric field tunability of the permittivity of BZN is not yet understood.

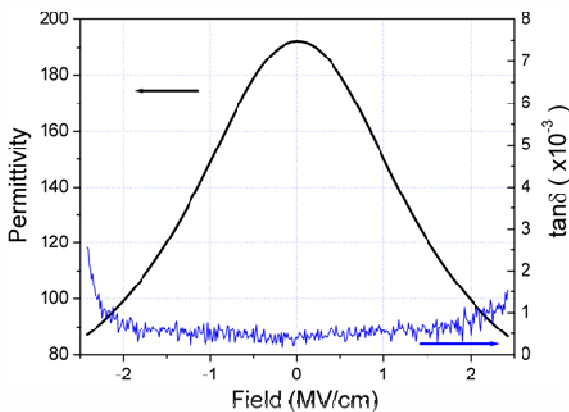
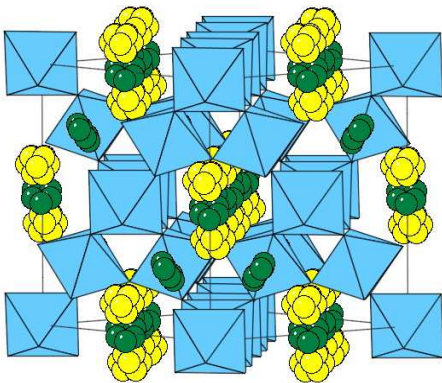


Fig. 1.17: (a) BZN structure with random off-centering of ions (yellow: O, green: Bi). (b) Applied bias field dependence of the permittivity and dielectric loss of a BZN film on $\text{Al}_2\text{O}_3/\text{Pt}$ at 1 MHz [46]

Nevertheless, ferroelectrics are the materials of main interest for voltage tunable devices today and BST is, despite the aforementioned problems, the most likely candidate to make the way towards commercially available applications since it is more studied both in terms of electrical performance, manufacturability and reliability.

Against the trend towards lead-free materials a new perovskite ferroelectric material, namely Lead Strontium Titanate, $(\text{Pb}, \text{Sr})\text{TiO}_3$, has attracted the interest of researchers nowadays. Although there are health and environmental concerns with lead-based materials, this material has remarkable advantages compared to BST or related ferroelectrics. It is easy to deposit crack-free via the sol-gel route, has relatively low loss and a high tunability ($\sim 80\%$), and can even be deposited directly on SiO_2 or SiN_x , facts that make it very interesting for direct applications or the integration of other frequently used perovskites like PZT which can not be deposited directly on SiO_2 .

1.4 References

1. Maurice Soenen, La Pharmacie à La Rochelle. Les Seignettes et le sel polychreste. Thèse de doctorat de l'Université de Bordeaux, 1910
2. Simon Boulduc, *Compt. rendus Acad. Roy. des Sciences* 1731
3. David Brewster, *Edinbg. J. of Science*, Vol. 1, No. II. 208-218 (1824). Observation on the Pyro-Electricity in Minerals
4. Jacques et Pierre Curie, *Compt. rend.* **91**, 294-295, 383-387 (1880). Développement par pression de l'électricité polaire dans des cristaux hémihédriques à faces inclinées.
5. A.M. Nicholson, Piezophony. U.S. Patent 1, 495, 429. Filed April 10, 1918. Patented May 27, 1924. A.M. Nicholson, Generating and Transmitting electric Currents, U.S. Patent 2, 212, 845. Filed April 10, 1918. Patented August 27, 1940
6. Paul Langevin, Procédé et appareils d'émission et de réception des ondes élastiques sous-marines à l'aide des propriétés piézoélectriques du quartz. Brevet d'Invention No. 505,703. Demandé le 17 septembre 1918. Délivré le 14 mai 1920
7. P. Debye, *Physik. Zeitschr.* XIII, 97-100 (1912). Einige Resultate einer kinetischen Theorie der Isolatoren (Vorläufige Mitteilung).

8. Erwin Schrödinger, Aus sen Sitzungsberichten der Kaiserl. Akademie der Wissenschaften in Wien. Mathem.-Naturw. Klasse; Bd. CXXI, Abt. Iia, November 1912. Studien üder Kinetik der Dielektrika, dam Schmelzpunkt, Pyro- und Piezoelektrizität.
9. J. Valasek, Phys. Rev. **15**, 537 (1920); **17**, 475-481 (1920). Piezoelectric and allied phenomena in Rochelle salt.
10. J. Valasek, Phys. Rev. **19**, 478-491 (1922); Piezo-electric activity of Rochelle salt under various conditions.
11. G. Steulmann, Z. Phys. **77**, 114-116 (1932). Die Dielektrizitätskonstante einer Anzahl von Kaliumsalzen und Alkalihalogeniden.
12. J. West, Z. Krist. **74**, 306 (1930). A quantitative X-Ray Analysis of the Structure of Potassium-Dihydrogen-Phosphate (KH₂PO₄)
13. G. Busch and P. Scherrer, Naturwiss. **23**, 737 (1935). Eine neue Seignetteelektrische Substanz
14. G. Busch, Helv. Phys. Acta **11**, 269-298 (1938). Neue Seignette-Elektrika.
15. J.C. Slater, J. Chem. Phys. **9**, 16-33 (1941). Theory of the Transition of KH₂PO₄.
16. H. Thurnaurer and J. Deaderick, U.S. Patent 2,429,588, Oct. 21, 1947, filed Oct. 2 1941
17. A. von Hippel, R.G. Breckenbridge, F.G. Chesley, and L. Tisza, Ind. Eng. Chem. **38**, 1097 (1946)
18. B. Wul and J.M. Goldman, C.R. Acad. Sci. URSS **51**, 21 (1946)
19. W. Känzig, Helv. Phys. Acta **24**, 175 (1951)
20. A.F. Devonshire, Phil. Mag. **40**, 1040 (1949), Phil. Mag. **42**, 1065 (1951)
21. H.D. Megaw, Ferroelectricity in Crystals. London: Methuen & Co., Ltd., 1957, p. 2
22. C.J. Bringer and G.W. Scherer, Sol-gel science: The physics and chemistry of sol-gel processing, Academic Press: London 1990.
23. W.H. Gourdin and W.D. Kingery, *J. Field Archaeology*, **2**, 133 (1976)
24. W.D. Kingery, P.B Vandiver and M. Pricket, *J. Field Archaeology*, **15**, 219 (1988)

25. J. Smeaton, Narrative of the building etc. of the Eddystone Lighthouse, London 1791
26. J.B. von Helmont, *De lithiase, Amstelodami*, **28** (1644)
27. T. Bergman, “De terra silicea“, *Upsala* 1779
28. J.J. Ebelman, *Ann. Chim. Phys.*, 16, 129 (1846)
29. L. Troost and P. Hautefeuille, *Ann. Chim. Phys.*, 7, 452 (1876)
30. E. Grimaux, *Bull. Soc. Chim.*, **41**, 50, 157 (1884)
31. W.A. Patrick, “Silica gel and process of making same” U.S. patent 1,297,724 (1919)
32. W.A. Patrick, “Catalyst” British Patent 208,656 (1923)
33. (*a selection*) W.A. Patrick, “Adsorbent and catalyst oxides” U.S. Patent 1,520,305 (1924); “Porous catalytic gels” U.S. Patent 1,577,186 (1926); “Gels for catalytic and absorbent purposes” U.S. Patent 1,577,190 (1926); “Tungstic oxide gel” U.S. Patent 1,682,239 (1928); “Stannic oxide gel” U.S. Patent 1,682,240 (1928); “Aluminum oxide gel” U.S. Patent 1,682,241 (1928); “Titanium oxide gel” U.S. Patent 1,682,242 (1928); “Catalytic and absorbent gel” U.S. Patent 1,696,644 (1928); “Tungsten oxide gel” U.S. Patent 1,848,266 (1932)
34. S.Gevorgian, in *Electroceraic-Based MEMS*, edited by N. Setter (Springer, New York, 2005), chap. 7, p. 133
35. A. Vorobiev, P. Rundquist, K. Khamchane, and S. Gevorgian, *Appl. Phys. Lett.* 83, 3144 (2003)
36. V.E. Demidov, B. A. Kalinikos, S. F. Karmanenko, A. A. Semenov, and P. Edenhofer, *IEEE Trans.. Microwave Theory Tech.* 51, 2090 (2003)
37. Q. X. Jia, J. R. Groves, P. Arendt, Y. Fan, A. T. Findikoglu, S. R. Foltyn, H. Jiang, and F. A. Miranda, *Appl. Phys. Lett.* 74, 1564 (1999)
38. S. Gevorgian, S. Abadei, H. Berg, and H. Jacobsson, *IEEE MTT-S Int. Microwave Symp. Dig.* 2, 1195 (2001)
39. H. H. Fiallo, J. P. Dougherty, S. J. Jang, R. E. Newnham, and L. A. Carpenter, *IEEE Trans. Microwave Theory Tech.* 42, 1176 (1994)
40. S. Gevorgian and E. Kollberg, *IEEE Trans. Microwave Theory Tech.* 49, 2117 (2001)

41. Chen Ang, A. S. Bhalla, and L. E. Cross, *Physical Review B*, **64**, 184104 (2001)
42. V. V. Lemanov, A. V. Sotnikov, E. P. Smirnova, M. Weihnacht, and R. Kunze, *Solid State Commun.* **110**, 611 (1999)
43. E. Kollberg, J. Stake, and L. Dillner, *Philos. Trans. R. Soc. London, Ser. A* **354**, 2383 (1996)
44. <http://agilematerials.com>
45. <http://www.globalspec.com/ParatekMicrowave>
46. J. W. Lu and S. Stemmer, *Appl. Phys. Lett.* **83**, 2411 (2003).
47. I. Levin, T. G. Amos, J. C. Nino, T. A. Vanderah, C. A. Randall, and M. T. Lanagan, *J. Solid State Chem.* **168**, 69 (2002).
48. S. Kamba, V. Porokhonsky, A. Pashkin, V. Bovtun, J. Petzelt, J. C. Nino, S. Trolier-McKinstry, M. T. Lanagan, and C. A. Randall, *Phys. Rev. B* **66**, art.no.054106 (2002).

I'm on the verge of a major breakthrough, but I'm also at the point where physics ends and chemistry begins, so I'll have to drop the whole thing.

Sidney Harris
Statistical and Thermal Physics (2003)

It would be better for the true physics if there were no mathematicians on earth.

Daniel Bernoulli
The Mathematical Intelligencer (1991)

For those who want some proof that physicists are human, the proof is in the idiocy of all the different units which they use for measuring energy.

Richard P. Feynman
The Character of Physical Law (1967)

Theoretical Considerations and Literature Review

2.1 Theory of the Dielectric Response of Tunable Materials

Ferroelectrics are known for their high dielectric constant and high tunability. These features of ferroelectrics are linked and the general trend “the higher the dielectric constant, the higher the tunability”. It holds for an “ideal ferroelectric” where the dielectric response is controlled by the lattice dynamics of the material. The effects of dielectric anisotropy do not usually play an essential role in the performance of tunable materials. For this reason, these effects are not addressed here. The following discussion will always consider the situation where the polarisation and electric fields are collinear.

2.1.1 Dielectric Permittivity

The origin of the high dielectric permittivity of ferroelectrics in the paraelectric phase is a delicate compensation of various kinds of atomic forces that maintains the material in



Fig. 2.1: Lew Dawidowitsch Landau

a non-poled state in the absence of an electric field (see Fig. 1.11(a)). Because of this compensation, the restoring force opposing the poling action of the applied field is relatively weak. This results in a high dielectric permittivity of the material. Since this thesis is devoted to microwave materials, the following discussion will address only the paraelectric phase of ferroelectrics. It is believed that only for this case will a material exhibit a high tunability and a relatively low dielectric loss at microwave frequencies, a combination of interest for microwave application.

The most straightforward description of the dielectric response of ferroelectrics is given by the conventional Landau theory and is based upon an expansion of the Helmholtz free energy F with respect to the vector macroscopic polarization \mathbf{P} . For the situation where the polarization is collinear with the macroscopic electric field \mathbf{E} in the material, the first terms of this expansion read [1]:

$$F = \frac{\alpha}{2} P^2 + \frac{\beta}{4} P^4 + \frac{\gamma}{6} P^6 - EP \quad [\text{Eq. 2.1}]$$

The equilibrium configuration is determined by finding the minimum of F , where

$$\frac{\partial F}{\partial P} = 0.$$

This equation gives an expression for the electric field \mathbf{E} as a function of the polarisation \mathbf{P}

$$E = \alpha P + \beta P^3 + \gamma P^5 \quad [\text{Eq. 2.2}].$$

The linear dielectric susceptibility χ above the transition can be determined by differentiation this equation with respect to \mathbf{P} and then setting $\mathbf{P}=0$ to obtain

$$\chi = \frac{P}{E} = \frac{1}{\alpha} \quad [\text{Eq. 2.3}].$$

In the Landau-Devonshire theory it is assumed that around the Curie point ($T \sim T_0$)

$$\alpha = \alpha_0 (T - T_0) \quad [\text{Eq. 2.4}]$$

and the other coefficients in the free energy expansion are independent of temperature.

Combining the last two equations leads to the expression for the dielectric stiffness

$$\kappa = \frac{1}{\chi} = \alpha_0 (T - T_0) \quad [\text{Eq. 2.5}],$$

which captures the Curie-Weiss behavior in χ observed in most ferroelectrics for $T > T_0$.

In terms of the dielectric permittivity $\epsilon = \epsilon_r \epsilon_0$ with $\epsilon_0 = 8.85 \cdot 10^{-12}$ F/m one can find

$$\epsilon = \frac{C}{T - T_0} \quad [\text{Eq. 2.6}]$$

where C is the Curie-Weiss constant. It should be noted here that the temperature T_0 where α changes sign is close but not exactly coincident with the Curie temperature T_C .

Including the linear temperature-dependence of α , leads to the general expression for the free energy in ferroelectrics:

$$F = \frac{1}{2} \alpha_0 (T - T_0) P^2 + \frac{1}{4} \beta P^4 + \frac{1}{6} \gamma P^6 - EP \quad [\text{Eq. 2.7}]$$

or for the electric field E :

$$E = \alpha_0 (T - T_0) P + \beta P^3 + \gamma P^5 \quad [\text{Eq. 2.8}]$$

where α_0 and γ are both positive in all ferroelectrics and β and γ describe the nonlinearity of the material.

2.1.2 Tunability

The tunability of a varactor made from high-permittivity material is defined as

$$n = \frac{C_{\max}}{C_{\min}} \text{ or } n(\%) = \frac{C_{\max} - C_{\min}}{C_{\max}} \cdot 100 \quad [\text{Eq. 2.9}],$$

where C_{\max} is the capacitance at zero bias and C_{\min} with non-zero bias. With the expansion for the temperature dependent electric field-polarisation relation (see section 2.1.1) and the relationships $E=V/d$ and $P=Q/A$, where V is the external applied voltage, d the capacitor thickness, Q the charge and A the area, one can find:

$$V = \frac{\alpha(T)d}{A}Q + \frac{\beta d}{A^3}Q^3 \quad [\text{Eq. 2.10}].$$

The device capacitance is defined by $C(V) = \frac{dQ}{dV}$ from which the zero-field capacitance is found as

$$C_{\max} = \left. \frac{dQ}{dV} \right|_{V=Q=0} = \frac{A}{\alpha(T)d} = \frac{\epsilon_0(T)A}{d} \quad [\text{Eq. 2.11}].$$

The result is not surprising – it is the formula of a parallel-plate capacitor with $\epsilon_0(T)=1/\alpha(T)$ the temperature dependent dielectric permittivity at zero bias.

For the following treatment it is helpful to introduce the normalised variables $v = \frac{V}{V_n}$ and $q = \frac{Q}{C_{\max}V_n}$ so that the governing equation becomes $v = q + \xi q^3$ where ξ is an empirical constant that is related to the tunability n . Using this equation, the normalised capacitance is

$$c(v) = \frac{C(V)}{C_{\max}} = \frac{dq}{dv} = \frac{1}{1 + 3\xi q^2} \quad [\text{Eq. 2.12}]$$

Defining the normalised charge $v=1$ as q_n the last two formulas require that $q_n(1 + \xi q_n^2) = 1$ and $n = 1 + 3\xi q_n^2$. These can be solved simultaneously to give

$$\xi = \frac{(n-1)(n+2)^2}{3^3}.$$

The equation $c(v) = \frac{1}{1+3\xi q^2}$ can be made an explicit function of voltage by inverting $v = q + \xi q^3$ [2] to give

$$q(v) = \frac{\psi(v)}{18^{1/3} \sqrt{\xi}} - \frac{(2/3)^{1/3}}{\sqrt{\xi} \psi(v)} \quad \text{where } \psi(v) = \left(9v\sqrt{\xi} + \sqrt{12+81\xi v^2}\right)^{1/3}. \quad [\text{Eq. 2.13}]$$

This result is exact, but awkwardly shaped. A simpler equivalent can be obtained using the substitution $q = \vartheta \sinh \theta$. Inserting this into $v = q + \xi q^3$ and rearranging gives

$$\sinh^3 \theta + \frac{1}{\xi \vartheta^2} \sinh \theta - \frac{v}{\xi \vartheta^3} = 0. \quad [\text{Eq. 2.14}]$$

By comparing this equation with the hyperbolic identity

$$\sinh^3 \theta + \frac{3}{4} \sinh \theta - \frac{1}{4} \sinh 3\theta = 0 \quad [\text{Eq. 2.15}],$$

one finds

$$\frac{1}{\xi \vartheta^2} = \frac{3}{4} \quad \text{and} \quad \frac{v}{\xi \vartheta^3} = \frac{1}{4} \sinh 3\theta. \quad [\text{Eq. 2.16}]$$

Combining this term with $q = \vartheta \sinh \theta$ results in the required charge-voltage and, hence, $c(v)$ relationship

$$c(v) = \frac{dq}{dv} = \frac{\partial q \partial \theta}{\partial \theta \partial v} = \frac{1}{2 \cosh 2\theta - 1} \quad \text{where } \theta = \frac{1}{3} \sinh^{-1} \left[\frac{v}{2} \sqrt{3^3 \xi} \right]. \quad [\text{Eq. 2.17}]$$

Replacing the normalised variables with physical meaningful quantities gives the desired end result

$$C(V) = \frac{C_{\max}}{\cosh \left[\frac{2}{3} \sinh^{-1} \left(\frac{2V}{V_2} \right) \right] - 1}. \quad [\text{Eq. 2.18}]$$

This formula describes the the nonlinear capacitance of a varactor made from high-permittivity materials like BST or PST in a simple and charming way. The new variable V_2 is defined as

$$V_2 = \frac{4V_n}{(n+2)\sqrt{n-1}} \quad [\text{Eq. 2.19}]$$

and is the “2:1” voltage at which $C(V_2) = C_{\max}/2$, an easily measured quantity. Experimentally there are only two parameters that define the ideal $C(V)$ curve: C_{\max} and

V_2 . Once V_2 is known for a given device, the last equation can be used to determine the voltage required to achieve a desired tunability.

Looking back to the beginning of this section one can note that the original Landau expansion can be rewritten as

$$P(E) = \frac{3}{2} \epsilon_0(T) E_2 \sinh \left[\frac{1}{3} \sinh^{-1} \left(\frac{2E}{E_2} \right) \right] \quad [\text{Eq. 2.20}]$$

where $E_2 = V_2/d$ is the field at which the permittivity at zero bias is reduced by the factor two. This is a potentially useful result for electromagnetic simulations.

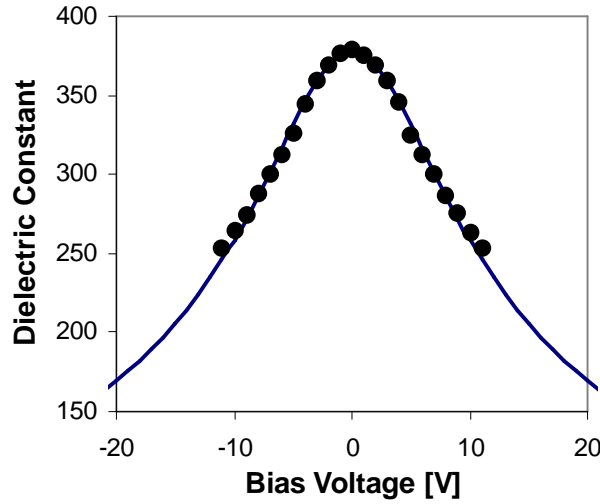


Fig. 2.2: Theoretical curve of the dielectric response (blue) compared to measured values of PST 50/50 from Fig. 5.7, Section 5.2.

2.1.3 Figure of Merit

The figure of merit (FOM) used throughout this work is defined as $\frac{\text{tunability}[\%]}{\text{loss}[\%]}$ and

allows a good comparison between different ferroelectric thin films for voltage tunable applications. It combines the two most important figures (tunability and loss) in just one number. A useful film for applications should have a FOM > 15.

2.2 Dielectric Loss in Ferroelectrics

In this study ferroelectrics of the displacive type in the paraelectric state at room temperature were used. The theory of dielectric loss for this type of ferroelectrics was developed by Gurevich and Tagantsev [3]. For a ferroelectric film both the intrinsic (fundamental phonon loss mechanism) and extrinsic losses (e.g. due to defects) need to be considered. The models of the dominant loss mechanism in ferroelectric films will be discussed in this section.

2.2.1 Intrinsic Losses

The origin of the fundamental loss is the interaction of the ac field with the phonons of the material. The theory of the loss stemming from this interaction has been developed for crystalline materials with a well defined phonon spectrum, i.e., for materials where the damping of phonons (average frequency of the inter-phonon collisions), Γ , is much smaller than their frequencies. According to this theory, in terms of quantum mechanics, the fundamental loss mainly corresponds to the absorption of the energy quantum of the electromagnetic field $\hbar\omega$ (ω is the ac field frequency) in collisions with the thermal phonons, which have much higher energies. This large difference in the energies makes it difficult to satisfy the conservation laws in these collisions. In such a complicated situation there exist three efficient schemes of absorption of the $\hbar\omega$ -quanta, which correspond to the three main fundamental loss mechanisms: (1) three-quantum, (2) four-quantum, and (3) quasi-Debye (Fig. 2.3).

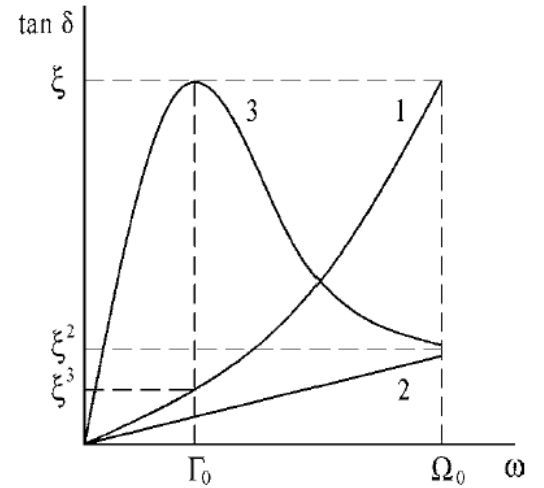


Fig. 2.3: Results of phonon transport theory. Schematic off-scale plot of the frequency dependence of the three-quantum (1), four-quantum (2), and quasi-Debye (3) contributions to the loss tangent due to interaction of the ac electric field with the phonons of the soft mode of a displacive type ferroelectric. Ω_0 and Γ_0 are the soft-mode frequency and damping, respectively. $\xi = \Gamma_0/\Omega_0$. The range of applicability of the theory is $\Gamma_0 \ll \Omega_0$ and $\omega \ll \Omega_0$ (at ω tending to Ω_0 the curves are only shown to guide the eye) [3].

a) Three-Quantum Mechanism.

The three-quantum mechanism corresponds to a process involving a $\hbar\omega$ -quantum and two phonons. Due to the big difference between the energy quantum of the electromagnetic field $\hbar\omega$ and those of the thermal phonons, the three-quantum processes can take place only in the regions of the wave-vector space (\vec{k} -space) where the difference between the frequencies of two different phonon branches is small, specifically, of the order of ω and/or of the phonon damping Γ . These regions are usually located in the vicinity of the degeneracy lines of the spectrum, i.e. the lines in \vec{k} -space where the frequencies of different branches are equal. In the materials of interest for tunable applications, the phonon spectrum contains lowlying (soft) optical modes controlling their high dielectric permittivity and the degeneracy lines formed with participation of these modes are of primary importance for the loss. Since the degeneracy of the spectrum is mainly controlled by the symmetry of the crystal, the explicit temperature dependence (which does not take into account the temperature dependence of the dielectric permittivity) and frequency dependence of the three-quantum loss are very sensitive to the symmetry of the crystal.

b) Four-Quantum Mechanism.

The four-quantum mechanism corresponds to the field-quantum absorption processes involving three phonons [4, 5]. The conservation (energy and quasi-momentum) laws do not impose strong restrictions on the type and energy of the phonons participating in these processes. For this reason, in contrast to the three-quantum processes, not only the degeneracy lines but also the whole thermally excited part of the \vec{k} -space nearly homogeneously contributes to the loss. Due to this fact, the explicit temperature and frequency dependence of the contribution of this mechanism to the imaginary part of the dielectric permittivity appears to be insensitive to the symmetry of the crystal. However, the three-quantum contribution is still leading in the total balance of the intrinsic loss [3, 6].

The three- and four-quantum mechanisms are the only two mechanisms which control the intrinsic loss in centrosymmetric crystals [3]. In the case of practical interest of the low-microwave-loss materials, the theory of phonon transport is applicable with quite good accuracy. This means that, possessing the complete information on the phonon spectrum and the constants of inter-phonon and ac field-phonon couplings, one can calculate the intrinsic dielectric loss with an accuracy equal to the relative damping of the typical phonons participating in the absorption of the ac field [3]. Thus, the result that the intrinsic loss in centrosymmetric crystals is given by the sum of the three- and four-quantum contribution can be considered as perfectly justified.

c) Quasi-Debye Loss Mechanism.

The origin of this mechanism is the relaxation of the phonon distribution function of the crystal [3, 7, 8]. In noncentrosymmetric crystals, the phonon frequencies are linear functions of a small electric field applied to the crystal. Thus, the oscillations of the ac field result in time modulation of the phonon frequencies; the latter in turn induces a deviation of the phonon distribution function from its equilibrium value. A relaxation of the phonon distribution functions gives rise to dielectric loss in a similar way as a relaxation of the distribution function of the dipoles gives rise to the loss in the Debye theory [9]. This analogy is expressed by the name “quasi-Debye”. The frequency dependence of the quasi-Debye contribution to the loss factor is of the Debye type, the average relaxation time of the phonon distribution function playing the role of the Debye relaxation time. In microwave materials for tunable application, which are typically centrosymmetric, the quasi-Debye mechanism does not contribute to the loss in the absence of the tuning bias. However, under a dc bias field, \vec{E}_0 , it becomes active due to the breaking of the central symmetry so that one is dealing with the *dc field-induced quasi-Debye mechanism*. An important feature of the quasi-Debye loss is that as a function of frequency, similar to the Debye loss, its contribution to the loss tangent passes through a maximum at $\omega \cong \Gamma$. For the materials used in this study, where the phonon damping Γ is of the order of 100 GHz, this means a certain slowing down of the linear

frequency dependence of the Quasi-Debye loss in the higher part of the microwave-frequency range.

2.2.2 Extrinsic Losses

The role of the intrinsic mechanisms in the total balance of the dielectric loss of a material is strongly dependent on the dielectric permittivity of the material and the measuring frequency: typically, the higher the frequency and permittivity, the more important the intrinsic loss. In the case of tunable ferroelectric materials at microwave frequencies, the intrinsic and extrinsic contributions are comparable so that the dominating contribution to the loss may be extrinsic or intrinsic depending on the quality of the material. A kind of extrinsic/intrinsic crossover in loss may also take place under the action of a dc bias field, i.e. without the field, the extrinsic contribution dominates the loss, whereas under the field the intrinsic one does. Among the known extrinsic loss mechanisms those listed below are considered as significantly contributing to the loss in tunable microwave materials: (1) loss owing to charged defects, (2) universal relaxation law mechanism, (3) quasi-Debye contribution induced by random-field defects.

a) Loss Owing to Charged Defects.

Motion of charged defects caused by an ac electric field results in a generation of acoustic waves at the frequency of the applied field. This brings about an additional loss mechanism that was proposed by Schlöman [10], formulated for high-dielectric-constant materials by Vendik and Platonova [11], and developed by Garin [12]. The contribution of this mechanism to the loss tangent can be approximated as follows:

$$\tan \delta_{ch} = F\varepsilon \frac{n_d Z^2 \omega}{\rho v_t^3 4\pi} \left[1 - \frac{1}{(1 + \omega^2 / \omega_c^2)^2} \right] \quad [\text{Eq. 2.21}]$$

where Z and n_d are the effective charge of the defects and their atomic concentration; ρ and v_t are the density and average transversal sound velocity of the material; F is a material-dependent numerical constant of the order of unity; $\omega_c = v_t/r_c$ where r_c is the correlation length of the charge distribution in the material. The physical meaning of r_c is

the minimal distance at which the electroneutrality is maintained. For Schottky defects r_c is of the order of the typical distance between the positively and negatively charged defects. This mechanism may play an essential role in thin film based tunable capacitors, where an elevated defect concentration compared to the bulk material is expected. In this case, the effect of semiconductor depletion of the carriers from the deep traps (caused by ferroelectric/electrode contact) [13, 14] will further increase the contribution of this mechanism via a strong reduction of $\omega_c = v_d/r_c$. This occurs in the depleted areas due to a strong increase of r_c up to the depletion length. An essential feature of this mechanism is that its contribution to the loss tangent is proportional to the permittivity of the material. This implies that this contribution is inversely dependent on the applied dc field.

b) Universal-Relaxation-Law Mechanism.

For all of the loss mechanisms discussed above, a linear frequency dependence of the loss tangent is typical at least for microwave frequencies and below. In reality, this dependence is usually observed at microwave and higher frequencies. For lower frequencies, a much weaker frequency dependence is usually observed, which is consistent with the so-called universal relaxation law which in turn corresponds to the following expression for the complex dielectric permittivity ϵ^* [15]:

$$\epsilon^* = G(i\omega)^{n-1} = G(\cos(n\pi/2) - i\sin(n\pi/2))\omega^{n-1} \quad [\text{Eq. 2.22}]$$

where G is a frequency-independent constant and $0 < n < 1$. In perovskite thin films in both frequency and time domains, dielectric relaxation corresponding to this equation (for n close to but smaller than unity) has been reported up to the microwave frequency range, e.g. in (Ba,Sr)TiO₃ [16]. The physical origin of this behavior is attributed to a variation in charge transport barriers, e.g. at the grain boundaries [17], or to creep of the boundary of the near-by-electrode depletion layer [18]. No information is available on the dependence of G on the dielectric constant of the material.

c) Impact of Local Polar Regions.

The typically centrosymmetric tunable materials may have local polar regions induced by various defects and structural imperfections. For example, infrared reflectivity investigations of SrTiO₃ ceramics revealed a clear presence of grain-boundary-induced polar phase inclusions [19]. Random field defects can also be responsible for the appearance of local polar regions [20]. In all these polar inclusions, the quasi-Debye mechanisms is expected to be active. Though the volume fraction of the polar phase is typically small, this “defects-induced” quasi-Debye mechanism may be important due to its large (compared to other intrinsic loss mechanisms) contribution per unit of volume. Though the theory of the “defect-induced” quasi-Debye mechanism is not developed, using the results on the quasi-Debye loss mechanism should be strongly ε -dependent. According to Ref. [6] in the ferroelectric phase of a displacive ferroelectric $\tan \delta_{QD} \propto \varepsilon^{3/2} P_S^2$ where P_S is the spontaneous polarization. In the case of non-polar tunable material with polar inclusions one can substitute the volume average of the local polarization squared, $\langle P_{loc}^2 \rangle$, for P_S^2 to evaluate the contribution of the “defect-induced” quasi-Debye mechanism as

$$\tan \delta_{dQD} \propto \varepsilon^{3/2} \langle P_{loc}^2 \rangle. \quad [\text{Eq. 2.23}]$$

2.4 Crystallography of Perovskites

The structural family of perovskites is a large family of compounds having crystal structures related to the mineral perovskite CaTiO_3 . In the ideal form the crystal structure of cubic ABX_3 perovskite can be described as consisting of corner sharing $[\text{BX}_6]$ octahedra with the A cation occupying the 12-fold coordination site formed in the middle of the cube of eight such octahedra. The ideal cubic perovskite structure is not very common and also the mineral perovskite itself is slightly distorted. The perovskite family of oxides is probably the best studied family of oxides. The interest in compounds belonging to this family of crystal structures arise in the large and ever surprising variety of properties exhibited and the flexibility to accommodate almost all of the elements in the periodic system. Pioneering structural work on perovskites were conducted by Goldschmidt *et al.* in the 1920s that formed the basis for further exploration of the perovskite family of compounds [21]. Distorted perovskites have reduced symmetry, which is important for their magnetic and electric properties. Due to these properties, perovskites have great industrial importance, especially the ferroelectric tetragonal and paraelectric cubic form of $(\text{Ba,Sr})\text{TiO}_3$ and $(\text{Pb,Sr})\text{TiO}_3$.

2.4.1 The crystal structure of perovskite

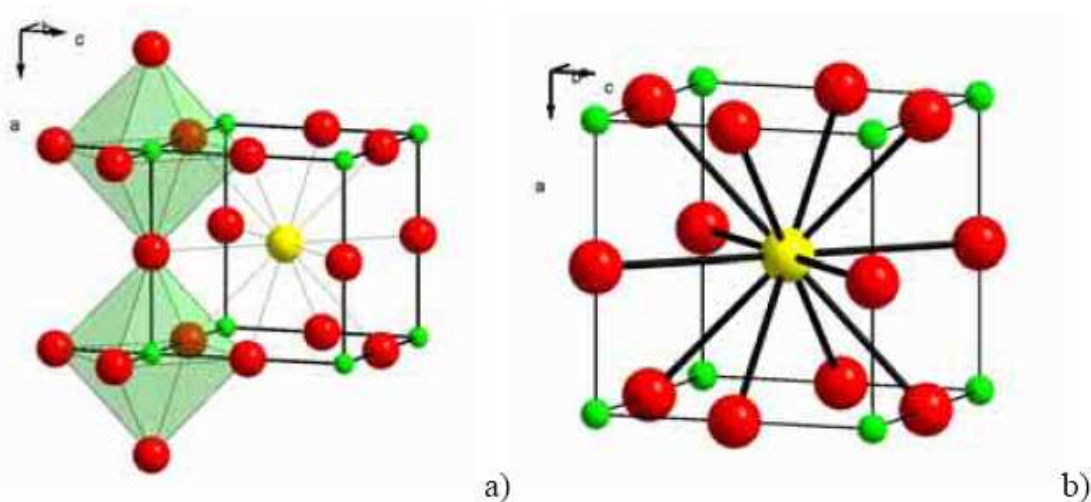


Fig. 2.4: Outline of the ideal cubic perovskite structure SrTiO_3 that has (a) a three dimensional net of corner sharing $[\text{TiO}_6]$ octahedra with (b) Sr^{2+} ions in the twelve fold cavities in between the polyhedra. Red = Oxygen green = Ti and yellow = Sr.

If the large oxide ion is combined with a metal ion having a small radius the resulting crystal structure can be looked upon as close packed oxygen ions with metal ions in the interstitials. This is observed for many compounds with oxygen ions and transition metals of valence +2, *e.g.* NiO, CoO, and MnO. In these crystal structures the oxygen ions form a cubic close packed lattice (ccp) with the metal ion in octahedral interstitials (*i.e.* the rock salt structure). Replacing one fourth of the oxygen with a cation of approximately the same radius as oxygen (*e.g.* alkali, alkali earth or rare earth element) reduces the number of octahedral voids, occupied by a small cation, to one fourth. The chemical formula can be written as ABX_3 and the crystal structure is called perovskite. X is often oxygen but also other large ions such as F and Cl are possible.

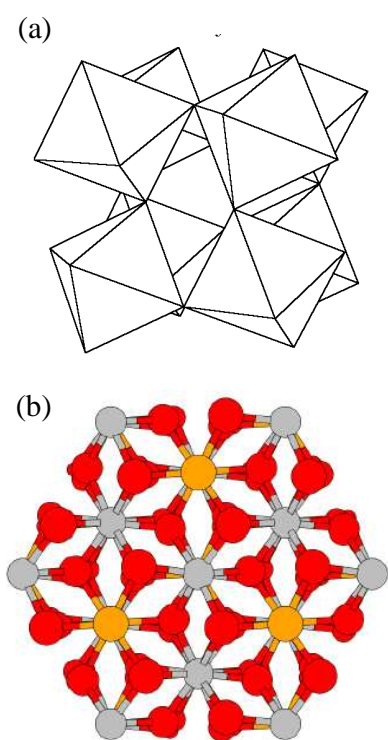


Fig. 2.5: Crystal structure of the RhF_3 (a) and ilmenite type (b)

The idealised cubic structure is realised in *e.g.* $SrTiO_3$. The latter can be described as Sr^{2+} and O^{2-} ions forming a cubic close packed lattice with Ti^{4+} ions occupying the octahedral holes created by the oxygens. The perovskite structure has a three dimensional net of corner sharing $[TiO_6]$ octahedra with Sr^{2+} ions in the twelve fold cavities in between the polyhedra, see Fig. 2.4. If the position of the Sr^{2+} ion (A) is vacant the remaining framework is that of the ReO_3 (Rhenium(IV)oxid) type. Partial occupation of the A position occurs in the cubic tungsten bronzes A_xWO_3 ($A = \text{alkali metal}$, $0.3 \leq x \leq 0.93$). The ReO_3 structure type can be converted to a more dense packing by rotating the octahedra until a hexagonal close packing is obtained of the RhF_3 (Rhodium(III)fluorid) type. The void in the centre has then an octahedral surrounding. If this octahedral hole is occupied we have the ilmenite structure, $FeTiO_3$, Fig. 2.5.

The perovskite structure is known to be very flexible and the A and B ions can be varied leading to the large number of known compounds with perovskite or related structures. Most perovskites are distorted and do not have the ideal cubic structure. Three main factors are identified as being responsible for the distortion: size effects, deviations from the ideal composition and the Jahn-Teller effect.

It is rare that a distortion of a certain perovskite compound can be assigned to a single effect. In most cases several factors act on the structure. As an example of the complexity BaTiO₃ has three phase transitions on heating: rhombohedral — -90°C → orthorhombic — 5°C → tetragonal — 120°C → cubic, Fig. 2.6.

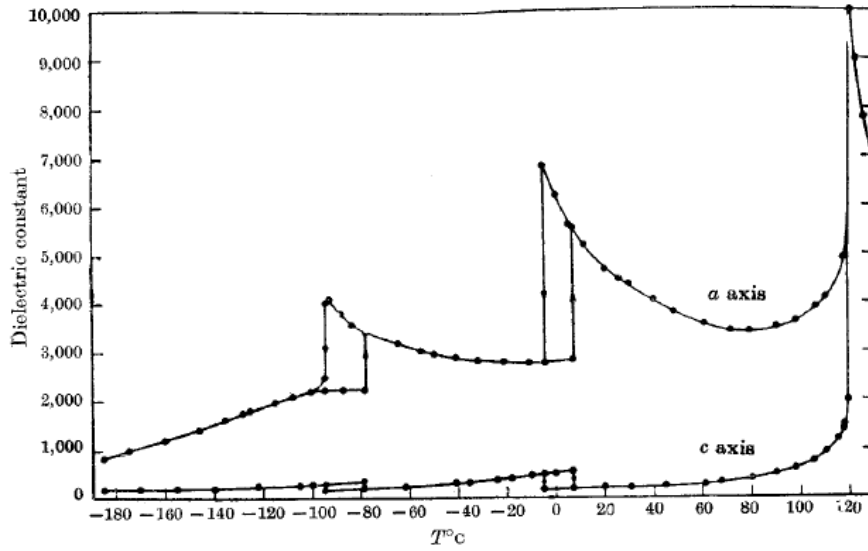


Fig. 2.6: Dielectric constant vs Temperature of BaTiO₃, Merz 1949 [22].

a) Size effects

In the ideal cubic case the cell axis, a , is geometrically related to the ionic radii (r_A , r_B , and r_O) as described in the following equation:

$$a = \sqrt{2}(r_A + r_B) = 2(r_B + r_O) \quad [\text{Eq. 2.24}]$$

The ratio of the two expressions for the cell length is called the Goldschmidt's *tolerance factor* t and allows us to estimate the degree of distortion. It is based on ionic radii *i.e.* purely ionic bonding is assumed, but can be regarded as an indication for compounds with a high degree of ionic bonding; it is described in the following equation:

$$t = \frac{(r_A + r_O)}{\sqrt{2}(r_B + r_O)} \quad [\text{Eq. 2.25}]$$

The ideal cubic perovskite SrTiO₃ has $t=1.00$, $r_A=1.44$ Å, $r_B=0.605$ Å, and $r_O=1.40$ Å. If the A ion is smaller than the ideal value then t becomes smaller than 1. As a result the

[BO₆] octahedra will tilt in order to fill the space. However, the cubic structure occurs if $0.89 < t < 1$ [23]. Lower values of t will lower the symmetry of the crystal structure. For example GdFeO₃ [24] with $t = 0.81$ is orthorhombic ($r_A = 1.107 \text{ \AA}$ and $r_B = 0.78 \text{ \AA}$), see Fig. 2.7a. Also the mineral perovskite itself, CaTiO₃, has this structure. With values less than 0.8 the ilmenite structure is more stable.

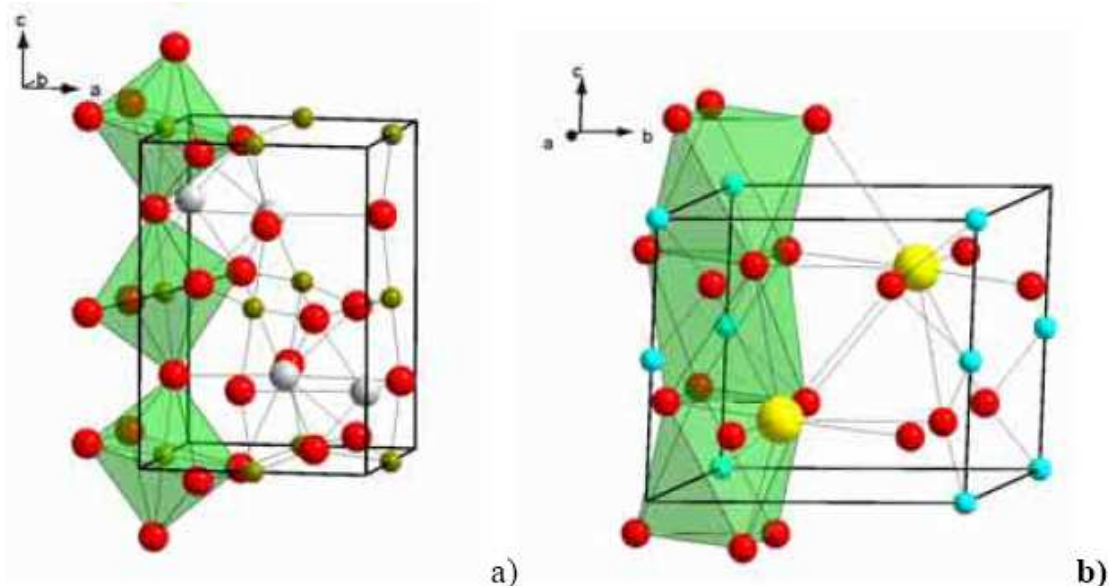


Fig. 2.7: (a) Low values of the tolerance factor t will lower the symmetry of the crystal structure. GdFeO₃ with $t = 0.81$ have tilted [FeO₆] octahedra and crystallize in the orthorhombic system ($r_A = 1.107 \text{ \AA}$ and $r_B = 0.78 \text{ \AA}$). (b) If t is larger than 1 due to a large A or a small B ion then hexagonal variants form of the perovskite structure. The t value for BaNiO₃ is 1.13 ($r_A = 1.61 \text{ \AA}$ and $r_B = 0.48 \text{ \AA}$).

On the other hand if t is larger than 1 due to a large A or a small B ion then hexagonal variants of the perovskite structure are stable, e.g. the BaNiO₃ type structures. In this case the close packed layers are stacked in a hexagonal manner in contrast to the cubic one found for SrTiO₃, leading to face sharing of the [NiO₆] octahedra, see Fig. 2.7b. The t value for BaNiO₃ is 1.13 ($r_A = 1.61 \text{ \AA}$ and $r_B = 0.48 \text{ \AA}$). Since perovskites are not truly ionic compounds and since the t values also depend on what values are taken for the ionic radii, the tolerance factor is only a rough estimate.

b) Changing the composition from the ideal ABO₃

An example is the family of compounds SrFeO_x ($2.5 \leq x \leq 3$). The valency of the Fe ions can be changed by heating a sample in either an oxidising or a reducing

environment. As a result the oxygen content can vary in between 2.5 and 3. In for example $\text{SrFeO}_{2.875}$ some Fe ions can be assigned to the oxidation state +3 and others to +4. The oxygen vacancies order so that FeO_5 square pyramids are formed, see Fig. 2.8. The SrFeO_x compounds are examples of defect perovskites.

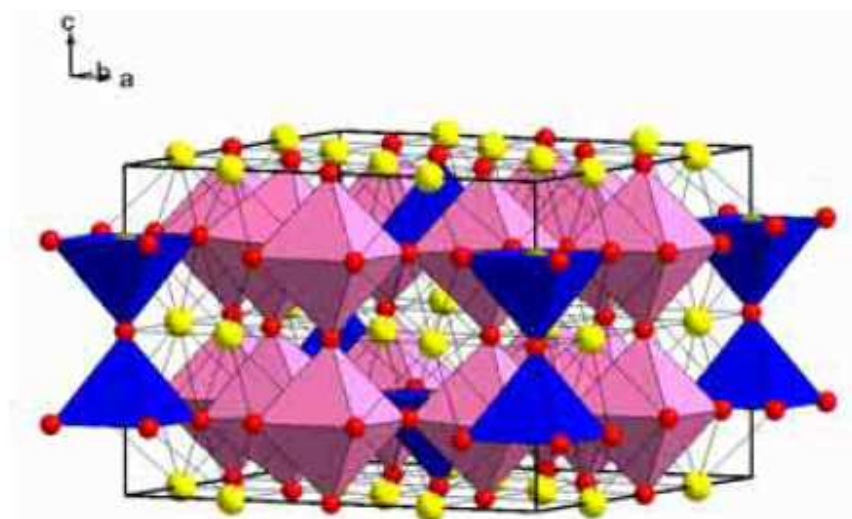


Fig. 2.8: Ordering of oxygen vacancies in $\text{SrFeO}_{2.875}$ ($=\text{Sr}_8\text{Fe}_8\text{O}_{23}$). Fe ions are located in both square pyramids and in octahedra.

Their chemistry can be described according to the homologous series $\text{A}_n\text{B}_n\text{O}_{3n-1}$, $n = 2 - \infty$. Several other types of vacancy orderings are known, e.g. the structures of $\text{Ca}_2\text{Mn}_2\text{O}_5$ and $\text{La}_2\text{Ni}_2\text{O}_5$ having $n = 2$ are shown in Fig. 2.9a-b.

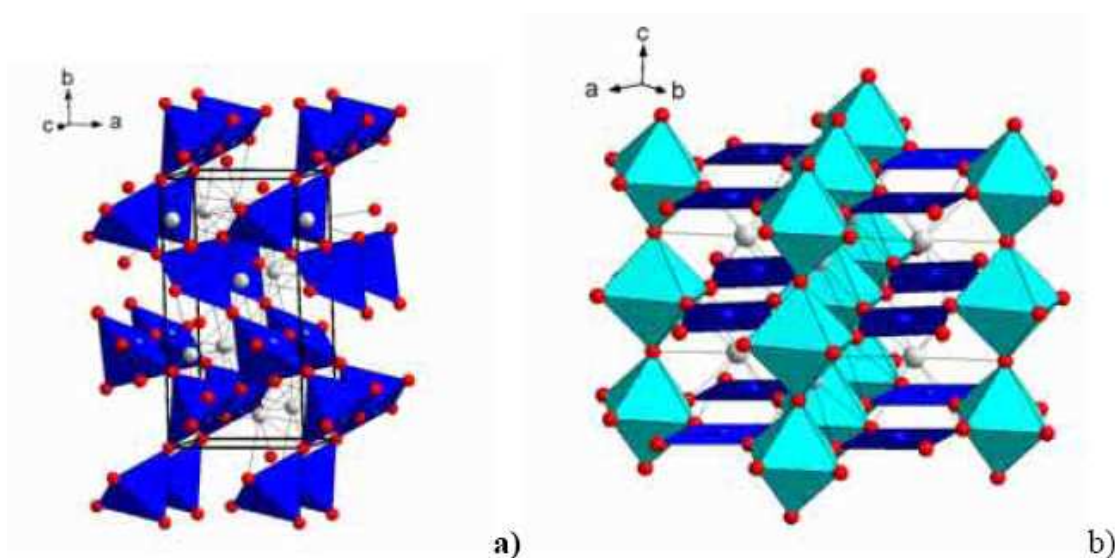


Fig. 2.9: Ordering of oxygen vacancies in (a) $\text{Ca}_2\text{Mn}_2\text{O}_5$ having $[\text{MnO}_5]$ square pyramids and (b) $\text{La}_2\text{Ni}_2\text{O}_5$ having $[\text{NiO}_6]$ octahedra and $[\text{NiO}_4]$ square planes.

3. Jahn-Teller effects

In some perovskites the distortion of the structure can be assigned to Jahn-Teller active ions at the B position. For example in LnMnO_3 ($\text{Ln} = \text{La, Pr or Nb}$) with Mn^{3+} ions the $3d^4$ electrons divide up into 3 t_g and 1 e_g electron. The odd number of electrons in the e_g orbital causes an elongation of the $[\text{MnO}_6]$ octahedron.

2.4.2 Electronic and Magnetic Properties of Perovskites

Perovskites with transition metal ions (TMI) on the B site show an enormous variety of intriguing electronic or magnetic properties. This variety is not only related to their chemical flexibility, but also and to a larger extent related to the complex character that transition metal ions play in certain coordinations with oxygen or halides [25]. While magnetism and electronic correlations are usually related to unfilled 3d electron shells of the TMI, pronounced dielectric properties are connected with filled 3d electron shells. Multiferrocity, a coexistence of spontaneous ferroelectric and ferromagnetic moments, is a rare phenomenon due to the small number of low-symmetry magnetic point groups that allow a spontaneous polarisation [26]. Nevertheless, in the presence of competing interactions [27], canted moments [28, 29] or in composites [30] large magneto-capacitive couplings have been reported.

In the following examples of materials properties are discussed in which transition metal perovskites and related structures prove to be outstanding. To some extent these aspects also touch application areas, as e.g. capacitors, transducers, actuators, sensors and electrooptical switches.

a) Dielectric and ferroelectric perovskites

High dielectric permittivity (ϵ) or ferroelectric materials are of enormous importance as electroceramics for engineering and electronics. Perovskites, e.g. titanium or niobium perovskites, BaTiO_3 and LiNbO_3 , have been intensively studied in the past [31]. A large ϵ is based on collective polar displacements of the metal ions with respect to the oxygen

sublattice and is a highly nonlinear and anisotropic phenomenon. The phase transition that leads to ferroelectricity is usually described by a soft-mode model [32].

To optimize dielectric and mechanical properties several routes have been followed from the structurally simple BaTiO_3 via the solid solution system $\text{Pb}(\text{Zr,Ti})\text{O}_3$ to other distinct families of materials. These routes explicitly take into account the flexibility for chemical manipulation and “docility” of the perovskites [31]. One of them is the relaxor ferroelectric. It is genuinely based on a multi-element substituted Pb titanate (PbTiO_3) with the composition $\text{A}(\text{B}'\text{B}'')\text{O}_3$ with a random occupation of the A and B sites by metal ions of different valence.

Relaxor ferroelectrics show enormously large dielectric constants, a pronounced frequency dispersion and variation of ϵ as function of temperature. These effects are due to slow relaxation processes for temperatures above a glass transition [33]. The length scales of fluctuating composition and spontaneous polarization are 2-5 nm, i.e. the effects are based on electronic inhomogeneities and the existence of polar nanoregions. The lattice part of the response is considered to be a local softening of transverse-optical phonon branch that prevents the propagation of long-wavelength ($q = 0$) phonons. It is interesting to note that the fundamental limit, the superparaelectric state, is still not reached for such small length scales [34]. Generic examples for relaxor ferroelectrics are PZN: $\text{Pb}(\text{Zn}_{1/3}\text{Nb}_{2/3})\text{O}_{3-x}\text{PbTiO}_3$ and PMN: $\text{Pb}(\text{Mg}_{1/3}\text{Nb}_{2/3})\text{O}_{3-x}\text{PbTiO}_3$, with PZN having a higher temperature scale compared to PMN.

Incipient ferroelectrics or quantum paraelectrics can be regarded as almost ferroelectric crystals [35]. Examples are KTaO_3 and SrTiO_3 [36]. Pronounced quantum fluctuations of ions suppress the phase-transition into the ferroelectric state and stabilize the soft transverse optical mode. The dielectric susceptibility shows a divergence in the limit T to 0 K together with pronounced phonon anharmonicities [36]. In these systems even minor substitutions or doping can induce phase transitions into ferroelectric states. Finally, perovskite related oxides with giant dielectric constants (GDC) where no evidence for a ferroelectric instability exists should be mentioned. These nonintrinsic permittivities are attributed to barrier layers and surface effects [37]. Examples are $\text{CaCu}_3\text{Ti}_4\text{O}_{12}$, [38] and the Li-ion conductor material $\text{La}_{0.67}\text{Li}_{0.25}\text{Ti}_{0.75}\text{Al}_{0.25}\text{O}_3$ [39].

b) Magnetism and electronic correlations

Magnetism or orbital (electronic) ordering phenomena of various kinds are observed in perovskites with TMI that have unfilled 3d electron shells (see Fig. 2.10). Electronic

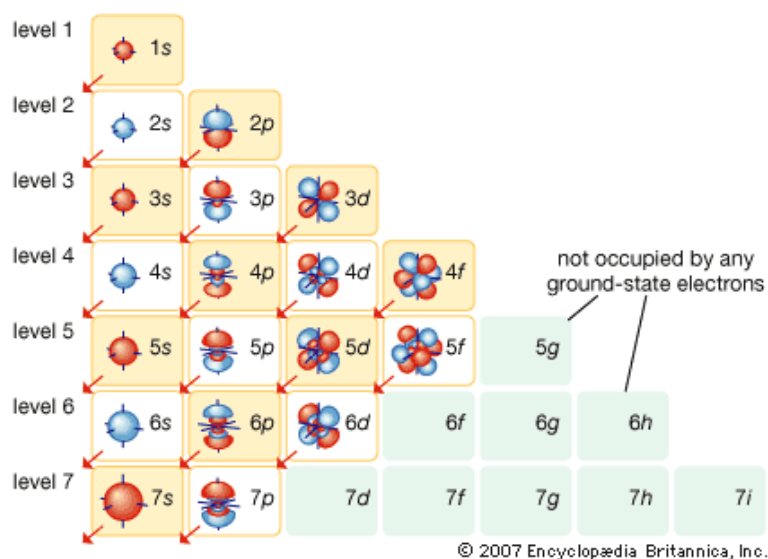


Fig. 2.10: An electron shell representation from the Encyclopædia Britannica

correlations [40] of such 3d states are generally strong, as the ratio U_d/W of the Coulomb repulsion energy U_d vs. the bandwidth W is larger compared to other electronic states, i.e. they have a more local character and a tendency for insulating states or metal-insulator transitions [41]. Hopping and superexchange of these electrons takes place via oxygen sites due to the overlap of the respective wave function. Thereby, the properties and

phase diagrams of a perovskite strongly depend on nonstoichiometries and even more on tilting or distortions of the $[\text{BO}_6]$ octahedra. Further aspects rely on order/disorder processes of the orbital part of the 3d wave function, charge doping and charge/orbital inhomogeneous states that lead to colossal response, e.g. to external magnetic fields [42].

Before, however, considering such effects the properties of the system are given by a hierarchy of energies based on the electronic structure, i.e. the number of 3d electrons, the Hund's Rule coupling, the crystalline electric field or Jahn-Teller splitting of the 3d electron states and finally due to exchange energies.

c) Cuprates, Jahn-Teller distortions and high temperature superconductors

This hierarchy of energies is well established for cuprates with Cu^{2+} in a $3d^9$ configuration. The hole in the d shell has $e_g x^2-y^2$ symmetry and contributes to an $s = 1/2$ spin moment. The orbital moment is quenched due to the crystalline electric field of the surrounding oxygen. The e_g electron is Jahn-Teller active, i.e. local or collective configurations with oxygen in distorted octahedra are energetically preferable. Extreme

limits are pyramidal [CuO₅] or even a planar [CuO₄] configuration of the oxygen neighbors. Thereby the superexchange and magnetic interactions between the $s = 1/2$ spin moments are restricted to a plane or, if building blocks are shifted by half a unit cell within the plane, to a quasi-one dimensional path. There are numerous realizations of such low-dimensional magnetic systems as in Sr₂CuO₃ (spin chain system) or SrCu₂O₃ (spin ladder system) [43]. Due to the small coordination number of the spin moments in one dimension and pronounced quantum fluctuations related to the small magnitude of the spin, such compounds do generally not show long range ordering. Strong fluctuations are evident as broad maxima in the magnetic susceptibility and continua in inelastic neutron scattering.

Superexchange and electronic correlations restricted to a two dimensional, weakly doped plane are the key ingredients of high temperature superconductors. The crystal structure of the prototype and perovskite related compound is YBa₂Cu₃O_{7-x}. For $x \approx 1$ the resulting Cu²⁺ with $s = 1/2$ moments show long antiferromagnetic range ordering with a Néel temperature¹ of more than 500 K. This high ordering temperature marks the exceptionally large energy scales and strong correlations involved in these materials. With smaller x doping is induced that leads to a drastic drop of the Néel temperature and the onset of high temperature superconductivity. The maximum superconducting transition temperature is $T_{Cmax} = 92$ K for this system.

Electronic correlations are essential to understand the effect of doping. The electronic structure of cuprates in the vicinity of the Fermi level is given by an occupied low-energy and an unoccupied, high energy band, the lower and the upper Hubbard band, separated by the Coulomb repulsion energy U_d of the 3d electrons. High temperature superconductors are charge transfer insulators, i.e. the oxygen is included in this scheme as an occupied, nonbonding 2p band separated by a smaller charge transfer energy Δ from the upper Hubbard band ($\Delta < U_d$). The doping process consists of introducing a novel correlated electron state, the Zhang-Rice singlet state [41], in the proximity of the oxygen band. This state of hybridized Cu and O character leads to a transformation from a long range Néel state to a high temperature superconductor. Although the number of

¹ The antiferromagnetic Curie point is called the Néel temperature in honour of the French physicist Louis Néel, who in 1936 successfully explained antiferromagnetism.

known high temperature superconductors seem to be large (of the order of 20 compounds) they all rely on this scheme of a doped, two dimensional perovskite related structure with pronounced electronic correlations [41, 44, 45].

d) Cobaltates, spin state transitions and oxygen deficiency

If the above mentioned hierarchy of energies is not well defined, the compound chooses certain ways to lift degeneracies of the electronic system. Important are spin state transitions or crossover behaviour, a partial metallisation of 3d electrons, or charge

disproportionation of the TMI sites. Perovskites based on cobalt and vanadium serve as model systems for such effects and the resulting interplay of electronic and structural degrees of freedom. In the following two cobaltates are discussed briefly to give an example for the resulting complexities.

In the cobalt perovskite LaCoO_3 with the same crystal structure as is shown in Fig. 2.4 all three spin states of Co^{3+} ($3d^6$) are close to degenerate. As these states correspond to slightly different ionic radii, with decreasing temperatures a crossover of the dominant populations from high spin ($s = 2$), intermediate spin ($s = 1$) to low spin ($s = 0$) Co^{3+} $3d^6$ states takes place. This process is mainly controlled by temperature and has no evident collective character. The magnetic susceptibility shows a broad maximum and a strong decrease at low temperatures [46]. The

different ionic radii of the spin states also couple the electronic configurations of the TMIs only weakly to other properties of the compound.

An ordered oxygen deficiency leads to a multiplication of the unit cell volume. It has also profound influence on the electronic and magnetic properties of the compound [47]. Due to the smaller coordination number of some TMI sites the respective bandwidth is

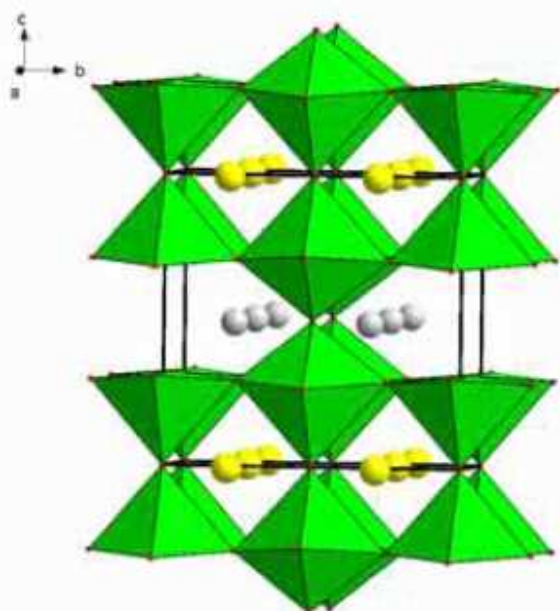


Fig. 2.11: The cobaltite $\text{GdBaCo}_2\text{O}_{5.5}$ has a perovskite related structure where 1/12 of the oxygen atoms are missing leading to that 50% of the Co atoms have square pyramidal $[\text{CoO}_5]$ coordination and 50% of the Co atoms have octahedral $[\text{CoO}_6]$ coordination. Ba atoms are yellow and Gd atoms are grey.

reduced and with increasing electronic correlations the tendencies for charge/orbital ordered states is enhanced. In Fig. 2.11 the perovskite cobaltite $\text{GdBaCo}_2\text{O}_{5.5}$ is depicted. Oxygen defects form chains of $[\text{CoO}_5]$ pyramids and $[\text{CoO}_6]$ octahedra along the crystallographic a -axis. Compared to the ideal perovskite LaCoO_3 , the behaviour is rather complex and highly collective. The phase diagram contains a metal-insulator transition and three different magnetic phases that include spin state ordering [48, 49].

e) Manganites and orbital degrees of freedom

In the manganite $(\text{La,Sr})\text{MnO}_3$ the ratio $\text{La}^{3+}/\text{Sr}^{2+}$ determines the oxidation state of Mn and thus the ratio $\text{Mn}^{3+}/\text{Mn}^{4+}$. This corresponds to the number of Mn sites with a single 3d e_g orbital occupied. Double exchange describes the situation where these states simultaneously hop via Mn^{4+} ions. The remaining 3 t_{2g} electrons on each Mn ion sum up to $s=3/2$ due to Hund's rule coupling and form a 'rigid background'. The band width and charge transport solely given by e_g states depends on the spin and orbital orientation of the exchange partners.

As function of composition different magnetic ground states and orbitally/charge ordered structures are observed. These degrees of freedom react rather cooperative due to the strong interlink of the octahedra in the perovskite structure [50]. Pronounced effects are observed in all physical quantities. However, most spectacular is the colossal magneto-resistance (CMR) at the borderline between a ferromagnetic insulating and ferromagnetic metallic phase

2.5 Sol-Gel Chemistry

There are many methods for ferroelectric thin film preparation, such as metal organic chemistry vapour deposition (MOCVD), pulsed laser deposition (PLD), magnetron sputtering and sol-gel. Thin films with high properties could be fabricated by all these methods, and comparatively perfect processing parameters were formed. The RF magnetron sputtering and sol-gel processing are relatively simple preparation methods while PLD produces films with superior quality. However, the drawback of PLD is the restriction to small sample sizes. The main advantage of the sol-gel method is the ease of doping (substitution of atoms on the A- and/or B site of the perovskite crystal) without purchasing new sputtering targets, and flexibility concerning the substrate size.

In this chapter the sol-gel processing of ferroelectrics is reviewed. The underlying chemical and physical aspects of the sol-gel deposition of these materials will be discussed, with a focus on understanding solution preparation, film deposition, and phase transformation (to the crystalline ceramic) which are occurring during film synthesis.

2.5.1 Solution Preparation

The general principle involved in the sol-gel deposition of perovskite films is to prepare a “homogeneous” solution of the necessary cation species that may later be applied to a substrate. The fabrication of thin films by this approach involves four basic steps: (1) synthesis of the precursor solution; (2) deposition by spin-coating where drying processes usually begin depending on the solvent; (3) low-temperature heat treatment for drying, pyrolysis of organic species (typically 300–400°C), and the formation of an amorphous film; (4) higher temperature annealing for densification and crystallization of the coating into the desired oxide phase (600–1100°C).

Solution preparation of perovskite materials generally involves the use of metalloorganic compounds that are dissolved in a common solvent. The starting reagents are typically metal alkoxide compounds, $M(OR)_x$, where M is a metal and R is an alkyl group, metal carboxylates, $M(OOCR)_x$, and metal β -diketonates, $MO_x(CH_3COCHCOCH_3)_x$. The selection of the starting reagents is dictated by solubility and reactivity considerations and the type of solution precursor species desired. The

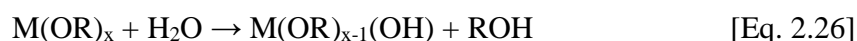
synthetic strategy used will define solution precursor properties such as equivalent solids content, extent of oligomerisation and cation interaction, degree of homogeneity and reactivity, type and number of modifying ligands, and precursor size, structure, and shape. The solution route used will also determine the temperature at which pyrolysis of organic species occurs, the weight loss associated with oxide formation, the densification and crystallisation behavior of the film, and stress development within the film. While some of these effects are now well understood, others are less clear, partly because of the difficulty in characterizing the solution precursor and the resulting amorphous film. In addition to precursor characteristics, film processing behavior, such as substrate wetting, can also play a role in determining the solution chemistry that must be developed. Film properties that can necessitate changes in solution chemistry include poor thickness uniformity (striations), crack formation, crystallization behavior and phase purity, and compositional nonuniformities [51, 52].

In this study a modified sol-gel route was used which is a mixture of two classical approaches:

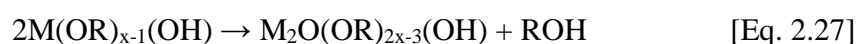
- 1) Sol-gel processes that use 2-methoxyethanol as a reactant and solvent [53 - 55].
- 2) Chelate processes that use modifying ligands such as acetic acid [56 - 58].

Although other alcohols have been utilized, the solvent 2-methoxyethanol ($\text{CH}_3\text{-OCH}_2\text{CH}_2\text{OH}$), is most extensively used in the chemical synthesis of perovskite materials. Processes based on 2-methoxyethanol [53, 54] are most appropriately considered sol-gel processes and the key reactions leading to the formation of the precursor species are hydrolysis and condensation of the alkoxide reagents, in which metal-oxygen-metal (M-O-M) bonds are formed:

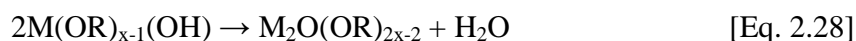
a) Hydrolysis:



b) Condensation (alcohol elimination):



c) Condensation (water elimination):



Another key reaction in the use of this solvent is the alcohol-exchange reaction that results in a decrease in the hydrolysis sensitivity of starting reagents such as zirconium n propoxide and titanium isopropoxide used in the production of PZT films:

d) Alcohol exchange:



where OR is a reactive alkoxy group and OR' is the less water sensitive methoxyethoxy group. 2-Methoxyethanol has also been found to be beneficial in the dissolution of carboxylate precursors such as lead acetate. In this case, by refluxing the lead acetate precursor in 2-methoxyethanol, one of the acetate groups is replaced, resulting in the formation of the soluble lead precursor, $\text{Pb}(\text{OOCCH}_3)(\text{OCH}_2\text{CH}_2\text{OCH}_3) \cdot 0.5\text{H}_2\text{O}$. Lead carboxylate compounds are usually employed due to the instability of lead alkoxides and their limited commercial availability. A typical process involves refluxing lead acetate and the alkoxide compounds in methoxyethanol in separate reaction vessels. This is followed by combining the solutions, further refluxing, distillation, and dilution to the desired volume. Prior to film formation, the stock solution prepared by the above process is then hydrolysed to promote oligomerisation.

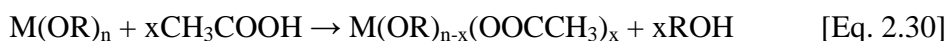
Solution processes based on the use of methoxyethanol are perhaps the most widely used of any of the CSD routes, primarily due to the ability of this solvent to solubilise a variety of starting reagents. When properly carried out, sol-gel processes offer excellent control and reproducibility of process chemistry, and nonhydrolysed solutions exhibit minimal aging effects. Thin films with excellent properties have been prepared by sol-gel for a number of materials including PZT, (high dielectric constant and ferroelectric hysteresis) [54], LiNbO_3 (electrooptic coefficient) [59, 60], BaTiO_3 (high dielectric constant) [61], and YBCO (high critical current capabilities) [62]. However, for the nonchemist, the procedures involved in solution synthesis can be rather complex.

Thus, while control over precursor characteristics is good, process simplicity is low. In addition, 2-methoxyethanol is a known teratogen, which presents a significant safety concern and inhibits its use in most manufacturing facilities.

Recently, the replacement of methoxyethanol by 1,3-propanediol in this process has been reported [63 - 65]. As with the original process, the key reaction that defines the nature of the precursor species is alcohol exchange between propanediol and the original alkoxy groups. Unlike 2-methoxyethanol, which is a bidentate nonbridging ligand, 1,3-propanediol is believed to act as a cross-linking agent in this process, resulting in the production of large oligomeric species. The rather unique properties of 1,3-propanediol also have an effect on film processing behavior, most notably in changing the characteristics of the deposited film. Due to the minimal volatility of this solvent at room temperature, aggregation of the precursor species after spin-casting is inhibited and film instability results. Rapid thermal treatment of the as-deposited layers serves to induce stability, resulting in films with good dielectric and ferroelectric properties [66]. Another key advantage of the diol sol-gel process is that single depositions result in layers between 0.5 and 1.0 μm , rather than the 0.1 μm thickness typically obtained with other sol-gel routes. Thicknesses in this range are of interest for manufacturing devices such as decoupling capacitors since these devices utilize perovskite layers that are $\sim 1.0 \mu\text{m}$ in thickness, and the films can thus be prepared with one or two deposition and heat treatment cycles [67].

A second class of solution synthesis approaches, i.e., the “hybrid” or “chelate” routes, also utilize alkoxide compounds as starting reagents for the B-site species. Unlike true sol-gel routes, these routes rely heavily on the molecular modification of the alkoxide compounds through reactions with other reagents, namely chelating ligands, such as acetic acid, acetylacetone (acac, 2,4-pentanedione), or amine compounds. Chelate processes share several common attributes with methoxyethanol-based sol-gel deposition, most importantly, the formation of small oligomeric species during solution synthesis. The most commonly used chelate processes are based on the solvent/chelating agent acetic acid, and although several steps are typically required for solution synthesis, solution preparation generally requires less than 1 h [68].

While hydrolysis and condensation reactions again play a role in chelate routes, the key reaction is chelation of the metal alkoxides, which is illustrated here for acetic acid:



The primary reason for using chelating agents is to reduce the hydrolysis sensitivity of the alkoxide compounds, resulting in solutions that are more easily handled in air. Chelating agents thus serve a similar function to methoxyethanol. Chelation also results in molecular modification of the alkoxide compounds, and chelating reagents thus also dictate the structure and properties of the resulting species. Since ligands such as acetate and acac have different decomposition pathways than do alkoxy ligands, other important changes in precursor properties, such as pyrolysis behavior, also result.

Compared to the 2-methoxyethanol process, chelate processes offer the advantages of relatively simple solution synthesis; involved distillation and refluxing strategies are not required. The addition of the chelating agent to the alkoxides is typically carried out during the initial process stages. Although the process eventually produces solutions that are water-insensitive, the initial phase of the process is usually still carried out under inert atmosphere conditions. As for 2-methoxyethanol processing, in the production of PZT films, lead acetate is used in conjunction with zirconium and titanium alkoxides. Either lead acetate is added to acetic acid for dissolution, followed by addition of the titanium and zirconium alkoxides [51], or the alkoxides are first chelated by acetic acid, followed by addition of lead acetate [56]. Alcohol and water are then typically added for control of solution viscosity and stability [51].

While chelate processes are simple and rapid, the chemistry involved in solution preparation is quite complex due to the number of reactions that occur. Key reactions were found to be chelation, esterification, and hydrolysis and condensation [69]. The complexity of the reactions results in a diminished ability to control precursor structure compared to true sol–gel approaches. The gain in process simplicity thus comes at a cost. However, precursor properties are still typically acceptable for film formation. While characterization of the precursor species formed in this process is not as complete as for the methoxyethanol route, studies of crystals generated from the reactions of acetic acid

and titanium isopropoxide would tend to indicate that they are small oligomers [70, 71]. Further information regarding the nature of the precursors was obtained through the addition of pyridine to a typical chelate solution [72]. Concentrating this solution resulted in the isolation of lead–pyridine crystals, indicating that as for the methoxyethanol sol–gel process, the lead species remain isolated from the titanium and zirconium. The precursors are thus chemically heterogeneous on an atomic scale.

Another drawback of chelate processes is that continued reactivity in the precursor solution following synthesis can result in a change in precursor characteristics over time (weeks to months) and thereby in a degradation in film properties. This occurs because substituent groups such as acetate, while less susceptible to hydrolysis than alkoxy groups, may still be attacked by water, resulting in a change in molecular structure. This reaction, continued esterification of the solution, and other reactions result in continued oligomerisation and realkoxylation of the species, eventually causing precipitation [73].

Combining these two approaches leads to an increased viscosity of the solution, resulting in a thicker single film thickness and an increased stability of the thus prepared solution.

2.5.2 Film Deposition

After the coating solution has been prepared, thin films are typically formed by spin-casting or dip-coating, and the desired ceramic phase is obtained by heat treatment. At the laboratory scale, deposition is usually achieved by simply depositing a few drops of the solution onto a cleaned, electroded Si wafer using a syringe with a 0.2 μm filter. The wafer is typically flooded during a static dispense, prior to spinning at 1000–8000 rpm.

An as-deposited film is amorphous and typically retains a significant organic fraction. Its nature at this stage is highly dependent on the characteristics of the solution precursor species and the solvent. The reactivity of the precursors is determined by the starting reagents, the type of modifying ligands used, and the extent of modification. Three general classes of films may be described according to the type of precursor interactions and the film gelation behavior. They are chemical gel films (i.e., significant condensation during or shortly after deposition), physical gel films (i.e., a physical aggregation of

precursor species that leads to film stability), and nongelling films (i.e., minimal precursor interactions due to low precursor reactivity and low solvent volatility). For the production of high-quality films, it was found that either chemical or physical gelation is important. For nongelling films, condensation reactions that lead to film stability and improvements in processing behavior can be induced by a heat-treatment step immediately after deposition. The nature of the as-deposited film, which is defined by the precursor properties and aggregation behavior during deposition, is important since it not only provides insight into the nature of the precursors but also influences film densification during heat treatment.

Titania films serve as a good model system for understanding the processing behavior of perovskite films such as BST, PST, and PZT because the film-processing behavior in these more complex systems is strongly influenced by the behavior of the B-site species (here, Zr and Ti). While numerous processing similarities have been observed between the single component and the perovskite systems, precursor effects have been studied in much greater detail for titania and zirconia; hence, this discussion will focus primarily on these two materials. There is sufficient data to indicate that the processing/property relationships discussed hold for perovskite thin-film processing.

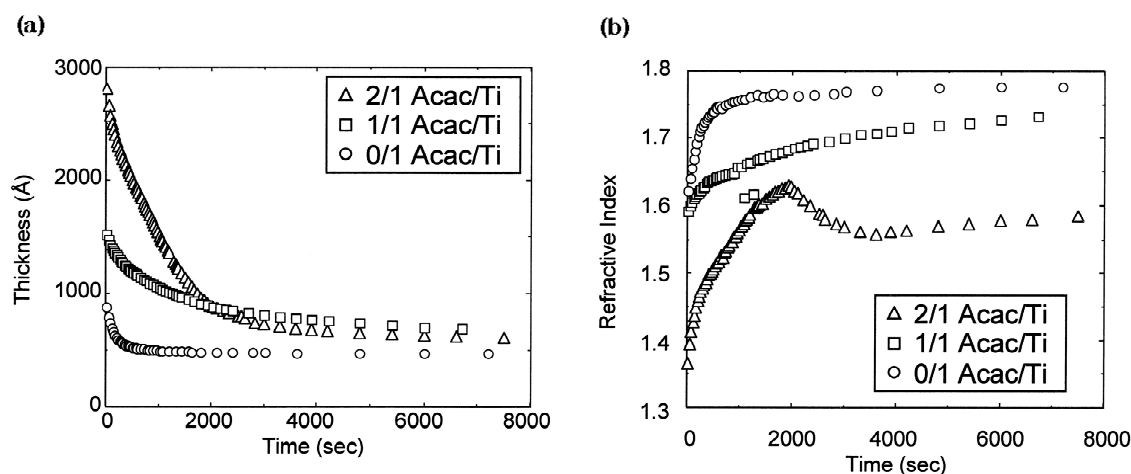


Fig.2.12: Consolidation behavior of titania thin films at room temperature immediately after deposition. (a) Ellipsometry results for thicknesses and (b) refractive indexes as a function of time. Solution precursors were prepared by reaction of $Ti(OBu^i)_4$ and acac; modifying ligand ratio (r) indicated in legend [74].

To investigate the effects of precursor properties on aggregation and film consolidation behavior, butanol-based solutions of titanium butoxide with varying amounts of the

modifying ligand acac were prepared [74]. Films were then fabricated by spin-casting at 3000 rpm for 30 s, and immediately following deposition, the variations in film thickness with time (at room temperature) were studied by single-wavelength ellipsometry. Results of this analysis are presented in Fig. 2.12 for the variations in film thickness, shrinkage and the initial refractive index. As the level of modification is increased from a molar ratio of 0 to 2 mol of acac/mol of Ti, the initial film thickness increases dramatically, and concurrently, the initial refractive decreases.

The observed results may be explained by considering (1) the effect of the acac ligand on precursor nature, (2) the properties of the modifying ligand compared to the parent groups (butoxy), and (3) the physical processes that occur during film formation. During the spin-off stage of deposition, as the concentration of the precursor species increases dramatically, they come together and begin to interact. Precursor properties governing this interaction include size, shape (fractal nature), and reactivity [75]. Since the viscosities of the solutions are similar, it is believed that the increase in initial film thickness with acac addition is due to a decrease in packing efficiency of the more highly modified precursors during aggregation, most likely as a result of increased precursor/oligomer steric bulk. Another indication of the lower packing efficiency of the more highly substituted precursors is the observed decrease in initial refractive index.

Film consolidation behavior also depends on precursor reactivity. Precursors that are less reactive (toward hydrolysis and condensation) are termed “transparent”, since they interpenetrate during aggregation and consolidation; those that tend to react are referred to as “opaque” [68, 74]. As greater amounts of acac are used, less reactive, more highly transparent precursors are formed. This is not only due to the fact that the acac ligand is less susceptible to hydrolysis than the butoxy ligand [76], but being sterically demanding, it can inhibit accessibility to any remaining (reactive) alkoxy species. Films prepared from more highly modified precursors should therefore consolidate to a greater extent than those prepared from more reactive (unmodified) species, because the precursors are more transparent and do not cross-link to as great an extent following deposition. An indication of this behavior may be the fact that even though, initially, the $r = 2$ film is significantly thicker than the $r = 0$ or $r = 1$ films, after drying at 25°C for about 2 h, the films display similar thicknesses (see Fig. 8). In the present case, even more pronounced

differences in film consolidation may not have been observed because the butoxy ligand itself is fairly insensitive to hydrolysis and condensation, much less so than many typically used alkoxy groups, e.g., ethoxy or isopropoxy. It is also worthwhile to note that variations in film consolidation behavior can be induced through the use of different chelating ligands (acetate versus acac, etc.), rather than by changing the reaction stoichiometry as in the present example. These variations can lead to films that are more chemical gel in nature than physical gel [74, 77].

Film consolidation following deposition is thus strongly related to the nature of the precursor species. Films that are ~ 1000 Å in thickness after crystallization may range in thickness from 2000 to 6000 Å immediately after deposition. Shrinkage during processing is thus extensive, and it occurs at room temperature because of capillary forces, during organic pyrolysis, and through the volume change that accompanies crystallization. Film shrinkage can also generate stresses in the films well in excess of 100 MPa. The magnitude of the stress, and whether film cracking occurs will depend, in part, on the reactivity of the precursors: less reactive precursors do not tend to form “solid” films as rapidly, and hence, the solvent can be removed without producing significant stress [78]. Consolidation is most pronounced at room temperature and during organic pyrolysis, where the film may shrink in the thickness direction by 50–70%. Since films with thicknesses ranging from 0.5 to 2.0 μm are required for many applications, they are typically fabricated by a multilayering approach, wherein deposition is immediately followed by pyrolysis, and then each layer is crystallized before the next deposition. Alternatively, multiple layers are deposited and pyrolysed prior to a single crystallization anneal.

In addition to precursor properties, solvent choice is an important consideration. As an example, consider the recent work to develop deposition processes to form thicker layers that is based on the use of 1,3-propanediol [63 - 65, 67] . It has been demonstrated that films between 0.5 and 1.0 μm /deposition can be prepared by this approach. However, in the preparation of films by this approach, as-deposited films appear liquid and tend to dewet the substrate surface, resulting in nonuniformities and a degradation in film quality. In this instance, the viscosity of the solvent is such that precursor interactions, either physical or chemical, are inhibited. The viscosity of propanediol is ~ 40 mP·s, while

more commonly used solvents are $\sim 0.5\text{--}1.0$ mP·s. The extremely low volatility of this solvent at room temperature also plays a role in inhibiting precursor interactions. In contrast, for films deposited from high-volatility solvents, vaporization of the solvent results in film drying, which forces interactions between the precursor species. These interactions are, at minimum, physical in nature and in some instances chemical, as condensation reactions may occur. While chemical gel films are not always desired, some level of aggregation seems critical to the preparation of stable films that will remain uniform throughout subsequent processing. For low volatility solvent systems such as propanediol, film dewetting can also become a problem due to the lack of either chemical or physical gelation during spinning [66].

2.5.3 Gel to Ceramic Conversion

In this study the two-step approach has been employed most of the time to convert the as deposited film into the crystalline perovskite phase. In this method, the as deposited film is first subjected to a separate pyrolysis step prior to the crystallization anneal. The film is typically placed on a hot plate held at 200-400°C for burnout of the organic species. While it might be expected that this type of rapid heat treatment would cause cracking, in reality, it appears that this is often the best approach. It has been proposed that this procedure allows for the removal of the organic constituents prior to the collapse of the amorphous network, which minimizes cracking and blistering. Lakeman *et al.* [79] have studied the rearrangements that occur within the film during pyrolysis and the development of the amorphous structure. As-deposited coatings were found to be amorphous but possessed short-range order. Following pyrolysis, the development of medium-range order was observed, and chemical heterogeneity at the nanometer length scale was evident. The degree of heterogeneity was observed to decrease with higher heat-treatment temperatures [79]. Films that have been pyrolysed may also still contain small amounts of residual organic and hydroxyl species. Pyrolysed films are subsequently heated to higher temperatures (500- 700°C) for crystallization, at heating rates that have ranged from 5 to 7500 °C/min. These latter rates have been obtained using rapid thermal annealing furnaces [80, 81].

2.6 References

1. P. Chandra and P.B. Littlewood; A Landau Primer for Ferroelectric; arXiv:cond-mat/0609347v1; 2006
2. J.D. Baniecki et. al., *J. Appl. Phys.*, vol. **89**, no. 5, 2873 (2004)
3. V.L. Gurevich and A.K. Tagantsev, "Intrinsic dielectric loss in crystals," *Adv. Phys.*, **40**, 719-767 (1991)
4. R. Stolen and K. Dransfeld, *Phys. Rev.*, **139**, 1295 (1965)
5. O.G. Vendik, *Sov. Phys. Solid State*, **17**, 1096 (1975)
6. A.K. Tagantsev, *Sov. Phys. JETP*, **59**, 1290 (1984)
7. G.J. Cooms and R.A. Cowley, *J. Phys. C*, **6**, 121 (1973)
8. A.K. Tagantsev, *Sov. Phys. JETP*, **50**, 948 (1979)
9. C. Kittel, *Introduction to Solide State Physics* (John Wiley & Sons, Inc., New York, London 1971.
10. E. Schlöman, *Phys. Rev.*, **135**, A413 (1964)
11. O.G. Vendik and L.M. Platonova, *Sov. Phys. Solid State*, **13**, 1353 (1971)
12. B.M. Garin, *Sov. Phys. Solid State*, **32**, 1917 (1990)
13. C.J. Brennan, *Integrated Ferroelectrics*, **7**, 93, (1995)
14. J.G. Simmons, *J. Chem. Solids*, **32**, 2581 (1971)
15. A.K. Jonscher, *Universal Relaxation Law*, (Chelsea Dielectrics Press, London, 1996.
16. J.D. Baniecki, R.B. Laibowitz, T.M. Shaw, P.R. Duncombe, D.A. Neumayer, D.E. Kotecki. H. Shen, and Q.Y. Ma, *Appl. Phys. Lett.*, **72**, 498 (1998).
17. R. Waser, in *Science and Technology of Electroceramic Thin Films*, vol. 286, *NATO ASI; Series E: Applied Science*, edited by O. Auciello and R. Waser (1995), p. 223.
18. Y. Fukuda, K. Numata, K. Akoki, and A. Nishimura, *Jpn. J. Appl. Phys.*, **35**, 5178 (1996)
19. J. Petzelt, , T. Ostapchuk, I. Gregora, I. Rychetsk, S. Hoffmann-Eifert, A.V. Pronin, Y. Yuzyuk, B.P. Gorshunov, S. Kamba, V. Bovtun, J. Pokorn, M.Savinov, V. Porokhonsky, D. Rafaja, P. Vanek, A. Almeida, M.R. Chaves, A.A. Volkov, M. Dressel, and R. Waser, *Phys. Rev., B*, **64**, 184111 (2001).

20. X.X. Xi, H.C. Li, W.D. Si, A.A. Sirenko, I.A. Akimov, J.R. Fox, A.M. Clark, and J.H. Hao, *Journal of Electroceramics*, **4**, 393 (2000).
21. A.S. Bhalla, R. Guo and R. Roy, The perovskite structure – a review of its role in ceramic science and technology, *Mat. Res. Innovat.* **4**, 3-26 (2000).
22. W.J. Merz, *Phys. Rev.*, **69**, 173 (1949)
23. A.F. Wells, (1995) *Structural Inorganic Chemistry*, Oxford Science publications.
24. For structural details of the discussed perovskites please refer to the Inorganic Crystallographic structure database (ICSD), Copyright © 2005 by FIZ Karlsruhe, Germany.
25. P. Lemmens and P. Millet, *Spin – Orbit – Topology, a triptych*, in “Quantum Magnetism”, Springer, Heidelberg, (2004).
26. H. Schmid, *Ferroelectrics*, **162**, 317 (1994).
27. J. Hemberger, P. Lunkenheimer, R. Fichtl, H.A.K. von Nidda, V. Tsurkan, and A. Loidl, *Nature* **434**, 364 (2005).
28. T. Kimura, T. Goto, H. Shintani, K. Ishizaka, T. Arima and Y. Tokura, *Nature* **426**, 55 (2003).
29. D. Higashiyama, N. Kida, S. Miyasaka, T. Arima, and Y. Tokura, *Phys. Rev. B* **70**, 174405 (2004).
30. H. Zheng, J. Wang, S. E. Lofland, Z. Ma, L. Mohaddes-Ardabili, T. Zhao, L. Salamanca-Riba, S. R. Shinde, S. B. Ogale, F. Bai, D. Viehland, Y. Jia, D. G. Schlom, M. Wuttig, A. Roytburd, and R. Ramesh, *Science* **303**, 661 (2004).
31. L.E. Cross and R.E. Newham, *History of Ferroelectrics, Ceramics and Civilization*, Volume 111. (1987) by The American Ceramic Society. Inc., <http://www.ieeeuffc.org>, and L. Cross, *Ferroelectrics* **76**, 241 (1987).
32. G. Shirane, *Rev. Mod. Physics* **46**, 437 (1974).
33. P. Lunkenheimer, U. Schneider, R. Brand, A. Loidl, *Contemporary Physics* **41**, 15 (2000).
34. N.A. Spaldin, *Science* **304**, 1606 (2004).
35. U.T. Höchli, K. Knorr, and A. Loidl, *Adv. Phys.* **39**, 405 (1990).
36. J.G. Bednorz, K.H. Müller, *Phys. Rev. Lett.* **52**, 2289 (1984).

37. P. Lunkenheimer, V. Bobnar, A.V. Pronin, A.I. Ritus, A.A. Volkov, and A. Loidl, *Phys. Rev. B* **66**, 052105 (2002).
38. A.P. Ramirez, M.A. Subramanian, M. Gardel, G. Blumberg, D. Li, T. Vogt, S.M. Shapiro, *Solid State Commun.* **115**, 217 (2000).
39. S. Garcia-Martin, A. Morata-Orrantia, M.H. Aguirre, and M.A. Alario-Franco, *Appl. Phys. Lett.* **86**, 043110 (2005).
40. P. Fazekas, *Lecture Notes on Electron Correlations and Magnetism* (World Scientific, Singapore, 1999).
41. M. Imada, A. Fujimori, Y. Tokura, *Rev. Mod. Phys.* **70**, 1039 (1998).
42. Y. Tokura, *Physics Today* **56**, 50, July (2003).
43. P. Lemmens, G. Guentherodt, C. Gros, *Physics Reports* **375**, 1 (2003).
44. E. Dagotto, *Review in Mod. Physics* **66**, 763 (1994).
45. J. Orenstein and A.J. Millis, *Science* **288**, 468 (2000).
46. M.A. Korotin, S.Yu. Ezhov, I.V. Solovyev, V.I. Anisimov, D.I. Khomskii, and G.A. Sawatzky, *Phys. Rev. B* **54**, 5309 (1996).
47. R. Vidya, P. Ravindran, P. Vajeeston, A. Kjekshus, and H. Fjellvag, *Phys. Rev. B* **69**, 092405 (2004).
48. F. Fauth, E. Suard, V. Caignaert, and I. Mirebeau, *Phys. Rev. B* **66**, 184421 (2002).
49. Yu.P. Chernenkov, V.P. Plakhty, V.I. Fedorov, S.N. Barilo, S.V. Shiryayev, and G.L. Bychkov, *Phys. Rev. B* **71**, 184105 (2005) and V.P. Plakhty, Yu.P. Chernenkov, S.N. Barilo, A. Podlesnyak, E. Pomjakushina, D.D. Khalyavin, E.V. Moskvina, S.V. Gavrilo, cond-mat/0407010 (2004).
50. K.-Y. Choi, P. Lemmens, T. Sahaoui, G. Güntherodt, Yu.G. Pashkevich, V.P. Gnezdilov, P. Reutler, L. Pinsard-Gaudart, B. Büchner, and A. Revcolevschi, *Phys. Rev. B* **71** 174402 (2005)
51. Yi. G.; Sayer, M. *Ceram. Bull.* **1991**, 70, 1173.
52. Schwartz, R. W.; et al. *J. Mater. Res.* **1997**, 12, 444.
53. Budd, K. D.; Dey, S. K.; Payne, D. A. *Brit. Ceram. Soc. Proc.* **1985**, 36, 107.
54. Dey, S. K.; Budd, K. D., Payne, D. A. *IEEE Trans. UFFC* **1988**, 35 (1), 80.
55. Coffman, P. K.; Dey, S. K. *J. Sol-Gel Sci. Technol.* **1994**, 1, 251.

56. Schwartz, R. W.; Assink, R. A.; Headley, T. J. *Mater. Res. Soc. Symp. Proc.* **1992**, 243, 245.
57. Yi, G.; Wu, Z.; Sayer, M. *J. Appl. Phys.* **1988**, 64, 2717
58. Takahashi, Y.; et al. *J. Mater. Sci.* **1990**, 25, 3960.
59. Hirano, S. I.; Kato, K. *J. Non-Cryst. Solids* **1988**, 100, 538.
60. Eichorst, D. E; Payne, D. A. *Mater. Res. Soc. Symp. Proc.* **1988**, 121, 773.
61. Hayashi, T.; et al. *Jpn. J. Appl. Phys.* **1993**, 32, 4092.
62. Kakihana, M. *J. Sol-Gel Sci. Technol.* **1996**, 6, 7.
63. Lourdes Calzada, M.; Sirera, R.; Carmona, F.; Jimenez, B. *J. Am. Ceram. Soc.* **1995**, 78, 1802.
64. Tu, Y. L.; Milne, S. J. *J. Mater. Res.* **1995**, 10, 3222.
65. Tu, Y. L.; Calzada, M. L.; Phillips, N. J.; Milne S. J. *J. Am. Ceram. Soc.* **1996**, 79, 441.
66. Schwartz, R. W.; Clem, P. G.; Reichert, T. L.; Dimos, D., and Liu, D., *Int. Ferro.* **1997**, 18, 275
67. Liu, D.; Mevissen, J., submitted to *Int. Ferro.* **1997**, 18, 263
68. Schwartz, R. W.; et al. *Int. Ferro.* **1995**, 7, 259.
69. Assink, R. A.; Schwartz, R. W. *Chem. Mater.* **1993**, 5, 511.
70. Doeuff, S; Dromzee, Y.; Sanchez, C. C. *R. Acad. Sci. Paris* **1989**, 308, 1409.
71. Alam, T. M.; Boyle, T. J.; Buchheit, C. D.; Schwartz, R. W.; Ziller, J. W. *Mater. Res. Soc. Symp. Proc.* **1994**, 346, 35.
72. Schwartz, R.W., Boyle, T.J., Lockwood, S.J., Sinclair, M.B., Dimos, D., and Buchheit, C.D., *Int. Ferro.*, 7, 259-277, (1995)
73. Boyle, T. J.; et al. *J. Mater. Res.* **1997**, 12, 1022.
74. Schwartz, R. W.; Voigt, J. A.; Boyle, T. J.; Christenson, T. A.; Buchheit, C. D. *Ceram. Eng. Sci. Proc.* **1995**, 16, 1045. *Reviews Chem. Mater.*, Vol. 9, No. 11, 1997 2339
75. Brinker, C. J.; et al. *J. Membr. Sci.* **1993**, 77, 165.
76. Sanchez, C.; Babonneau, F.; Doeuff, S.; Leautic, A. In *Ultrastructure Processing of Advanced Ceramics*; MacKenzie, J. D., Ulrich, D. R., Eds.; Wiley-Interscience: New York, 1988; pp 77- 87.

77. Schwartz, R. W.; Voigt, J. A.; Buchheit, C. D.; Boyle, T. J. *Ceram. Trans., Ferroic Mater.: Design, Prepr. Char.* **1994**, *43*, 145.
78. Croll, S. G. *J. Coatings Technol.* **1979**, *51*, no. 648, 64.
79. Lakeman, C. D. E.; Xu, Z.; Payne, D. A. *J. Mater. Res.* **1995**, *10*, 2042.
80. Reaney, I. M.; Brooks, K.; Klissurka, R.; Pawlaczyk, C.; Setter, N. *J. Am. Ceram. Soc.* **1994**, *77*, 1209.
81. Griswold, E. M.; Weaver, L.; Sayer, M.; Calder, I. D. *J. Mater. Res.* **1995**, *10*, 3149.

I stand at the seashore, alone, and start to think:

*There are the rushing waves
mountains of molecules
each stupidly minding its own business
trillions apart
yet forming white surf in unison.*

*Ages on ages
before any eyes could see
year after year
thunderously pounding the shore as now.
For whom, for what?
On a dead planet
with no life to entertain.*

*Never at rest
tortured by energy
wasted prodigiously by the sun
poured into space.
A mite makes the sea roar.*

*Deep in the sea
all molecules repeat
the patterns of another
till complex new ones are formed.
They make others like themselves
and a new dance starts.*

*Growing in size and complexity
living things
masses of atoms
DNA, protein
dancing a pattern ever more intricate.*

*Out of the cradle
onto dry land
here it is standing:
atoms with consciousness;
matter with curiosity.*

*Standing at the sea, wondering: I
a universe of atoms
an atom in the universe.*

Richard P. Feynman

“Classic Feynman - All the Adventure of a curious character... “

Characterisation of Ferroelectric Thin Films

(Ba,Sr)TiO₃ and (Pb,Sr)TiO₃ thin films were deposited on pieces of prime-grade 4" Si-wafers with 200 nm thermal oxide. For the characterisation of electrical and physical properties of the ferroelectric thin films a standard procedure, which was developed for Pb(Zr,Ti)O₃ (PZT), was adopted. In this scheme a Ti/Pt, 8nm/100nm, bottom electrode was deposited on top of the oxide layer. It is common knowledge that this metallisation layer enhances the crystallisation of PZT and nearly all other ferroelectrics. In a later chapter we will see that this is not necessary for PST.

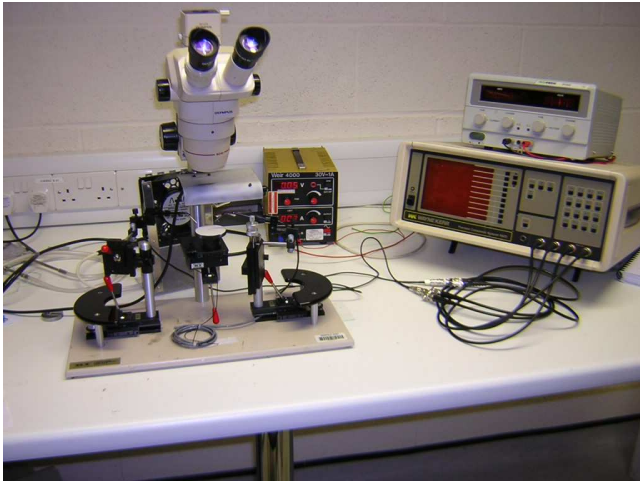


Fig. 3.1: The Wayne Kerr precision component analyser 6425 with probe station and power supply for the measurement of the tunability

However, after the sol-gel deposition and XRD-, AFM-, and SEM-characterisation of either BST or PST Cr/Au dots were evaporated through a shadow mask. Electrical properties, e.g. permittivity, loss and tunability, were measured on a probe station with a Wayne Kerr precision component analyser 6425, the hysteresis was measured using a RT66 ferroelectrics test system (Radiant Technologies, USA), and the permittivity-temperature dependence (Curie-temperature) was characterised with the help

of a poling-rig, which could operate in a temperature range of -40°C to $+60^{\circ}\text{C}$ while keeping the sample under constant vacuum to avoid condensation of water. Auger analysis of the PST-, PZT-SiO₂ interface was the last experiment with remarkable results in this study.

In this chapter some of these methods and techniques are described in more detail.

3.1 Sputter deposition and Thermal Evaporation

3.1.1 Sputter Deposition

Sputter deposition involves the bombardment of a target with energetic ions in order to generate a vapour that subsequently deposits onto a substrate. In this study two types of sputtering were used: DC magnetron sputtering for the deposition of Pt (target: Pi-KEM, UK 99.9% purity) and RF magnetron sputtering for the deposition of Ti (target: Pi-KEM, UK 99,7% purity). The basic principle behind both techniques is the same and begins with the evacuation of the process chamber below $1.3 \cdot 10^{-3}$ Pa, into which Ar gas is introduced at low pressure of 1.3 Pa. A glow-discharge plasma is struck between the target (cathode) and an adjacent shield (anode) by applying either a steady voltage (DC sputtering) or an AC voltage (RF sputtering). Positive Ar ions are accelerated towards the target and “sputter” atoms, through momentum exchange, out into the chamber. Those that hit the substrate condense to form a thin film. Secondary electrons are also emitted through the bombardment of the target and these maintain the plasma by ionising further Ar atoms. Permanent magnets behind the target form a toroidal field that confines the plasma to a ring close to the target. Because the path length of electrons within the plasma is increased, the minimum gas pressure to sustain the plasma is reduced. This helps to boost sputtering rates since the sputtered atoms are subjected to fewer collisions on their way to the substrate. RF sputtering is advantageous for insulating targets or targets with reduced conductivity as it prevents charge build up and also reduces the drive voltage necessary to maintain the plasma.

A Nordiko 2000 sputtering system was used during this investigation. This machine was equipped with three magnetrons (two for RF sputtering and one for DC sputtering). Samples were loaded onto one of six substrate holders, which, in turn were fitted to a motorised central spindle. A computer was used to rotate the samples into the correct position above the relevant target. A 10 min pre-sputter was employed to remove surface oxide and/or contaminations from the Ti target. In case of Pt, a shorter, 2 min pre-sputter was used that took into account the reduced reactivity of the material and its significant monetary value. The standard procedure involved depositing an 8 nm Ti adhesion layer, followed by 100 nm of Pt, without breaking the vacuum. Adhesion layers are used to join

layers in a thin film system that would otherwise be incompatible. Since Ti is a relatively reactive metal it can break the Si-O bond on the Si-surface to form a Ti-O or Ti-Si bond. Conversely, Pt, being a noble metal, cannot do this and thus has limited adhesion to Si. However, Pt can form strong metallic bonds with unoxidised Ti. Hence, with an intermetallic reactive layer, Pt can be made to adhere well to the Si-substrate.

3.1.2 Thermal evaporation

Thermal evaporation was used to deposit Cr/Au top electrodes onto the ferroelectric thin films. The technique is very simple and involves heating an evaporating source under vacuum, by passing a large current through it (Joule effect). Refractory metals, metals with a high melting point, such as W, Ta and Mo are examples of commonly used evaporating sources. The evaporant, which has a lower melting point, is inserted into the source and the chamber is evacuated. As the current is increased, the evaporant vaporises and condenses on a substrate placed above the source. Vacuum pressures below $1.33 \cdot 10^{-3}$ Pa are necessary to prevent oxidising of the atoms in the vapor before coming in contact



Fig. 3.2: The Edwards E480 thermal evaporator

with the substrate and to ensure a large mean free path.

The amount of heat generated through the Joule heating is I^2R , where R is the parallel resistance of the source and evaporant at the evaporation temperature. This temperature is nonuniform because some heat is conducted down the electrodes. Therefore, unlike sputter deposition, it is essential to monitor the evaporation rate in situ as it is highly variable.

One common method is to use a crystal rate monitor. This utilises the resonant properties of piezoelectric quartz wafers to detect a vapour flux and give an estimate of the amount of material that is deposited on a substrate during the evaporation. The quartz wafer generates an oscillating voltage across itself when vibrating at its resonant frequency. Metal electrodes on opposite faces of the wafer

act as electrical coupling. During a deposition one side of the wafer is exposed to the vapour flux and proceeds to accumulate mass, which subsequently reduces the resonant frequency of the crystal. By comparing the reduced frequency with the resonant frequency of a reference crystal, located in the control unit, the mass of the deposit can be calculated. Measurements of any quantity relative to a reference value of similar magnitude is always more accurate than making an absolute measurement and such the instrument has a submonolayer resolution.

An Edwards E480 thermal evaporator was used. The system was pumped down to a pressure below $3 \cdot 10^{-4}$ Pa before the evaporation. A W wire source was used to evaporate Cr granulates and a Mo boat for Au. Top electrodes were produced by evaporating 15 nm of Cr (adhesion layer) and 100 nm of Au through a shadow mask with hole-areas of 0.48 mm^2 .

3.2 Analysis

3.2.1 X-ray Diffraction Analysis (XRD)

The phase composition and degree of preferential orientation in the ferroelectric thin films were determined by X-ray diffraction (XRD) using the Bragg-Brentano goniometer geometry, Fig. 3.3.

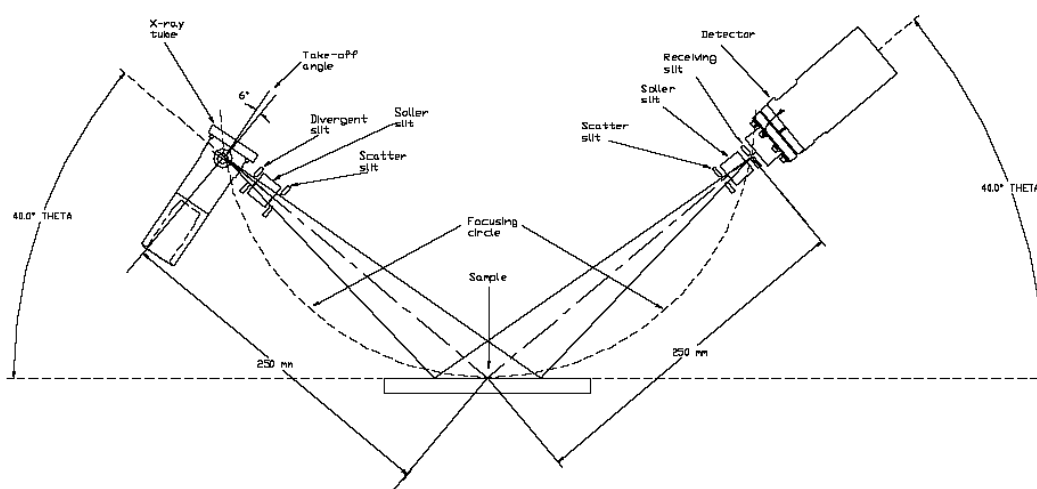


Fig. 3.3: The Bragg Brentano Theta:Theta setup

In this geometry the sample is moved through an angle θ whilst the detector is scanned through an angle 2θ – producing a so-called θ - 2θ scan. At values of 2θ for which the lattice spacing d satisfies the Bragg condition $n\lambda=2d\sin\theta$ a peak appears from which d can be derived. The peak intensity gives a qualitative measure of the preferential orientation.

In this study a Siemens D5005 diffractometer was used for all the XRD measurements. The X-ray tube emitted $\text{CuK}\alpha$ radiation ($\lambda=1.5406 \text{ \AA}$) at 40 kV and 30 mA. In general, θ - 2θ scans were conducted between 20 and 60° in increments of 0.04° with a dwell time of 1 sec per increment. The main peaks in the XRD-spectra of both BST and PST were the (100), (110) and (111) lattice planes. The latter one was hidden under the strong Pt (111) peak. By knowing the position of these peaks one could characterise the crystallisation of the perovskite thin film.

3.2.2 Scanning Electron Microscopy (SEM)

Scanning electron microscopy (SEM) was the primary imaging technique used throughout this study. Its many benefits include minimal sample preparation requirements, a wide magnification range and the ability to resolve features below 10 nm. The system used during the investigation was a Sirion XL30 Schottky Field Emission Gun (SFEG) SEM. This type of SEM utilises a sharp, tungsten-based tip at which a very high electric field concentrates ($> 10^7 \text{ V/m}$). Under these circumstances electrons can tunnel through the reduced potential barrier and are then accelerated up to the required beam voltage. Field emission SEMs have a very high brightness (current density per solid angle) compared to conventional thermionic emitters. This means that they can provide a high electron density over a smaller spot area, obtaining high resolution (better than 1.5 nm under ideal conditions) at relatively low acceleration voltage (5 kV).

Samples inspected under the SEM were prepared in such a way as to minimise the effect of charging on the image. Wafers and flat samples were attached to the sample holder using double sided adhesive conductive carbon tapes. Cross sections were held by a metallic spring. For low resolution imaging ($< 5,000\times$) an Everhart-Thornley secondary electron detector was used. Higher resolutions were achieved by setting the

working distance to ≤ 5 mm and using the through-the-lens secondary electron detector (TLD). This detector was mounted within the lens and received electrons in the immediate vicinity of the scanned area.

3.2.3 Polarisation Hysteresis Measurement

An RT66A Standardised Ferroelectric Test System was used to analyse the ferroelectric hysteresis properties of some of the thin films produced during this study. This instrument combines the features of a function generator, an electrometer and a digital oscilloscope in a single PC controlled unit. Details of the sample, such as thickness and electrode size, are inputted into the software, which then executes the appropriate hardware commands and collects and processes the data. The results are displayed in form of polarisation vs. electric field curves.

The system can produce polarisation hysteresis curves in two ways: the conventional Sawyer-Tower circuit mode or the virtual ground circuit mode. The Sawyer-Tower circuit consists of a linear sense capacitor connected in series to the sample. The voltage across the sense capacitor measures the charge stored on the sample, which is related back to the polarisation. This is a simple technique but requires an accurately known sense capacitance of far greater magnitude than the sample capacitance. In contrast, the virtual ground circuit is composed of a current integrator connected in series with the sample. By measuring the charge collecting on the integrating capacitor, the polarisation is easily calculated. This circuit improves reproducibility and allows smaller capacitances to be measured with greater accuracy than the Sawyer-Tower method. All measurements in this study were made using the virtual ground circuit mode.

The inbuilt power supply of the system can apply a maximum of ± 20 V across a sample. If the thickness of a sample exceeds $1 \mu\text{m}$ then it is likely that this drive voltage will not be able to overcome the coercive field. In this circumstance a high voltage interface can be used in combination with a Trek 610D amplifier.

3.2.4 Atomic Force Microscopy (AFM)

A Digital Instruments Dimension 3000 AFM was used to analyse the surface topography of samples. Contact mode was used to make high-resolution topographical images. The tips used during this study were composed of boron-doped p-type Si and manufactured by NANOSENSORS (Nano World AG).

3.2.5 Curie Temperature Measurement

For the measurement of the Curie temperature, the transition point between



Fig. 3.4: The vacuum chamber of the Poling Rig

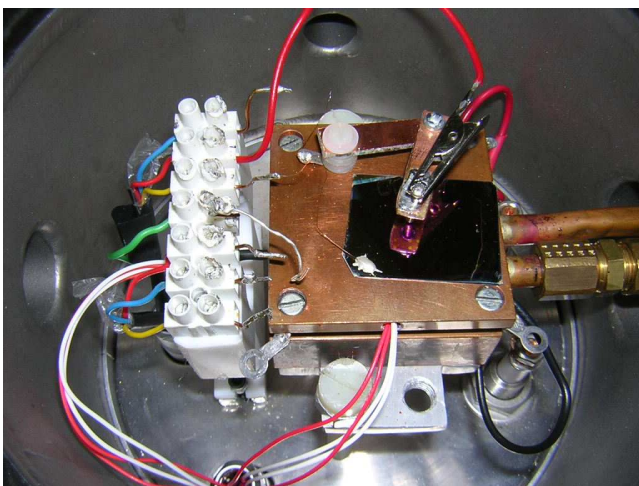


Fig. 3.5: The opened vacuum chamber with a fitted test sample

ferroelectric tetragonal and paraelectric cubic, of PST the Poling Rig, build within the Nanotechnology Centre, was used. It was constructed to pole ferroelectric PZT samples under different temperatures in a vacuum atmosphere to avoid the condensation of water around 0°C. The temperature range was limited by the plastic materials inside the vacuum chamber and not by the heating (peltier and electrical stage heating) or cooling (peltier or liquid nitrogen) system. A safe temperature range was from -40 to +60°C. The transition point of the materials used in this experiment, Mn doped PST 40/60 (40% Pb and 60% Sr), is under but close to room temperature, thus the temperature range of the rig was sufficient. However, it was not build for this purpose. High losses, time consuming and relatively complex calibration of the system and other side effects, e.g. an ever increasing trend of the permittivity with

temperature, make the results of these measurements vulnerable. But still, a peak in the permittivity is a peak. As a reference the permittivity vs. temperature curve of bulk BaTiO₃ was measured, Fig. 3.6, and compared with the well known results from Merz, Fig. 2.6.

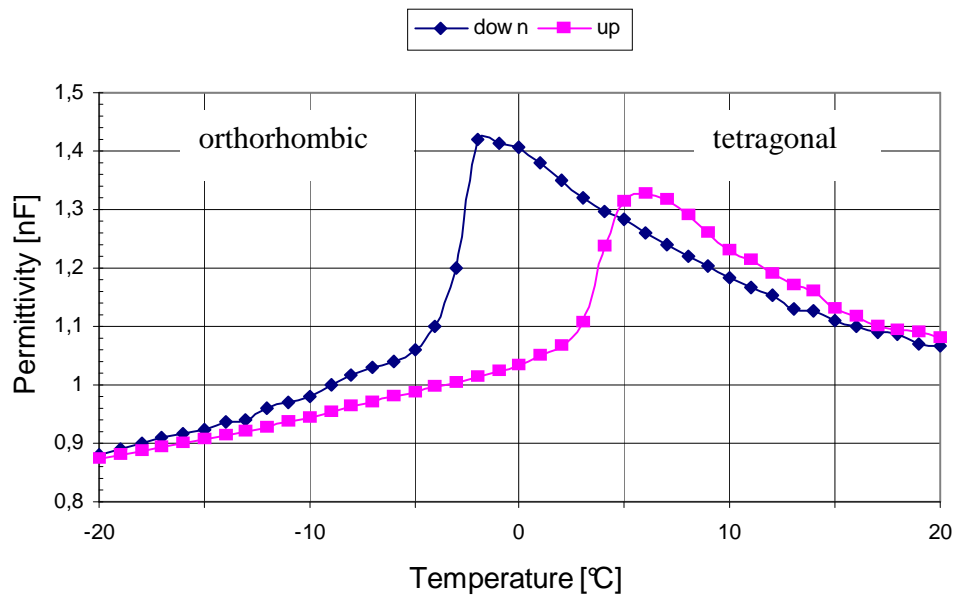


Fig. 3.6: Permittivity vs Temperature of bulk BaTiO₃. Measured in the Poling Rig.

The result shows that the peaks in permittivity are in the right position compared to Merz measurements. Therefore this method can be used to measure the transition temperature qualitative without doubts.

3.2.6 Auger Emission Spectroscopy (AES)

Auger Emission Spectroscopy (AES), or Auger Analysis, is a technique used in the identification of elements present on the surface of the sample. AES involves the bombardment of the sample with an energetic primary beam of electrons. This process generates, among other things, a certain class of electrons known as Auger electrons.

The mechanism by which an Auger electron is released starts with an electron being ejected by the primary electron beam from its shell, say, the K-shell. Another electron from an outer shell (say, the L1-level) of the same atom emits energy in the form of a

photon in order to go down to the K-shell position vacated by the ejected electron. The photon released by the second electron will either get lost or eject yet another electron from a different level, say, L2. Auger electrons are electrons ejected in this manner, such as the third electron from L2 in the example. Thus, the generation of an Auger electron requires at least three electrons, which in the example above are the K, L1, and L2 electrons. In this example, the emitted Auger electron is referred to as a KLL Auger electron. Hydrogen and Helium atoms have less than three electrons, and are therefore undetectable by AES.

The energy content of the emitted Auger electron is unique to the atom where it came from. Thus, AES works by quantifying the energy content of each of the Auger electrons collected and matching it with the right element.

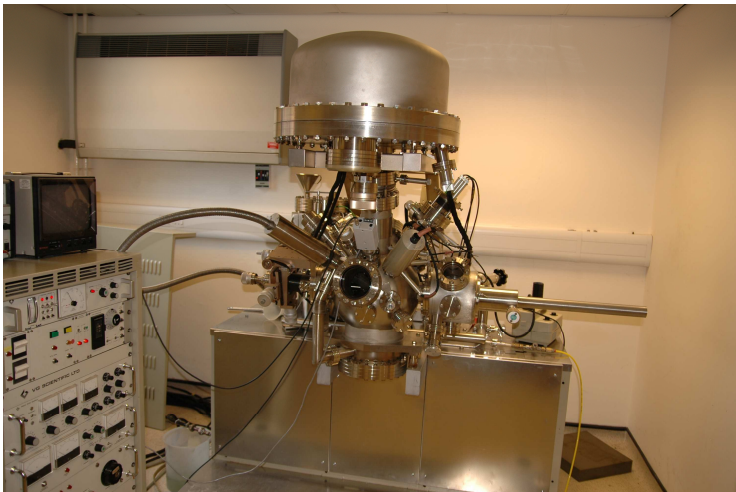


Fig. 3.7: The VG ESCA Lab Mk 2 AES-Lab in Cranfield

The energy of Auger electrons is usually between 20 and 2000 eV. The depths from which Auger electrons are able to escape from the sample without losing too much energy are low, usually less than 50 Å. Thus, Auger electrons collected by the AES come from the surface or just beneath the surface. As such, AES can only provide compositional information about the surface of the sample. In order to use

AES for compositional analysis of matter deep into the sample, a crater must first be milled onto the sample at the correct depth by ion-sputtering.

AES has the ability to provide excellent lateral resolution, allowing reliable analysis of very small areas (less than 1 micron). It also offers satisfactory sensitivity, detecting elements that are less than 1% of the atomic composition of the sample.

The output of AES is referred to as an Auger spectrum. This spectrum would show peaks at Auger electron energy levels corresponding to the atoms from which the Auger electrons were released [1] (sometimes called binding energy).

3.3 References

1. <http://www.siliconfareast.com/augeranalysis.htm>

I love fools' experiments. I am always making them.

Charles R. Darwin

In Francis Darwins "*The Life of Charles Darwin*", 1902

Kohn's Second Law: An experiment is reproducible until another laboratory tries to repeat it.

Alexander Kohb

In N Sreedharans "*Quotations of Wit and Wisdom*", 2007

You make experiments and I make theories. Do you know the difference? A theory is something nobody believes, except the person who made it. An experiment is something everybody believes, except the person who made it.

Albert Einstein

In Gerald Holtons, "*The Advancement of Science, and Its Burdens*", (1986),

Barium Strontium Titanate (BST)

It should be well known by now that BaTiO_3 is a ferroelectric perovskite and has been well studied in bulk ceramic form where the measured permittivities are well in the thousand (see Fig. 2.4). By substituting the the A-site atom (Ba-atom) with Sr the Curie temperature, T_C , can be shifted down from 120°C to around room temperature (Fig. 1.12). The linear drop of T_C is ca. 3.4°C per mol%. Therefore, 30 mol% Sr ($x=0.3$) would bring the T_C of $\text{Ba}_{1-x}\text{Sr}_x\text{TiO}_3$ down to room temperature. Due to this fact BST was and still is an attractive candidate for voltage tunable devices like varactors, phase shifters, DRAMs etc., where the ferroelectric crystal or thin film should be in the paraelectric state viz. the operating temperature should be above T_C .

BST films are, like PST, polycrystalline. Their properties heavily depend on composition, stoichiometry, microstructure (grain size and size distribution), film thickness and homogeneity of the film. The BST or/and PST thin film growth method significantly affects the composition, stoichiometry, crystallinity, and grain size of the film and, consequently, its dielectric properties. A variety of techniques have been used to deposit these films (see introduction section of chapter 2.4).

BST 60/40 was chosen as a starting material in this study because it is widely investigated and used for voltage tunable thin films. A wide range of publications makes it relatively easy to gain access in this topic.

In this chapter a short review of BST deposition is given, followed by the description of the synthesis and characterisation of BST thin films developed in the beginning of this study. It concludes with a comparison between two different approaches of BST sol-gel synthesis, pointing out the dominant role of the interfacial layer and the capacitance-density.

4.1 A Short Review of BST Deposition

The beginning of success in sol-gel deposition of BST thin films seems to be the early 1990s. D. Tahan *et al.* [1, 2] wrote two papers in 1995 and 96 where he studied the effects of composition and processing parameters. The sol was prepared by dissolving an appropriate ratio of barium and strontium acetate in acetic acid under nitrogen atmosphere. This was followed by the addition of a stoichiometric amount of titanium IV isopropoxide. Ethylene glycol was added to a portion of this solution, in an acetic acid to ethylene glycol ratio of 3 to 1. This ratio allowed the acetates to dissolve easily, along with increased solution stability. This solution was then heated at 90°C for approximately 1 hour to permit reaction between the acetic acid and the ethylene glycol. Both the acetic acid and the acetic acid/ethylene glycol solutions were studied in terms of solution stability, crystallisation temperature and film quality.

Films were prepared by spin coating the solutions at 7500 rpm for 90 sec onto Si and Pt/Ti/SiO₂/Si substrates. The films were heated on a hot plate at 300°C to dry and pyrolyse the organics, followed by a heat treatment in air or oxygen at 550°C to 750°C. This process was repeated to produce multilayer films.

Upon comparing the acetic acid solution to the acetic acid/ethylene glycol solution, it was noticed that the former solution yielded a white precipitate after only a couple of days, while the latter remained stable to precipitation. The perovskite BST began to crystallise at 600°C and 500°C for films made from acetic acid and the acetic acid/ethylene glycol solution, respectively. It was thereby found that ethylene glycol is a necessary component of the solution, increasing the stability of the sol and decreasing the film crystallisation temperature. Yi *et al.* (1988) [3] and Giridharan *et al.* (2001) [4] pointed out that ethylene glycol also helps to reduce significantly the tendency of film cracking during annealing at high temperatures in both Pb(Zr,Ti)O₃ and BST. The cause of the film cracking is due to the large volume change when the wet solution is fired to inorganic oxides. The high boiling point and latent heat of vaporization of ethylene glycol retains the atom mobility and helps to get a crack free thin film.

However, Tahan *et al.* did not mention cracks. The dielectric constant of the thin film was approximately 400 with a barium content of 80 mol% (ferroelectric state) and a thickness of 400 nm, with a dielectric loss ($\tan \delta$) less than 0.05 (5%).

Also in 1995 Nazari *et al.* [5] reported the fabrication of 2 μm thick BST thin film at 700°C on Pt foil from an alkoxide-isopropanol solution. However, even after firing at 700°C these films showed poor crystallinity. Sedlar *et al.* [6] reported the fabrication of cerium doped BST thin films between 700-725°C in the same year. These films were derived from Ba/Sr acetates and titanyl acetate precursors dissolved in 2-methoxyethanol and ethylene glycol.

1997 Paik *et al.* [7] used barium hydroxide, strontium hydroxide and titanium butoxide to derive a BST thin film on Pt/Si with a dielectric constant of 450 and a $\tan \delta$ of 0.039 at 10 kHz. The film was annealed at 800°C.

It was soon noticed that the lattice constant of Si (5.4310 Å) does not match the lattice constant of BST (3.96 Å) very well and MgO (4.13 Å), sapphire Al_2O_3 (4.748 Å) and LaAlO_3 (3.821 Å) became the substrates of choice for most of the researchers. In 2001 Majumder *et al.* [8] prepared the first phase shifter device using sol-gel derived BST on LaAlO_3 (LAO). In this study barium and strontium acetates were codissolved in acetic acid. Ethylenglycol was added to completely dissolve these precursors. The solution was heated slightly above room temperature for complete dissolution of the precursor materials. Ti isopropoxide was dissolved in acetic acid and the solution was added to the Ba-Sr complex solution at 50°C. The sol was then stirred for 30 min for complex formation. For thin film deposition the sol was diluted to a concentration of 0.35 ML^{-1} by adding acetic acid. Films were deposited by spinning it onto LAO substrates at a 3000 rpm for 5 sec. Just after deposition, the films were inserted into a preheated furnace kept at 600°C and fired for 5 min for the removal of organics. The coating and firing cycles were repeated ten times to attain a film thickness of about 350 nm. The films were finally annealed at 1100°C for 6 h in air for crystallisation. At zero bias field the estimated dielectric constant at 100 kHz was found to be about 1500, while maintaining a dissipation factor ($\tan \delta$) as low as 0.004. The tunability was 7% ($E \sim 0 - 2.34 \text{ V}/\mu\text{m}$) and the figure of merit $\text{FOM} = (C_0 - C_V)/(C_0 \tan \delta_0)$ was 12.67. In terms of phase shift

applications the maximum phase shift obtained at 15.5 GHz was 320.4°, and the insertion loss was 8.435 dB, leading to a FOM of 37.98°/dB.

It should be noted that the reported values of the dielectric constant of thin film BST rarely exceed 800. The higher dielectric constant in Majumders paper was attributed to the highly oriented nature of the film.

Probably the latest achievement in the sol-gel preparation of BST for applications is described in a paper from M. Jain *et al.* [9] in 2004, who was working in the same group as Majumder at the University of Puerto Rico on BST phase shifters. Therefore he adopted his slightly modified synthesis of BST, but he used a BST:MgO layer sequence for the preparation of heterostructured BST films. The film was prepared by depositing thin, single coatings of both MgO and BST alternatively, with MgO as the initial (on the LaAlO₃ substrate) and BST as the terminating layer, that resulted into a BST:MgO volume ratio of 68:32. After annealing at 1100°C for 6 h his phase shifter achieved a record FOM of 96°/dB at 16 GHz. The room temperature dielectric properties of the pure and heterostructured BST:MgO films measured at 1 MHz and an applied electric field of 25.3 kV/cm are listed below:

Film	Dielectric constant	$\tan\delta$	Tunability	FOM (%)
Pure BST50	2714	0.0215	51.87	24.08
BST50:MgO	1277	0.0052	28.48	55.12

Table 4.1: Room temperature dielectric properties of the pure and heterostructured BST:MgO films measured at 1MHz and applied electric field of 25.3 kV/cm [9]

However, low loss substrates like MgO or LAO are relatively expensive, small and components mounting techniques to fabricate a hybrid microwave-integrated circuit using these substrates are not so simple [10]. If the technology of tunable ferroelectric microwave devices is to be realized, materials solution allowing the optimal properties in economical or manufacturable embodiments must be developed.

One solution is to go back to Si and look for another type of metallization scheme since the noble metals which are normally used in BST-based and other thin film perovskite

devices like Pt and Au have a high resistance and a high loss in the microwave region. Copper could be the material of choice. A Cu electrode exhibits a much lower bulk resistivity ($1.7 \mu\Omega\text{cm}$) than Pt ($10.8 \mu\Omega\text{cm}$), which can greatly reduce the total device loss (see section 5.3 for details) and boost the switching speed of BST thin film devices for high-frequency applications. Fan *et al.* [11, 12] introduced a TiAl/Cu/Ta electrode on Si for BST devices in 2003. The Ta layer served as a diffusion barrier to inhibit deleterious Cu diffusion into the Si substrate, while the TiAl layer provided an excellent barrier against oxygen diffusion into the Cu layer to inhibit Cu oxidation during the deposition and annealing of the BST thin film. As a result they deposited 160 nm BST with a relatively high dielectric constant (280) and a low loss (0.007).

But despite all the research and sophisticated developments in both, solution chemistry and device integration, BST has never made the step to commercial available applications up to now because there are four major limitations within BST thin films:

1. The relative large leakage current density limits the use of thinner films in DRAMs.
2. The relative high growth temperature is detrimental for the integration to semiconductor devices.
3. High losses, especially in the microwave region, are existing.
4. Crack formation during the sol-gel processing are a major obstacle as we will see in the next section.

4.2 Synthesis and Characterisation of BST

The multicomponent BST precursor solution was prepared using high purity barium acetate, $\text{Ba}(\text{CH}_3\text{CO}_2)_2$, strontium acetate, $\text{Sr}(\text{CH}_3\text{CO}_2)_2$ and titanium butoxide, $\text{Ti}(\text{OC}_4\text{H}_9)_4$. First the strontium acetate and barium acetate were mixed in a stoichiometric ratio in acetic acid. Heating was needed to help the dissolution of the precursors. After a while titanium butoxide was added under constant stirring. The solution was then stirred for 2 hours at room temperature. Finally ethylene glycol was added to prevent cracking and to stabilise the solution.

The solution was then spin coated on Pt/Ti/SiO₂/Si at 3000 rpm for 30 sec. The as deposited wet films were heated in a three-step heating process using two different hot plates and a furnace. In the first heating step at low temperature of 300°C for 40 seconds the gel was dried and subsequently pyrolysed at 550°C for 2 minutes on a second hot plate. These steps were repeated several times to obtain the necessary thickness. At the end the film was inserted into a furnace for annealing and crystallisation. The annealing

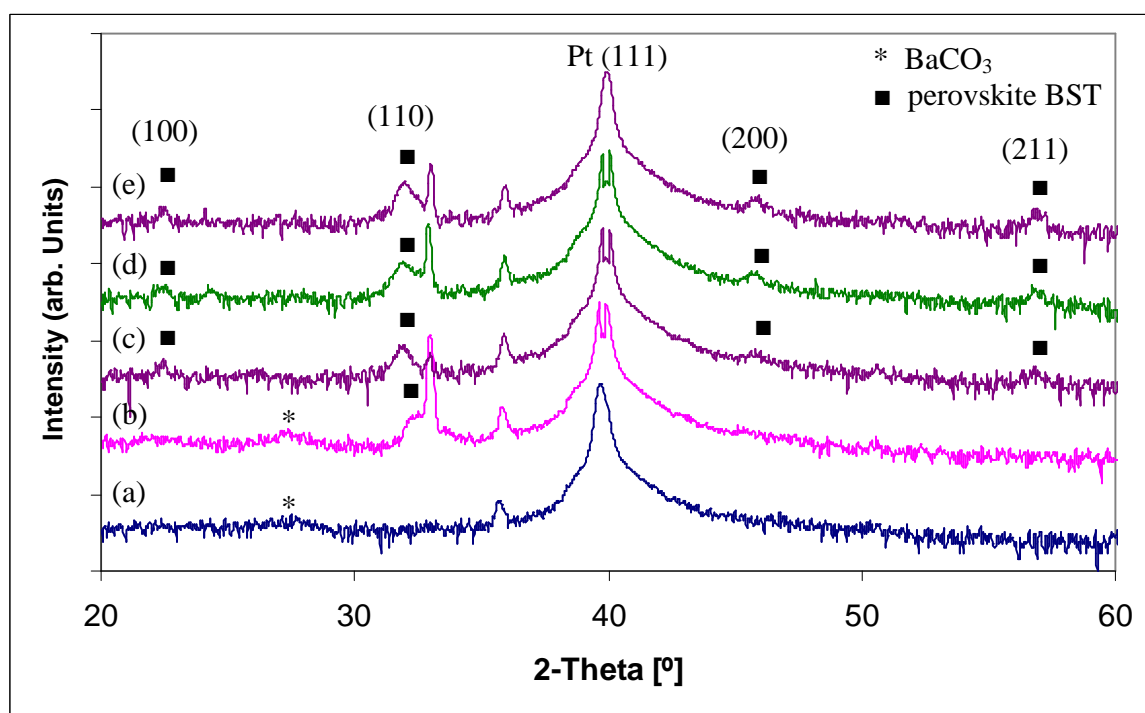


Fig. 4.1: X-ray diffractograms of BST (a) pyrolysed at 550°C; annealed at (b) 600°C, (c) 700°C, (d) 800°C, and (e) 900°C for 30 minutes.

time was 30 minutes at different temperatures from 600°C up to 900°C to get information about the lowest crystallisation temperature.

Fig. 4.1 shows that the dry gel first begins to crystallise into barium carbonate, BaCO₃, in the pyrolysing step at 550°C [8]. During the annealing bake at 600°C the perovskite BST (110) phase begins to crystallise while the BaCO₃-phase is still present. Finally, after 700°C the BST is fully crystallised. The (100), (110), (200), and (211) phases are present and the BaCO₃-phase has vanished. A further increase in the annealing temperature has no visible effect in the X-ray diffractograms.

That the crystallisation of the film is relatively time independent at these temperatures shows Fig. 4.2. The BST thin film is fully crystallised after 30 minutes at 700°C and there is no change detectable in the X-ray diffractogram after 1 hour or even 2 hours.

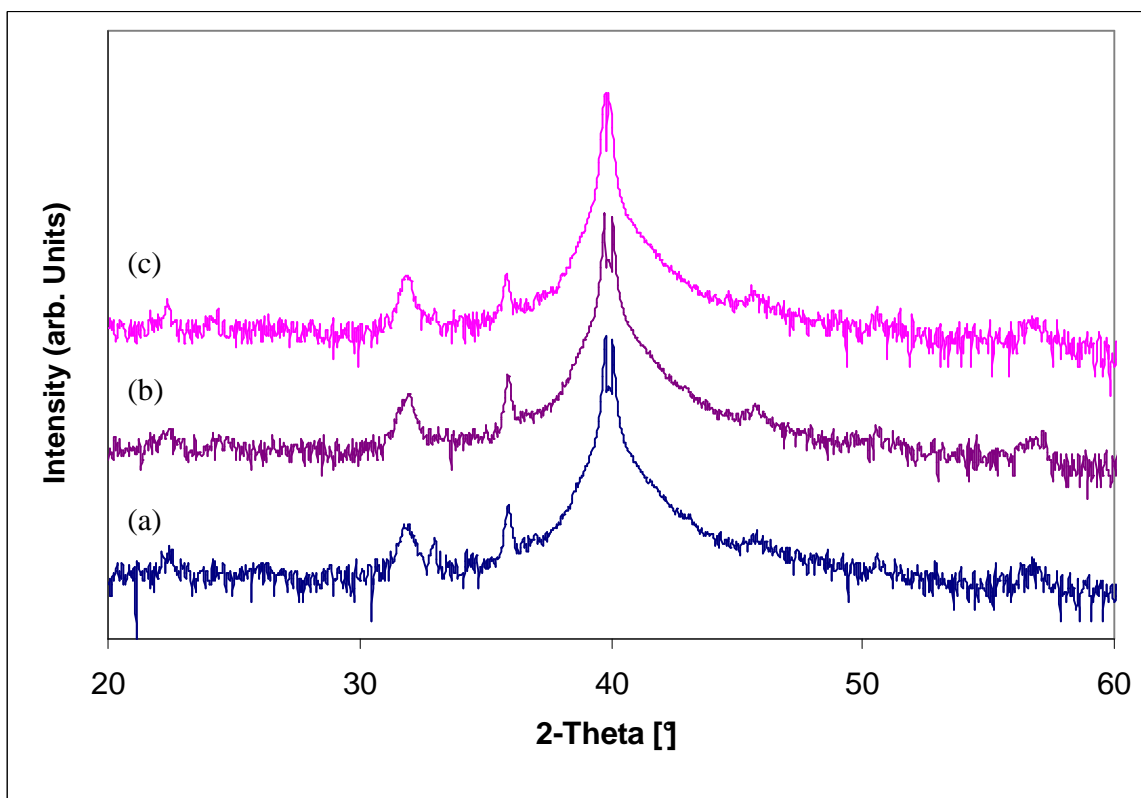


Fig. 4.2: X-ray diffractograms of BST annealed at 700°C for (a) 30 minutes, (b) 1 hour, and (c) 2 hours

However, annealing in a furnace has two major drawbacks, dramatically film cracking and contamination with particulates from the furnace (Fig. 4.3).

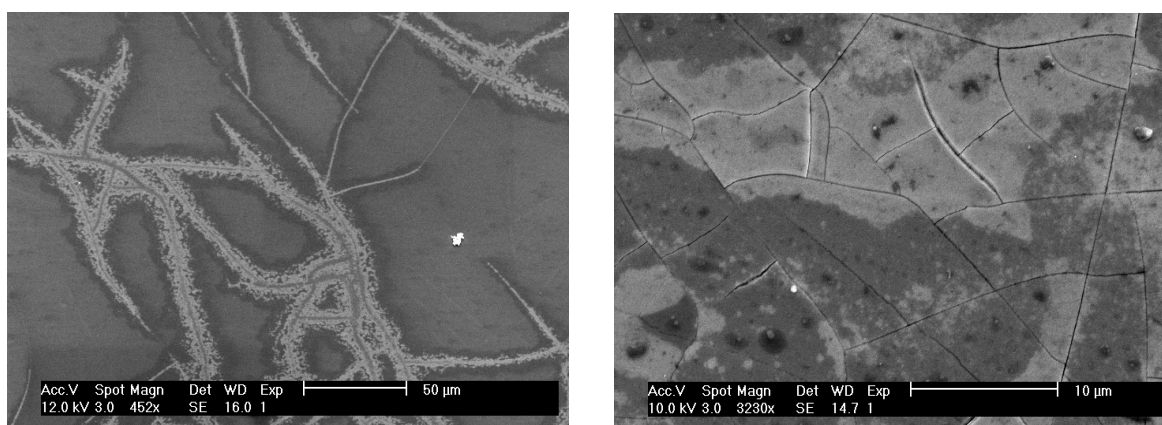


Fig. 4.3: Cracks in and particles on BST thin films after annealing in a furnace

Barium Strontium Titanate (BST)

From these results it was decided to use a third hot plate at 700°C for the annealing bake after each deposition step to reduce film cracking and contaminations from the furnace. The optimised deposition process was the following:

Spin coating	3000 rpm	30 sec
Drying	330 °C	2 min
Pyrolyse	600 °C	5 min
Annealing	700 °C	10 min

Table 4.2: Optimised deposition parameters for BST.

Fig. 4.4 presents SEM-images of the best BST thin film which was realised in this study. Single BST layers with a thickness of ≈ 50 nm are visible in the cross section. The white layer is the platinum bottom electrode with a thickness of ≈ 100 nm. While cracks are still clearly visible in the top view, it was possible to characterise the dielectric properties of the film indicating that no shorts were present.

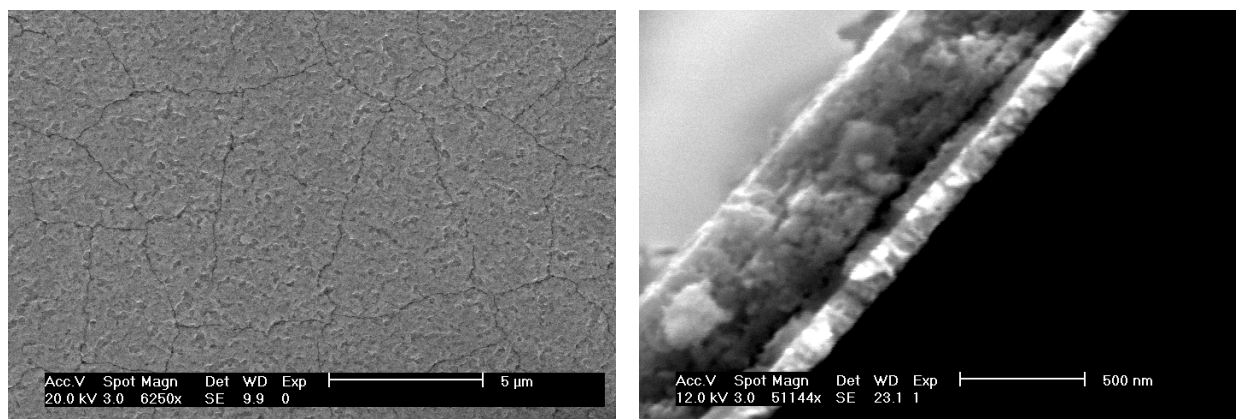


Fig.4. 4: Top view and cross section of BST thin films annealed at 700°C on a hot plate

Fig. 4.5 shows the dielectric constant and the dielectric loss versus frequency and the tunability versus an applied bias field of a 500 nm thick BST thin film. The dielectric loss increases sharply after 100 kHz while the dielectric constant remains relatively stable up to this frequency but decreases afterwards. The tunability was 14% under an applied electric field of ~ 50 kV/cm.

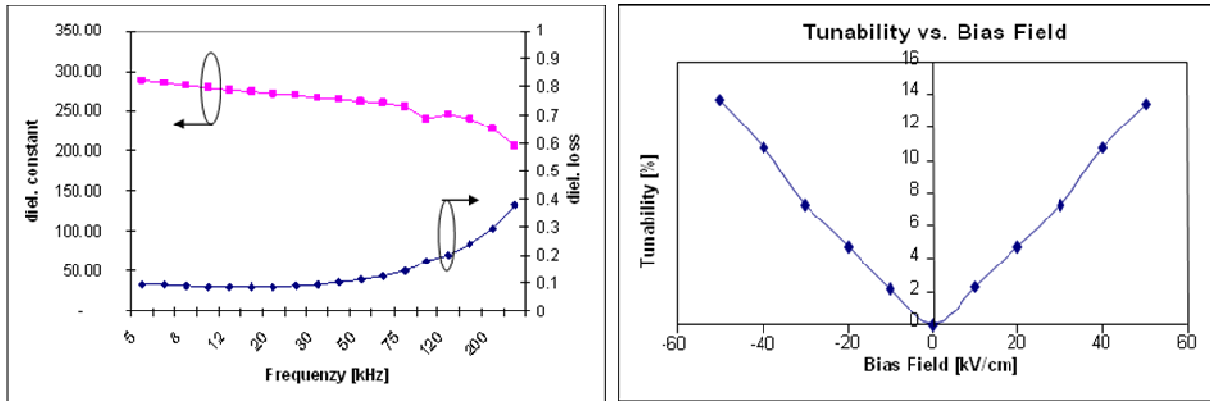


Fig. 4.5: Dielectric properties of BST 60/40. Left dielectric constant and loss vs. frequency, right tunability vs. an applied electric field.

4.3 Discussion

Fig. 4.6 shows the frequency dependence of the dielectric constant and loss of a 250 nm thick BST 50/50 film prepared by sol-gel deposition and rapid thermal annealing at 700°C for 5 minutes on platinised Si with a thin Ti adhesion layer [13].

The behavior of the loss is relative the same: Stable around 10% until ~100 kHz with a strong increase afterwards. This can be attributed to the three- and four quantum loss mechanism in thin films. The dielectric constant in Fig. 4.6 decreases nearly linear with increasing frequency until ~ 1 MHz while it seems to be rather stable up to 300 kHz in Fig. 4.5. However, the dielectric constant in Fig. 4.6 is remarkably higher than in Fig. 4.5 (nearly twice as high at 10 kHz). Why?

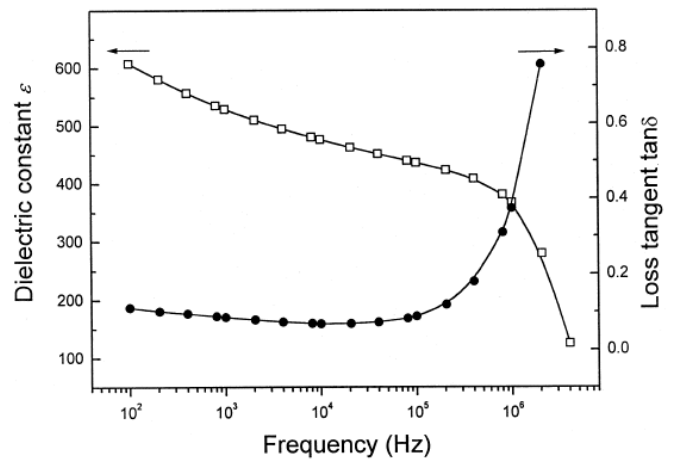


Fig. 4.6: Frequency dependence of dielectric constant and loss of a BST capacitor rapid thermal annealed at 700°C for 5 min [13]

Film thickness has been established to impact the zero bias permittivity through a thickness dependence of the first order coefficient of the Landau-Ginzberg-Devonshire approach [14, 15]. The dependence of the inverse of the zero bias capacitance density of

BST thin film to its thickness is often attributed to the presence of a constant-valued capacitance density, C_i/A , represented by the nonzero intercept, in series with the thickness-dependent capacitance density of the bulk of the film. The constant capacitance is usually thought to represent some type of interfacial layer between the dielectric and one or both of the electrodes (sometimes called *dead layer*), and might arise from surface contaminations of the BST, nucleation or reaction layers at the film/electrode interfaces, or changes in the defect chemistry at the dielectric-electrode interfaces. The apparent capacitance density at zero bias may then be expressed as

$$\frac{A}{C_{app}} = \frac{A}{C_i} + \frac{A}{C_B} = \frac{t_i}{\epsilon_i \epsilon_0} + \frac{(t-t_i)}{\epsilon_B \epsilon_0} \quad [\text{Eq. 4.1}]$$

where A is the area, C_{app} the apparent capacitance, C_i the interfacial capacitance, C_B the bulk film capacitance, ϵ_B the film bulk permittivity, ϵ_i the interfacial layer permittivity, ϵ_0 the permittivity of free space, t the total film thickness and t_i the interfacial layer thickness. The nonlinear, ferroelectric response is a long range cooperative phenomenon and the true permittivity may quite well change with film thickness. Noh *et al.* [16] suggested that the observed thickness dependence of the crystallisation in BST might be

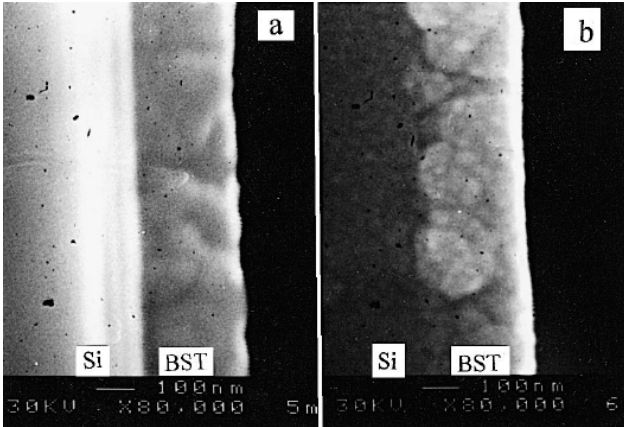


Fig. 4.7: Cross-sectional SEM micrographs of (a) BST thin film rapid thermal annealed at 700°C for 5 min and (b) BST thin film annealed at 700°C for 60 min with 5°C/min temperature ramp rate [13]

related to the film substrate interfacial behavior during crystallisation. In thin films, the amorphous phase first transforms to an intermediate metastable phase (see Fig. 4.1). Since the energy barrier from the metastable phase to the perovskite phase is higher than that from the amorphous to the perovskite phase, the crystallisation temperature in the thin films is higher. In thick films, the amorphous phase transforms directly to the perovskite phase at relatively low annealing temperature.

Cross-sectional SEM micrographs of BST films, derived from different annealing processes, are shown in Fig. 4.7(a) and 4.7(b). For BST films rapid thermal annealed at 700°C for 5 minutes, the interface between BST and Si substrate is clear and sharp, as

shown in Fig. 4.7(a). No apparent inter-diffusions are observed, indicating a relatively small interfacial layer. However, in Fig. 4.7(b), the interface between Si substrate and BST films crystallised by conventional annealing at 700°C for 60 minutes with a temperature ramp rate of 5°C/min is not sharp as the one shown in Fig. 4.7(a). Several large grains across the interface can be seen indicating a relatively huge interfacial layer. The better BST/Si interface prepared by RTA comes from shorter annealing time, which results in less inter-diffusion.

The existence of an interfacial layer between BST film and the Pt bottom electrode was confirmed by high resolution TEM (HRTEM) by Paek *et al.* [17]. The interfacial layer appeared to have crystallinity different from both the BST thin film and the Pt bottom electrode which resulted in variation of the interfacial states between BST and Pt. As the thickness of the BST film decreased from 300 to 50 nm, the thickness of the interfacial layer increased from 9.5 to 11 nm. The dielectric constant of the interfacial layer calculated from its measured overall capacitance and thickness, confirmed by HRTEM, was ca. 30. This low-dielectric constant interfacial layer has been shown to affect the electrical degradation of BST thin films with decreasing thickness. The role of the interface becomes increasingly dominant in the overall electrical conduction process when the film thickness is typically < 100 nm.

Back to the present example. Fig. 4.8 shows a close-up view of the top view in Fig. 4.4. The BST thin film has cracks and is porous but the dielectric loss in Fig. 4.5 indicates that there are no shorts within the film viz. the overall density of the 500 nm thick BST film is low resulting in a thinner effective thickness and thicker effective interfacial layer, or *dead layer*. The cross section in Fig. 4.4 confirms the physical existence of defects and porosity. Additionally the thickness of the interfacial layer in [13] is decreased due to less inter-diffusion at the BST/Si-interface by the use of RTA, which offers shorter annealing times. Thus, the resulting capacitance-density in the BST prepared in this study

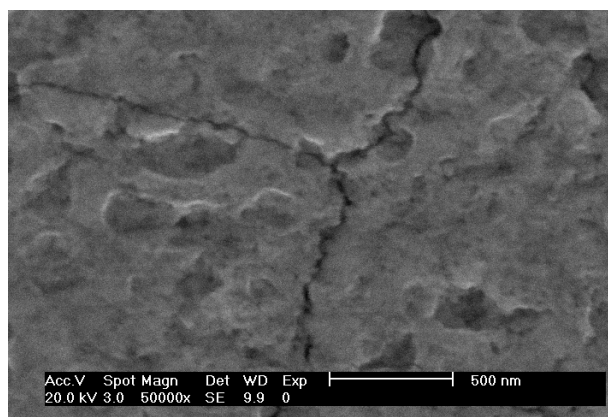


Fig. 4.8: A close-up view of the top view of Fig. 4.4. The BST film has cracks and is porous

is lower as the one off Wu *et al.*, resulting in a lower dielectric constant while the loss remains unaffected.

4.4 References

1. D. Tahan, A. Safari, L.C. Klein; Sol-Gel Preparation of Barium Strontium Titanate Thin Films; 1995 IEEE
2. D.M. Tahan, L.C. Klein, A. Safari; Processing and Dielectric Property Evaluation of Barium Strontium Titanate Thin Films Prepared by a Sol-Gel Technique; 1996 IEEE
3. G. Yi, Z. Wu, M. Sayer; Preparation of Pb(Zr,Ti)O₃ thin films by sol gel processing: Electrical, optical, and electro-optic properties; J. Appl. Phys. 64 (1988) 2717
4. N.V. Giridharan, R. Jayavel, P. Ramasamy; Structural, Morphological and Electrical Studies on Barium Strontium Titanate Thin Films Prepared by Sol-Gel Technique; Cryst. Res. Technol., 36, 2001, 1, 65-72
5. A. Nazeri, M. Khan, T. Kidd, J. Mater. Sci. Lett. 14, 1085 (1995)
6. M. Sedlar, M. Sayer, L. Weaver, J. Sol-Gel Sci. Tech. 5, 201 (1995)
7. D.S. Paik, A.V. Prasada Rao, S. Komarneni, Ba Titanate and Barium/Strontium Titanate Thin Films from Hydroxide Precursors: Preparation and Ferroelectric Behavior, L. Sol-Gel Sci. Tech. 10, 213 (1997)
8. S.B. Majumder, M. Jain, A. Martinez, R.S. Katiyar, F.W. Van Keuls, F.A. Miranda; Sol-gel derived grain oriented barium strontium titanate thin films for phase shifter applications; J. Appl. Phys. 90, 2 (2001) 896
9. M. Jain, S.B. Majumder, R.S. Katiyar, A.S. Bhalla, F.A. Miranda, and F.W. van Keuls; Tailoring of BST and MgO Layers for Phase Shifter Applications; *Integrated Ferroelectrics*, 60: 59–68, 2004
10. H-S. Kim, H-G. Kim, I-D. Kim, K-B. Kim, J-C. Lee; High-tunability and low-microwave-loss Ba_{0.6}Sr_{0.4}TiO₃ thin films grown on high-resistivity Si substrates using TiO₂ buffer layer, Appl. Phys. Lett. 87, 212903, 2005

11. W. Fan, S. Saha, J.A. Carlisle, O. Auciello, R.P.H Chang, R. Ramesh; Layered Cu-based electrode for high-dielectric constant oxide thin film-based devices; *Appl. Phys. Lett.* 82, 9 (2003) 1452
12. W. Fan, B. Kabius, J.M. Hiller, S. Saha, J.A. Carlisle, O. Auciello, R.P.H. Chang, R. Ramash; Materials science and integration bases for fabrication of $(\text{Ba}_x\text{Sr}_{1-x})\text{TiO}_3$ thin film capacitors with layered Cu-based electrodes; *J. Appl. Phys.* 94, 9 (2003) 6192
13. D. Wu, A. Li, H. Ling, X. Yin, C. Ge, M. Wang, N. Ming; Preparation of $(\text{Ba}_{0.5}\text{Sr}_{0.5})\text{TiO}_3$ thin films by sol-gel method with rapid thermal annealing; *Applied Surface Science* 165 (2000) 309-314
14. C. Bascari, S.K. Streiffert, A.I. Kingon, R. Waser; *J. Appl. Phys.* 82 (1997) 2497
15. G.W. Dietz, M. Schumacher, R. Waser, S.K. Streiffert, C. Bascari, A.I. Kingon; *J. Appl. Phys.* 82 (1997) 2359
16. D.Y. Noh, H.H. Lee, T.S. Kang, J.H. Je; *Appl. Phys. Lett.* 72 (1998) 2823
17. S. Paek, J. Won, K. Lee, J. Choi, C. Park; *Jpn. J. Phys.* 35 (1996) 5757

The most exciting phrase to hear in science, the one that heralds new discoveries, is not 'Eureka!' (I found it!) but 'That's funny ...'

Isaac Asimov (1920 - 1992)

Equipped with his five senses, man explores the universe around him and calls the adventure Science.

Edwin Powell Hubble
The Nature of Science, 1954

In physics, you don't have to go around making trouble for yourself - nature does it for you.

Frank Wilczek

Lead Strontium Titanate (PST)

It may be not surprising that $(\text{Pb,Sr})\text{TiO}_3$ behaves very similar to $(\text{Ba,Sr})\text{TiO}_3$. In general all the physical properties discovered for BST in previous chapters hold on for PST. The Curie temperature for the cubic to tetragonal transition, for instance, can be adjusted over an exceedingly large temperature range by varying the Pb/Sr ratio (Fig. 5.1). The reason for this behaviour is the change of the lattice parameters of the a- and c-axis of the perovskite crystal structure (Fig. 5.2). With increasing Sr-content, the a-axis gradually increases and the c-axis largely decreases, resulting in a decrease of the cell volume. At room temperature the c/a-ratio reaches unity in the shaded region – this is the cubic to tetragonal transition area at room temperature. This result, confirmed by P. Du *et al.* and M. Jain *et al.* [3, 4] later on, will become important in a later chapter.

Nomura and Sawada [5] studied the $\text{SrTiO}_3\text{:PbTiO}_3$ solid solution system in 1955. They found an easy and crack-free formation of good homogeneous compositions, and observed only one phase transition in the PST system, as compared to three transitions in the case of BST or BaTiO_3 (see Fig. 2.3). PST, doped or undoped, has been investigated intensively in terms of tunability and dielectric loss, the best achieved values were around 50% and 1% for the tunability and loss, respectively.

Therefore, Cross and co-workers suggested 46 years after Nomuras and Sawadas work, PST with its higher tunability and lower loss for tunable microwave applications [6]. Not only the general performance of PST is better than that of BST in such applications,

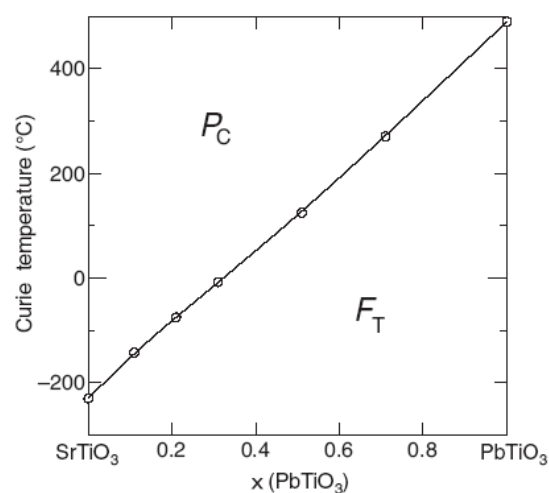


Fig. 5.1: Phase diagram for $(\text{Pb,Sr})\text{TiO}_3$ [1]

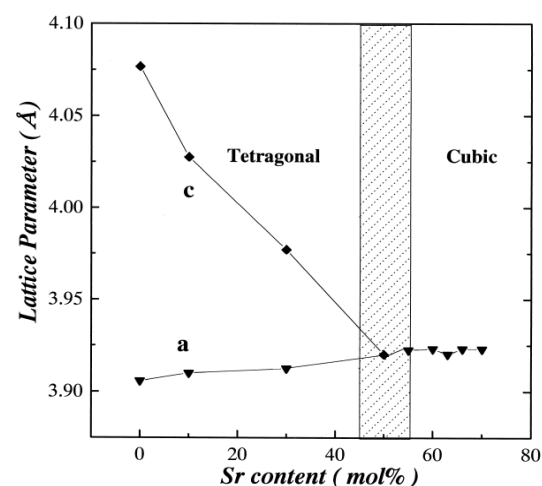


Fig. 5.2: Lattice parameters for $(\text{Pb,Sr})\text{TiO}_3$ vs. Sr content [2]

moreover, the processing temperature is lower in lead-based materials compared to BST, which offers an additional advantage. This signaled the beginning of extensive research and the number of papers about PST are rocketing since Cross's suggestion. Maybe an other case like roman cement (see section 1.2).

In the following chapters the synthesis, characterisation, some realised applications and benefits of PST 50/50 and 40/60, doped and undoped, are described and investigated.

5.1 Synthesis and Crystallisation of PST

The multicomponent PST precursor solution was prepared using high purity lead acetate, $\text{Pb}(\text{CH}_3\text{CO}_2)_2$, strontium acetate, $\text{Sr}(\text{CH}_3\text{CO}_2)_2$ and titanium butoxide, $\text{Ti}(\text{OC}_4\text{H}_9)_4$. First lead acetate and strontium acetate were mixed in a stoichiometric ratio in 8 ml acetic acid and 5 ml 1.3 propanediol. Heating was needed to help the dissolution of the precursors. After a while titanium butoxide, diluted in 15 ml acetic acid to minimise reaction with humidity, was added under constant stirring. The so-called parent solution was then stirred over night at room temperature. Finally, 2-methoxyethanol was added up to ~ 46 ml (0.4 M) to stabilise the solution.

The solution was then spin coated on Pt/Ti/SiO₂/Si at 3000 rpm for 30 sec. The as deposited wet films were heated in a three-step heating process using different hot plates. In the first heating step the gel was dried at a temperature of 350°C for 30 seconds and subsequently pyrolysed at 600°C for 5 minutes on a second hot plate. These steps were repeated several times to obtain the necessary thickness. Finally a third hot plate was used to crystallise the film at different temperatures for 15 minutes to investigate the crystallisation pathway.

Fig. 5.3 shows that the dry gel begins to crystallise into the perovskite PST (110)-phase in the pyrolysing step at 500°C. The (100)-, (200)-, and (211)-phases start to appear at 550°C and are increasing in intensity until 650°C. After 650°C the film is fully crystallised. The peak, which appears after a relatively low annealing temperature of 400°C around 33° is often related to the (200) Si-“ghost peak”. A peak which arises sometimes by destructive interference in case of Si (100) standard substrates at approximately 32.9°. However, the behavior of this peak is strange in this case.

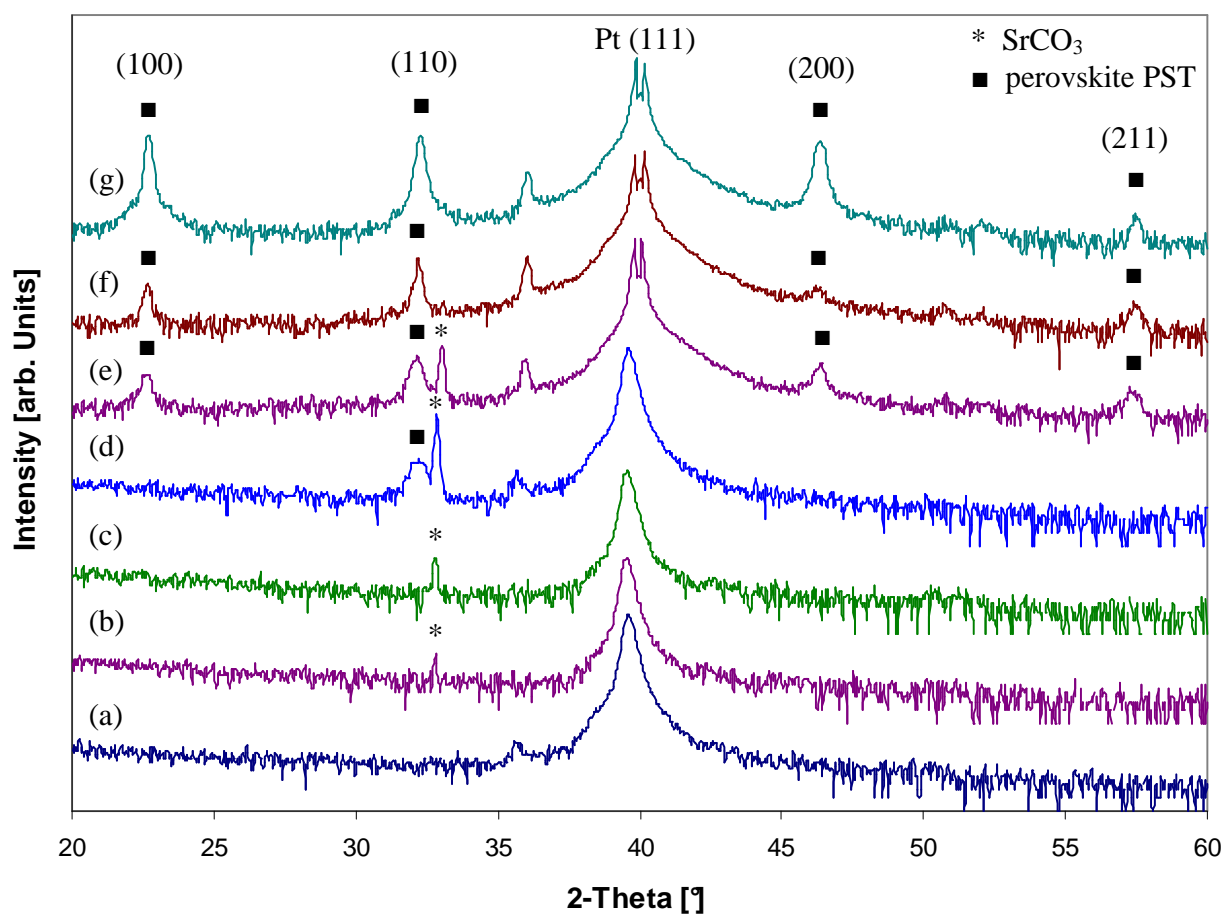


Fig. 5.3: X-ray diffractograms of PST after 15 minutes at (a) 350°C, (b) 400°C, (c) 450°C, (d) 500°C, (e) 550°C, (f) 600°C and (g) 650°C.

The peak seems to increase in intensity with increasing temperature up to 500°C. Thereafter its intensity decreases and it vanishes nearly completely at 600°C. In exactly this temperature range the PST (100)-, (200)-, and (211)-peaks arise and the PST (110)-peak increases.

The Si-“ghost peak”, being a result of destructive interference, is not effected by temperature and/or annealing time (see Fig. 4.1). Hence a second experiment was designed. The temperature was kept at 450°C, at this temperature the peak was clearly visible without a distracting PST peak, and the annealing time was varied from 5 to 20 minutes. Fig. 5.4 shows the result.

It shows clearly that the peak is increasing with annealing time. With other words: *This peak can not be a Si-“ghost peak”*. It must be a second phase peak, which crystallises at

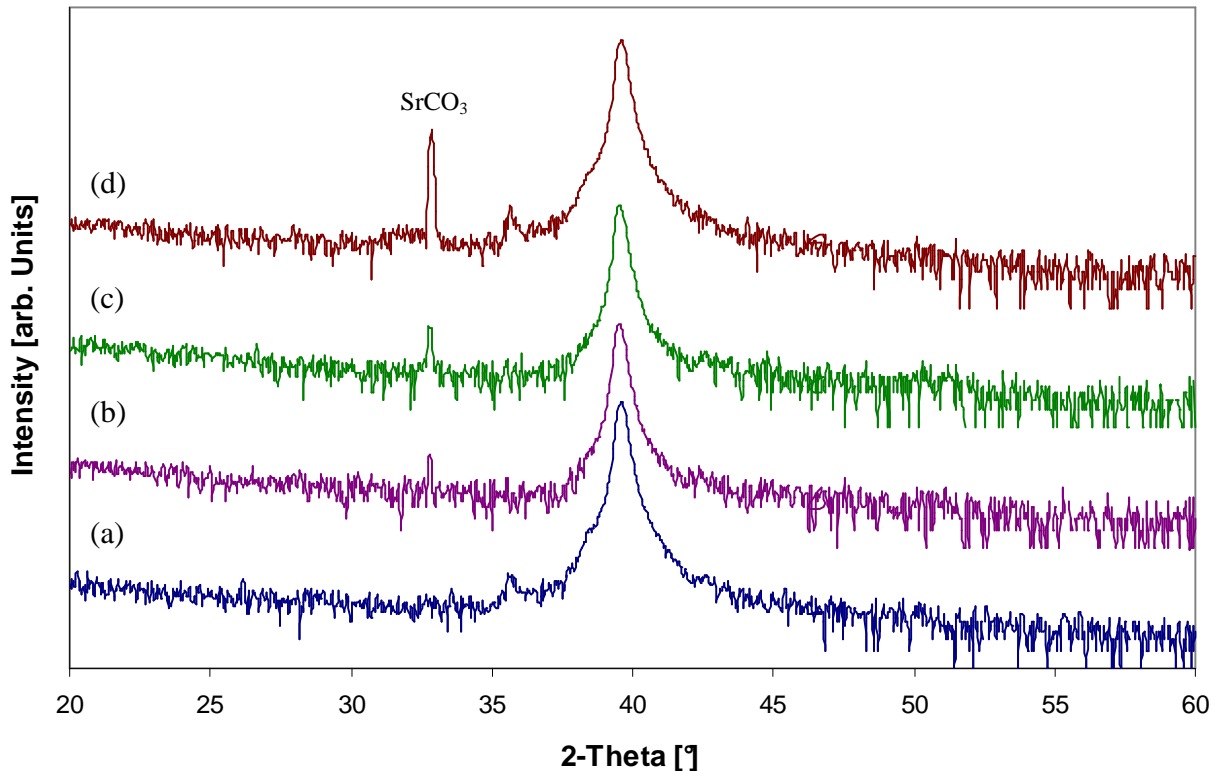


Fig. 5.4: X-ray diffractograms of PST annealed at 450°C for (a) 5 minutes, (b) 10 min, (c) 15 min, and (d) 20 min

lower temperatures and transforms into the perovskite PST phases at higher temperatures. Unfortunately it is not possible to identify the composition of this peak from the X-ray diffractogram. But from the crystallisation pathway of BST (Fig. 4.1), where identical solvents and chemicals were used, and where the second phase belongs to BaCO_3 , it is most likely that this peak represents SrCO_3 .

Additional XRD results from SrCO_3 nanorods [7 – 9] show a SrCO_3 peak at exactly this position confirming the result presented here. However, F. Du *et al.* identified this peak to be SrCO_3 (121) [7], whereas S. Li *et al.* labeled this peak as (201) [8] and G.S. Guo *et al.* as (012) [9] making it unclear which phase we see in the present study

However, the above discussed PST films were fabricated (out of practical and experimental reasons) with only one annealing bake of six single layers, which gave a total PST film thickness of approximately 300 nm, which in turn resulted in a good XRD response, at the end of the process. Due to the thickness of the film, the induced thermal

stress during the annealing bake resulted in minor cracks, Fig. 5.5. To realise a total crack-free film over a large area, viz. an entire 4''-wafer, a layer by layer annealing step was adopted. In addition it was observed that the pyrolysing step at 600°C is not necessary for PST. The optimised process flow for the deposition of PST, which is used throughout this study from now on (unless stated) is listed in Table 5.1.

Fig. 5.6 shows 3-dimensional AFM images of the thus prepared film. The rms-roughness was 1.334 nm for the 2x2 µm scan and 1.154 nm for the 1x1µm scan, indicating a very smooth surface. The single grain size can be estimated from the 1·1µm scan. A value of approximately 150 nm seems reasonable.

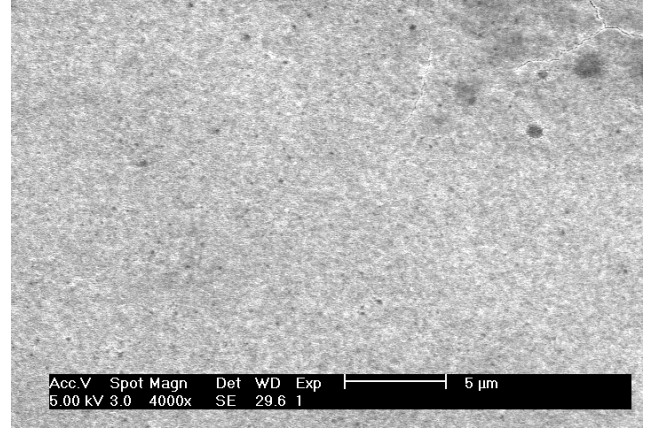


Fig. 5.5: SEM image of the surface of six layers PST. Only one annealing bake was carried out at the end. Minor cracks are visible on the upper right corner of the image.

Spin coating	3000 rpm	30 sec
Drying	350 °C	10 min
Annealing	650 °C	15 min

Table 5.1: Optimised deposition parameters for PST.

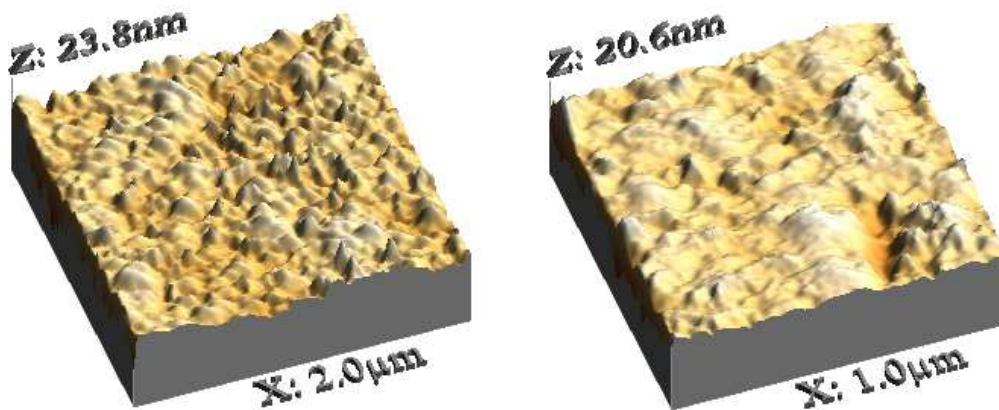


Fig. 5.6: AFM images of PST thin films. RMS roughness: (left) 1.334 nm, (right) 1.154 nm

5.2 Dielectric Properties of PST 50/50

Fig. 5.7 shows the permittivity and dielectric loss of PST 50/50 versus frequency and under bias at low frequencies (10 – 300 kHz).

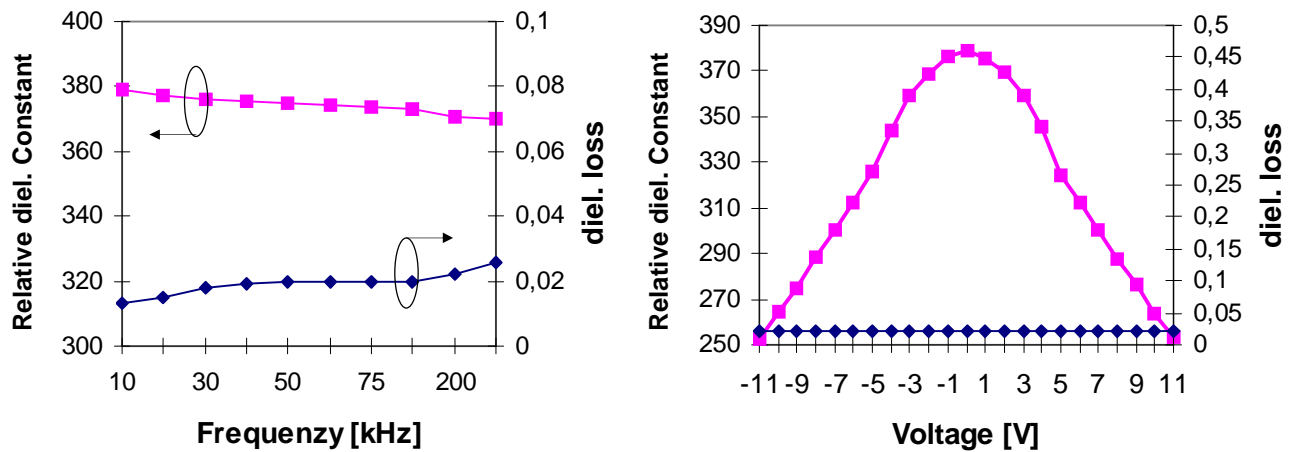


Fig. 5.7: Permittivity and dielectric loss of PST 50/50 versus frequency and bias.

The permittivity is higher than 370 up to 300 kHz and the dielectric loss is under 3% in the measurement region. The tunability was measured under a frequency of 100 kHz and has a maximum value of 33.2% under a bias of ± 11 V ($E = 36.7$ V/ μm) which results in a FOM of 16.6.

Measurements from 10 MHz up to 110 MHz were carried out at the University of Birmingham and the results are presented in Fig. 5.8 and 5.9

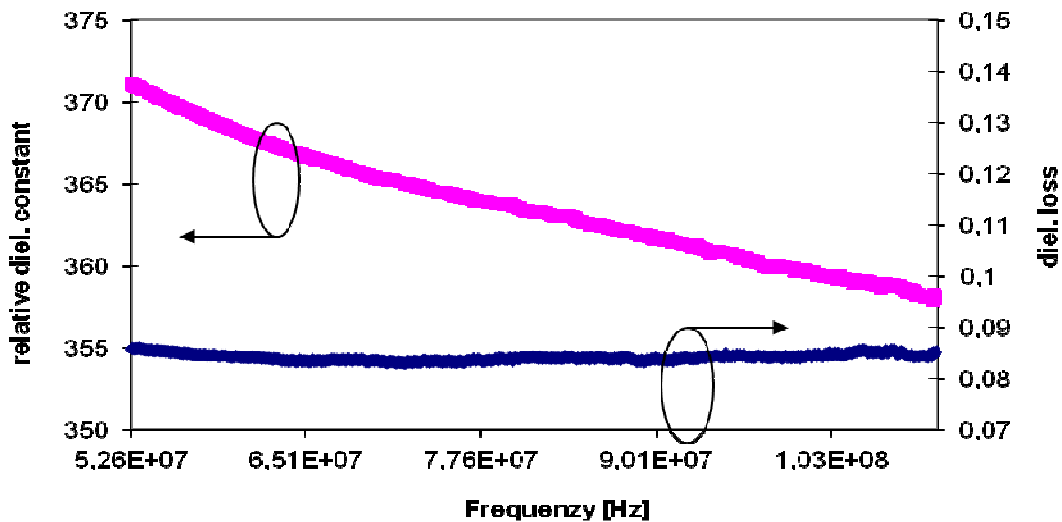


Fig. 5.8: Permittivity and dielectric loss of PST 50/50 from 50 to 110MHz

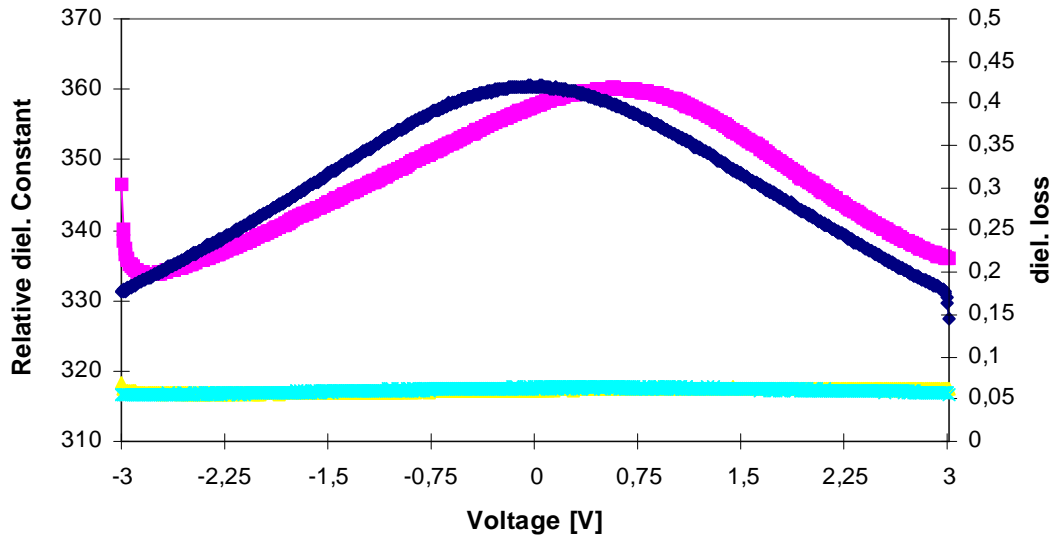


Fig. 5.9: Permittivity and dielectric loss of PST 50/50 from $-3V$ to $+3V$ at $10MHz$

To measure the permittivity and dielectric loss in this frequency range by using the equipment the University of Birmingham offers, a CPW², with all the involved advantages and disadvantages (substrate losses, fringing fields etc. ...), was build upon the PST thin film. The dielectric constant and loss were measured twice, at the end auf the CPW and in the middle. The variance of the dielectric constant of both measurements was found to be negligible, whereas the extraction of the true loss needed a more profound mathematical treatment, Fig. 5.10. For a detailed description of the measurement and the physical background see Ref. 15.

The permittivity was measured between 370 and 360 with a little decrease up to 110 MHz, this compares well with the measurement at low frequencies. The dielectric loss is with measured 7 % approximately 5 % higher compared to the low frequency range. But the

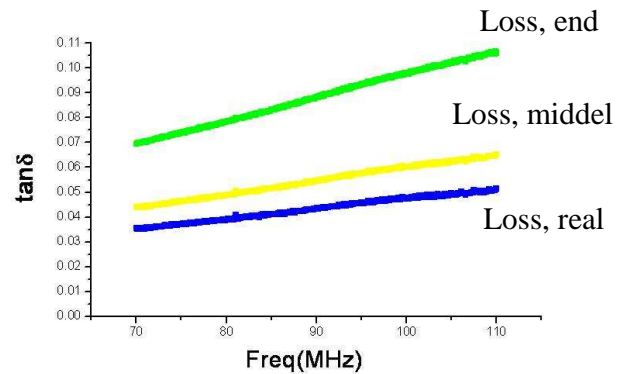


Fig. 5.10: Comparison of measured losses on a CPW.

$$\tan \delta_{real} = \frac{4}{3} \tan \delta_{middel} - \frac{1}{3} \tan \delta_{end}$$

² CPW (Coplanar Waveguide). A short and good introduction is given at: www.microwaves101.com/encyclopedia/coplanarwaveguide.cfm

behavior of the loss is very stable, no increase with frequency is observable. This may indicate that the additional 5 % in loss are due the CPW measurement technique.

However the voltage dependence of the PST thin film up to ± 3 V is well comparable. At 3 V the tunability was both ~ 8 % at low and high frequencies.

By taking all these results into account one can say that the dielectric properties of PST are stable in a relatively large frequency range up to 110 MHz and that measurements in the low frequency range, which are less complicated and time consuming, are sufficiently enough to characterise the properties of PST. However, at much higher frequencies, e.g. in the GHz-region, where the effect of phonon damping, ~ 100 GHz for PST, begins to play a role, the Quasi-Debye loss has to be taken into account.

Coming back to Fig. 5.9. A little hysteresis in the dielectric response of the PST thin film can be observed. According to Fig. 5.2 the tetragonal-cubic transition area of PST 50/50 is exactly at room temperature. The hysteresis shows that PST 50/50 does not behave like an ideal cubic-paraelectric material, it is has a “little” tetragonal-ferroelectric characteristic. Being a “bit” ferroelectric means having additional losses due to the switching of dipole moments. Shifting the transition point to lower temperatures by reducing the Pb-content will help to reduce the overall loss, as we will see later on.

5.3 PST 50/50 Varactors with Copper Electrodes

The above discussed PST 50/50 thin film was used as a functional dielectric layer in a voltage tunable parallel-plate capacitor (varactor) with copper electrodes [10]. As mentioned in Section 4.1, the commonly used Pt bottom electrode is, from the electrical point of few, not ideal. The desirable properties of Pt, such as chemical stability and ability to withstand the high-temperatures and oxidizing conditions during film deposition, comes with the cost of a relatively high electrical resistivity and loss at microwave frequencies. By looking at a data sheet for the bulk electrical resistivity, one can find that Pt has a bulk resistivity of $10.8 \mu\Omega\text{cm}$. Compared to the bulk resistivity of Au ($2.2 \mu\Omega\text{cm}$) or even Cu ($1.7 \mu\Omega\text{cm}$) this value is more than five times higher.

The total device loss for a varactor can be defined in terms of quality factors Q, as:

$$\tan \delta_{device} = \frac{1}{Q_{device}} = \frac{1}{Q_{dielectric}} + \frac{1}{Q_{electrode}}, \text{ with } Q_{electrode} = \frac{1}{\omega R_s C} \quad [\text{Eq. 5.1}]$$

with R_s the series resistance of the electrodes. It should be clear that a low electrode resistivity means a high electrode quality factor and thus a low total device loss.

Fan *et al.* [11, 12] has confirmed this concept as described in section 4.1. However, his realisation of a Cu bottom electrode for BST was relatively complicated due to the fact that different diffusion barrier layer were needed on either sides of the Cu electrode: a Ta diffusion barrier on top the Si substrate to inhibit Cu diffusion, and a TiAl layer as barrier against oxygen diffusion into the Cu layer to inhibit Cu oxidation during the deposition and annealing of the BST thin film.

A layer transfer method was used in this example. The method relies on the transfer of a ferroelectric film from an auxiliary- to a device substrate, and thus completely prevents the exposure of the bottom electrode to high temperatures and destructive reactive atmospheres. Here, the bottom electrode no longer serves as a seed layer for ferroelectric film growth and therefore can be freely chosen. This enables the use of low resistivity materials like Au and Cu, which due to their thermal instability and corrosive properties are not commonly used in conventional parallel-plate capacitors.

However, the initial process steps are the same as described above. A 4''-Si- wafer, with a Ti/Pt seed layer and 10 layers of PST 50/50. For adhesion purposes, a thin TiW layer (10 nm) was sputtered on top of the PST on which a 650 nm thick Cu bottom

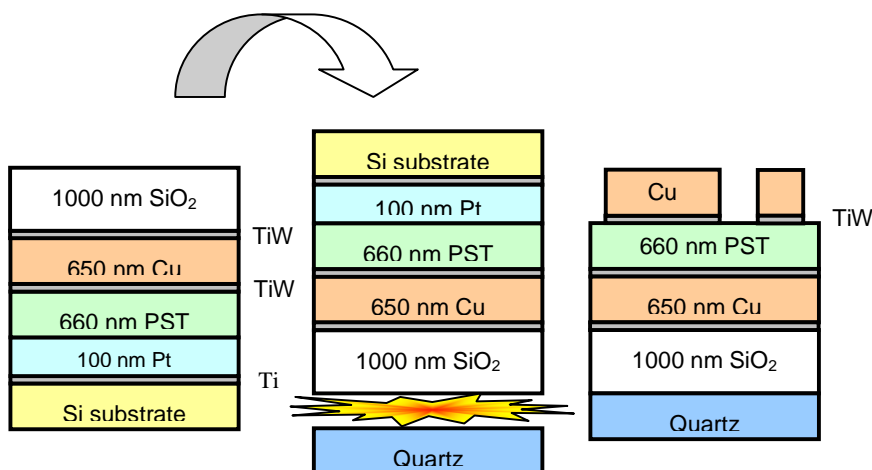


Fig. 5.11: Schematic illustration of the fabrication of Cu/PST/Cu varactors by layer transfer

electrode was deposited, followed by another TiW film (20 nm). SiO₂ was grown by plasma enhanced chemical vapor deposition (PECVD) up to a thickness of 1000 nm and

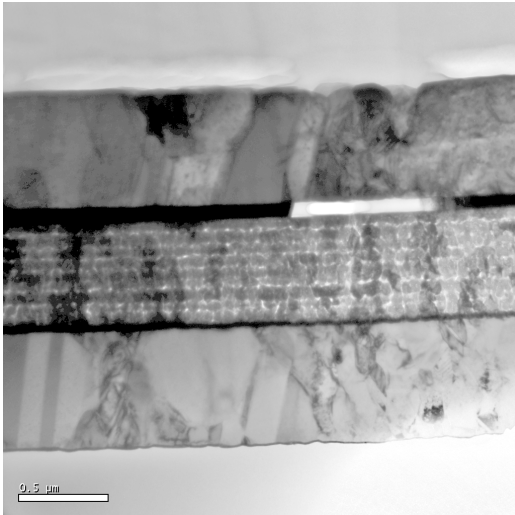


Fig. 5.12: Bright-field TEM of the Cu/PST/Cu varactor

was subsequently planarised by chemical-mechanical polishing. Layer transfer to a 100 mm quartz substrate was achieved by vacuum bonding at room temperature and the bond was subsequently strengthened by heating at 200°C for two hours. The auxiliary silicon substrate was then thinned by grinding to < 100 μm which then automatically peeled off along the Pt/PST interface. Finally, a 650 nm thick Cu top electrode with a 20 nm TiW adhesion layer was sputtered and patterned by photolithography for electrical characterization. These process steps are schematically illustrated in Fig. 5.11.

Dielectric measurements were performed with an Agilent-4294A precision impedance analyzer and a HP-8720D network analyzer. The capacitor test structures were connected to the analyzers by Cascade microprobes whereby one of the legs contacted a well-

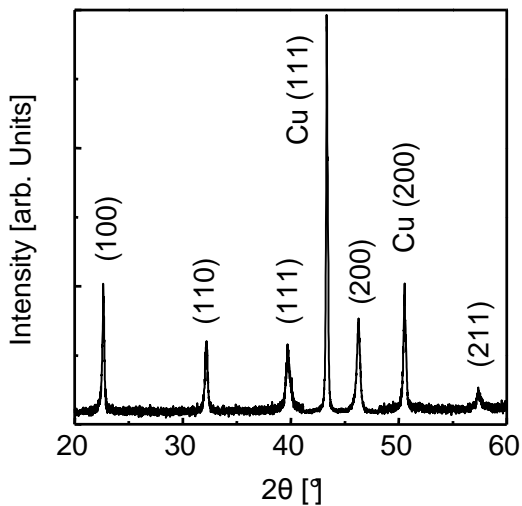


Fig. 5.13: X-ray diffractogram of PST on Cu

defined small electrode and the other a much larger area that efficiently coupled to the continuous bottom electrode. Standard tape tests on the final multilayer stack revealed good adhesion between the individual layers.

Fig. 5.12 shows a bright-field transmission electron microscopy (TEM) image of the PST parallel-plate capacitor with Cu bottom- and top electrodes. The PST film consists of several distinctive granular layers which are the result of multiple spin coating and drying steps during the sol-gel deposition process. The randomly distributed PST grains are polycrystalline as

illustrated by the X-ray diffractogram, Fig. 5.13. The magnetron sputtered Cu layers, on

the other hand, contain some misoriented grains with (111) and (100) out-of-plane texture and electron diffraction patterns (not shown) indicate the presence of twins, defects that are quite common in Cu. No clear epitaxial relationship between the PST film and the Cu electrodes does exist.

More detailed bright-field TEM images of the electrode/oxide interfaces are shown in Fig. 5.14 and 5.15. The Cu bottom electrode and the PST film are separated by a rough interlayer with dark contrast. This layer corresponds to TiW that, when grown *on top* of the relatively rough ferroelectric film, diffused into the PST grains. In contrast, the interface between the PST film and the Cu top electrode is sharp. This clearly indicates that the original PST/Pt interface on the sacrificial substrate was relatively smooth. Moreover, limited adhesion between Pt and PST films facilitated the complete removal of Pt after layer transfer. Finally, subsequent sputtering of the Cu top electrode on the newly exposed PST film did not introduce pronounced interface roughness. There is a relatively sharp interface observable between the PST layers that were formed during the first and second sol-gel spin-coating step. The different layer morphology is due to dissimilarities between the films onto which these layers were spun, i.e. Pt and PST, respectively.

Fig. 5.16 shows the bias dependence of the dielectric properties of a Cu/PST/Cu parallel-plate capacitor at a frequency of 1 MHz. The zero-bias dielectric constant at room temperature is 420 and the dielectric tunability reaches 73% at a breakdown voltage of 35 V. The dielectric loss (not shown) was 3.8%, leading to a figure of merit of 19.21.

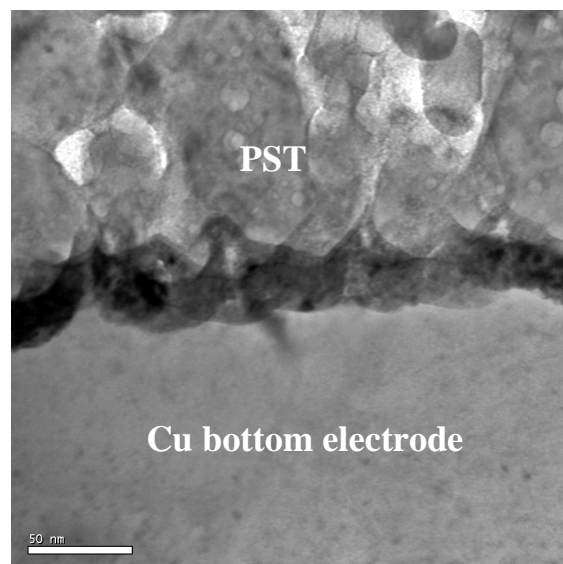


Fig. 5.14: TEM image of the Cu bottom electrode/PST interface

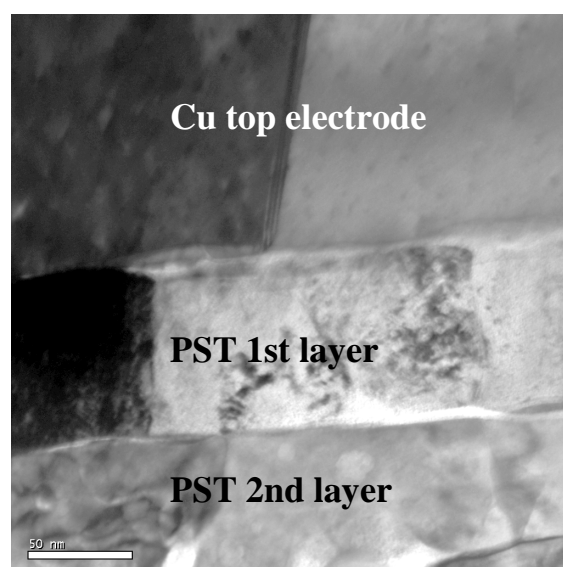


Fig. 5.15: TEM image of the PST/Cu top electrode interface

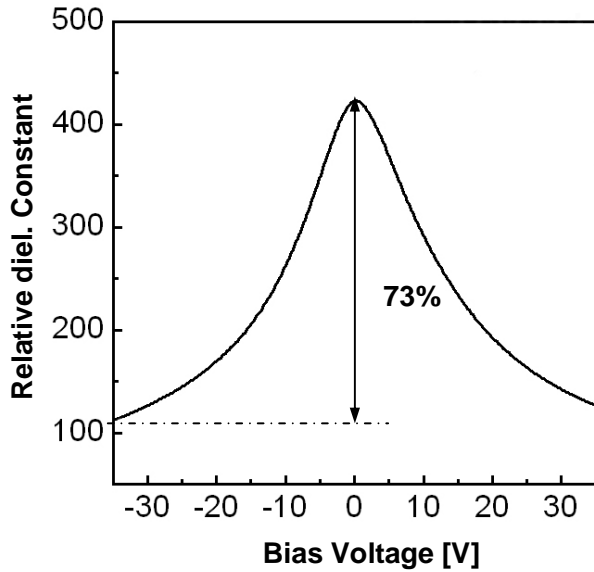


Fig. 5.16: Permittivity vs bias voltage at 1 MHz at room temperature

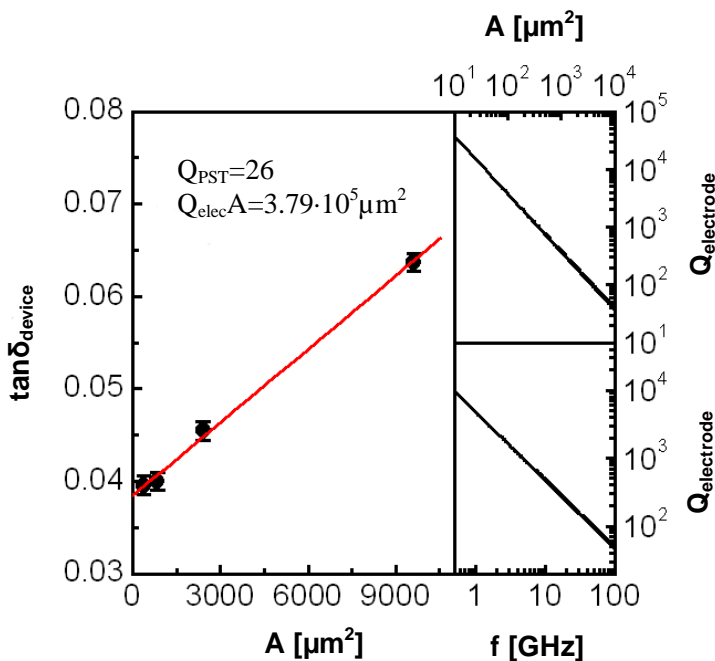


Fig. 5.17: Measured dielectric loss as a function of Cu/PST/Cu capacitor area at 1 GHz. The upper right and lower right graphs show the variation of the electrode quality factor as a function of capacitor size at 1 GHz and frequency for a capacitor with a diameter of 10 μm .

Since the electrode loss scales with the size of the capacitor, the quality factors of the PST film and electrodes can be determined separately by measuring the loss tangents as a function of capacitor area [13]. The experimental results at a frequency of 1 GHz are shown in Fig. 5.17. In this case, $\tan \delta$ is defined as $1/Q_{PST} + A/(Q_{elec}A)$, fitting the data give $Q_{PST} = 26$ and $Q_{elec}A = 3.79 \cdot 10^5 \mu\text{m}^2$. The quality factor of the electrodes is very large, which is mainly due to the use of high-conductivity Cu on both sides of the PST film. For a capacitor with a diameter of 10 μm , for example, it is nearly 5000 at 1 GHz. Moreover, as $Q_{elec} \sim 1/f$, the quality factor of the electrodes is anticipated to remain larger than 100 up to a frequency of about 50 GHz. This clearly demonstrates the potential of the layer transfer method for the fabrication of ferroelectric parallel-plate capacitors with low-loss electrodes, which holds a great promise for microwave device applications. In addition, it enables measurements of true losses in ferroelectric films at high frequency.

Besides the obvious advantage of high-conductivity bottom and top electrodes, the layer transfer method also facilitates the use of microwave-compatible device

substrates. Thick electrodes that are normally utilized to minimize substrate losses are therefore no longer a prerequisite for low-loss operation at high frequencies. In particular silicon, a popular substrate choice for conventional parallel-plate capacitors, will contribute to dielectric losses if the electrode thickness is smaller than the electromagnetic penetration length or so-called skin depth. For Pt and Cu electrodes, for example, the skin depth at a frequency of 10 GHz is about 1.648 μm and 0.660 μm , respectively. By transferring the ferroelectric film onto a microwave compatible substrate like quartz, the substrate losses are small even for relatively thin metallic electrodes.

Finally, the auxiliary substrate and seed layers can be chosen such that their thermal expansion characteristics mimic those of the ferroelectric film. This limits the formation of cracks and the build-up of thermal strain after high-temperature film growth, features that tend to reduce the performance of parallel-plate capacitors [14]. As the auxiliary substrate and seed layers are removed after layer transfer, their selection is not compromised by their high-frequency properties.

5.4 References

1. T. Fujii and M. Adachi, "Preparation of (Pb,Sr)TiO₃ Films by Sol-Gel Technique", Japanese Journal of Applied Physics, Vol. 44, No. 1B, 2005, pp. 692–694
2. D.H. Kang, J.H. Kim, J.H. Park, and K.H. Yoon, "Characteristics of (Pb_{1-x}Sr_x)TiO₃ thin film prepared by a chemical solution processing", Materials Research Bulletin 36 (2001) 265-276
3. P. Du, X. Li, Y.Liu, G. Han, and W. Weng, "Effect of La doping on tunable behavior of soö-gel-derived PST thin film", Journal of the European Ceramic Society 26 (2006) 2147 – 2150
4. M. Jain, S.B. Majumber, R.Guo, A.S. Bhalla, and R.S. Katiyar, "Synthesis and characterization of lead strontium titanate thin films by sol-gel technique", Materials Letters 56 (2002) 692 – 697
5. S. Normuna and S. Sawada, J. Phys. Soc. Jpn. 10 (1955) 108

6. Y. Somiya, A.S. Bhalla, and L.E. Cross, “Study of (Pb,Sr)TiO₃ ceramics on dielectric and physical properties”, *Int. J. Inorg. Mater.*, 3 (2001) 706 – 714
7. F. Du and L. Shi, “Solvothermal growth of single-crystal hexagonal prismatic SrCO₃ microrods”, *Cryst. Res. Technol.* **42**, No. 3, 216 – 220 (2007)
8. S. Li, H. Zhang, J. Xu, and D. Yang, „Hydrothermal synthesis of flower-like SrCO₃ nanostructures”, *Materials Letters* **59** (2005) 420 – 422
9. G.S. Guo, F.B. Gu, Z.H. Wang, and H.Y. Guo, “Low-temperature Growth of Single-crystal SrCO₃ Nanoneedles” *Chinese Chemical Letters* **16**, No. 8, 1101 – 1104 (2005)
10. T. Riekkinen, T. Mattila, S. van Dijken, A. Lüker, Q. Zhang, P.B. Kirby, A.M. Sánchez; “Ferroelectric parallel-plate capacitors with copper electrodes for high-frequency applications”, *Appl. Phys. Lett.* **91**, 252902, 2007
11. W. Fan, S. Saha, J.A. Carlisle, O. Auciello, R.P.H Chang, R. Ramesh; Layered Cu-based electrode for high-dielectric constant oxide thin film-based devices; *Appl. Phys. Lett.* 82, 9 (2003) 1452
12. W. Fan, B. Kabius, J.M. Hiller, S. Saha, J.A. Carlisle, O. Auciello, R.P.H. Chang, R. Ramash; Materials science and integration bases for fabrication of (Ba_xSr_{1-x})TiO₃ thin film capacitors with layered Cu-based electrodes; *J. Appl. Phys.* 94, 9 (2003) 6192
13. D.C. Dube, J. Baborowski, P. Muralt, and N. Setter; The effect of bottom electrode on the performance of thin film based capacitors in the gigahertz region; *Appl. Phys. Lett.* **74**, 3546 (1999)
14. T.R. Taylor, P.J. Hansen, B. Acikel et al., *Appl. Phys. Lett.* **80**, 1978 (2002)
15. P Bao, T J Jackson and M J Lancaster, Dielectric characterization of a ferroelectric film in the sub-GHz region, *J. Phys. D: Appl. Phys.* **41** (2008) 185410

There are no physicists in the hottest parts of hell, because the existence of a 'hottest part' implies a temperature difference, and any marginally competent physicist would immediately use this to run a heat engine and make some other part of hell comfortably cool. This is obviously impossible.

Richard Davisson

That theory is worthless. It isn't even wrong!

Wolfgang Pauli

Science is facts; just as houses are made of stones, so is science made of facts; but a pile of stones is not a house and a collection of facts is not necessarily science.

Henri Poincare (1854 - 1912)

B Site Doping of PST 40/60

In section 5.2 it was discovered that the Curie temperature of PST 50/50 is too close to room temperature, resulting in increased losses due to domain switching. By decreasing the Pb-content down to 40% the transition temperature is pushed to lower temperatures. No other change in the preparation of the solution or deposition procedure is necessary, one of the big advantages of the so-gel deposition method.

It has been shown for BST that some dopants including Mg^{2+} , Ni^{2+} , Fe^{3+} , Mn^{2+} , Mn^{3+} , Co^{2+} , Co^{3+} , Al^{3+} , Cr^{3+} and Bi^{3+} , which can occupy the B site of the ABO_3 perovskite structure and behave as electron acceptors, can lower the dielectric loss, enhance the dielectric constant and thus the tunability and figure of merit [1 – 10]. For PST, being a relatively new system under increasing investigation for voltage tunable devices, only a few papers on B site doping can be found [e.g. 11 – 13] and the shown results are not very clear and satisfying. Manganese has been used in our lab to improve successfully the ferroelectric and pyroelectric properties of sol-gel derived PZT thin films [14 – 16]. The aim of the study in this chapter is to improve the material performance of PST further more by doping of the B site with manganese (Mn^{2+}), which has an ionic radius of 0.67 Å, comparable to that of Ti^{4+} (0.68 Å), and to gain a deeper understanding of the effect of doping.

6.1 Synthesis and Characterisation of $(Pb_{0.4},Sr_{0.6})(Ti_{1-x},Mn_x)O_3$

To prepare a 40/60 composition of (Pb,Sr) TiO_3 with, for example, 3 mol% of manganese, 1.591 g of lead acetate and 1.177 g of strontium acetate were dissolved in a mixture of 5 ml 1.3 propanediol and 8 ml acetic acid. Stirring and slightly heating helped to get a clear solution. Meanwhile 3.245 g of titanium butoxide and 0.0495 g of manganese acetate were mixed in a glove box and diluted with 15 ml acetic acid. Both solutions were mixed and stirred at room temperature over night. The final solution was diluted with 2-methoxyethanol up to a volume of 50 ml to adjust the concentration of the solution to 0.4 M.

The thus prepared precursor solution was deposited via spin coating onto silicon substrates using a spin speed of 3000 rpm for 30 seconds. In each trial the sample was placed on a hotplate at 350°C for 10 min to evaporate the solvents, and annealed either on a second hotplate at 700°C for 15 min or in a RTA (rapid thermal anneal) at 700°C for 2 min. The single film thickness was approximately 50 nm and to obtain thicker films the process was repeated several times.

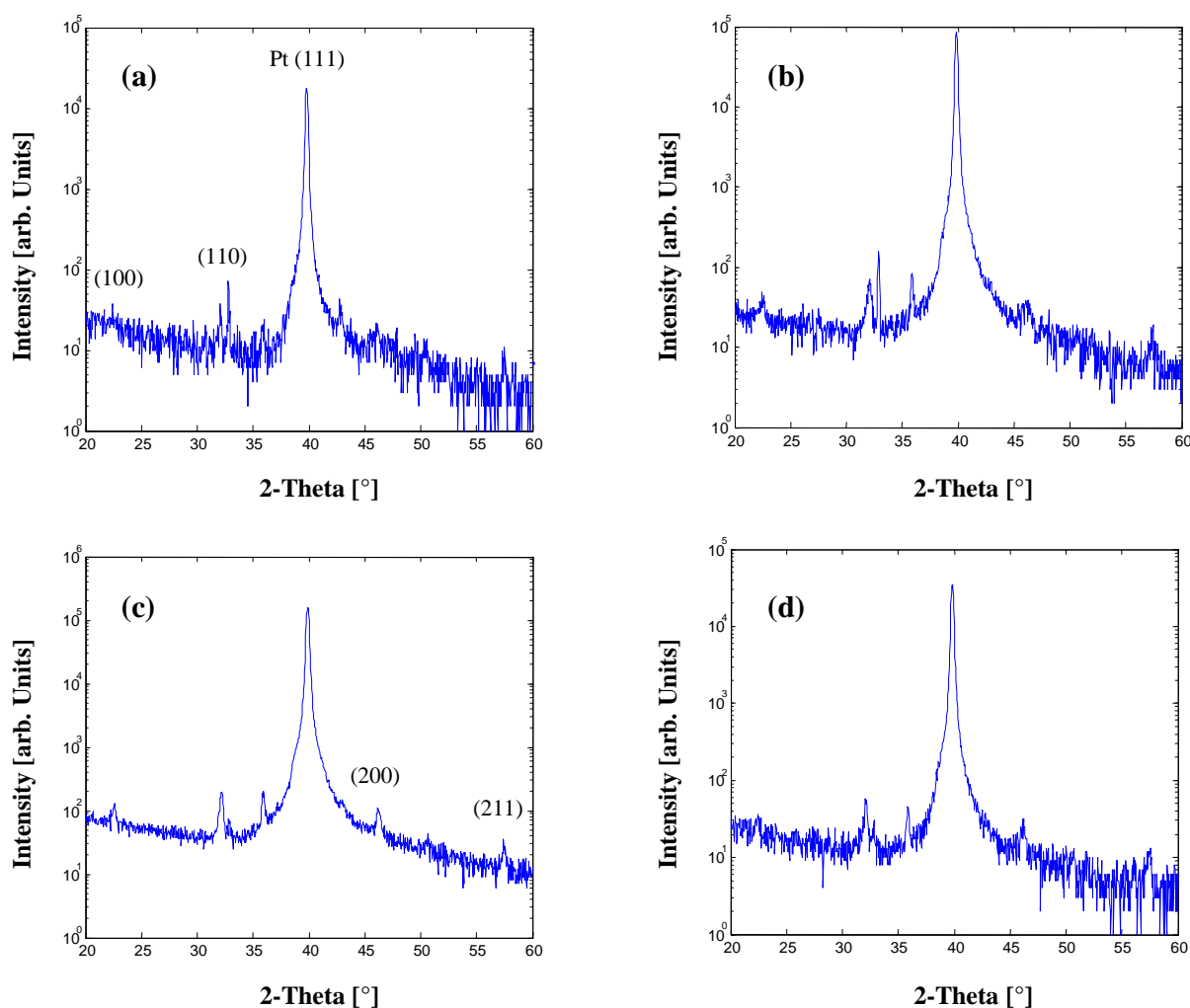


Fig. 6.1: X-ray diffractograms of $(Pb_{0.4}Sr_{0.6})(Ti_{1-x}Mn_x)O_3$. (a) $x=0$, (b) $x=0.01$, (c) $x=0.03$ and (d) $x=0.05$.

Fig. 6.1 shows the X-ray diffractograms of PST 40/60 doped with 0, 1, 3 and 5 mol% Mn. The films are randomly (100) and (110) orientated and no big differences between the different compositions are detectable. However, from the X-ray diffractograms of

section 5.1 it can be said that the films are well crystallised. SEM (Fig. 6.2) and AFM pictures (Fig. 6.3) can confirm this.

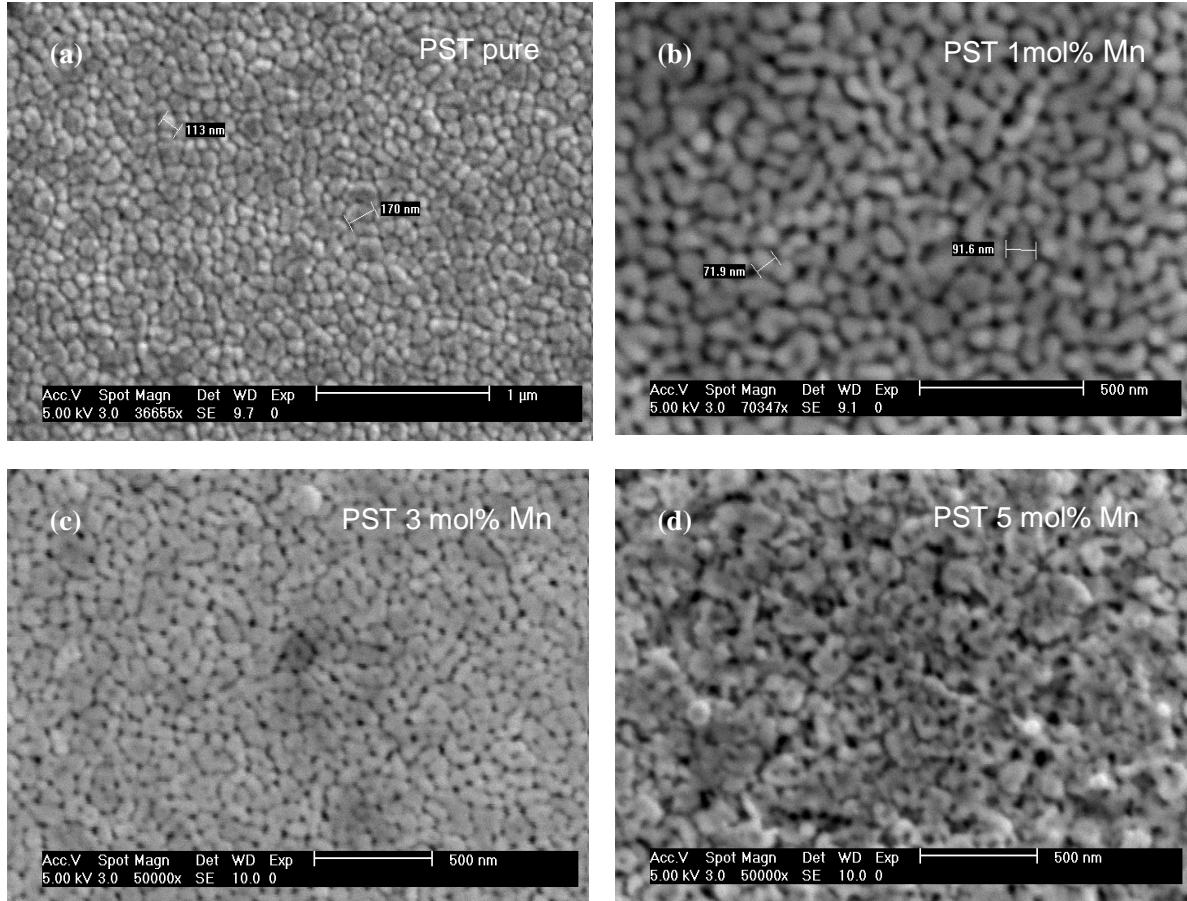


Fig. 6.2: SEM images of $(Pb_{0.4}, Sr_{0.6})(Ti_{1-x}Mn_x)O_3$. (a) $x=0$, (b) $x=0.01$, (c) $x=0.03$ and (d) $x=0.05$

It is quite obvious that the increasing Mn content has a remarkable influence on the microstructure of $(Pb,Sr)TiO_3$. The clearly visible grains in 6.2(a) have an average grain size of 150 nm. With increasing Mn content the grains become smaller, ~ 80 nm in 6.2(b), and indistinct in 6.2(c), finally in 6.2(b), the microstructure has a sponge-like appearance.

The AFM images indicate a decrease of the roughness with increasing Mn content from 3.37 nm for pure PST down to 1.69 nm for PST with 5 mol% Mn. Sun *at al.* [17] have doped the A site of BST with K^+ and showed a clear relationship between grain size/surface roughness and dielectric properties of BST thin films. Both, the roughness/grain size and dielectric constant increased with the doping level up to 7.5

mol% K^+ and decreased afterwards. However, no such relationship could be found for B site Mn doped PST, Fig. 6.4.

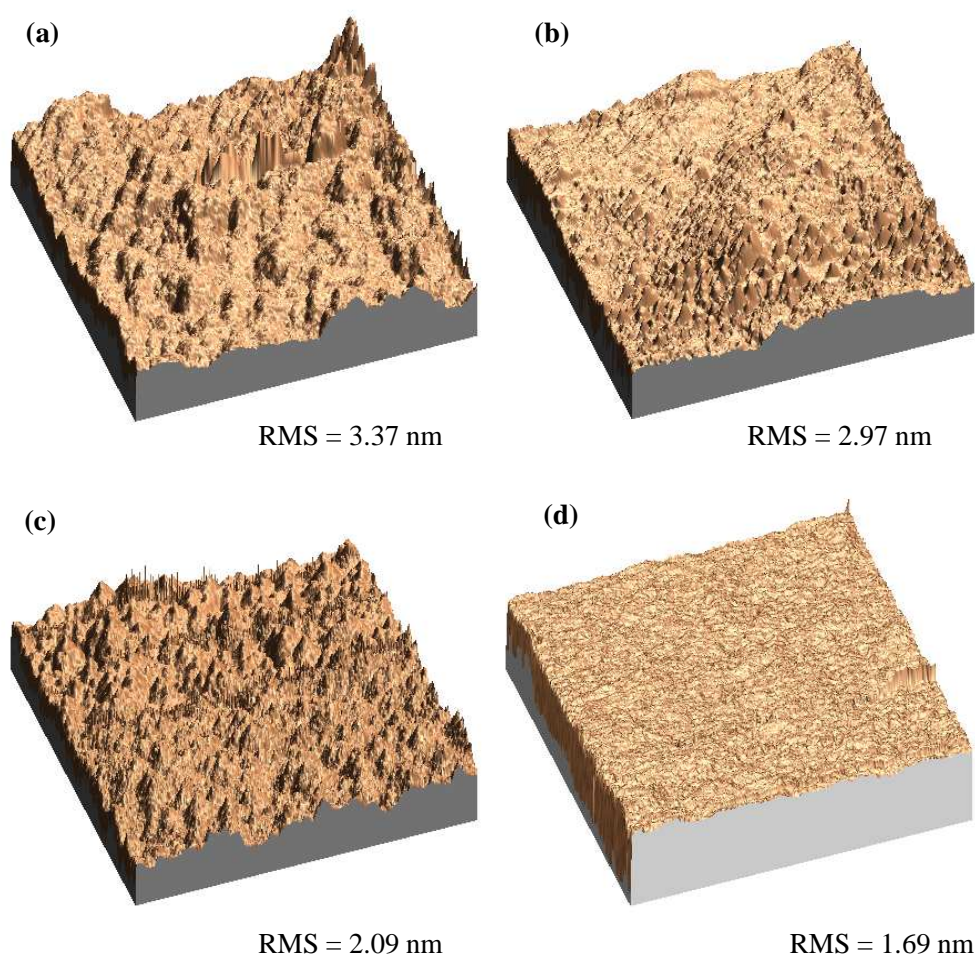


Fig. 6.3: AFM images of $(Pb_{0.4}Sr_{0.6})(Ti_{1-x}Mn_x)O_3$. (a) $x=0$, (b) $x=0.01$, (c) $x=0.03$ and (d) $x=0.05$. Scan size: $2.2 \mu m$

The dielectric constant increases with increasing Mn content viz. decreasing roughness/grain size. But there is a sharp decrease in the dielectric constant after 3 mol% Mn while the roughness/grain size is still decreasing. The dielectric constant of PST with 5 mol% Mn is even lower (~ 300) than of pure PST. Hence there is no clear evidence that the film roughness/grain size is related to the dielectric behaviour in B site doped PST like Sun *et al.* reported for A site doped BST.

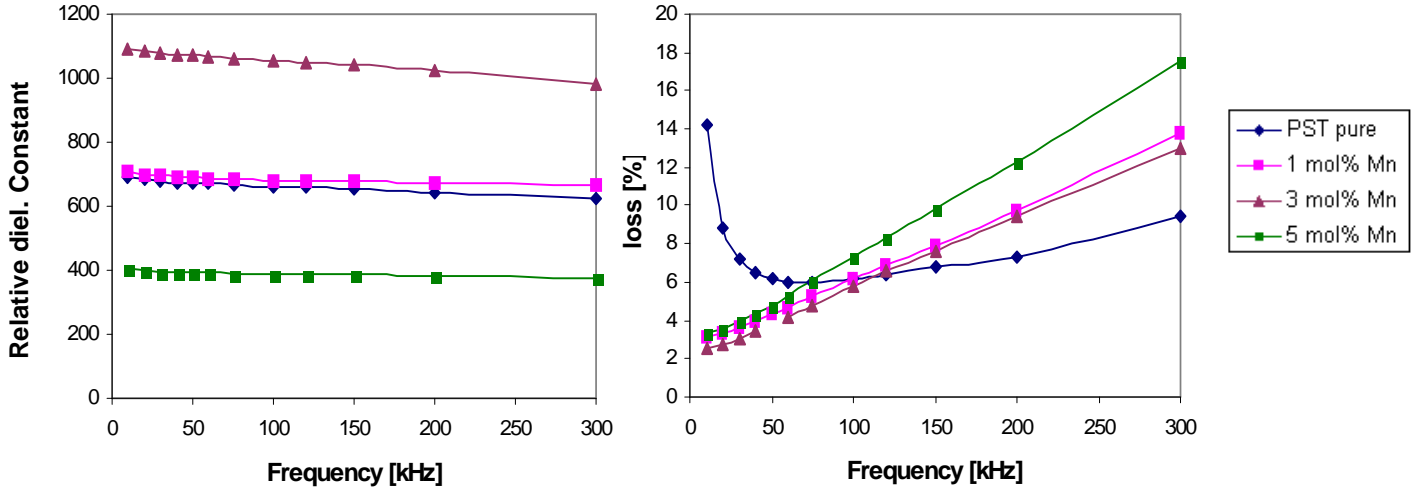
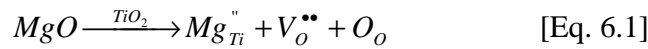


Fig. 6.4: Dielectric Constant and loss vs. frequency for PST 40/60 with different Mn content

Li *et al.* have doped the B site of PST 40/60 with Mg^{2+} [12]. They found that the dielectric constant increases with increasing doping level up to 3 mol% Mg^{2+} with a sharp decrease afterwards. They attributed this behaviour to the generation of oxygen vacancies.

Generally, oxygen vacancies are generated by heat treatment under non-oxidising atmosphere. In thin films, which were annealed in ambient atmosphere, they also form the so-called dead-layer at the interface of the bottom electrode and the ferroelectric thin film. In the case of Mg doped PST Mg^{2+} replaces Ti^{4+} in the PST lattice due to a similar ionic radii of Mg^{2+} ($r = 0.72 \text{ \AA}$) and Ti^{4+} ($r = 0.68 \text{ \AA}$), hence B site doping. The defect reaction equation can therefore be written as



where $V_O^{\bullet\bullet}$ is an oxygen vacancy with two singly positive charges³ controlled by the Mg content. That means, according to Li *et al.*: “When the Mg substitutes for Ti ion in the PST thin film system as $x < 0.03$, the positive charge of the [intrinsic] oxygen vacancies is balanced by the negative charge induced by Mg in the structure. The phase formation ability is therefore increased with increasing Mg up to 0.03. As $x > 0.03$, excessive Mg

³ Kröger-Vink nomenclature [18]: $V_O^{\bullet\bullet}$: main character: chemical species, V = vacancy; subscript: site (for example, O = regular oxygen site); superscript: charge relative to perfect lattice; •, •, x correspond to singly positive, singly negative, and neutral effective charge.

doping brings out more negative charge defects and thus excessive oxygen vacancies. The lattice distortion of the perovskite phase will increase and then the formation ability will decrease with the increase in Mg.”

In other words: proper Mg addition ($0 < x < 0.03$) in $\text{Pb}_{0.4}\text{Sr}_{0.6}\text{Mg}_x\text{Ti}_{1-x}\text{O}_3$ thin films could be used as acceptors in the ABO_3 perovskite structure. It induces a negative charge and thus balances the positive of the oxygen vacancies. Then with the charge being compensated, the lattice distortion ratio in the system decreases, viz. the lattice structure of $\text{Pb}_{0.4}\text{Sr}_{0.6}\text{Mg}_x\text{Ti}_{1-x}\text{O}_3$ becomes more perfect (cubic). According to the thermodynamic theory, the phase formation ability of the crystal is therefore increased with increasing Mg content up to 0.03. At the same time, more polarisation path may be provided when the lattice structure becomes more perfect. So the dielectric constant of the film is correspondingly increased.

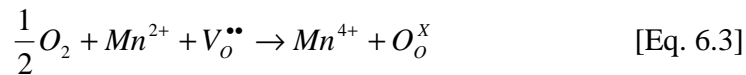
However, with further Mg doping, excessive oxygen vacancies would be created in the system. The lattice distortion ratio of the perovskite phase structure of the film would be increased and then the phase formation ability decreased. The dielectric constant is degraded with increasing Mg doping.

At first glance the explanation from Li *et al.* for the behaviour of the dielectric constant in Mg doped PST may as well fit for Mn doped PST. But Mn is a “freakish”, multivalence ion – it can appear as Mn^{2+} ($r = 0.67 \text{ \AA}$), Mn^{3+} ($r = 0.61 \text{ \AA}$) and Mn^{4+} ($r = 0.53 \text{ \AA}$), all with different impacts on the charge balance of the crystal.

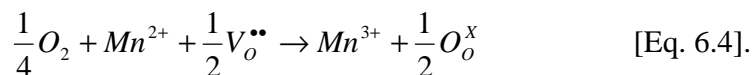
As mentioned before the ferroelectric and pyroelectric properties of PZT were improved via Mn^{2+} doping [14 – 16] in our Lab and it has been suggested that the formation of oxygen vacancies is facilitated by the conversion of Ti^{4+} to Ti^{3+}



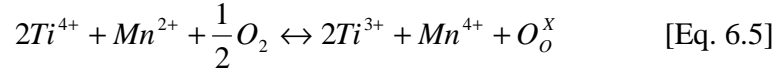
By adding Mn^{2+} ions (and some oxygen from e.g. the atmosphere) we may find



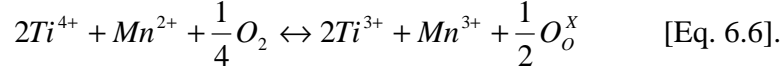
or



Combining these two reactions we obtain two possible total reactions [19]:



or



In other words: Mn^{2+} doping actually consumes oxygen vacancies in PST and may reduce the possibilities of their segregation at the electrode interface. This result is quite different from the second conclusion of Li *et al.*, where additional oxygen vacancies were created with further doping ($x > 0.03$) to balance the total system. However, the first conclusion from Li *et al.* was perfectly right, it was just seen from a different point of view.

What is happening here for $x > 0.03$? As we could see Mn^{2+} needs oxygen vacancies to get incorporated as Mn^{3+}/Mn^{4+} at the Ti^{4+} site of the $Pb_{0.4}Sr_{0.6}Mn_xTi_{1-x}O_3$ perovskite crystal structure. It is easy to imagine that, at some point, no oxygen vacancies are available anymore. J. Yang *et al.* described what happened thereafter [13]. They doped PST 50/50 thin films with up to 5 mol% Mn and investigated the dc conductivity and the dielectric response at various temperatures. Their results reveal that there are obvious hopping conductions and dielectric relaxations at low frequencies, which can only be ascribed to the thermal-activated short range hopping of localised charge carriers through trap sites separated by potential barriers with different heights, namely, localised electron hopping between Mn^{2+} , Mn^{3+} and Mn^{4+} . They specified the activation energy for the dc-conductivity and charge carrier hopping to be 0.42 and 0.47 eV, respectively. Far to low for the oxygen vacancies hopping, very common in perovskite-type oxides, whose activation energy is reported to be ~ 1 eV [20, 21].

The hopping conduction due to the hopping of the charge carriers between Mn sites begins to occur in 2 mol% Mn doped PST, and then becomes distinct in 5 mol% doped films. This type of hopping process is therefore associated with a certain amount of Mn dopant and more Mn amount can provide more pathways for the total hopping process. It has been reported elsewhere that the activation energies of carrier hopping between mixed valence Mn sites are about 0.4 – 0.5 eV in Mn doped perovskite-type oxides like $LaGaO_3$ and $Bi_3PbSr_3Ca_3Cu_4O_3$ glasses [22, 23], which is in agreement with the value

given by Yang *et al.* The evidence that there are multivalence Mn ions (namely Mn^{2+} , Mn^{3+} and Mn^{4+}) in 0.2 – 1 mol% Mn doped BaTiO_3 has been extensively observed by electron-spin-resonance spectrum [24]. Moreover Tkach *et al.* have studied Mn-doped SrTiO_3 using electron paramagnetic resonance (EPR) measurements [32] and Raman spectroscopy [33]. They found that Mn^{4+} substitutes for Ti^{4+} and Mn^{2+} for Sr^{2+} . In addition they sintered $\text{SrTi}_{0.95}\text{Mn}_{0.05}\text{TiO}_3$ ceramics in O_2 and N_2 atmosphere. Sintering in O_2 favors the formation of Mn^{4+} , whereas sintering in N_2 promotes $\text{Mn}^{2+/3+}$ on the B site, typically compensated by $V_o^{\bullet\bullet}$. However, they assumed an ionic radius of $\sim 1.27 \text{ \AA}$ for Mn^{2+} , a value which is nearly twice as much as reported elsewhere.

For the purpose of this thesis the theoretical work presented by J. Yang *et al.* is adopted and it is believed that the hopping conduction due to the hopping of the charge carriers between Mn sites lowers in the end the dielectric constant and increases the loss in PST thin films.

6.2 Enhanced Tunability and Ferroelectricity in Mn doped PST

Fig. 6.5 confirms the rule of thumb for tunable ferroelectrics “a high dielectric constant gives a high tunability”. It shows the tunability and loss vs. electric field at 150 kHz of $(\text{Pb}_{0.4},\text{Sr}_{0.6})(\text{Mn}_x,\text{Ti}_{1-x})\text{O}_3$ thin films with different Mn content. The overall loss remains under 7.5% for $x = 0, 0.01, \text{ and } 0.03$ and increases for $x = 0.05$. The increase is attributed to the hopping conduction due to the hopping of the charge carriers between Mn sites which begins to occur at $x = 0.02$. The tunability seems to reach a maximum of 78% for $x = 0.03$ and an applied field of 350 kV/cm (10.5 V).

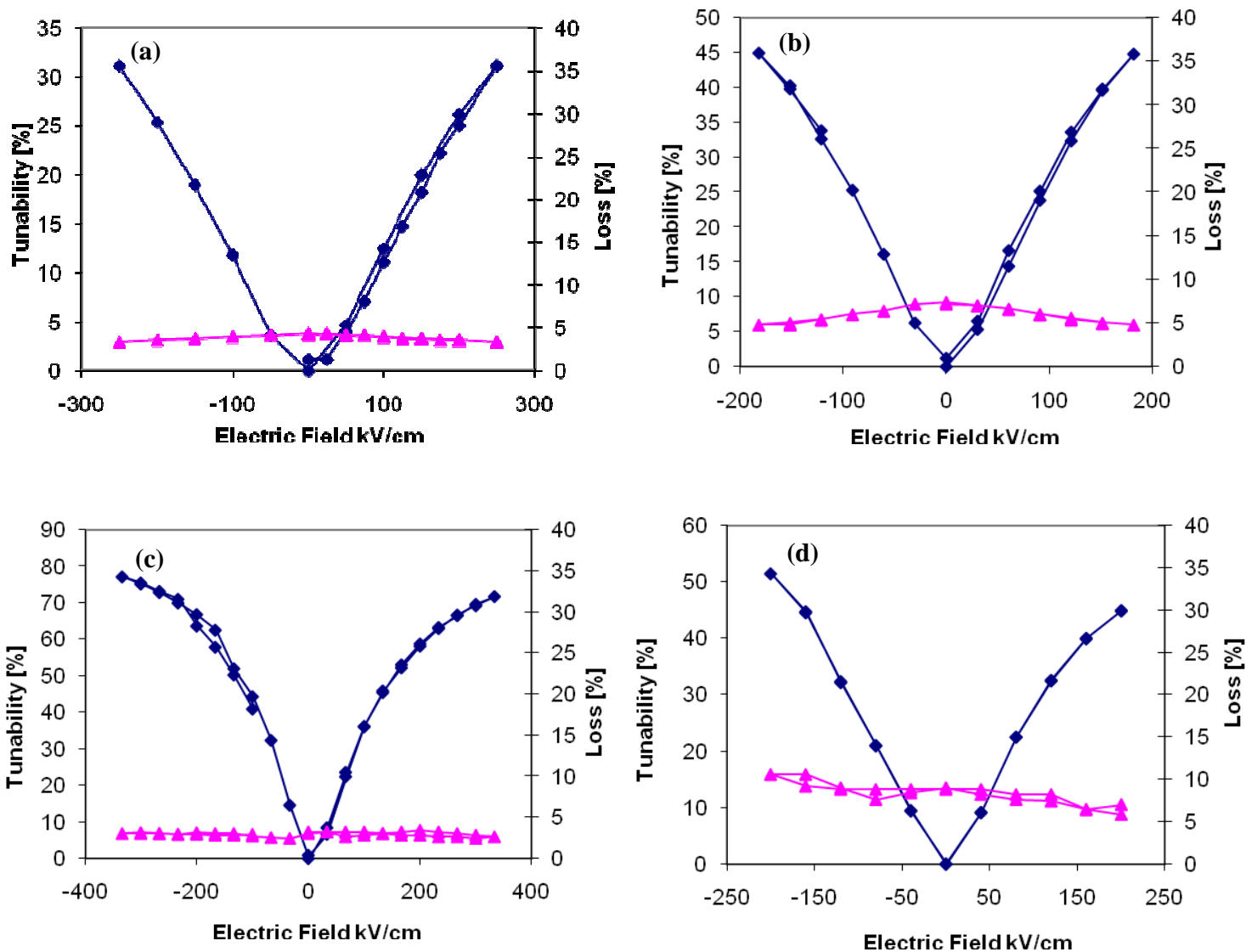


Fig. 6.5: Tunability and loss vs electric field at 150 kHz of $(\text{Pb}_{0.4},\text{Sr}_{0.6})(\text{Ti}_{1-x}\text{Mn}_x)\text{O}_3$. (a) $x=0$, (b) $x=0.01$, (c) $x=0.03$ and (d) $x=0.05$

Unfortunately the Cr/Au top electrodes of the four samples blistered away at different fields, making a direct comparison of the shown data in Fig. 6.5 rather complicated. The blistering could be a result of different adhesion strengths due to contaminations of the surface of the ferroelectric thin films prior to the deposition of the electrodes or an insufficient vacuum during the evaporation. To get a clearer picture the formula developed in section 2.1.2 was fitted to the measured data. The result is plotted in Fig. 6.6

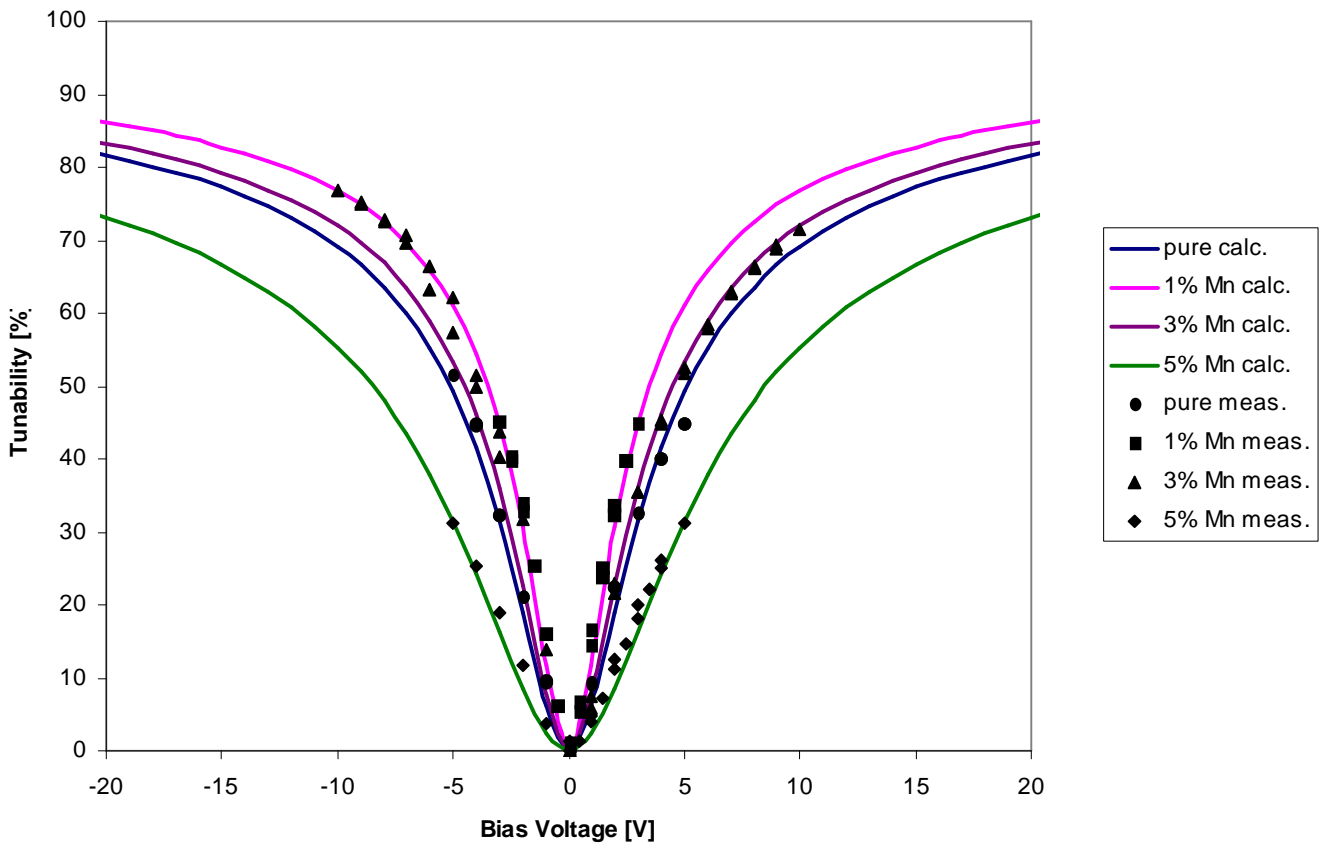


Fig. 6.6: Comparison of the measured and calculated tunability of $(\text{Pb}_{0.4}\text{Sr}_{0.6})(\text{Ti}_{1-x}\text{Mn}_x)\text{O}_3$.
The fitting parameters $C_{\max}[n\text{F}]/V_2[\text{V}]$ are: pure 9.5/5.1; 1% 15/3.5; 3% 13.8/4.5; 5% 5.7/8.5

The result shows that the tunability of $\text{Pb}_{0.4}\text{Sr}_{0.6}\text{Mn}_{0.01}\text{Ti}_{0.99}\text{O}_3$ is slightly higher than that of $\text{Pb}_{0.4}\text{Sr}_{0.6}\text{Mn}_{0.03}\text{Ti}_{0.97}\text{O}_3$. Actually no surprise as we discovered in the last section that the hopping of the charge carriers between the Mn sites begins to occur in 2 mol%

Mn doped PST. As a consequence the perovskite PST crystal is already slightly degraded with a Mn content of 3 mol%, as it can be seen in Fig. 6.2.

It is quite interesting to note that the measured behaviour of $\text{Pb}_{0.4}\text{Sr}_{0.6}\text{Mn}_{0.03}\text{Ti}_{0.97}\text{O}_3$ with negative bias is comparable to the theoretical one of $\text{Pb}_{0.4}\text{Sr}_{0.6}\text{Mn}_{0.01}\text{Ti}_{0.99}\text{O}_3$. Altogether the measured data fits better to the theoretical curves with positive bias. Maybe that indicates a systematical error in the measurements.

However, the decrease in the oxygen vacancy concentration due to the generation of higher valance Mn ions leads as well to a restraint domain pinning, and in turn to an improvement of ferroelectric properties because oxygen vacancies are always considered as the major pinning cause of ferroelectric domain wall motions [25]. The enhancement of ferroelectric properties in $\text{Pb}_{0.4}\text{Sr}_{0.6}\text{Mn}_x\text{Ti}_{1-x}\text{O}_3$ with increasing Mn content is shown in Fig. 6.7.

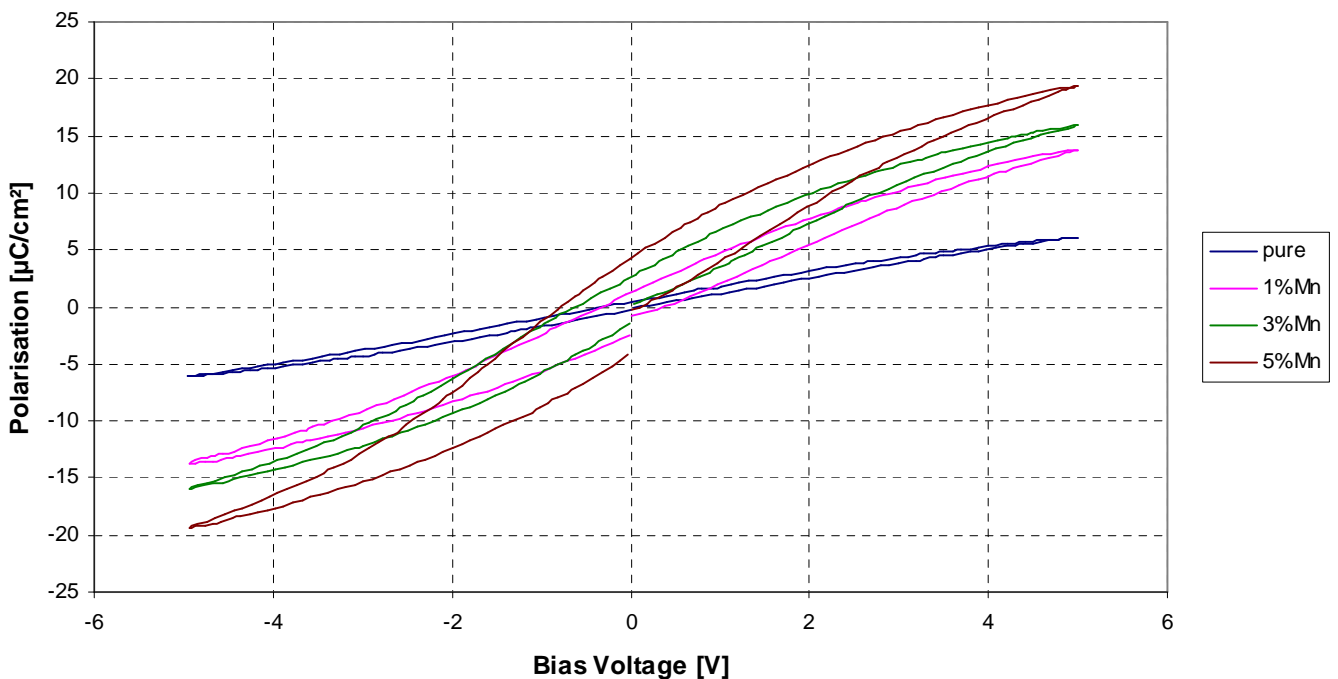


Fig. 6.7: Hysteresis loops of $\text{Pb}_{0.4}\text{Sr}_{0.6}\text{Mn}_x\text{Ti}_{1-x}\text{O}_3$. The film is paraelectric with $x=0$ and the ferroelectricity improves with x .

The polarisation-voltage hysteresis loop of pure PST 40/60 shows a typical paraelectric behaviour – a straight line at room temperature. With increasing Mn content both the

remnant polarisation and the coercive field increase indicating the enhancement of ferroelectricity. It should be noted that only the first loop of the hysteresis was measured. The hysteresis loops are very slim compared to those of real ferroelectric materials like PZT (see chapter 8) and are similar to those observed in relaxors. Relaxors are a kind of ferroelectric material in which the dielectric constant maximum does not correspond to a transition from a non-polar phase to a ferroelectric polar phase, such as observed in Lead Magnesium Niobate (PMN) [26]. The other distinct features in the relaxor ferroelectrics are frequency dispersion of the dielectric maximum, slim-loop hysteresis, and an optical isotropy at the temperatures below the dielectric maximum when there is no external field [27]. On the fundamental science side it is still a challenge to develop an understanding of the many interesting and peculiar features by this kind of materials, because the interactions responsible for the relaxor ferroelectric phenomena are on the macroscopic scale. On the application side, this class of materials offers a high dielectric constant and high electrostriction, which are attractive for a broad range of devices [27].

Hua Xu *et al.* [34] deposited $\text{Pb}_{0.5}\text{Sr}_{0.5}\text{TiO}_3$ ferroelectric films onto Pt/Ti/SiO₂/Si substrates by pulsed laser deposition. The state of the films was described as a mixed state, with both ferroelectric and relaxor-like features. The films exhibited high dielectric constant and tunability at room temperature. At 10 kHz, the dielectric constants of the 200-nm- and 400-nm-thick films were 771 and 971, with the tunability of 60.2% and 70.9%, respectively. The temperature-dependent dielectric properties were studied and the relaxor-like behavior was observed in both the thinner and thicker PST films, which could be established in terms of diffuse phase transition characteristics and Vögel–Fulcher relationship. In addition, the contribution of the film–electrode interface layer to the dielectric properties was evaluated and the true dielectric properties of the films were reconstructed. Consequently, the relaxor-like character of the PST films was mainly ascribed to the effect of the film-electrode interfaces.

That the film-electrode interface has a strong effect on the characteristic of ferroelectric thin films was already discussed in section 4.3 for BST but needs to be verified for PST as well as the relaxor-like characteristic of sol-gel derived PST. The interface between SiO₂ and PST is the topic of the next chapter.

However, measurements of the permittivity versus temperature revealed an other

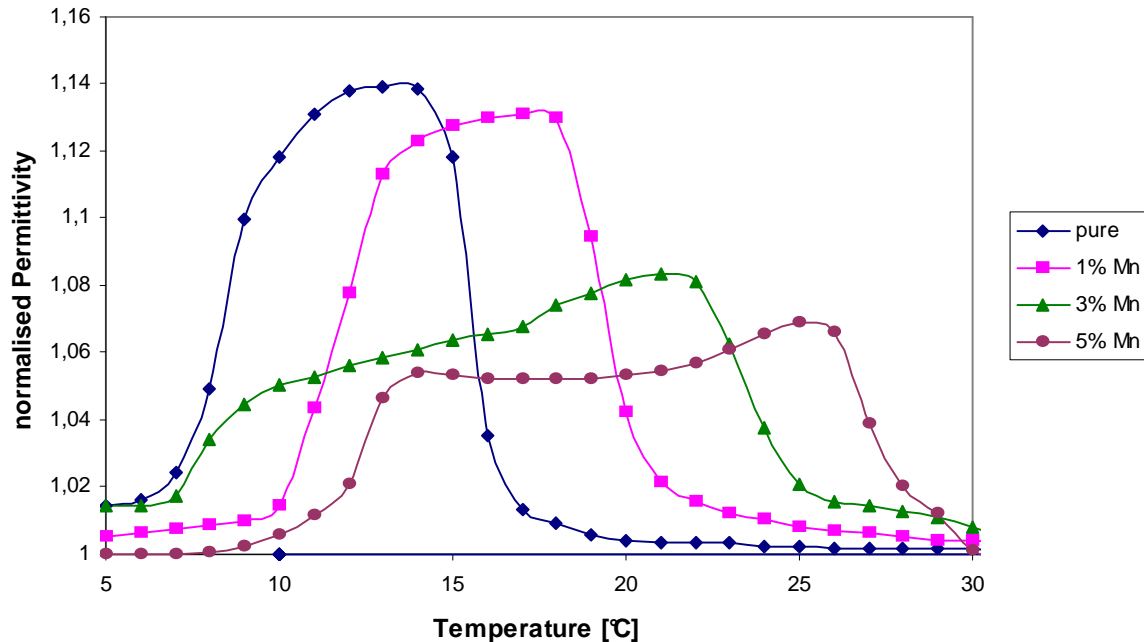


Fig. 6.8: Normalised Permittivities vs temperature of $Pb_{0.4}Sr_{0.6}Mn_xTi_{1-x}O_3$

interesting feature of Mn doped PST, Fig. 6.8.

In this graph the individual permittivities were normalised for simplicity. It shows the change of permittivity at 150 kHz with temperature of PST with a Mn content of $x = 0, 0.02, 0.03,$ and 0.05 . First of all a shift of the transition temperature to higher temperatures with increasing Mn content is clearly observable. This is contradictory to most papers which reported a shift of the Curie temperature due to doping of BST or PSZT, a mixture of PST and PZT, to lower temperatures [17, 28 – 30]. Sun *et al.*, Liou *et al.*, and Liang *et al.* [17, 28, 29] pointed out that “acceptor ions occupying the Ti^{4+} ion site result in oxygen vacancies and lead to a “break” of the cooperative vibration of the Ti-O chains and therefore shift the BST system to lower Curie temperatures”. Rema *et al.* [30] observed an increase of T_C in Mn doped PSZT for a doping level equal or less 0.1 mol% and attributed this to an incorporation of the Mn^{2+} ion into the A site of the perovskite crystal at a very low doping levels.

However, following our discussion of the decrease of the oxygen vacancy concentration due to the generation of higher valence Mn ions and the thus resulting enhancement of

ferroelectrics properties in Mn doped PST thin films, an increase of the transition temperature is only a logical consequence and proves the theory developed in the former section.

The second remarkable feature in Fig. 6.8 is the broadening of the peak for 3 mol% and the double peak for 5 mol% Mn. This could be another indication of an increasing relaxor behavior of PST with increasing Mn content. Unfortunately the home-made measuring equipment was not sensitive enough (see section 3.2.6) to measure the frequency dispersion of the dielectric maximum, which would be a clear indication of relaxor ferroelectrics.

Anyway, relaxor or not, from Fig. 6.8 it is clear why the tunability of PST doped with 5 mol% Mn is degraded. The dielectric maximum, T_C for ferroelectrics or T_m for relaxors, is higher than room temperature, ~ 25 °C, and the crystal is therefore not anymore in the paraelectric cubic state, the tunability decreases.

At the end of this chapter it is worth pointing out that localised electron hopping between mixed-valence Mn ions provides a possibility to induce double exchange effects of Mn^{2+} and Mn^{3+} or Mn^{4+} and thus brings about magnetic properties [13]. This may be the mechanism behind the magnetic effect in Mn doped $PbTiO_3$ observed by Kumar et al. [31]. The coexisting of ferroelectric and ferromagnetic properties in a single PST thin film would provide a fresh method to obtain multiferroics.

6.3 References

1. M.W. Cole, C. Hubbard, E. Ngo, M. Ervin, M. Wood, and R.G. Geyer; *J. Appl. Phys.* 92, 475 (2002)
2. P.C. Joshi and M.W. Cole; *Appl. Phys. Lett.* 77, 289 (2000)
3. M.W. Cole, W.D. Nothwang, C. Hubbard, E. Ngo, and M. Ervin; *J. Appl. Phys.* 93, 9218 (2003)
4. Y.A. Jeon, T.S. Seo, and S.G. Yoon; *Jpn. J. Appl. Phys., Part 1*, 40, 6496 (2001)
5. L. Radhapiyari, A.R. James, O.P. Thakur, and C. Prakash, *Mater. Sci. Eng., B* 117, 5 (2005)
6. M. Jain, S.B. Majumder, R.S. Katiyar, F.A. Miranda, and F.W. Vam Keuls, *Appl. Phys. Lett.* 82, 1911 (2003)

7. S.Y. Wang, B.L. Cheng, C. Wang, S.Y. Dai, H.B. Lu, Y.L. Zhou, Z.H. Chen, and G.Z. Yang, *Appl. Phys. Lett.* 84, 4116 (2004)
8. S.Y. Wang, B.L. Cheng, C. Wang, H.B. Lu, Y.L. Zhou, Z.H. Chen, and G.Z. Yang, *J. Cryst Growth* 259, 137 (2003)
9. K.B. Chong, L.B. Kong, L. Chen, L. Yan, C.Y. Tan, T. Yang, C.K. Ong, and T. Osipowicz, *J. Appl. Phys.* 95, 1416 (2004)
10. K.T. Kim and C.I. Kim, *Thin Solid Films* 472, 26 (2005)
11. P. Du, X. Li, Y. Liu, G. Han, W. Weng; *J. Europ. Ceram. Soc.* 26, 2147 (2006)
12. X.T. Li, W.L. Huo, C.L. Mak, S. Sui, W.J. Weng, G.R. Han, G. Shen, and P.Y. Du; *Mater. Chem and Phys* 108 (2008) 417-420
13. J. Yang, X.J. Meng, M.R. Shen, L. Fang, J.L. Wang, T. Lin, J.L. Sun, and J.H. Chu, *J. Appl. Phys.* 104, 104113 (2008)
14. Q. Zhang and R.W. Whatmore, *J. Appl. Phys.* 94, 5228 (2003)
15. Q. Zhang and R.W. Whatmore, *Mater. Sci. and Eng. B* 109, 136 (2004)
16. Q. Zhang, *J. Phys. D: Appl. Phys.* 37, 98 (2004)
17. X. Sun, B. Zhu, T. Liu, M. Li and X.Z. Zhao, *J. Appl. Phys.* 99, 084103 (2006)
18. F.A. Kröger, *Chemistry of Imperfect Crystals*, North-Holland, Amsterdam, 1964
19. F.W. Poulsen, *Solid State Ionics* 129 (2000) 145– 162
20. N.S. Almodovar, J. Portelles, O. Raymond, J. Heiras, and J.M. Siqueirosa, *J. Appl. Phys.* 102, 124105 (2007)
21. Z.H. Zhou, J.M. Xue, W.Z. Li, J. Wang, H. Zhu, and J.M. Miao, *J. Phys. D* 38, 642 (2005)
22. N. Noginova, G.B. Loutts, E.S. Gillman, V.A. Atsarkin, and A.A. Verevkin, *Phys. Rev. B* 63, 174414 (2001)
23. S. Bhattacharya, D.K. Modaka, P.K. Pal, and B.K. Chaudhuri, *Mater. Chem. Phys.* 68, 239 (2001)
24. X. Wang, M. Gu., B. Yang, S.N. Zhu, and W.W. Cao, *Microelectron. Eng.* 66, 855 (2003)
25. X. Wang and H. Ishiwara; *Appl. Phys. Lett.* 82, 2479 (2003)
26. G. A. Smolenskii and A. I. Agronovskaya. *Sov. Phys. Tech. Phys.*, 3, 1380 (1958)
27. L. E. Cross. *Ferroelectrics*, 76, 29 (1987)

28. J.W. Liou and B.S. Chiou, *Jpn. J. Appl. Phys.*, 36, 4359 (1997)
29. R.H. Liang, X.L. Dong, P.H. Xiang, and H.D. Li, *J. Appl. Phys.*, 43, 201 (2004)
30. K.P. Rema and V. Kumar; *J. Am. Ceram. Soc.*, 91, 164 (2008)
31. M. Kumar and K.L. Yadav, *J. Phys.: Condens. Matter.* 19, 242202 (2007)
32. V. V. Laguta, I. V. Kondakova, I. P. Bykov, M. D. Glinchuk, A. Tkatch, P. M. Vilarinho; *Phys. Rev. B: Condens. Matter Mater. Phys.* 2007, 76, 054104
33. A. Tkach, P. M. Vilarinho, A. L. Kholkin, I. M. Reany, J. Pokorny, J. Petzelt; *Chem. Mater.* 2007, 19, 6471
34. H. Xu, M. Shen, L. Fang, D. Yao and Z. Gan; *Thin Solid Films*; 493 (2005) 197

*Neutrinos, they are very small.
They have no charge and have no mass
And do not interact at all.
The earth is just a silly ball
To them, through which they simply pass,
Like dustmaids down a drafty hall
Or photons through a sheet of glass.
They snub the most exquisite gas,
Ignore the most substantial wall,
Cold shoulder steel and sounding brass,
Insult the stallion in his stall,
And, scorning barriers of class,
Infiltrate you and me. Like tall
And painless guillotines they fall
Down through our heads into the grass.
At night, they enter at Nepal
And pierce the lover and his lass
From underneath the bed—you call
It wonderful; I call it crass.*

John Updike

From TELEPHONE POLES AND OTHER POEMS, 1960

PST directly on SiO₂

Ferroelectric thin films like PZT and BST often need a metallic like layer on top of the substrate to promote a crack-free and highly orientated growth. The most common metallic layer is Pt due to its high chemical resistance, relative good lattice match to the ferroelectric film, and its stability to the high temperatures required for the growth of ferroelectric thin films. Pt is a precious material and therefore a not insignificant part of the cumulative overall costs of ferroelectric devices and applications. Moreover, sometimes it is beneficial from the technological site of view to have the ability to work with a patterned bottom electrode rather than a continuous one.

Fig. 7.1 and Fig. 7.2 show examples of realised applications with PST on a patterned Pt bottom electrode. The Ti/Pt layer was first deposited on a thermal oxidised Si substrate like described in section 3.1.1. Standard photolithography and a liftoff process were used to define the bottom electrode prior to the deposition of 500 nm $\text{Pb}_{0.4}\text{Sr}_{0.6}\text{Mn}_{0.03}\text{Ti}_{0.97}\text{O}_3$. To form the specific capacitor areas and provide access to the bottom electrode, the PST film was then patterned using a deionized water diluted HF and HCl etch solution. To protect the relevant PST areas, a Shipley S18181 photoresist mask was used, again using standard photolithography. After etching, the resist layer was dissolved with acetone. A 1.7 μm thick Nickel layer serves as top electrodes.

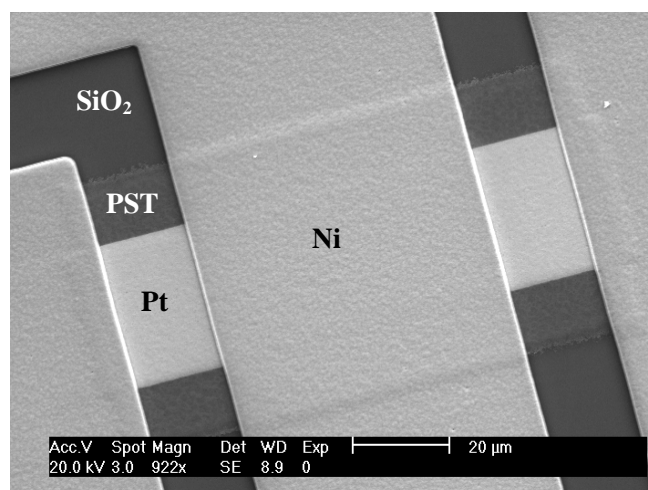


Fig. 7.1: PST on SiO₂ and a patterned Pt bottom electrode

Fig. 7.1 shows a simple design of a varactor produced this way while Fig. 7.2 shows a more sophisticated varactor design, a slotted varactor, to minimize the variation of the capacitor area due to mask alignment errors [1].

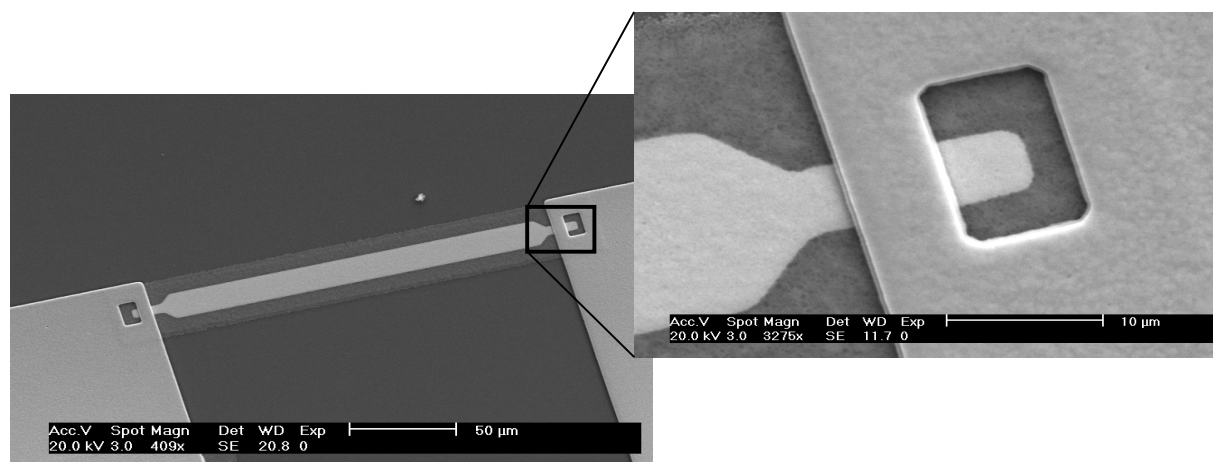


Fig. 7.2: A slotted PST varactor to minimise the variation of the capacitor areas due to mask alignment errors.

These two examples show clearly that sol-gel deposition of PST directly onto SiO₂ is possible without any limitations. In the following sections the growth of PST 40/60 doped with 3 mol% Mn directly onto SiO₂ is studied in more detail using XRD-, SEM-, AFM- and Auger analysis.

7.1 The growth of PST on SiO₂

X-ray-diffractograms of PST deposited directly onto SiO₂ and annealed at different temperatures from 350°C to 650°C are depicted in Fig. 7.3. These are diffractograms of just one layer PST (~ 40-50 nm), therefore the overall intensities are lower than in Fig. 5.3 for 6 layers. It is believed that if one layer is crystallised the subsequent layers will crystallise as well using the same deposition process, thus the study in this section is limited to one layer PST only.

It can be seen that the PST deposited directly onto SiO₂ begins to crystallise around 550°C into the (110) phase. That is approximately 50°C higher compared to PST on Ti/Pt. No other orientations of the perovskite crystal structure are visible. But that can be a result of the low intensities.

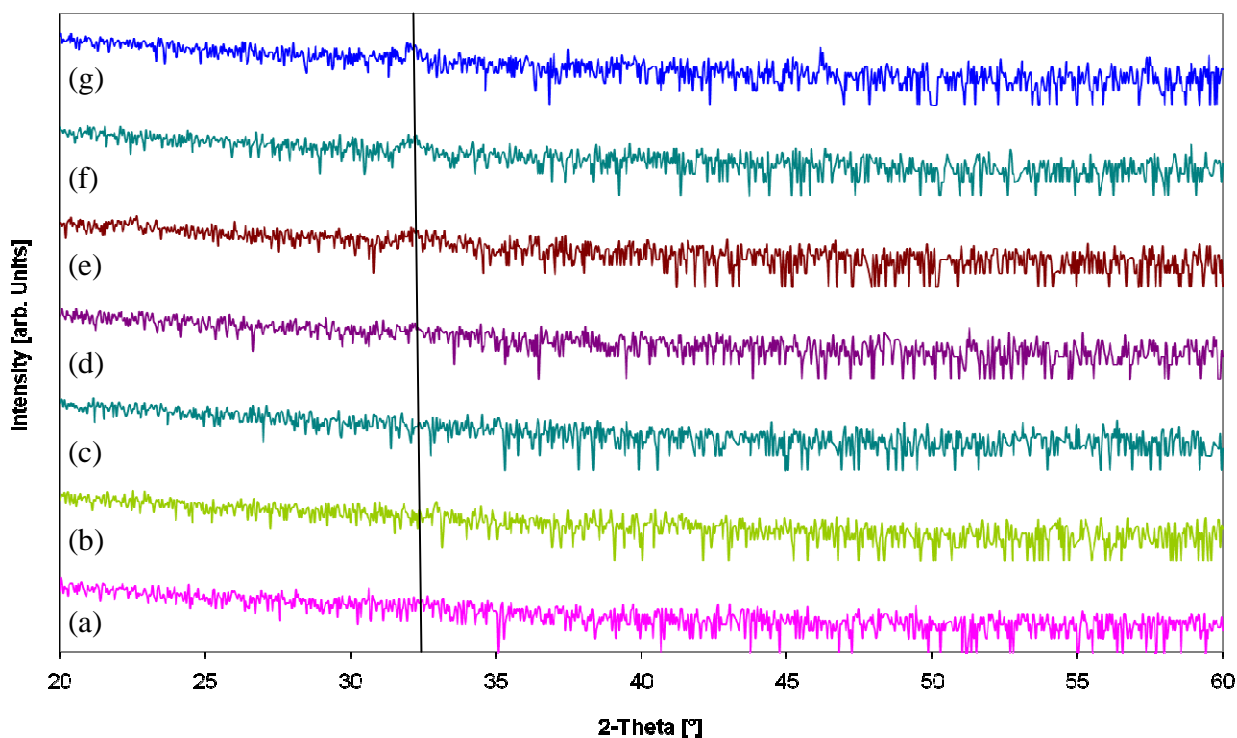


Fig. 7.3: X-ray diffractograms of one layer of PST deposited directly onto SiO_2/Si and annealed for 15 minutes at (a) 350°C, (b) 400°C, (c) 450°C, (d) 500°C, (e) 550°C, (f) 600°C and (g) 650°C.

Further information can be obtained from AFM- and SEM analysis, Fig. 7.4. The roughness is increasing with annealing temperature from 0.686 to 7.905 nm for 550 and 650 °C respectively, indicating an increase in the crystallinity. The little pools which are seen in Fig. 7.4(a) have a depth of approximately 2 nm and their number is increasing with annealing temperature while their size is clearly decreasing. This could be described by an gradual crystallisation with temperature. Finally the PST thin film can be regarded to be fully crystallised after an annealing bake of 650°C since no changes in the morphology were observable with higher temperatures up to 750°C.

Before discussing the formation of the interface, a short review of the clean silicon surface and its change due to O and Sr adsorption might be helpful. On the unreconstructed silicon surface the atoms form a square array. Owing to a lack of upper bonding partners, each atom has two singly occupied dangling bonds pointing out of the surface. Pairs of silicon atoms dimerise, using up one dangling bond per atom to form a dimer bond. This is called the “dimer row” reconstruction and is shown in Fig. 7.5(a). A

PST directly on SiO₂

second rearrangement leads to the “buckled row” reconstruction, Fig. 7.5(b), in which one atom of each dimer lifts up and the other shifts down, resulting in a buckled dimer. This buckling causes both electrons to localise in the upper silicon atom of a dimer, whereas the other silicon atom with the empty dangling bond prefers a more planar arrangement [2].

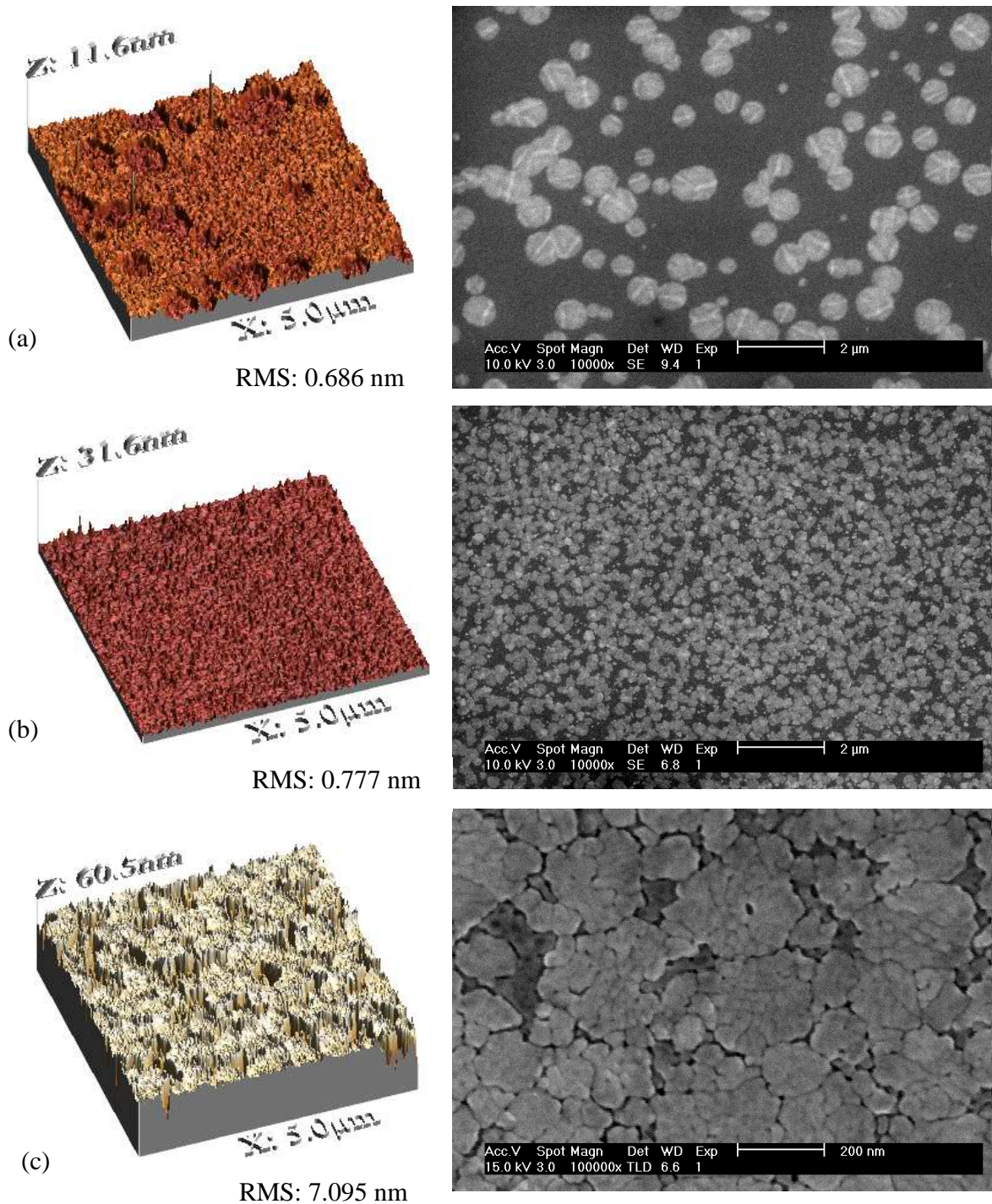


Fig. 7.4: AFM- and SEM images of PST on SiO₂/Si annealed at (a) 550°C, (b) 600°C, and (c) 650°C

Even at room temperature, the buckling pattern is dynamic, with the dimers executing a kind of "rocking" motion or oscillation around the idealized structure of Figure 7.5(a). As a result the surface dimers are chemically very reactive and can serve as receptors for certain types of atoms or even molecules.

The most common atom in nature which docks onto this structure is O, forming the native SiO₂ layer, Fig.7.6. But Sr ad-atoms will saturate the dangling bonds of one silicon dimer with its two valence electrons as well. A saturated dimer loses its buckling, since all dangling bonds are filled and both Si atoms prefer the tetragonal sp³ configuration. The Sr atom first occupies the trough between the dimer rows, in the center of four dimers.

C.J. Först *et al.* [3, 4] have simulated this adsorption process of Sr ad-atoms onto Si in more detail. The result is shown in Fig. 7.7. One of the Sr neighboring Si dimers is unbuckled due to the electron donation from the ad-atom. The others three dimers are orientated such that the upper, and thus negatively charged Si atom points towards the Sr²⁺ ion. The energy penalty for placing a lower and thus positively charged silicon atom next to a Sr ad-atom is roughly 0.4 eV. Therefore the ad-atoms pin the dimer buckling as observed experimentally [5]. The filled dimer offers a

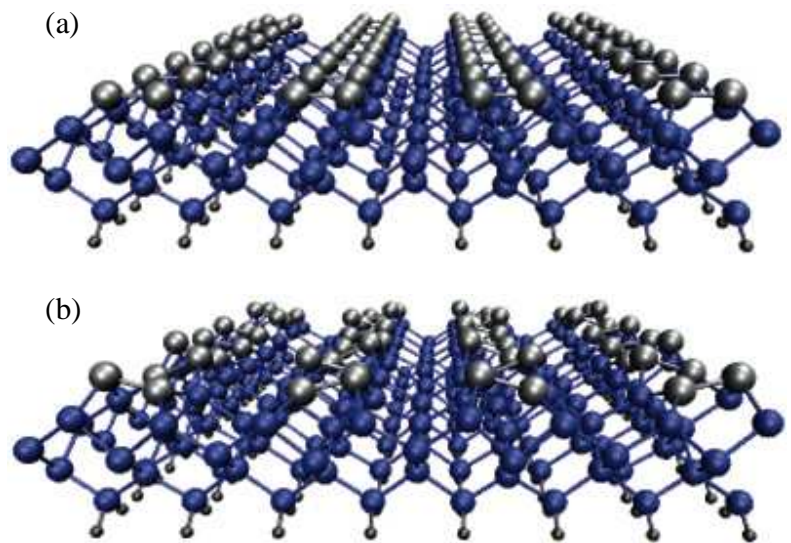


Fig. 7.5: The top surface of silicon; (a), the "dimer row" reconstruction, and (b), the "buckled row" reconstruction [2].

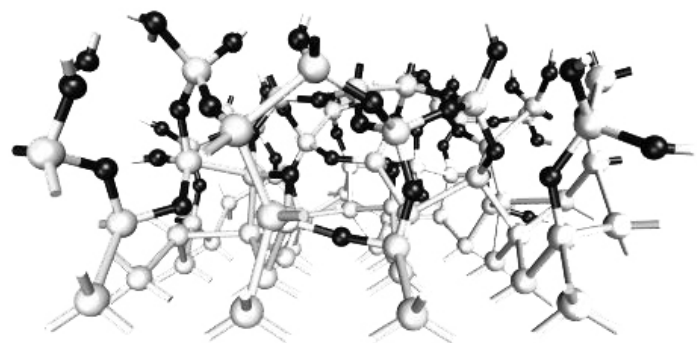


Fig. 7.6: The Si-SiO₂ interface. Black atoms are Oxygen

preferred adsorption site in the next valley as indicated by the open circle. As a result, diagonal and zig-zag chain structures turn out to be the thermodynamically stable reconstructions at low coverages. At $1/6$ monolayer these chains condense. It is not possible to stack them with a separation of only two instead of three lattice constants

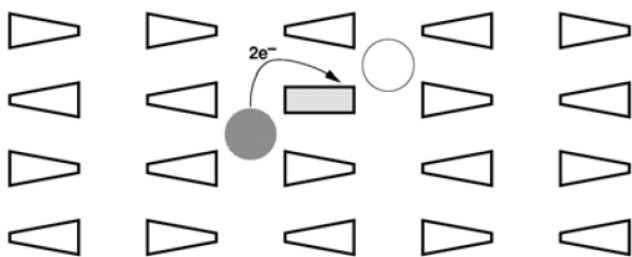


Fig. 7.7: Schematic representation of the adsorption process of a Sr ad-atom onto a silicon top surface [3].

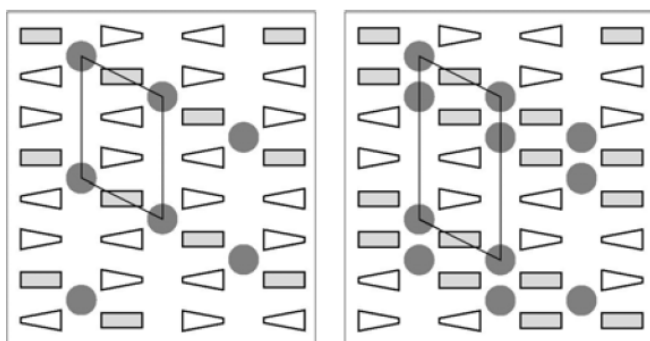


Fig. 7.8: Chain structures of Sr ad-atoms at low coverages. Left: Condensed diagonal chains of Sr at a coverage of $1/6$ ML. Right: Diagonal double chains of Sr at a coverage of $1/4$ ML [3].

Above $1/2$ monolayer, the electrons donated by Sr ad-atoms enter the dimer anti-bonding states leading to a partial breakup of the dimer bonds. At $2/3$ monolayer a reconstruction with alternating rows of Si dimers and isolated Si atoms was observed by C.J. Först *et al.*

7.1.1 The interface between SrTiO₃ and Si

The chemical bonding between silicon and SrTiO₃ is fundamentally different. While silicon is a covalently bonded material, SrTiO₃, being a perovskite, is an ionic crystal

because that would imply that the lower and thus positively charged Si atom points towards a Sr ion which involves a larger energy penalty. This is the reason for a distinct phase at a coverage of $1/6^{\text{th}}$ monolayer. The next stable phase is made of double chains at $1/4$ monolayer as shown in Fig. 7.8.

However, at one half monolayer, the Sr ad-atoms occupy all favorable positions in the center of four dimers and all dangling bonds are saturated. The surface is now isoelectronic to a hydrogen terminated silicon surface and thus is expected to be chemically comparable inert. And indeed it has been found out that the silicon surface is exceptionally inert against oxidation at $1/2$ monolayer of Sr [6].

with some covalent character in the Ti-O bonds. It is electronically saturated and unable to form covalent bonds. An electronically saturated Si-SrTiO₃ stack must thus exhibit an interfacial layer which provides a covalent bonding environment towards the silicon substrate and in addition an ionic template compatible with that of SrTiO₃. The only Sr covered surface meeting these requirements is the reconstruction at 1/2 monolayer [3, 4]. It is the only one which saturates all silicon dangling bonds and does not have surface states in the band gap of silicon. The quasi-ionic interaction of Sr with Si furthermore prepares an ionic template with a formal charge distribution as depicted in Fig. 7.9. The resulting two-dimensional ionic layer is compatible with the NaCl-type charge of a SrO-terminated SrTiO₃ crystal. The resulting structure is shown in Fig. 7.10.

Depending on growth and annealing conditions, the oxygen content of the interface can change. Oxygen can be introduced during growth, or it can diffuse in from the oxide. It first attacks the filled bonds of the silicon dimer atoms. The resulting interface structure is shown in the right panel of Figure 7.10.

Experiments have shown that there is no fundamental difference between the growth

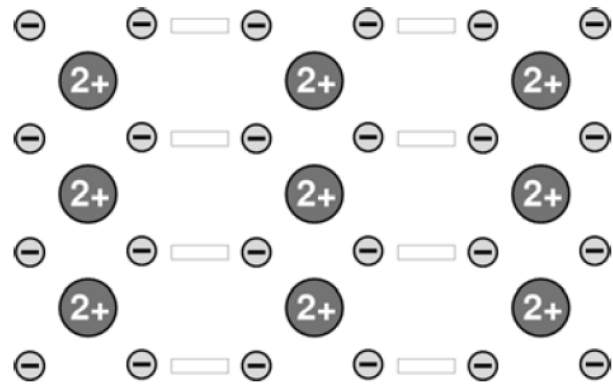


Fig. 7.9: Charge pattern of the silicon surface covered by 1/2 monolayer of Sr. The Sr ions have a formal charge of 2+, Si of 1- due to the filled dangling bond. The empty rectangles denote the dimer bond. [3]

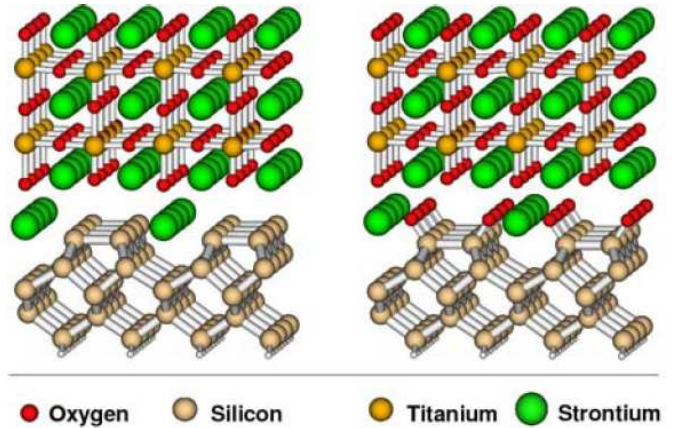


Fig. 7.10: The two relevant interface structures between silicon and SrTiO₃ [3]

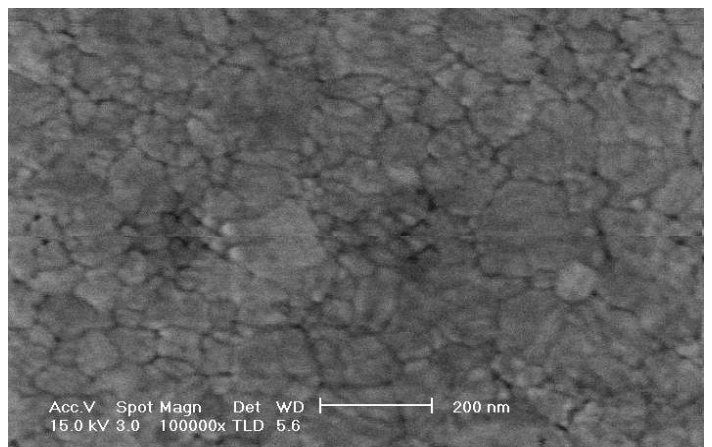


Fig. 7.11: PST directly on Si.

of PST onto SiO₂ or directly onto Si, where the native oxide was removed prior to the deposition via an HF-dip, Fig. 7.11. Furthermore, due to the well known Pb diffusion into Si or/and SiO₂, the above described formation of the interface between SrTiO₃ and Si/SiO₂ holds in first approximation for PST as well. After the interface is established, the growth of further layer of PST follows the normal observed pattern.

7.2 Auger Analysis of PST on SiO₂

Auger spectroscopy allows the study of the compositional change in thin films and the interface to the substrate. One single film of PST was deposited and annealed at 650°C on a silicon substrate with 200 nm thermal oxide. Between each measurement the sample was etched for 100 sec using the ion-sputtering unit with an ion current of 2kV and 0.75μA (1.5 mW). Fig 7.11 shows the compositional change in the PST and interfacial layer.

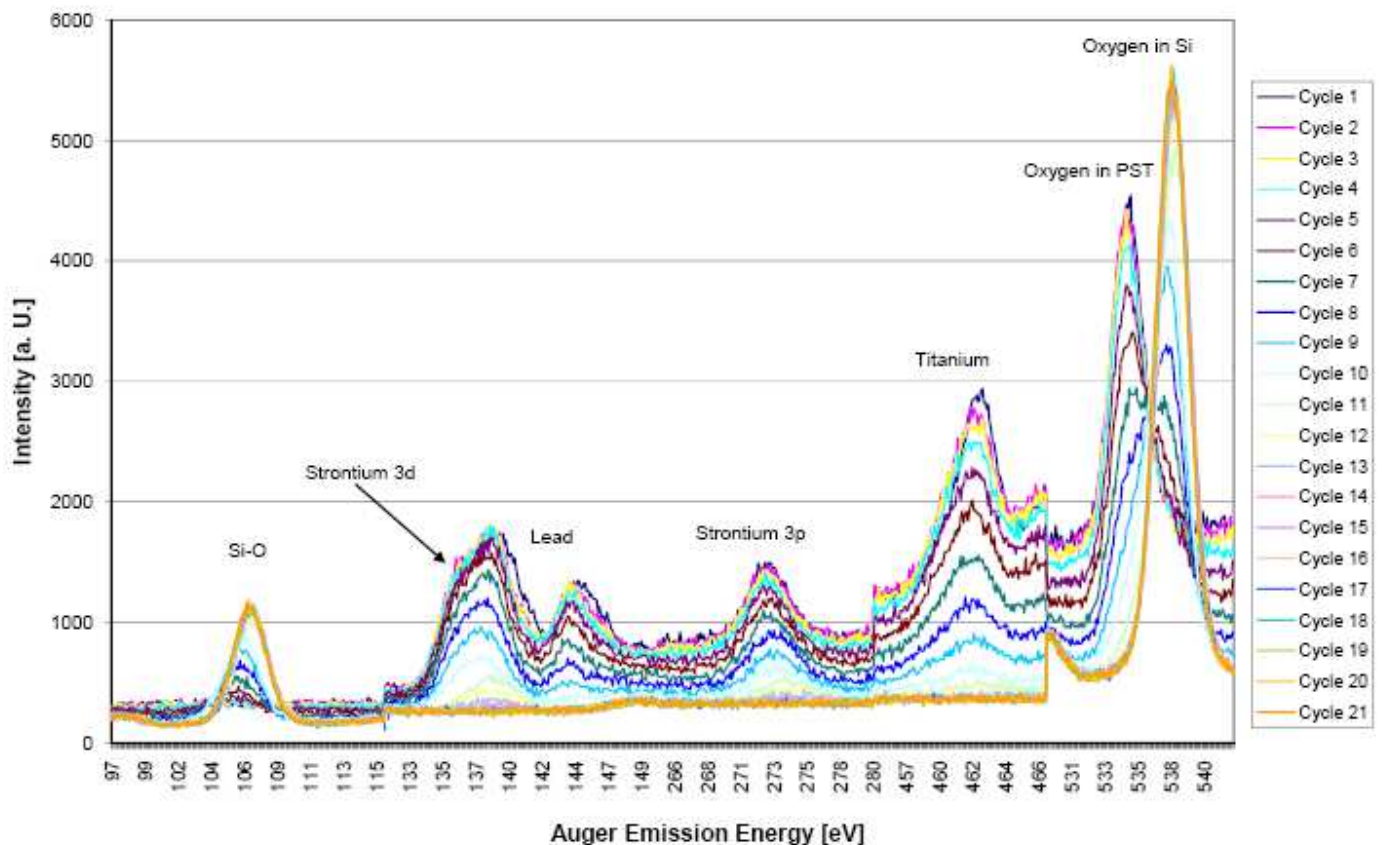


Fig. 7.11: Auger spectra of one layer PST and its interface to the Si/SiO₂ substrate

The dark blue trace, which is best seen at the top of the titanium peak at 462 eV, indicates the first measurement without an etching step. At this point only the lead peaks at 137 and 144 eV, the strontium peaks at 135 and 272 eV and the oxygen peak at 535 eV are traceable furthermore. The intensities of these peaks are decreasing with increasing etching time. After the fifth etching step (the brownish red trace) the Si-O peaks at 105 eV and 536 eV begin to appear. That marks the beginning of the interfacial layer. The position of these two peaks are shifting to higher energies and the intensities are increasing with increasing etching time while the titanium, lead, strontium and oxygen peaks of the PST layer are decreasing. Finally, after the 14th etching step (the orange trace) the PST peaks are vanished and the spectra is only governed by the Si-O peaks – the end of the interfacial layer.

The SiO₂ layer is comparable thick. Nearly forty etching steps were necessary to reach the main Si substrate as depicted in Fig. 7.12. After that only the main Si-Si bond at ~100 eV is traceable.

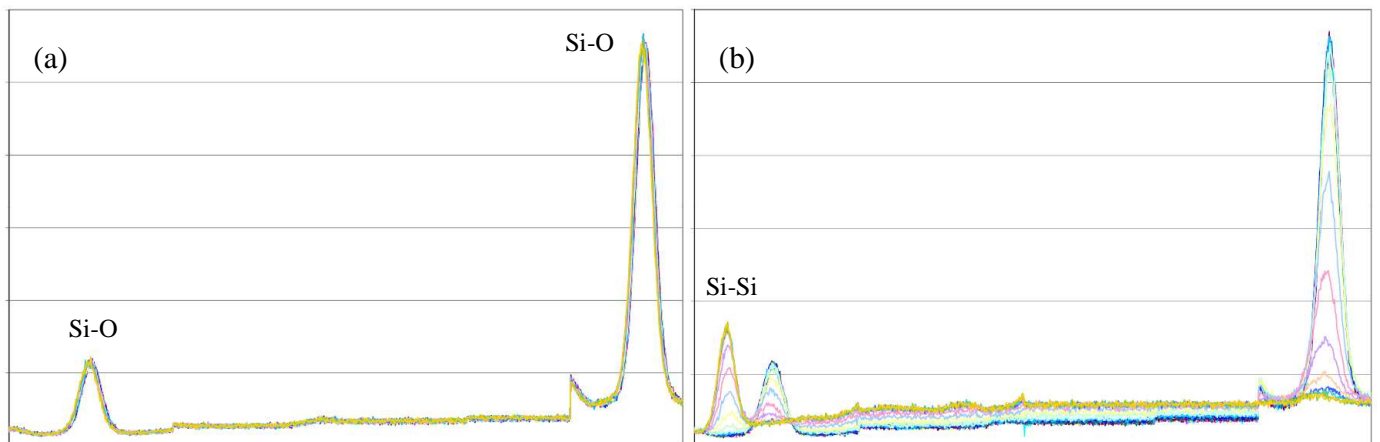


Fig. 7.12: Auger spectra of the SiO₂ layer (a) and the interface to the Si main substrate (b).

Fig. 7.13 shows the translation of these results into a depth profile. It should be noted that the unit of the abscissa is etch cycle number. Different elements and/or compounds, normally have different etch rates; therefore it is impossible to make a clear statement of the real thickness without knowing the specific etch rates. However, we know that the SiO₂ layer is 200 nm and the PST layer ~50 nm thick, leading to an etch

rate of approximately 0.029 nm/(mW·s) and 0.033 nm/(mW·s) for SiO₂ and PST respectively.

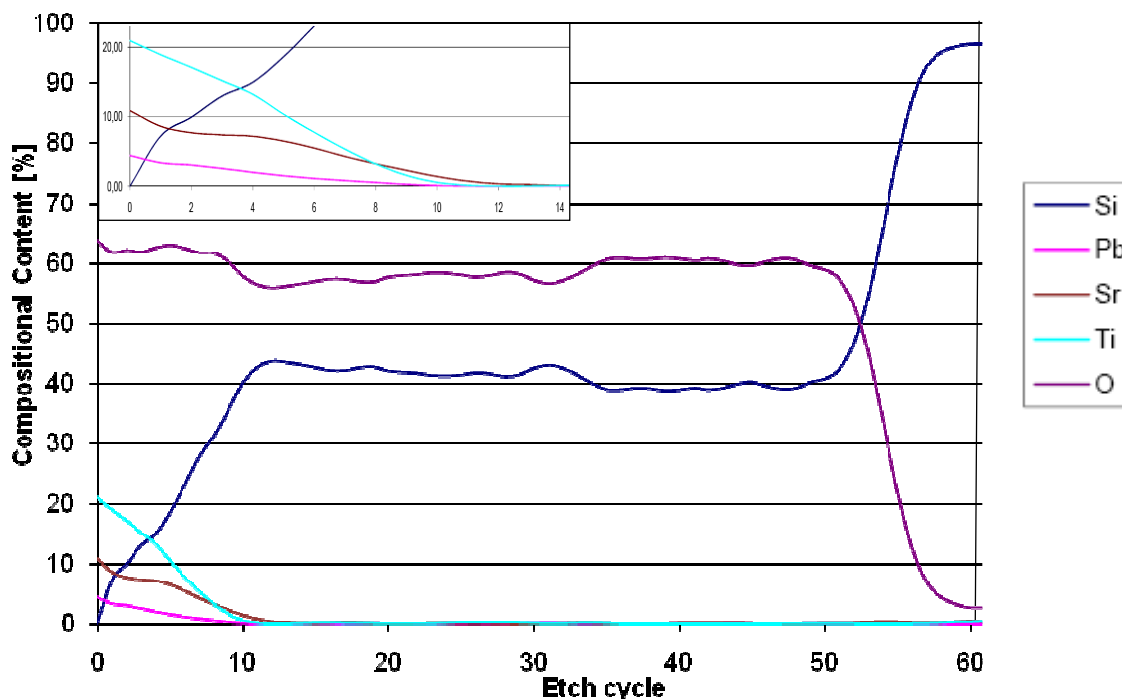


Fig. 7.13: Depth profile of one layer PST on SiO₂/Si. The interface regions are clearly visible.

The diffusion area of the PST-SiO₂ interface is relatively small. After ten etching steps the diffusion of titanium and lead stops. Only strontium diffuses further on until it is not traceable anymore after the 14th etching step (inset in Fig. 7.13). The silicon diffuses strongly into the PST layer due to the large Si-source. The broad SiO₂ area is the dominant feature in this graph and the SiO₂-Si interface is clearly distinguishable.

As a comparison a sample with a single layer of PZT directly onto SiO₂/Si was prepared. It is well known that PZT suffers from a strong lead diffusion into the substrate, therefore 10% Pb excess is normally given to the solution to compensate the Pb loss during the heat treatment of the thin film. Although PZT needs a lower annealing temperature and time ($\leq 600^{\circ}\text{C}$ for 5 min, depending on the composition) the film was annealed at 650°C for 15 min for better comparison. The depth profile of this sample is shown in Fig. 7.14.

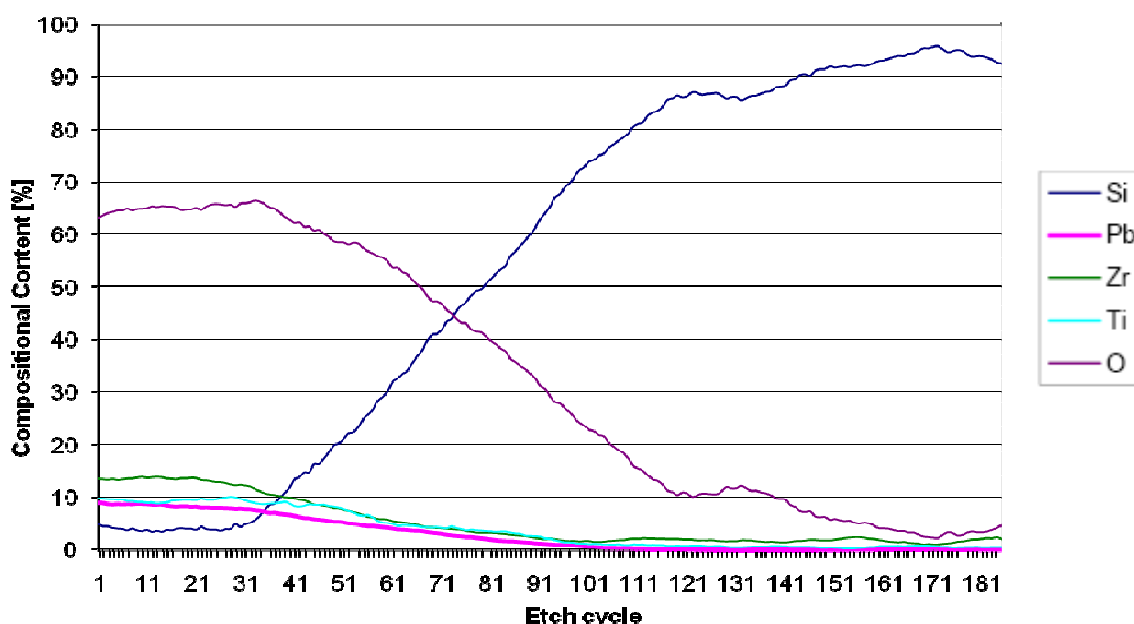


Fig. 7.14: Depth profile of one layer PZT on SiO_2/Si . The interface regions are blurred.

The etch rates in this system are considerably lower compared to the PST sample. The etching parameters were adjusted to 100 s, 2 kV and 0.9 μA (1.8 mW) for each etch step. Although that means a higher ion beam output more etch cycles were needed to reach a comparable depth. Assuming the same layer thicknesses than above this leads to an etch rate of 0.009 nm/(mW·s) for PZT and 0.012 nm/(mW·s) for the SiO_2 interdiffusion layer. The lower etch rate of the latter layer was explained by a formation of some lead silicate (PbSiO_3), which is harder to etch than SiO_2 using the ion sputtering unit [7].

Fig. 7.15 shows the details of the Auger analysis for the Pb, O and Si traces. The first two traces after etch cycles 15 and 32 (top blue and magenta in the Pb and O spectra) show that Pb and O are present in a similar way like in Fig. 7.11, viz a Pb double peak at 140 and 146 eV and an O_{PZT} peak at 536 eV. The Si is not really traceable in this region. After etch cycle 54 (thick black curve) a second O peak begins to appear at 539 eV and the Si shows two weak peaks at 102 and 107 eV. At the same time the Pb double peak moves slightly to lower energies and begins to “wobble” around with increasing depth until it vanishes after the 94th etch cycle (blue curve). After the Pb is not traceable anymore O shows only one peak at higher energy and the Si only one at lower energy.

The oxygen peak is decreasing and the Si is increasing while shifting again to higher energies with further etch cycles.

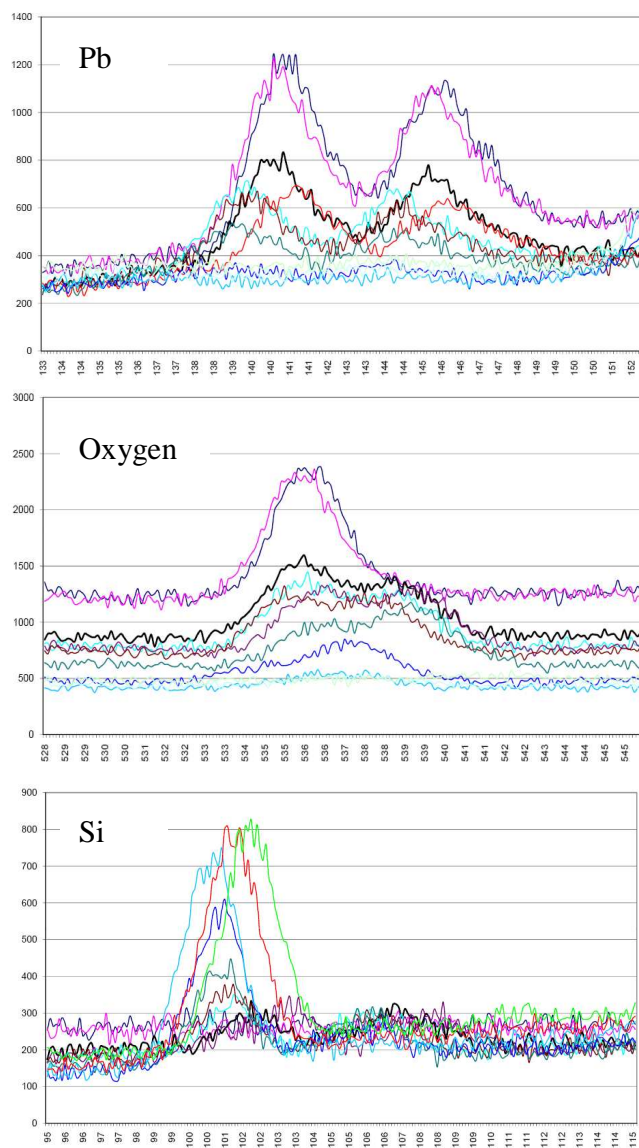


Fig. 7.15: Details of the Auger analysis for Pb, Oxygen and Si in the interfacial region of PZT on SiO₂/Si. Black, thick trace: etch cycle 54.

These results indicate that the region between the 54th and the 94th etch cycle can be regarded as the main diffusion area of these three elements. The appearance of the second O peak and the Si double peak, together with the shift of the Pb peak to lower energies indicate further on a bonding mechanism between Pb, O and Si. The rocking motion of the Pb double peak system and the disappearance of the Si peak at 107 eV may be explained by a variable stoichiometric composition of these three. The formation of some lead silicate $x\text{PbO}(1-x)\text{SiO}_2$ in this region is the most likely process to explain this behavior.

However, back to Fig. 7.13 and 7.14. As expected the Pb diffusion in the PZT system is higher than in the PST system. Sr diffuses slightly more into the SiO₂ layer than Ti in Fig. 7.13, followed by Pb, which diffusion stops almost immediately, whereas in Fig. 7.14 Pb, Zr and Ti are diffusing to the same extent. The shift of the Sr peaks in Fig. 7.11 after etch step 11, 12, and 13 to higher energies indicates

that the Sr changes its bonding partner towards SiO₂. This demonstrates that Sr grows first on top of the SiO₂ layer and makes it chemically inert to further oxidation or possible reactions with other elements, thus preventing interdiffusion in both ways. Remarkable is the missing of a clear distinct SiO₂ region in Fig. 7.14. It is assumed that

the formation of some lead silicate in this region may be a possible explanation. This would also explain the lower etching rate in the PZT-SiO₂ system.

All these results show again that the Sr content in PST is the reason for a possible growth of PST directly onto SiO₂/Si. It inhibits the interdiffusion of all components of PST into the SiO₂/Si and vice versa. These offers the possibility to realise a thin interfacial layer for future integrations of ferroelectrics in all kind of devices like non-destructive read out ferroelectric RAMs [8, 9, 10, 11] or simply as a buffer layer for the realization of PZT onto Si without the common Ti/Pt bottom electrode. This will be discussed in the next chapter.

7.3 References

1. Y-H-. Chun, C. Fragkiadakis, P. Bao, A. Lüker, R.V. Wright, J-S. Hong, P.B. Kirby, Q. Zhang, T.J. Jackson, M.J. Lancaster, “Tunable Bandstop Resonators and Filter on Si-Substrate with PST Thin Film by Sol-Gel Deposition”, 38th European Microwave Conference, EuMC2008
2. M. Tuckerman, R. Hayes; Organic Meets Inorganic *In Silico*, Chemistry in the “Virtual Laboratory”, Supercomputing at NYU, http://www.nyu.edu/its/pubs/connect/spring07/tuckerman_chemistry.html
3. C.J. Först, C.R. Asham, K. Schwarz, and P.E Blöchl, “Ab-initio simulations on growth and interface properties of epitaxial oxides on silicon”
4. C.J. Först, C.R. Asham, K. Schwarz, and P.E Blöchl, “The interface between silicon and a high-*k* oxide” Nature, 427, 53, January 2004
5. X. Xiao, X. Hu, D.Sarid, Z. Yu, J. Wang, D.S. Marshall, R. Droopad, J.K. Abrokwhah, J.A. Hallmark, and W.J. Ooms; Phys. Rev. B 59, 5115 (1999)
6. Y. Liang, S. Gan, M. Engelhard; Appl. Phys. Lett. 79, 3591 (2001)
7. Communication with Dr. Matthew Kershaw.
8. D.S. Shin, S.T. Park, H.S. Choi, I.H. Choi, and L.Y. Lee; Thin Solid Films 354 (1999) 241-255
9. M.N.K. Bhuiyan, H. Kimura, T. Tambo, and C. Tatsuyama; Appl. Surf. Sci. 249 (2005) 419-424

10. C.C. Lin, L.W. Lai, C.Y. Lin, and T.Y. Tseng; *Thin Solid Films* 515 (2006) 8005 – 8008
11. X. Hu, H. Li, Y. Liang, Y. Wei, Z. Yu, D. Marschall, J. Edwards, R. Droopad, and J. Kulik; *Appl. Phys. Lett.* 82, 203 (2003)

When you start in science, you are brainwashed into believing how careful you must be, and how difficult it is to discover things. There's something that might be called the 'graduate student syndrome'; graduate students hardly believe they can make a discovery.

Francis Harry Compton Crick

All science is either physics or stamp collecting.

Ernest Rutherford
in J. B. Birks "Rutherford at Manchester" (1962)

An experiment is a question which science poses to Nature, and a measurement is the recording of Nature's answer.

Max Planck
Scientific Autobiography and Other Papers, 1949

PST as a buffer layer for PZT on SiO₂

As mentioned previously the most common and probably studied ferroelectric thin film prepared via sol-gel today is PZT. A huge number of devices and applications, like FBARs for mobile phones, infrared detectors, sonar transducers for military but also for medical reasons and so on, have been realised with this material. As MEMS applications are concerned, a thin and flexible structural layer is employed with PZT films deposited onto it and followed by further processing to realise on-chip sensing and actuation depending on specific device design. The most commonly used structural material is an

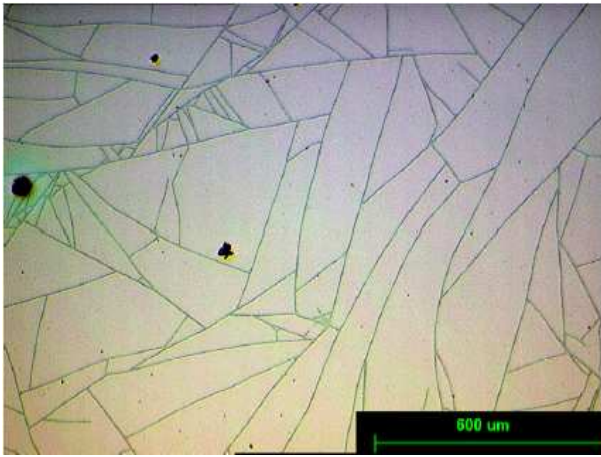


Fig. 8.1: Cracks in a PZT thin film on SiO₂/Si

active Si layer on SOI (silicon-on-insulator) wafers. Another choice is silicon nitride, Si₃N₄ (SiN_x) layer, as it can be prepared with low stress on standard Si substrates and is used as membranes in MEMS devices or LIGA applications. SiN_x as a structural layer could also provide better tunability of stress-induced pre-bending of PZT cantilever in a well-designed device structure. Ideally the PZT device structures consist of PZT thin films sandwiched

between two electrodes and usually integrated onto a Si substrate, typically resembling a planar capacitor layer design (see Appendix A). The quality of PZT thin films and its fatigue behaviour depend on various factors such as thermal compatibility of the compositional layers, their interfaces, the microstructures, crystal defects and oxygen vacancies, thereby influencing the performance and reliability of the final PZT microdevices in MEMS applications [1, 2].

A key concern in integrating ferroelectric films is the suppression of interdiffusion of the constituent elements and compositional fluctuation in multi-layer stacks forming the microdevices. It is now established that thermal stability of the electrodes is crucial for high quality growth of PZT thin film, and platinum (Pt) is widely used as a bottom electrode because of its stability and good lattice match to PZT films. In addition, Pt also provides the fleeting formation of a favourable intermetallic phase, namely Pt₃Pb,

promoting nucleation and the formation of preferred PZT (111) perovskite grains during crystallisation of PZT films on its top [3, 4]. However, a suitable diffusion barrier layer must be inserted between the bottom Pt electrode and Si substrate to limit the diffusion of lead (Pb) during PZT crystallisation at elevated temperature in an oxidising atmosphere, thereby preventing microcracks and delamination caused by Pt hillock formation [5], see Fig. 8.1 and 8.2. The buffer layer plays a significant role in improving interfaces in PZT device structures and provides better adhesion between the substrate and PZT device layers that should ensure

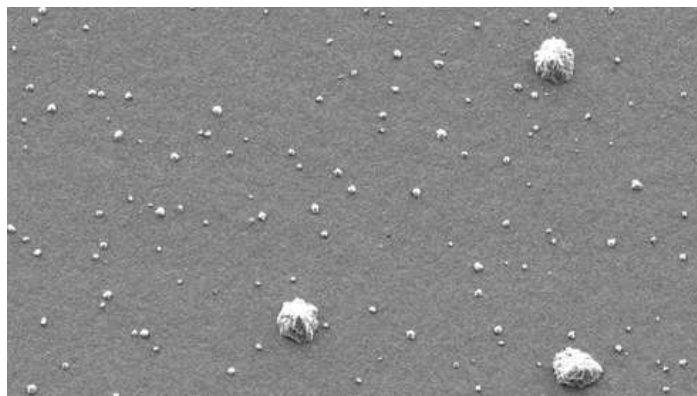


Fig. 8.2: Pt hillock formation due to high temperatures.

favourable PZT microstructures development with dense and homogeneous grain distribution [6]. It is evident that the buffer layer can influence the crystalline phase nucleation of the PZT by altering the activation energy and the nucleation temperature in PZT transducer stacks. The structural evaluation of the diffusion barrier is, therefore, necessary to optimise the PZT transducer design and enhance the piezoelectric performance of the PZT microdevices. Until recently most research studies have been considered with incorporating various oxides and intermetallic materials as the diffusion barrier layer to obtain crack-free PZT thin film on a Si and SiN_x structural layer. Barrier layers studied extensively include TiO₂, ZrO₂, Al₂O₃, Ti-Al, Ir(Pt)/TiN and LaNiO₃, produced using a wide range of deposition techniques [4, 6, 7].

The results of the last chapter are encouraging enough to study PST as a buffer layer between PZT and SiO₂. PST has a similar perovskite-type crystal structure and a lattice mismatch of only ~3% to PZT thin films [8] and it was shown here that PST crystallises crack-free into the perovskite crystal structure on SiO₂. In integrating PZT microdevices at wafer-scale, it is often desirable to deposit PZT thin films on non-uniform surface by modifying the process layout that allows patterning of the bottom Pt/Ti electrode as the first step, prior to spin-coating of PZT. This is important because patterning of the PZT transducer stacks by plasma etching from the top electrode to bottom substrate

sequentially may introduce damage to the device layers and degrade the properties of the functional materials. However there is a possibility in the modified process design that PZT may suffer from post-annealing issues such as PZT bubbling and microcracks during PZT crystallisation on non-uniform patterned Pt/Ti/SiO₂/Si substrates. A crack-free PST layer as a diffusion buffer could prevent PZT bubbling during PZT crystallisation on a patterned Si substrate and is expected to be beneficial to wafer-scale integration of the PZT microdevices. In addition, high quality PST films can be deposited cheaper with easy composition control using sol-gel technique, similar to PZT films deposition, thus reducing the process complexity, undesired damage to PZT device layers and overall process time.

8.1 XRD-Studies

In order to study the growth and quality of PZT thin films on top of a buffer PST layer, XRD analysis was carried out on a batch of samples prepared with various types of device layers. These comprised PZT films deposited directly on a PST/SiO₂/Si template and PZT on platinised Si substrates suitable for transducer design, for example PZT/Pt/Ti/PST/SiO₂/Si composites with PST barrier deposited at different annealing temperatures. As shown in Fig. 8.3, it was observed in all the various device structures

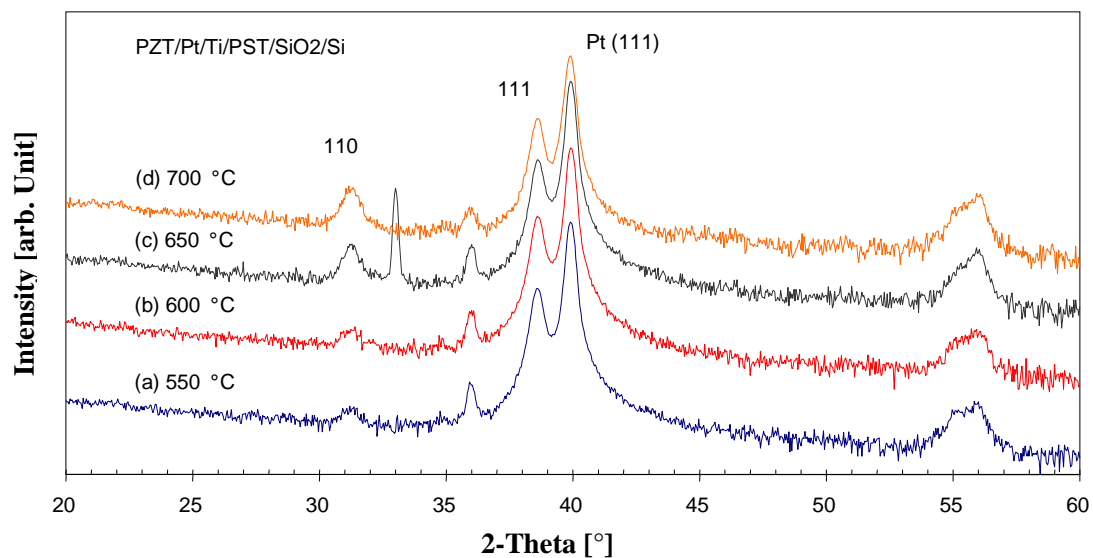


Fig. 8.3: X-ray diffractograms of PZT deposited on Pt/Ti/PST/SiO₂/Si. The PST layer was annealed at (a) 550°C, (b) 600°C, (c) 650°C, and (d) 700°C.

with bottom Pt/Ti electrode investigated here that the PZT film was preferentially (111) oriented with a less pronounced (110) orientation.

The peak intensity of PZT (110) phase was lowest from the device structure with underneath PST layer crystallised at 550°C and gradually became stronger and sharper with higher annealing temperature of PST films as depicted in Fig. 8.3(a-d). However the PZT (111) peak has still higher intensity than (110) peak in all the samples revealing the fact that the piezoelectric properties in these device structures will be dominated by the preferred perovskite (111) grains as expected with PZT film of 30/70 compositions [3]. It was further noticed that the PZT device layer with buffer PST crystallised at lower temperature of 550°C, as shown in Fig. 8.3(a), exhibited maximum intensity for preferred PZT (111) phase along with lowest intensity and broadest (110) peak compared to other samples with PST deposited at higher annealing temperatures. The phase behaviour of the PZT film was studied further on by estimating the relative intensity profile of dominant PZT (111) grains against the annealing temperature of the underlying PST layer that is expected to give an insight to the optimum crystallisation conditions for the PST diffusion barrier to promote the preferred grain orientation of the top PZT film. In one approach the relative intensity of the PZT (111) peak was calculated by setting the intensity for the PZT stacks with buffer PST deposited at 550°C as unity and normalising all other intensity profiles of PZT/Pt/Ti/PST stacks with PST deposited at higher annealing temperatures to this setting (approach 1) [9]. The relative intensity of the PZT (111) peak was also estimated by considering the impact of the Pt (111) peak on the nucleation and growth of the PZT film, e.g., $I_{rel} = I_{PZT}/(I_{Pt} + I_{PZT})$ where I_{PZT} and I_{Pt} were intensities of the PZT (111) and Pt (111) peak respectively (approach 2). The relative intensity profile of PZT as illustrated in Figure 8.4 exhibited similar nature of the plots for both types of evaluation techniques. These indicate strongest orientation of the PZT preferred (111) phase with buffer PST layer annealed at 550°C and a sharp decline in PZT (111) peak intensity at and beyond PST crystallisation temperature of 650°C. It was observed from initial XRD analysis that the crystallisation conditions of the underlying PST layer can be monitored and optimised to obtain high quality PZT films on its top. In this case annealing of PST diffusion barrier in the temperature range of 550-600°C could promote the PZT preferred (111) phase with a stronger and sharper peak and is, therefore,

expected to provide favourable growth conditions for high quality PZT device layer in PZT transducer stacks.

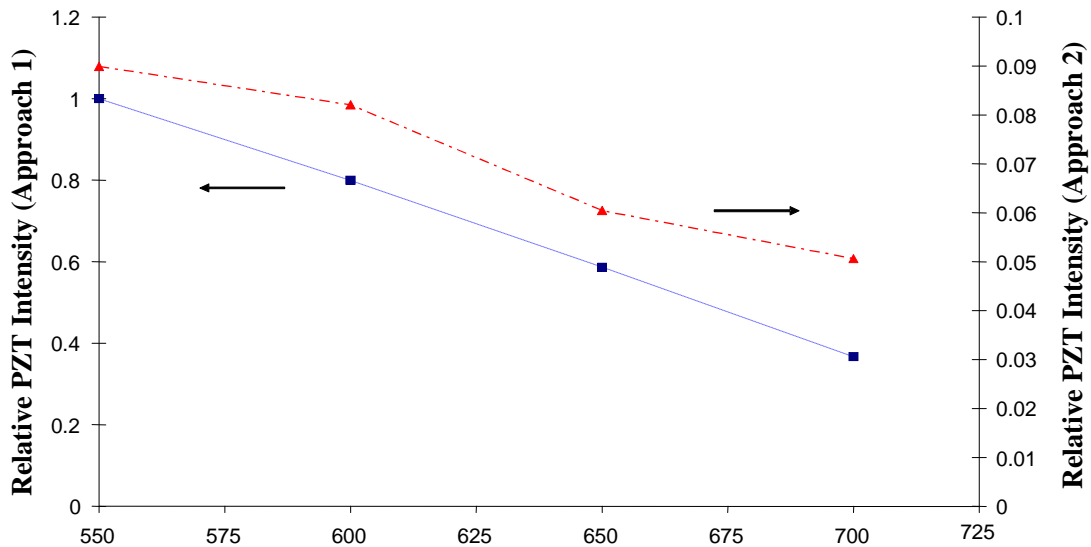


Fig. 8.4: The relative PZT (111) intensity calculated by two different approaches

A further experimental study was undertaken to compare the performance of the PST layer with other widely employed materials as a barrier in the design of PZT transducers. In this case TiO₂ was chosen as a buffer layer, as it was successfully integrated to realise PZT FBAR devices (Thin Film Bulk Acoustic Resonator) and FBAR filters for mobile phones [10]. In this study different combinations of structural layer and barrier were selected, e.g. PST/SiO₂/Si and TiO₂/SiN/Si templates with PST and TiO₂ layer deposited at 550°C and 700°C respectively to develop a better understanding of their influences on PZT microstructures and grain orientations. Fig. 8.5 (a) and (b) show XRD spectra of PZT composites without a bottom Pt/Ti electrode, produced on both types of templates with a buffer PST and TiO₂ respectively. XRD patterns of PZT stacks on both types of buffer layers exhibited similar polycrystalline nature of the PZT film having random orientations that comprised of (100), (110), (111), (200), (210) and (211) peaks and having low peak intensity. It was noted that the PZT (110) peak has slightly higher intensity compared to (100) and (111) peaks but broader, whereas the PZT (111) peak was sharper. It is evident from XRD spectra that the PZT stacks were not completely

crystallised into perovskite structures resulting in a mixture of nanocrystalline and amorphous phases in both cases. This is not quite surprising and reflects the need of a seed layer, in most cases a Pt seed layer with Pt (111) grains that enhances the PZT phase transformation introducing nucleation sites with the formation of intermetallic phase, Pt_3Pb and reducing the surface energy [3, 11].

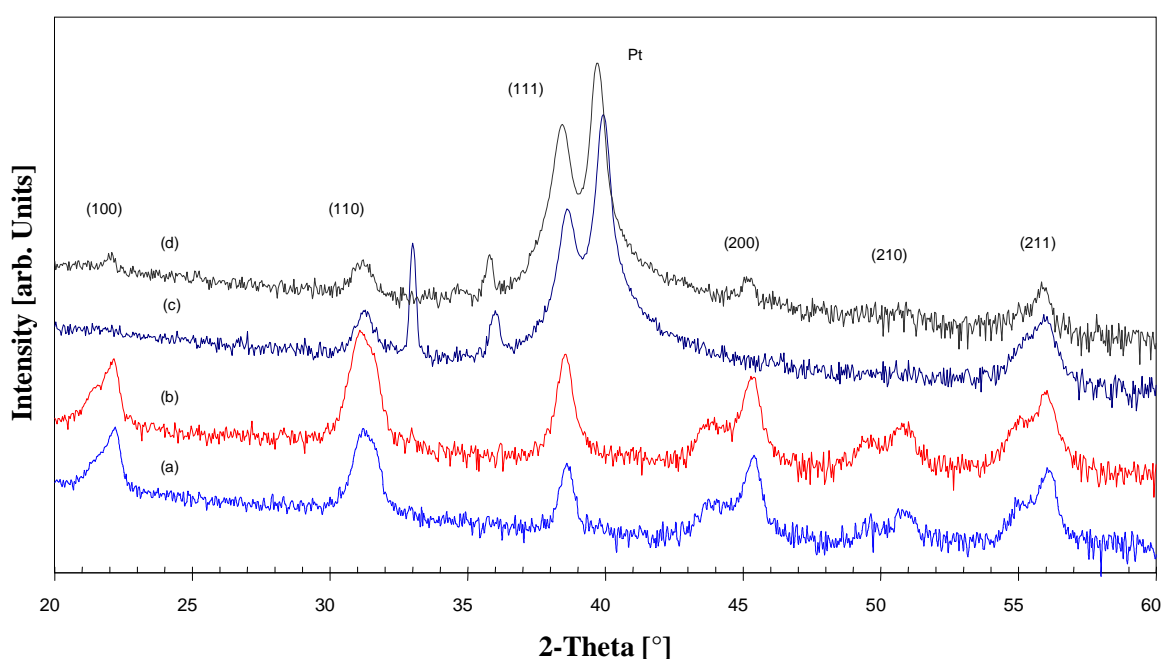


Fig.8.5: X-ray diffractograms of PZT on (a) PST/SiO_2 , (b) TiO_2/SiN , (c) $\text{Pt}/\text{PST}/\text{SiO}_2$, and (d) $\text{Pt}/\text{TiO}_2/\text{SiN}$

In fact, the XRD analysis of the PZT device structures having platinised bottom electrode along with PST and TiO_2 barrier configurations exhibited a preferred (111) phase with higher peak intensity and less preferred (110) peaks that confirmed the well-crystalline PZT grain formation. It was further noted that the $\text{PZT}/\text{Pt}/\text{Ti}/\text{TiO}_2/\text{SiN}$ stacks showed also a diminished (100) peak and introduced a slight shift in Pt (111) and PZT (111) peaks towards lower angles in contrast to $\text{PZT}/\text{Pt}/\text{Ti}/\text{PST}/\text{SiO}_2$ device structure. The relative shift in Pt and PZT peak positions reflects an incremental change in lattice parameters, when PZT films were deposited on different types of barrier layer and templates. XRD patterns of PZT films deposited on $\text{PST}/\text{Pt}/\text{Ti}/\text{Si}$ templates look very similar to those obtained from the PZT device structures incorporating barrier TiO_2 layer.

Initial results established that the PST film was perfectly crystallised in perovskite phases on different types of structural layers and templates, e.g. SiO₂/Si and SiN_x/Si under carefully controlled process conditions and promoted stronger preferred (111) PZT orientation in PZT transducer stacks.

8.2 Microstructure Evaluation

The surface morphology of the PST and PZT microstructures deposited on various types of templates were analysed using SEM and AFM methods to understand the impact of crystallisation process conditions on the film texture. Fig. 8.6 (a) and (b) show optical micrographs of the surface of PZT films to indicate again the inherent problems of PZT

bubbling and cracks across the surface, which occurred during PZT crystallisation stage following spin-coating directly on SiO₂/Si and SiN_x/Si membranes without any underlying electrode and diffusion barrier layers.

The resulting surface is very poor having discontinuities with formation of bubbles, pin-holes and cracks that are well-known phenomena due to diffusion of Pb from the sol into the SiO₂ or SiN layers during crystallisation of the PZT layer and the formation of lead silicates causing delamination. However, the PZT film often needs to be deposited directly on SiO₂/Si and SiN_x/Si templates, in particular on patterned Pt/Ti bottom electrode configuration during batch fabrication of PZT thin film devices at wafer-scale depending on specific transducer design and process layout. To prevent the crazing and delamination of the overlying electrode as

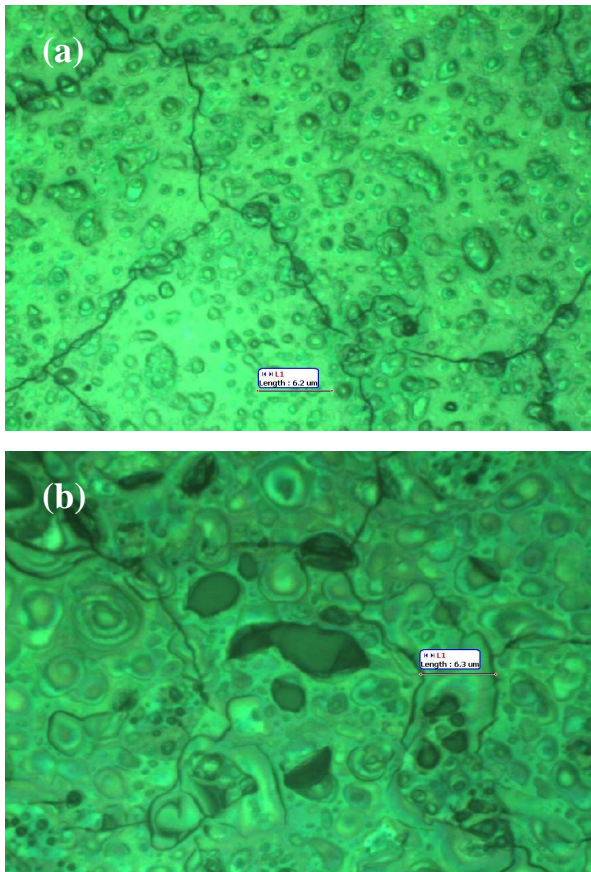


Fig. 8.6: PZT directly on (a) SiO₂ and (b) SiN_x

discussed, a suitable barrier layer is, therefore, commonly incorporated in device structures prior to PZT coating. As shown in the previous chapter for various types of PST films

deposited on SiO₂/Si substrates under different annealing conditions, the surface of the films was found to be smooth without any discontinuities in terms of crazing and microcracks, see Fig. 7.4, 7.11.

Based on these results and the finding of the last section, that the XRD analysis of the PZT/PST composites with underneath PST grown at 700°C exhibited lower peak intensity of perovskite (111) phase in comparison to PZT/PST structure with PST layer at 550°C, an AFM surface analysis of PZT films on platinised structures, i.e. Pt/Ti/PST/SiO₂/Si with buffer PST deposited at 550°C was carried out. The result is illustrated in Figure 8.7(a) and was also compared with PZT surface having the same PZT film thickness, grown on a different template, in this case a PZT/Pt/Ti/TiO₂/SiN_x/Si device structure with TiO₂ as a barrier deposited at 700°C as shown in Figure 8.7(b).

The estimated RMS surface roughness was 0.7 nm and 0.9 nm in these platinised PZT/PST/SiO₂ and PZT/TiO₂/SiN_x transducer stacks respectively. These results indicate that a homogenous film surface with lower roughness can be achieved by employing PST as a diffusion barrier in the PZT device structures, similar to commonly used barrier TiO₂ layer. The apparent variation in texture of the PZT films in these two device structures as depicted in Figure 8.7 can be explained in terms of the effect of incorporating different types of templates in device structural layer design, properties of the barrier materials, the different deposition techniques and thermal treatment of the barrier layers which altered the film density,

porosity and crystalline phase nucleation, thus having an impact on final PZT microstructures. There are several contributing factors in determining quality of the PZT

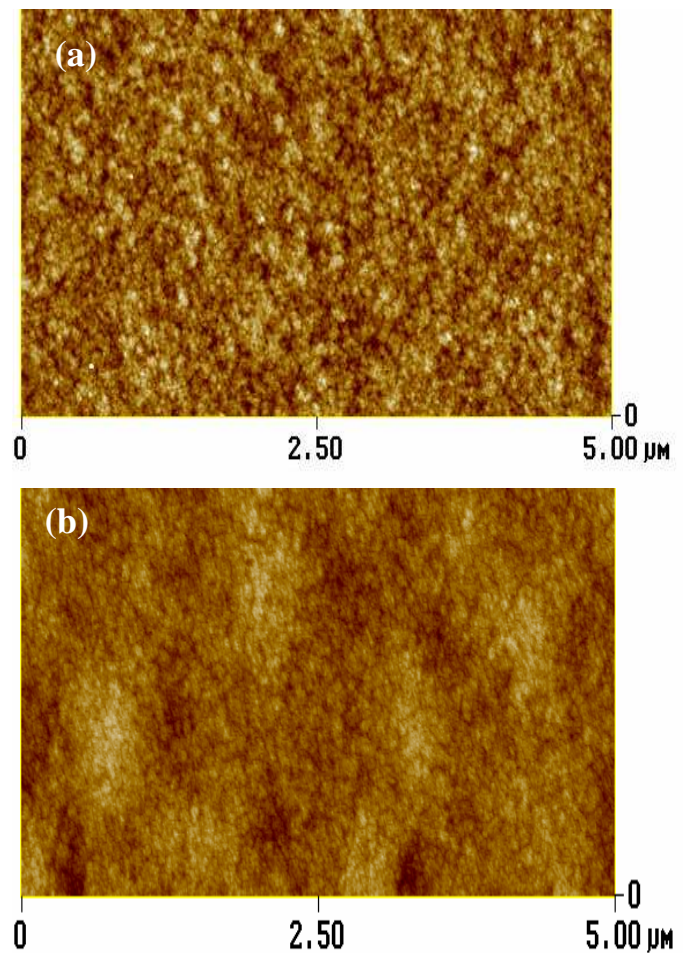


Fig. 8.7: AFM surface images of PZT on Pt/Ti on (a) PST/SiO₂/Si and (b) TiO₂/SiN. The roughness rms is (a) 0.7 and (b) 0.9 nm

device structures such as lattice mismatch and thermal expansion coefficient mismatch between the buffer PST and the substrates, and strain in the film arising during deposition process [3, 12, 13]. For example, the lattice parameter (a-axis) of PST (60/40) composition is 0.3919 nm, giving a lattice mismatch of only ~2.9% between PZT ($a = 0.4035$ nm for 111) and PST whereas the lattice mismatch between Pt ($a = 0.3923$ nm) and PST is only ~0.11% [2, 8].

A systematic analysis of thermal stress between PZT and PST films with various Sr content and the nature of the resulting stress between those two, e.g. tensile or compressive caused by the thermal treatment including its relation with porosity and film density are still required to develop an in-depth knowledge of the films and subsequently the device properties which is believed to be still ongoing. Here and now only a qualitative analysis of the PST film as a barrier focusing on the possible integration in PZT transducer stacks could be initiated and compared with other commonly used barrier materials such as TiO₂ films. The preliminary results on structural evaluation of the PZT/PST composites demonstrated that among other factors to grow high quality PZT thin films, the crystallisation temperature of the barrier PST layer plays a vital role to optimise the interfaces of substrate/barrier/electrode structures and ultimately the texture of the PZT films including its grain orientations. For example, PZT films without a seed layer often exhibit a texture consisting of rosette-like clusters that cause serious problems in the reliability of the FRAM devices due to inhomogeneous grain distribution of larger size (1-3 μm in diameter) [14]. It is therefore necessary to control the microstructure and porosity of the barrier layer that is expected to develop into a smooth textured film with fine, dense and uniform grains under optimised thermal treatment. In particular, PST possesses perovskite-type structure similar to PZT films having lower lattice mismatch to PZT and Pt layers. PST films could provide energetically favourable growth conditions producing sufficient nucleation sites during its crystallisation on Si substrates that ensure a thermally stable PZT/PST interface to grow PZT thin film on its top subsequently. A controlled thermal treatment of underneath PST layer, which looked apparently in the range of 550-600°C at onset of its crystallisation phase, could produce a crack-free smooth crystalline surface enhancing further the transformation of preferred perovskite phase of top PZT thin films without degrading the ferroelectric properties of PZT device structures.

8.3 Electrical Characterisation of PZT with a PST buffer layer

The electrical characterisation of PZT/PST device structures was performed to assess the dielectric properties and polarisation hysteresis of the PZT composites with underneath PST film deposited at 550°C. It is to be noted that the capacitor design was comprised of PZT film sandwiched between top Cr/Au and bottom Pt electrodes, and its dielectric properties should not, in principle, be affected by the PST film properties, e.g. in terms of Sr content, tetragonal-cubic phase transformation and voltage-dependent dielectric properties typically as observed in PST device structures. The electrical performance was also analysed by comparing the dielectric properties of PZT composite having similar thickness of around 0.5-0.6 μm grown on a different template, in this case PZT/Pt/Ti/TiO₂/SiN_x/Si with TiO₂ as a barrier layer. Fig. 8.8 shows the frequency dispersion of the dielectric constant (ϵ_r) and loss factor ($\tan\delta$) obtained from both types of PZT device structures.

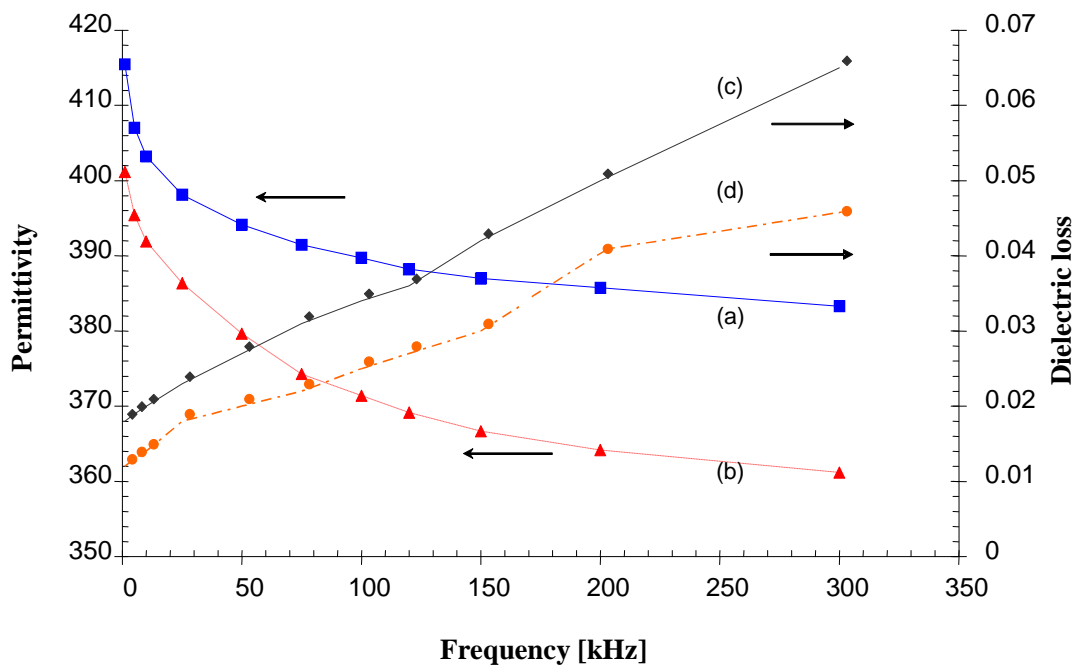


Fig. 8.8: Permittivity and dielectric loss of PZT on (a), (c) PST and (b), (d) TiO₂ as a buffer layer

The frequency range for these measurements was chosen between 1 KHz to 300 KHz applying a weak ac voltage excitation of 100 mV to preserve the polarisation state of the films. The dielectric constants in both PZT samples with buffer PST and TiO₂ layers estimated at 1 kHz were 415 and 401 respectively and are quite similar to typically observed values in PZT films of 30/70 compositions [15]. These results revealed the fact that the buffer layer, in general, does not contribute to the dielectric properties of PZT thin film capacitors. As the frequency was increased, the dielectric constants in PZT samples with different types of templates exhibited a small variation of around 5% only, for example a higher value of $\epsilon_r = 390$ at 100 KHz obtained from PZT stacks with buffer PST. This can be attributed to the interface effects produced by the different combinations of buffer layers and templates on PZT films including the lattice mismatch, thermal expansion mismatch, grain size and the possible contribution of domain structures [16]. In these particular structures under study, the PST thin film annealed at 550°C appeared to consist of mixed phases of nanocrystalline and amorphous structures, whereas TiO₂ was fully crystallised into a stable rutile phase that is expected to influence the PZT film characteristics apparently. In fact, the dielectric loss measurements as illustrated in Fig. 8.8 gave rise to similar indication of interfacial effects showing a slightly higher loss factor, $\tan\delta$ in PZT/PST structures compared to PZT/TiO₂ stacks. However the dielectric loss was not significant in either type of structures and was very low only 0.034 and 0.025 at 100 KHz in PZT/PST and PZT/TiO₂ stacks respectively showing good dielectric properties in agreement with published results obtained from typical PZT thin film devices [16, 17]. The ferroelectric behaviour of the PZT films with underneath PST was assessed by measuring the polarisation hysteresis loop as shown in Fig. 8.9. The saturation polarisation, remnant polarisation and coercive field were 39 $\mu\text{C}/\text{cm}^2$, 28 $\mu\text{C}/\text{cm}^2$ and 104 kV/cm respectively at the maximum applied voltage of 19 V which is consistent with data obtained from PZT films on standard platinised substrates [3, 15]. As the piezoelectric coefficients (d_{31} and d_{33}) are proportional to the remnant polarisation, the large value of the remnant polarisation obtained from the PZT/PST device structures is expected to produce stronger piezoelectric effect [17]. The initial characterisation of PZT device structures established that the PZT films with PST as a diffusion buffer had fully crystallized in the perovskite phase exhibiting good dielectric and ferroelectric behaviour. Although the piezoelectric

coefficients of the PZT films were not measured directly in this study, it is envisaged from the experimental data of the dielectric constant and hysteresis loop that the PZT/PST composite has potential to provide good and comparable piezoelectric performances as typically observed in PZT device structures grown on commonly used barrier layers.

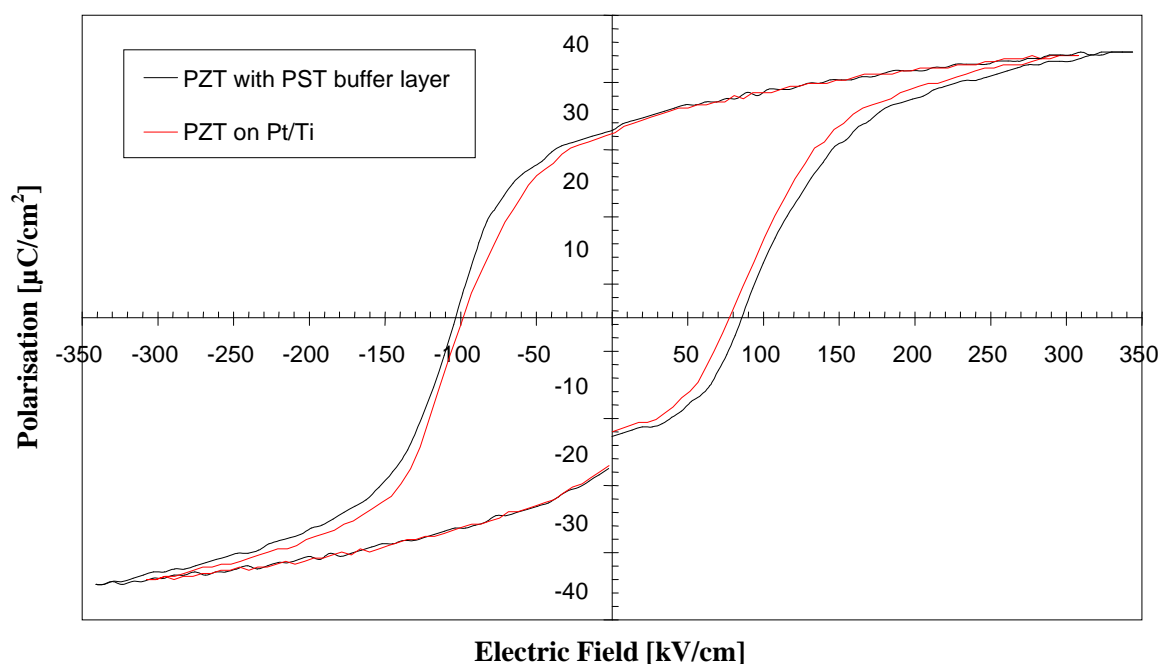


Fig. 8.9: PE-loops of PZT 30/70 on a PST buffer layer and on a common Pt/Ti bottom electrode

8.4 References

1. P. Muralt, "Texture control and seeded nucleation of nanosize structures of ferroelectric thin films" *J. Appl. Phys.*, Vol. 100, p.051605 (1-11), September, 2006.
2. K.H. Park, C.Y. Kim, Y.W. Jeong, H.K. Won, K.Y. Kim, J.S. Lee, S.T. Kim, "Microstructures and interdiffusion of Pt/Ti electrodes with respect to annealing in the oxygen ambient", *J. Material Res.*, Vol. 10 (7), p.1791-94, 1995
3. Z. Huang, Q. Zhang and R.W. Whatmore, "Low temperature crystallisation of lead zirconate titanate thin films by a sol-gel method", *J. Appl. Phys.*, Vol. 85 (10), p. 7355-61, May 1999

4. T. Maeder, L. Sagalowicz and P. Muralt, "Stabilized platinum electrodes for ferroelectric film deposition using Ti, Ta and Zr adhesion layers", *Jpn. J. Appl. Phys.*, Vol. 37 (4A), p.2007-12, 1998
5. W.W. Jung, K.S. Choi, S.Y. Kweon, S.J. Yeom, "Platinum (100) hillock growth in a Pt/Ti electrode stack for ferroelectric random access memory", *Appl. Phys. Lett.*, Vol. 83 (11), p. 2160-62, September, 2003
6. B.T. Liu, K. Maki, S. Aggarwal, B. Nagaraj, V. Nagarajan, L. Salamanca-Riba, R. Ramesh, A.M. Dhote, D. Auciello, "Low temperature integration of lead-based ferroelectric capacitors on Si with diffusion barrier layer", *Appl. Phys. Lett.*, Vol. 80 (19), p. 3599-61, May, 2002
7. B.G. Chae, Y.S. Yang, S.H. Lee, M.S. Jang, S.J. Lee, S.H. Kim, W.S. Baek, S.C. Kwon, "Comparative analysis for the crystalline and ferroelectric properties of Pb(Zr,Ti)O₃ thin films deposited on metallic LaNiO₃ and Pt electrodes", *Thin Solid Films*, Vol. 410, p.107-113, 2002
8. M. Jain, S.B. Majumder, R. Guo, A.S. Bhalla, R.S. Katiyar, "Synthesis and characterisation of lead strontium titanate thin films by sol-gel technique", *Mater. Lett.*, Vol.56, p.692-97, November 2002
9. Z. Huang, Q. Zhang and R.W. Whatmore, "The role of an intermetallic phase on the crystallisation of lead zirconate titanate in sol-gel process", *J. Mater. Sc. Lett.*, Vol. 17, p. 1157-59, 1998
10. P.B. Kirby, E. Komuro, M. Imura, Q. Zhang, Q.X. Su and R.W. Whatmore; "High frequency thin film ferroelectric acoustic resonators and filters", *Integrated Ferroelectrics*, Vol. 41 (1-4), p. 1743-52, 2001
11. S.Y. Chen and I.W. Chen, "Texture development, microstructure evaluation, and crystallisation of chemically derived PZT thin films", *J. Am. Ceram. Soc.*, Vol. 81(1), p. 97-105, January 1998
12. G.A. Rossetti, L.E. Cross K. and Kushida K., "Stress induced shift of the Curie point in epitaxial PbTiO₃ thin films", *Appl. Phys. Lett.* Vol. 59 (20), p.2524-26, November, 1991.
13. J. Zhai, X. Yao, Z. Xu, and H. Chen; "Ferroelectric properties of Pb_xSr_{1-x}TiO₃ and its compositionally graded thin films grown on the highly oriented LaNiO₃

- buffered Pt/Ti/SiO₂/Si substrates”, J. Appl. Phys., Vol. 100 (3), p.034108 (1-8), August, 2006.
14. S.H. Kim, C.E. Kim, Y.J. Oh, “Influence of Al₂O₃ diffusion barrier and PbTiO₃ seed layer on microstructural and ferroelectric characteristics of PZT thin films by sol-gel spin coating method”, Thin Solid Films, Vol. 305, p.321-326, 1997.
 15. Y.J. Song, Y. Zhu, and S.B. Desu, “Low temperature fabrication and properties of sol-gel derived (111) oriented Pb(Zr_{1-x}Ti_x)O₃ thin films”, Appl. Phys. Lett., Vol. 72 (21), p.2686-88, May, 1998
 16. Haccart, T., Cattan E. and Remiens D., “Dielectric, ferroelectric and piezoelectric properties of sputtered PZT thin films on Si substrates: influence of thin film thickness and orientation”, Semicon. Phys. Quan.Electron. & Optoelectron., Vol. 5(1), p.78-88, 2002
 17. F.M. Pontes, S.H. Leal, M.C. Santos, E.R. Leite, E. Longo, L.B. Soledade, A.J. Chiquito, M.C. Machado, and J.A. Varela; “Structural and ferroelectric properties of Pb_{1-x}Sr_xTiO₃ thin films”, Appl. Phys. A- Mater. Sc. & Process, Vol. 80 (4), p.875-80, February, 2005

Final Discussions, Conclusions and Future Work

Fig. 9.1 represents the journey we took within this work in terms of the figure of merit (FOM) and different ferroelectric perovskite thin films.

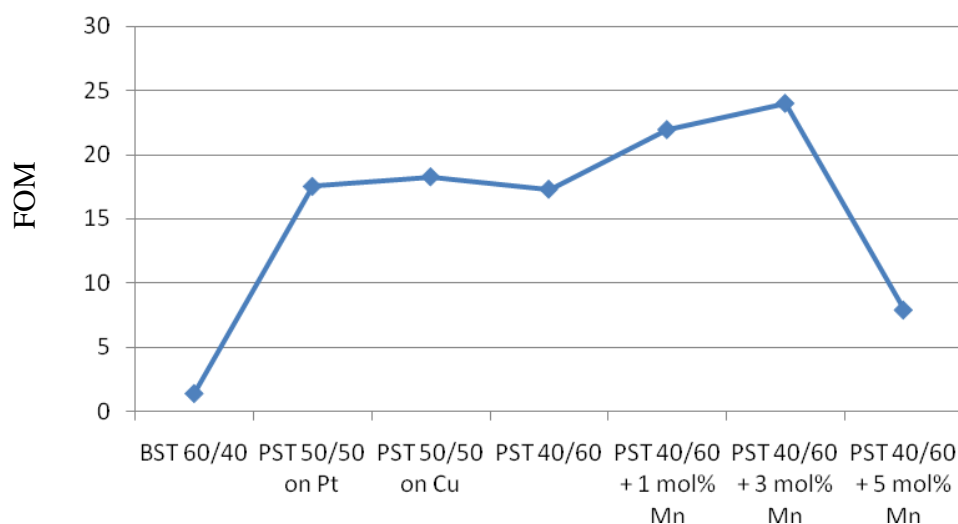


Fig. 9.1: The figure of merit of different ferroelectric perovskite thin films presented in this thesis.

We started with BST 40/60 thin films with a very low FOM of 1.4 which is a result of severe film cracking during the high temperature annealing bake. With the change to PST 50/50, a system which is very friendly in terms of film cracking, the FOM increased rapidly up to a value of 16.6. A small improvement of 1.65 could be made with the change of the electrode from Pt to Cu. This was explained with the lower resistivity of Cu which increased the quality factor of the overall material system. But it was observed that the response of PST 50/50 to an applied electric field showed a hysteresis (see fig. 5.9) indicating that the thin film is in the ferroelectric tetragonal state with a permanent electric dipole moment which in turn increases the loss. By decreasing the Pb content down to 40% the Curie temperature was ensured to be below room temperature viz. the film was in the favoured paraelectric state without a permanent dipole moment. However, the FOM decreased slightly. Doping of the B site with Mn altered the charge balance inside the perovskite film.

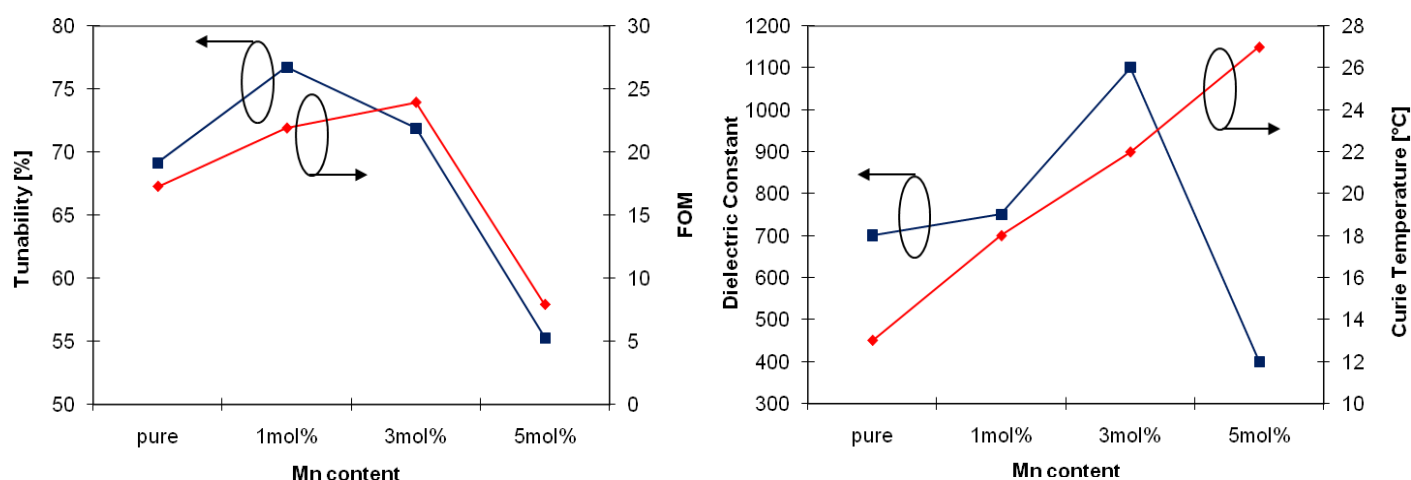


Fig. 9.2: Tunability and figure of merit at 10V and dielectric constant and Curie temperature at zero bias of PST 40/60 with different Mn content

Fig. 9.2 summarises the effect of Mn doping in more detail. The dielectric constant reaches a maximum of 1100 with 3 mol% Mn; the maximum value of the tunability with 10 V is 76.72% with 1 mol% Mn and the FOM reaches 23.96 with 3 mol% Mn. This compares well with results from Du *et al.* [1], who reported a tunability of 80% and a FOM of 14.17 in pure PST 40/60 and 70% and 7 in La doped PST, or Sun *et al.* [2], who achieved a tunability of 69.4% and a FOM of 28.9 in $(\text{Pb}_{0.25}\text{Ba}_{0.05}\text{Sr}_{0.7})\text{TiO}_3$.

All these values drop significantly when the Mn doping level exceeds 3 mol% and we identified two possible reasons for this behaviour. First, Mn^{2+} doping consumes oxygen vacancies to get incorporated as Mn^{3+} and/or Mn^{4+} at the Ti^{4+} site of the (Pb,Sr) TiO_3 perovskite crystal structure. The negative charged Mn ions balance the positive induced charge of the oxygen vacancies leading to a more “perfect” (cubic) and electronically saturated perovskite. At the same time, more polarisation path may be provided when the lattice structure becomes more perfect. This results in an increase of the dielectric constant, tunability and FOM.

At a doping level of 2 mol% Mn the crystal is totally saturated. With further doping a hopping conduction due to the hopping of the charge carriers between Mn sites begins to occur and becomes distinct in 5 mol% doped films. This type of hopping process is therefore associated with a certain amount of Mn dopant and more Mn amount can

provide more pathways for the total hopping process. The dielectric constant, tunability and FOM decrease.

On the other hand the transition temperature from cubic paraelectric to tetragonal ferroelectric increases with increasing Mn content as it can be seen in Fig 9.2. The Curie temperature is above room temperature with a doping level of 5 mol% resulting in an increased loss mechanism due to the permanent electric dipole moment of the ferroelectric state. This influences the tunability and FOM significantly. Hysteresis measurements show the effect of an enhanced ferroelectric characteristic in Mn doped PST and give rise to the question whether a relaxor like behaviour is also observable or not.

All these results indicate that PST 40/60 with an Mn content of 2 mol% should result in an optimal ferroelectric thin film for voltage tunable frequency agile applications at room temperature. In combination with Cu electrodes such a device should have superior performance with a very high quality factor.

PST was successfully deposited directly onto SiO₂. This is an important and interesting feature of this perovskite thin film since similar films like PZT or BST blister without an additional seed layer. Pt is the most common metallic layer on which these films crystallise well. It is chemically robust and withstands high temperatures needed for the crystallisation of ferroelectrics. The drawback is the price of this noble material and the relatively high electrical resistivity. The Sr content in PST makes it possible to grow this ferroelectric thin film on SiO₂, SiN_x and even bare Si. While Si is a covalently bonded material, PST is an ionic crystal that is unable to form covalent bonds. An electronically saturated Si-PST stack must thus exhibit an interfacial layer which provides a covalent bonding environment towards the silicon substrate and in addition an ionic template compatible with that of PST or SrTiO₃. SrO covalently saturates all Si dangling bonds by forming SrSiO₃ and/or Sr₂SiO₄. This provides the necessary ionic template towards the perovskite SrO-terminated SrTiO₃, on which PST can grow further on. Up to now it is unclear why this is not the case for BST, which cracks and blisters like PZT on SiO₂.

Furthermore the SrSiO₃/Sr₂SiO₄ interfacial layer proves to be a fabulous barrier layer which stops not only the Pb diffusion into the Si substrate very efficiently. It inhibits the

interdiffusion of all components of PST into the SiO₂/Si and vice versa. This offers the possibility to realise a thin interfacial layer for future integrations of ferroelectrics in all kind of devices like non-destructive read out ferroelectric RAMs [3 - 6] or simply as a buffer layer for the realisation of ferroelectrics onto Si without the common Ti/Pt bottom electrode [3, 7 - 9]. A first step was done in this study with PST as a buffer layer for PZT onto SiO₂. A direct comparison between PZT deposited on a common Ti/PT and a PST buffer layer revealed no large differences in the final electrical and piezoelectrical properties of PZT. This is a very promising result for the realisation of piezoelectric functional thin films without the use of a metallic bottom electrode.

All the above presented result are a good framework for further research and investigations. It would be beneficial to increase the viscosity of the actual sol to decrease the number of single layers to achieve thicker films. First trials to thicken it with an higher amount of 1,3-propanediol lead to a thicker single film but poorer performance in terms of tunability and loss. The measurement technique to determine the transition temperature needs to be improved. The homemade kit used in this study was not sensitive enough to measure the frequency dispersion of the maxima in the dielectric constant which is an essential characteristic of relaxor ferroelectrics. Our measurements show that the Curie temperature increases with increasing Mn content. The peak of the maximum permittivity broadens with increasing Mn content and develops a double peak characteristic with could not be explained at the moment.

A detailed theoretical understanding of the effects due to Mn doping of PST was presented. However, Mn is a special kind of dopant, it is a multivalence ion – it can appear as Mn²⁺, Mn³⁺ and Mn⁴⁺. Especially Mn⁴⁺ substitutes Ti⁴⁺ directly and consumes positive charged oxygen vacancies to get incorporated. Therefore it is unclear if one can catalogue this kind of substitution as donor or acceptor doping in the classical sense. It is necessary to use dopants which can be clearly identified, like for instance Nb as a donor or Ni as an acceptor dopant, to develop a full picture of the effect of B side doping of PST.

Furthermore it would be necessary to verify the adopted theory of the localised electron hopping between mixed Mn ions using either electron paramagnetic resonance (EPR) measurement, or inelastic neutron-scattering measurements.

At the end it is worth pointing out that localised electron hopping between mixed-valence Mn ions provides a possibility to induce double exchange effects of Mn^{2+} and Mn^{3+} or Mn^{4+} and thus brings about magnetic properties [10]. This may be the mechanism behind the magnetic effect in Mn doped PbTiO_3 observed by Kumar *et al.* [11]. The coexisting of ferroelectric and ferromagnetic properties in a single PST thin film would provide a fresh method to obtain multiferroics.

9.1 References

1. P. Du, X. Li, Y. Liu, G. Han, W. Weng; J. Europ. Ceram. Soc. 26, 2147 (2006)
2. X. Sun, H. Huang, S. Wang, M. Li, and X. Zhao; Thin Solid Films 516 (2008) 1308-1312
3. D.S. Shin, S.T. Park, H.S. Choi, I.H. Choi, and J.Y. Lee; Thin Solid Films 354 (1999) 251-255
4. C.C. Lin, L.W. Lai, C.Y. Lin, and T.Y. Tseng; Thin Solid Films 515 (2007) 8005-8008
5. X. Hu, H. Li, Y. Liang, Y. Wie, Z. Yu, D. Marshall, J. Edwards, R. Droopad, X. Zhang, A.A. Demkov, K. Moore, and J. Kulik; Applied Physics Letters 82 (2), 2003
6. Md.N.K. Bhuiyan, H. Kimura, T. Tambo, and C. Tatsuyama; Applied Surface Science 249 (2005) 419-424
7. Y. Wang, C. Ganpule, B.T. Liu, H. Li, K. Mori, B. Hill, M. Wuttig, R. Ramesh, J. Finder, Z. Yu, R. Droopad, and K. Eisenbeiser; Applied Physics Letters 80 (1), 2002
8. B.T. Liu, K. Maki, Y. So, V. Nagarajan, R. Ramesh, J. Lettieri, J.H. Haeni, D.G. Schlom, W. Tian, X.Q. Pan, F.J. Walker, and R.A. Mc Kee; Applied Physics Letters 80 (25), 2002

9. Y-H. Chun, C. Fragkiadakis, P. Bao, A. Lüker, R.V. Wright, J-S. Hong, P.B. Kirby, Q. Zhang, T.J. Jackson, M.J. Lancaster, “Tunable Bandstop Resonators and Filter on Si-Substrate with PST Thin Film by Sol-Gel Deposition”, 38th European Microwave Conference, EuMC2008
10. J. Yang, X.J. Meng, M.R. Shen, L. Fang, J.L. Wang, T. Lin, J.L. Sun, and J.H. Chu, *J. Appl. Phys.* 104, 104113 (2008)
11. M. Kumar and K.L. Yadav, *J. Phys.: Condens. Matter.* 19, 242202 (2007)

Appendix A: PZT actuated Diamond Cantilever Technology

Diamond cantilever actuators show high resonance frequencies but need also high actuation forces, pointing towards piezoelectric actuation by a PZT/diamond unimorph. In this study, which was a collaboration between Cranfield University and the University of Ulm/Germany, lead zirconate titanate ($\text{Pb}(\text{Zr},\text{Ti})\text{O}_3$, PZT) layers have been deposited onto nanocrystalline diamond films by sol-gel deposition to realize high-speed MEMS actuators. The fabrication technology is based on self-aligned patterning and on optical lithography. A mechanical resonance frequency of 3.9 MHz has been obtained for 30 μm cantilever length dominated by the nanodiamond Young's modulus of diamond of approximately 1000 GPa.

A.1 Introduction

Switches are an essential passive part of any electrical circuit. Used on-chip they need to be manufactured using microtechnology. However, in integrated circuits they are realized by switch transistors in many cases like for example in transmit/receive (TR) modules. But the conductivity limit in semiconductors will cause noticeable losses, even if heterostructure field effect transistors with high electron mobility channels are used. In some cases like phase shift antenna structures signal levels may be extremely low and transistor structures are difficult to integrate. An alternative concept is of course to use mechanical switches, which can be integrated into the semiconductor circuitry by direct monolithic integration or hybrid integration. Especially in the last case new materials may be implemented. However, although switching transistors have a high insertion loss, their signal delays may be in the ps-range, whereas most mechanical structures can only switch with μs -speed. In this investigation nanodiamond has been investigated as base material for cantilever switches operating at high switching speeds up to the ns-range. As figure of merit, the mechanical resonance frequency was chosen, which should then reach into the MHz-range.

Nanodiamond should provide a high resonance frequency of the basic cantilever, because of its high stiffness and low mass density. In respect to the driving principles, which may be considered, these are the electrostatic, electrothermal, and piezoelectric drives [1]. Each one has specific advantages and drawbacks. The electrostatic drive is fast but needs high driving voltages in combination with stiff materials, which may then interfere with the signal path. The thermoelectric bi-metal driving principle can provide high bending moments, but switching may be limited by thermal time constants. The piezoelectric actuation can generate high bending moments at low voltages, if a material with high piezo-coefficients like lead zirconate titanate ($\text{Pb}(\text{Zr,Ti})\text{O}_3$, PZT) can be used and if high driving fields can be generated without losses. It may therefore represent an optimum compromise, if the resonance of the diamond cantilever is not degraded by the mass density of the PZT piezoceramic. In this investigation a diamond/PZT unimorph has been investigated, using PZT deposited by a sol-gel technique as described previously [2]. This bimorph structure was then analysed theoretically, manufactured using a self-aligned patterning technique and dynamically tested.

A.2 Design

A.2.1 Modes of operation

Typically, two different modes can be used in the design of a piezoelectrically actuated unimorph. This is firstly the longitudinal mode (d_{33} -mode; Fig. 1a), where the polarisation of the piezo ceramic is laterally developed in the deposited film, which is in direction of the cantilever length. Both associated electrodes may be placed on top of the film. An applied electrical field stimulates elongation or contraction ($\epsilon_{x,1}$) depending on the polarization of the stimulating bias. Normally contraction is limited by the materials stability and therefore very limited in use. Elongation results in downward bending of the actuator, if the piezoelectric film is deposited on top of the beam.

In the transversal mode (d_{31} -mode; Fig. 1b) piezoelectrically induced stress is in the vertical direction and the film is either vertically stretched and contracted ($\epsilon_{x,2}$), with stretching being the more stable regime. In this case the beam is lifted up.

In general, the longitudinal piezoelectric strain coefficients of PZT (d_{33}) are approximately twice as large as the longitudinal ones (d_{31}) and can reach values up to 630 pm/V [3]; therefore this mode of operation is usually preferred. In this study, however, the transversal mode is used in order to make use of a self-aligned fabrication technology.

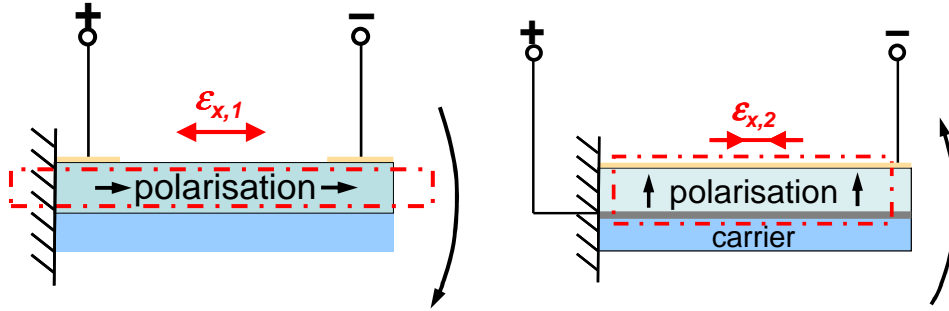


Fig. A1: Longitudinal and transversal mode of a piezoelectric unimorph. (a) Longitudinal mode: an applied electrical field induces an elongation of the piezo ceramic and leads thus to downward bending of the cantilever structure. (b) Transversal mode: an applied electrical field induces a contraction of the piezo ceramic and thus leads to upward bending of the cantilever structure.

A.2.2 Resonance Behaviour

Piezoelectric actuators are mostly used in switches or mechanical resonators. In both applications the mechanical resonance frequency represents the first limit in the speed of deflection. To the first order, the resonance frequency f_r of a bi-layer system like a piezoelectric PZT/NCD unimorph is given by [4]:

$$f_r = \frac{1.875^2 t}{4\pi L^2} \sqrt{\frac{E_{PZT}}{3\rho_{PZT}}} \left[\frac{A^2 B^4 + 2A(2B + 3B^2 + 2B^3) + 1}{(1 + BC)(AB + 1)(1 + B)^2} \right]^{1/2} \quad (\text{Eq. A1})$$

where E_{PZT} and ρ_{PZT} denote the Young's moduli and density of mass of the piezo ceramic, t and L are the total thickness and length of the cantilever beam, $A = E_{NCD}/E_{PZT}$ are the ratio of the Young's moduli of NCD and PZT, and $B = t_{NCD}/t_{PZT}$ the ratio of the layer thicknesses of NCD and PZT, respectively. A fixed thickness ratio of the NCD/PZT

results in a reciprocal square law relationship with cantilever length (see also slope of graphs in fig. A2).

It is seen, that high resonance frequencies are expected for thick and short beams on the one hand, and for stiff materials with low density of mass on the other hand. However, in these cases also high deflection forces are needed. Diamond is best suited as seen from table A1, and needs now to be combined with a deflection mechanism of high force, which had already been mentioned in the introduction and is the piezoelectric PZT/diamond unimorph.

Material	NCD	silicon	SiC	Al	Pt	PZT
Young's modulus (YM) [GPa]	~1000	160	400	70	168	80
Density of mass (ρ_m) [g/cm ³]	3.52	2.33	3.21	2.70	21.09	7.50
$\sqrt{YM/\rho_m}$ [10 ³ m/s]	16.9	8.4	11.2	5.1	2.8	3.3

Table A1: Materials properties for PZT and various base materials.

Fig. A2 illustrates the resonance frequencies, which can be obtained with these various base materials assuming a beam thickness of 2.0 μm as function of beam length using finite element analysis (FEA). The MHz-range is reached for diamond cantilevers of approximately 60 μm length, whereas in Si this length would need to be below 40 μm .

If diamond is employed as base material, the fully operational actuator would also need to contain an interfacial adhesion layer between the diamond and PZT ceramic layer, which is a 100 nm Pt film also serving as the bottom electrode, a 0.5 μm thick PZT film and a top electrode, which has been 50 nm Al in our case. Fig. A2 shows the resonances corresponding to each material and the shift due to the additional masses added in the multilayer stack for different cantilever lengths. It is observed, that the PZT film degrades

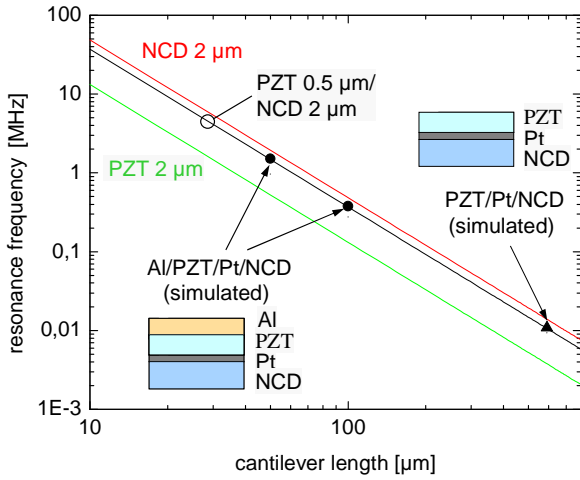


Fig. A2: Calculated resonance frequencies (Eq. A1) of single layer cantilevers of 2.0 μm PZT and NCD and multilayer stacks of 0.5 μm PZT / 2.0 μm NCD. Also plotted are three points for the simulation of three complete Al/PZT/Pt/NCD stacks of 50, 100, and 590 μm length with thicknesses as mentioned in the text; for Young's moduli see Table A1.

the resonance frequency by only 15 %. Adding the metallization layer will not cause any noticeable additional degradation.

A.2.3 Cantilever deflection

When applying an electrical field across the piezoelectric film, the strain generated between the piezoelectric film and the carrier substrate leads to a bending moment, which can either cause a deflection of the beam or can generate a force onto a base plate after the air gap is closed (see Fig. A3).

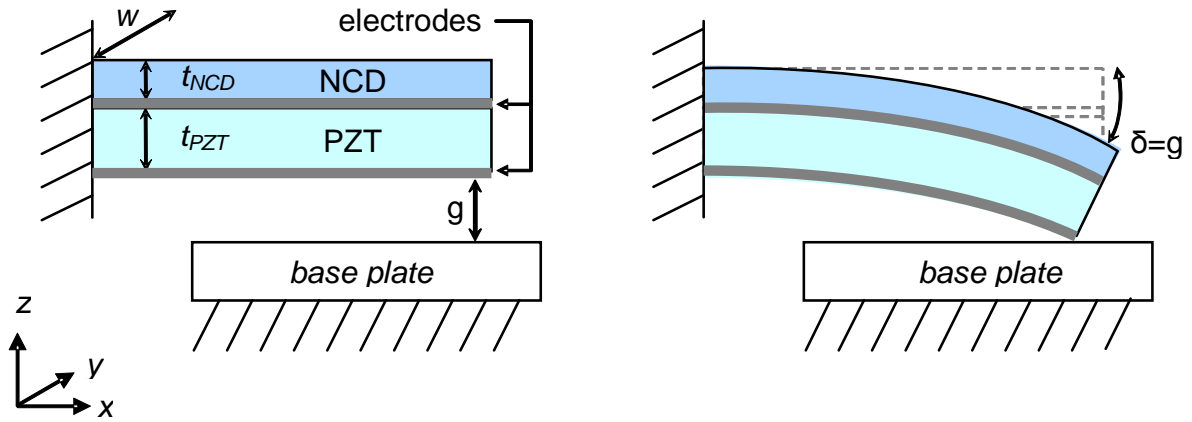


Fig. A3: Operation of PZT/NCD unimorph. Applied electrical load induces cantilever bending until an initial airgap (g) towards a base plate is closed ($\delta=g$); for even higher loads a force (F) onto the base plate is generated.

The Data of the bending moment, deflection and force respectively can be obtained from Eq. A2 and A3 [4]:

$$\delta = \frac{3L^2}{2t} \cdot \frac{2AB(1+B)^2}{A^2B^4 + 2A(2B + 3B^2 + 2B^3) + 1} \cdot d_{31} \frac{V}{t_{PZT}} \quad (\text{Eq. A2})$$

$$F = \frac{3wt^2 E_{PZT}}{8L} \cdot \frac{2AB}{(AB+1)(1+B)} \cdot d_{31} \frac{V}{t_{PZT}}, \quad (\text{Eq. A3})$$

where L , t , w are the cantilever length, thickness ($t_{PZT} + t_{di}$), width, d_{31} the transversal piezoelectric coefficient, V the applied voltage, E_{PZT} the Young's modulus of the piezoelectric layer, $A = E_{di}/E_{PZT}$ the ratio of the Young's moduli of diamond and PZT, and $B = t_{di}/t_{PZT}$ the ratio of the layer thicknesses, respectively.

As actuator in a switch application, in the quiescent condition (without external electrical field) the switch is typically in the open condition and the cantilever separated from the base plate contact by an airgap. A force onto the base is therefore generated only after the cantilever has touched the base plate and the deflection is equal to the airgap. The diagram in Fig. A4 shows a calculation of the generated force for a 0.2 μm airgap as function of applied voltage (cantilever data:

0.5 μm PZT on 2.0 μm NCD, width = 6 μm). It can be observed that the force increases for shorter cantilevers up to a maximum; for very short beams, where the maximum applicable field (~ 240 kV/cm; determined by device failure) results in a voltage which is too low to close the airgap, no contact force can be generated.

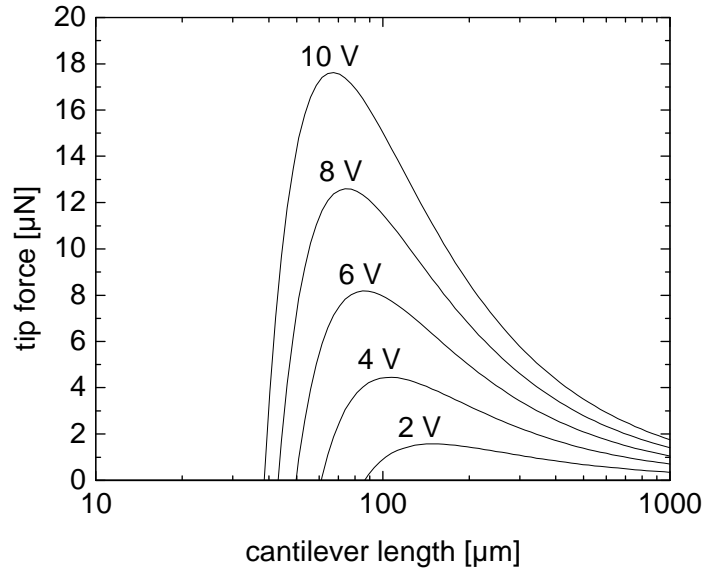


Fig. A4: Calculated tip contact force of PZT/NCD unimorph depending on beam length for different applied voltages (using equations (1) and (2)).

A.3 Technology

The starting material for the cantilever actuator structure was a 2.0 μm thick NCD film with a grain size of approx 50 nm deposited onto a (100)-oriented Si substrate. The film was grown by MWPECVD with high re-nucleation rate to obtain a stress balanced film (3D NCD; [5]). Usually the following step is the deposition of a metallic bottom electrode. This layer serves also as oxygen diffusion barrier during PZT deposition and the following post annealing step and as adhesion layer to accommodate the high bending moments required by the high diamond stiffness. PZT can be deposited by MOCVD [6], pulsed laser deposition [7], sputter deposition [8], ECR-PECVD [9], or sol-gel spin-on [10]. Most of these methods need a post-annealing step for dipole orientation in the

perovskite structure in the range of 550 – 650 $^{\circ}\text{C}$. In this work a sol-gel process was used for PZT deposition. The adhesion layer and bottom electrode was PVD platinum. The sol-gel PZT was deposited using a spin-coater and post-annealed at 570 $^{\circ}\text{C}$ in ambient atmosphere [2]. This method and material combination benefits from homogenous and large area deposition at low thermal budget. A

cross sectional view of this material system is illustrated with Fig. A5.

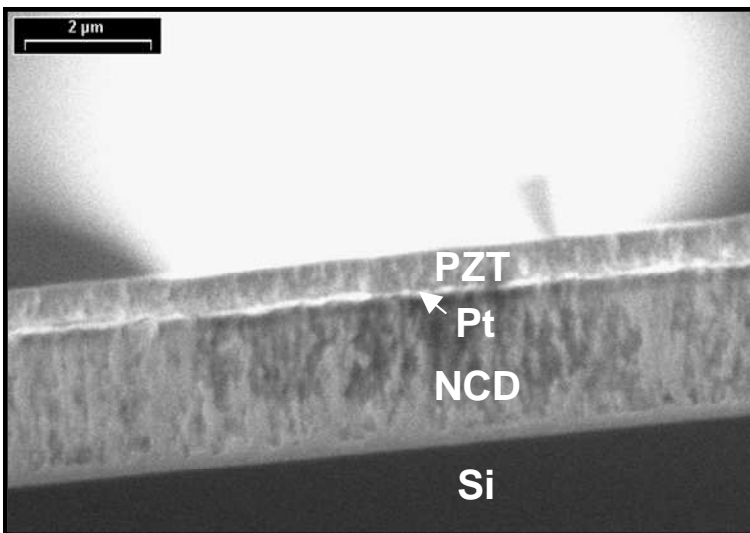


Fig. A5: Cross section SEM view of a sol-gel derived PZT film on NCD including Pt adhesion layer.

After realisation of the Si/NCD/Pt/PZT material stack the Al top electrode is deposited by evaporation and patterned by lithography to define the cantilever geometry. This pattern serves then as a hard mask for the anisotropic dry etching of the PZT/Pt/NCD stack in different atmospheres of Ar and Ar/O₂, respectively, and the undercut isotropic plasma etching in CF₄/O₂ of the Si-substrate to release the cantilever beam. It is therefore self-aligned and the top electrode covers the entire cantilever surface to obtain a uniform electrical field across the piezoceramic. In a last step the bottom Pt electrode is contacted

through a wet chemically etched window. Fig. A6 shows SEM micrographs of a processed 50 micron cantilever.

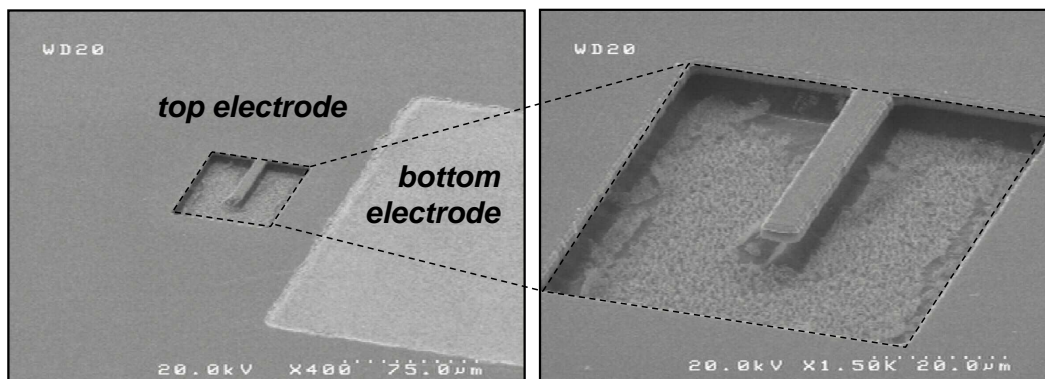


Fig.A6: Fabricated cantilever actuator with 50 μm length.

A.4 Results

Fig. A7 shows the PE hysteresis loops obtained after deposition of PZT. It can be observed that PZT indeed shows piezoelectric behaviour and is well suited for actuator fabrication.

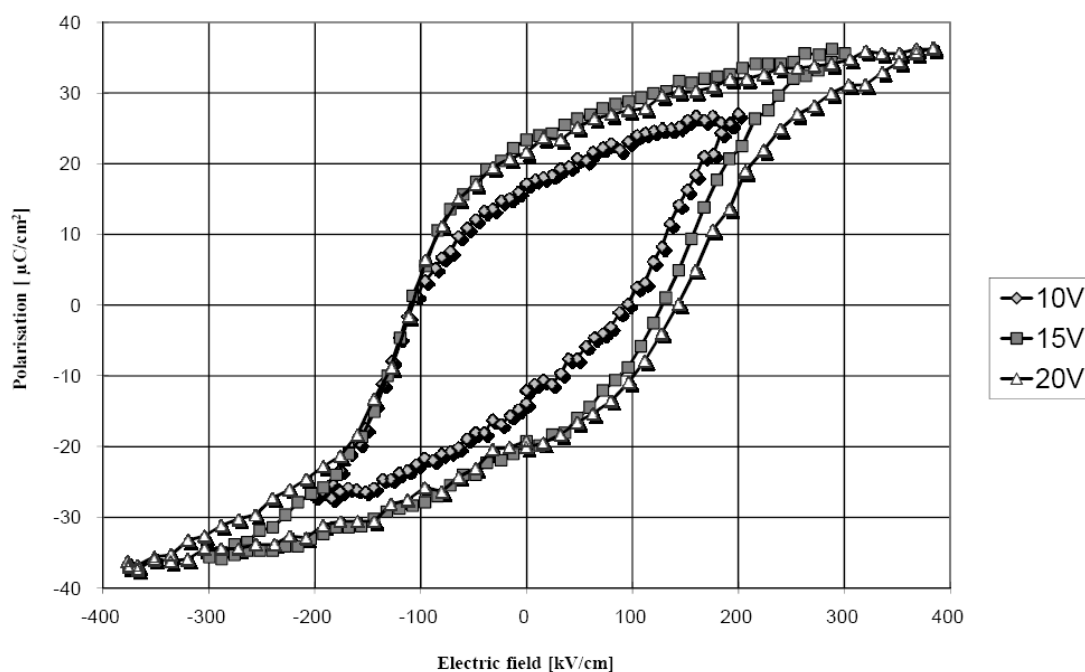


Fig. A7: Measured hysteresis curve of sol-gel PZT on NCD

Additionally, to optimise piezoelectric properties and prepare for operation the PZT film was poled at 120 °C under an electrical field of 200 kV/cm for 60 min. After this step DC leakage current density was determined under an electrical field of 50 kV/cm

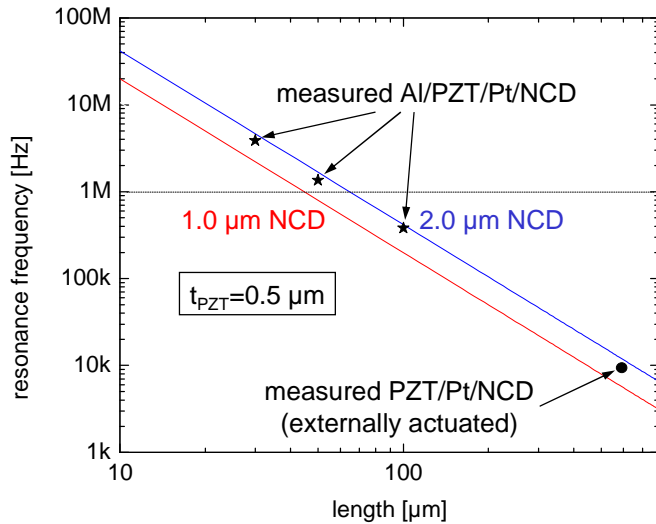


Fig. A8: Measured resonance frequencies of piezo actuators having different cantilever lengths. The 30 μm and 50 μm beams possess resonance frequencies in the MHz range as simulated.

where they are compared with their calculated performance using Eq. A1 for two NCD film thicknesses of 2.0 and 1.0 μm. This represents the experimental spread of thickness of the wafer used. It is seen, that the measured data follow indeed the theoretical prediction. Accordingly, resonances in the MHz-range are measured for the two shortest lengths of 50 μm and 30 μm with the highest resonance of 3.9 MHz for the 30 μm cantilever beam.

A.5 Conclusions

Nanodiamond piezoelectric cantilever actuators were realized using a sol-gel spin-on PZT piezoelectric ceramic film to demonstrate MHz mechanical resonance performance. Indeed cantilevers with 30 μm length exhibited 3.9 MHz resonance frequency, identified visually when being stimulation by a sinusoidal signal. The result is in full agreement with calculated and simulated data. Diamond piezoelectric actuators may therefore be considered a realistic concept to realize high speed resonators and switches. In comparison to the thermoelectric and electrostatic actuation this concept needs only a

approximately $2 \cdot 10^{-8} \text{ A/cm}^2$, which corresponds to a resistivity in the TeraΩcm regime.

To determine the mechanical resonance, the beams were stimulated by a sinusoidal signal and the resonance oscillation identified visually. To avoid inverse polarity across the piezo ceramic, a DC offset of half of the peak voltage was added. Cantilevers of 30, 50, 100 and 590 μm lengths have been stimulated.

Measured data are compiled in Fig. A8, where they are compared with their

small actuation voltage without static losses, it does not suffer from snap-in when used in switches, and pull back when opening the switch may be accelerated by reversing the driving potential.

A.6 References

1. J. Kusterer, P. Schmid, and E. Kohn, *New Diamond and Frontier Carbon Technology* 16 (2006) 295.
2. J. Kusterer, A. Lüker, W. Ebert, Qi Zhang, P. Kirby, E. Kohn: “Pb(Zr)O₃ on CVD Diamond – A New Material System for MEMS Applications”, *Diamond 2006, 17th European Conference on Diamond, Diamond-Like Materials, Carbon Nanotubes, Nitrides & Silicon Carbide*, 3-8 September 2006, Estoril, Portugal, [5.6.08].
3. APC International Ltd., “Piezoelectric Ceramics: Principles and Applications”, ISBN 0-9718744-0.
4. Q.-M. Wang, Q. Zhang, B. Xu, R. Liu, L.E. Cross, *J. Appl. Phys.* 86 (1999) 3352.
5. T. Zimmermann, K. Janischowsky, A. Denisenko, F.J. Hernández Guillén, M. Kubovic, D.M. Gruen and E. Kohn, *Diamond and Related Materials* 15 (2006) 203.
6. J.S. Zhao, D.-Y. Park, M.J. Seo, C.S. Hwang, Y.K. Han, C.H. Yang, K.Y. Oh: *J. Electro Chemical Society* 151 (2004) C283.
7. Q. Wan, N. Zhang, L. Wang, Q. Shen, C. Lin: *Thin Solid Films* **415** (2002) 64.
8. S. Srinivasan, J. Hiller, and B. Kabius, O. Auciello, *Applied Physics Letters* 90 (2007), 134101.
9. S.-O. Chung, H.-C. Lee, W.-J. Lee: *Jpn. J. Appl. Phys.* **39** (2000) 1203.
10. SJ. Zeng, L. Wang, J. Gao, Z. Song, X. Zhu, C. Lin, L. Hou, E. Liu: *J. Crystal Growth* **197** (1999) 874.

Appendix B: Curriculum Vitae

Arne Lüker

Wachtelweg 11 ▪ 32609 Hüllhorst/Holsen ▪ Germany

Email: arnelueker@aim.com



Personal Details:

Date of birth: 04.05.1975
Place of birth: Bremen
Citizenship: EU-German
Marital status: single

Additional Qualifications:

2006 – 2007 Marie Curie Fellow at IMEC,
Leuven/Belgium
Sputter deposition of AlN
1994 – 1995 Camphill-Rudolf Steiner-School,
Aberdeen/Scotland
Supervisor of children with special needs
Certificate of Completion,
Practice in Integrated Therapeutic
Communities

Work Experience:

2008 *Research Assistant, Cranfield University/England*
Characterisation of Ni/Ti-SMA Alloys
2004 – 2005 *Project Engineer, Research Center Karlsruhe/Germany*
Development of MEMS for space science applications
1996 – 2002 *Technik & Design, Lübbecke/Germany*
Independent draftsman

Studies:

2005 – 2008 *Ph.D Student, Cranfield University/England*
Material Science and Nanotechnology
Thesis: *Sol-Gel derived Ferroelectric Thin Films for Voltage Tunable Applications*
1999 – 2004 *University of Applied Sciences Münster/Germany*
Engineering Physics, major Micro-Engineering
Thesis: *Sub-Micron 100 keV E-Beam Lithography for Self Supporting Metallic High Aspect Ratio Structures Electroplated Directly onto Silicon*

1995 – 1998 *Carl-Severing-Schools Bielefeld/Germany*

Polytechnic qualification as a professionally recognized
Physical-Technical Assistant

1989 – 1994 *Waldorf School Evinghausen/Germany*

Internships:

2002 Research Center Karlsruhe

1997 Deutsche Wurlitzer GmbH and University Osnabrück

Memberships:

2005 – 2008 Cranfield University Walking Club

Scientific Publications:

1. A. Lüker, O. Sternberg, H. Hein, J. Schulz, K.D. Möller; „Thick capacitive meshes on polyimide substrates”; *Infrared Physics & Technology*, **45**, 2, 153, 2004
2. J. Kusterer, A. Lüker, Y. Men, W. Ebert, P. Kirby, M. O’Keefe, E. Kohn; „Pb(Zr,Ti)O₃ on CVD Diamond – A New Material System for MEMS Actuators”, Diamond 2006, Estoril (PT), September 2006
3. J. Kusterer, A. Lüker, W. Ebert, Q. Zhang, P.B.Kirby, E. Kohn; „ Piezo-actuated Nanodiamond Cantilever Technology for High Speed Applications”, Diamond 2007, Berlin (DE), September 2007
4. J. Kusterer, E. Kohn, A.Lüker, P.B. Kirby, M.F. O’Keefe; „Diamond high speed and high Power MEMS switches”, 4th EMRS DTC Technical Conference – Edinburgh 2007
5. T. Riekkinen, T. Mattila, S. van Dijken, A. Lüker, Q. Zhang, P.B. Kirby, A.M. Sánchez; “Ferroelectric parallel-plate capacitors with copper electrodes for high-frequency applications”, *Appl. Phys. Lett.* **91**, 252902, 2007
6. A. Lüker, H. Hein, J. Schulz, N. Dambrowsky, O. Sternberg, M.J.Sweetgall, K. Abdijalilov, K.D. Möller, H. Grebel; “Band pass filters in the 1 µm spectral region: Thick metal screens”, *Infrared Physics & Technology*, **51**, 3, 178, 2008
7. J. Kusterer, A. Lüker, P. Herfurth, Y. Men, W. Ebert, P. Kirby, M. O’Keefe, E. Kohn; „Piezo-actuated Nanodiamond Cantilever Technology for High Speed Applications” *Diamond and Related Materials*, **17**, 7-10, 1429, 2008
8. Y-H. Chun, C. Fragkiadakis, P. Bao, A. Lüker, R.V. Wright, J-S. Hong, P.B. Kirby, Q. Zhang, T.J. Jackson, M.J. Lancaster, “Tunable Bandstop Resonators and Filter on Si-Substrate with PST Thin Film by Sol-Gel Deposition”, 38th European Microwave Conference, EuMC2008.
9. C. Fragkiadakis, A. Lüker, R.V. Wright, L. Floyd, and P.B. Kirby; “Growth and high frequency characterization of Mn doped sol-gel Pb_xSr_{1-x}TiO₃ for frequency agile applications” *Journal of Applied Physics* **105**, 1 (2009)

10. D. Bhattacharyya, A. Lüker, Q. Zhang and P.B. Kirby, "Structural evaluation of sol-gel derived lead strontium titanate diffusion barrier for integration in PZT transducer design", accepted by *Thin Solid Films*, October 2009
11. A. Lüker, Q. Zhang, and P.B. Kirby, "Study of compositional change in the interfacial regions between lead strontium titanate (PST)/SiO₂ and lead zirconate titanate (PZT)/SiO₂ by Auger Emission Spectroscopy", accepted to *Thin Solid Films*, November 2009,
12. A. Lüker, Q. Zhang, and P.B. Kirby, "The Effect of Mn Doping on the Tunability of Lead Strontium Titanate (PST)" submitted to *Journal of Physics D*, 2009

Other Publications:

1. A. Lüker; "Ferroelectric Phase Shifters", www.microwave101.com, April 2006
2. A. Lüker; "Over Hill and Dale", *Entropy*, May 2006
3. A. Lüker; "Leuven it up...", *Entropy*, December 2006
4. A. Lüker; "How To Do Paris In Three Days...", *Entropy*, February 2007
5. A. Lüker; "Phased Array Antennas", www.microwave101.com, December 2008

Awards:

1. "Best Poster Award":
J. Kusterer, A. Lüker, Y. Men, W. Ebert, P. Kirby, M. O'Keefe, E. Kohn;
„Pb(Zr,Ti)O₃ on CVD Diamond – A New Material System for MEMS Actuators”,
Diamond 2006, Estoril (PT), September 2006
2. Cranfield University Walking Club 2005-2006 "Stella Artois Navigation Award"